UNIVERSITY OF CALIFORNIA
SANTA CRUZ

Toward resolving stable high-resolution kinematic rupture models of large earthquakes by joint inversion of seismic, geodetic and tsunami observations

A dissertation submitted in partial satisfaction
of the requirements of the degree of

DOCTOR OF PHILOSOPHY

in
EARTH SCIENCES
with an emphasis in GEOPHYSICS

by

Han Yue
June 2014

The Dissertation of Han Yue is approved:

_____
Professor Thorne Lay, Chair

_____
Professor Susan Schwartz

_____
Professor Quentin Williams

_____
Dr. Rushan Wu

_____
Tyrus Miller
Vice Provost and Dean of Graduate Studies

Table of Contents

List of figures

Figure 7.3 ••• 248

Figure 7.4 ••• 257

Figure 7.5 ••• 260

Figure 7.6 ••• 262

Figure 7.7 ••• 265

Figure 7.8 ••• 267

Figure 7.9 ••• 268

Figure 7.10 ••• 275

Figure 7.11 ••• 278

Figure 7.S1 ••• 287

Figure 7.S2 ••• 289

Figure 8.1 ••• 293

Figure 8.2 ••• 296

Figure 8.3 ••• 298

Figure 8.4 ••• 307

Figure 8.5 ••• 309

Figure 8.6 ••• 313

Figure 8.7 ••• 315

Figure 8.8 ••• 318

Figure 8.9 ••• 319

Figure 8.10 ••• 322

Abstract

Toward resolving stable high-resolution kinematic rupture models of large earthquakes by joint inversion of geodetic, teleseismic and tsunami observations

Han Yue

In this thesis, I summarize the research that I have done at UC Santa Cruz involving my development of joint inversion approaches using hr-GPS, teleseismic body and surface waves, regional seismic, campaign GPS, InSAR and tsunami datasets, to investigate the kinematic rupture patterns of large earthquakes. In eight different studies of rupture models of the 2011 Tohoku earthquake, 2012 Indo-Australia earthquake, 2012 Costa Rica earthquake, 2013 Craig earthquake, 2010 Mentawai earthquake, 2013 Pakistan earthquake, 2010 Chile earthquake and 2014 Iquique earthquake, I adopted each available dataset progressively in my joint inversion algorithm, so that in my current approach I can model all of the types of datasets simultaneously. As noted in this thesis, the teleseismic datasets provide good temporal resolution of the rupture process, while geodetic datasets have good spatial resolution. Tsunami datasets have good spatial resolution of slip near the trench. The joint inversion combines the advantage of each dataset, yielding stable and high-resolution rupture models with detailed spatial and temporal information. Resolving a robust and detailed rupture model helps us to understand co-seismic rupture properties,

such as depth dependent energy release patterns, super-shear rupture, and tsunami excitation. Comparing the inter-seismic locking pattern and post-seismic stress release pattern with the co-seismic rupture model helps to investigate the locking and releasing behavior of the fault plane through the earthquake cycle, the stress release level of large earthquakes and the relationship between the main shock ruptures, aftershocks and non-seismogenic deformation.

Vita

Degree	Attending year	School	Advisors
Ph. D.	2010-	UC Santa Cruz	Thorne Lay
M. S.	2007-2010	Peking University	Yongshun Chen
B. S.	2003-2007	Peking University	

Publications

13. Yue H., Lay T., Rivera L. An C. Vigny C. Tong X. (2014) Fault slip to the trench in the Mw = 8.8 2010 Maule, Chile earthquake from joint inversion of hr-GPS, teleseismic, InSAR and tsunami observations. *Journal of Geophysical Research: Solid Earth, (in revision)*

12. Lay, T., Yue, H., Brodsky, E. E., & An, C. (2014). The April 1, 2014 Iquique, Chile Mw 8.1 earthquake rupture sequence. *Geophys.Res. Lett.* doi: 10.1002/2014GL060238

11. Yue H. Lay T., Rivera L. Bai Y. Yamazaki Y.. Cheung K.F. Hill E.M., Sieh K., Konko W. and Muhari A. ,(2014), Rupture process of the 2010 Mw 7.8 Mentawai tsunami earthquake from joint inversion of near-field hr-GPS and teleseismic body wave recordings constrained by tsunami observations. *Journal of Geophysical Research: Solid Earth, (in revision)*

10. Yue, H., T. Lay, J. T. Freymueller, K. Ding, L. Rivera, N. A. Ruppert, and K. D. Koper (2013), Supershear rupture of the 5 January 2013 Craig, Alaska (Mw 7.5) earthquake, Journal of Geophysical Research: Solid Earth, 118(11), 2013JB010594; doi:10.1002/2013JB010594

9. Yue H., T. Lay, S. Y. Schwartz, L. Rivera, M. Protti, T. H. Dixon, S. Owen andA. V. Newman, (2013) The 5 September 2012 Nicoya, CostaRica Mw 7.6 earthquake rupture process from joint inversion of high-rate GPS,strong-motion, and teleseismic P wave data and its relationship to adjacentplate boundary interface properties. J. Geophys. Res. 2013JB010187;doi:10.1002/jgrb.50379

8. Yue, H. and T. Lay (2013), Source Rupture Models for the Mw 9.0 2011 Tohoku Earthquake from Joint Inversions of High-Rate Geodetic and Seismic Data. Bull. Seis. Soc. Amer. May

2013103:1242-1255, doi:10.1785/0120120119

7. Yue, H, T. Lay and K. D. Koper (2012), En Echelon and Orthogonal Fault Ruptures of the 11 April 2012 Great Intraplate Earthquakes. Nature, 490, 245-249,doi:10.1038/nature11492.

6. Yue, H., Y. J. Chen, E. Sandvol, J. Ni, T. Hearn, S. Zhou, Y. Feng, Z. Ge, A. Trujillo, Y. Wang, G. Jin, M. Jiang, Y. Tang, X. Liang, S. Wei, H. Wang, W. Fan, and Z. Liu (2012), Lithospheric and upper mantle structure of the northeastern Tibetan Plateau, J. Geophys. Res., 117, B05307, doi:10.1029/2011JB008545.

5. Lay, T., H. Kanamori, C. J. Ammon, K. D. Koper, L. Ye, H. Yue, and T. M. Rushing (2012), Depth-varying rupture properties ofsubduction zone megathrust faults, J. Geophys. Res., 117, B04311,doi:110.1029/2011JB009133.

4. Yamazaki,Y., T. Lay, K. F. Cheung, H. Yue and H. Kanamori (2011), Modeling near-field tsunami observations toimprove finite-fault slip models for the 11 March 2011 Tohoku earthquake, Geophys.Res. Lett., 38, L00G15 doi:10.1029/2011GL049130.

3. Yue, H., and T. Lay (2011), Inversion of high-rate (1 sps) GPS data for rupture process of the 11 March 2011 Tohoku earthquake (Mw 9.1), Geophys. Res. Lett., 38, L00G09,doi:10.1029/2011GL048700.

2. Wei, S.,Y.J. Chen, E. Sandvol, S. Zhou, H. Yue,G. Jin et. al. (2010), Regional earthquakes in northern Tibetan Plateau:Implications for lithospheric strength in Tibet, Geophys Res. Lett,37(19), L19307.doi: 10.1029/2010GL044800

1. Yue H., Zhang Z. and Chen Y. J., (2008) Interaction between adjacent left-lateralstrike-slip faults and thrust faults: the 1976 Songpan earthquake sequence. ChinessSci. Bull. Volume 53, Number 16, 2520-2526 doi:10.1007/s11434-008-0210-z.

Acknowledgements

My study as a graduate student at UC Santa Cruz has come to an end. In my four years at UC Santa Cruz, I learned much from colleagues around here and I would not have been able to reach this point and finish this thesis without extensive help from them. I am deeply grateful to all of them. In particular, I am in great debt to my advisor, Professor Thorne Lay. Thorne helped me find interesting projects to work on and shared his deep scientific insight and knowledge with me. He always encourages me to go to different meetings to present my work, has an open door to me answering my questions with patience, wants to hear about latest research results, and has endless suggestions of new ways to approach problems. Thorne has been a great support for me through hard times with his encouragement and confidence in me. I am grateful beyond words for this life changing and great experience to work with him.

I would also like to acknowledge the members of my dissertation committee. I thank Prof. Susan Schwartz for her support for me to attend several SCEC meetings and for giving me the opportunity to participate in the 2010 Nicoya earthquake research. I thank Prof. Quentin Williams for his suggestions about mineral physics and seismic image interpretation which helped a lot in my first JGR publication. I thank Dr. Rushan Wu who extended my understanding of seismic scattering and imaging.

My deep gratitude also goes to Prof. Emily Brodsky who holds seismo coffee almost every morning, in which I keep up with the most recent developments of

seismology and physics of earthquakes. She always opens her door and provides sincere suggestions to me. I also thank the faculty members who taught classes to me, particularly Francis Nimmo and Patrick Chuang, whose Order of Magnitude Estimation is the most interesting and helpful class I have had; Elise Knittle, whose Mineralogy class filled in the gap of my knowledge about earth materials; Eli Sillver, for whom I TAed for two quarters learned much more about tectonics. Xiao-bi Xie also taught me lots of basics of seismology for multiple scales.

I would also like to thank my advisor in Peking University, Yongshun John Chen, who brought me to geophysics and seismology and inspired me. His direction and recommendation brought me here to study in the US to have a brighter future. Thanks also go to all my teachers in Peking University, whose teaching not only built up my basic knowledge of earth science, but also built up my view of life, career and the world. I consider myself a slug but even more a PKUer, where I started to find myself.

Great thanks also goes to all my co-authors, especially Luis Rivera, Yoshiki Yamazaki, Jeffrey Freymueller, Keith Koper, Emma Hill, Marino Protti, Chao An and Xiaopeng Tong, who helped my research in many different ways. Luis essentially computed seismic Green functions for almost all of our inversion studies. Yoshiki performed tsunami modeling for tens of our rupture models, providing strong constraints on our rupture patterns. Keith provides us with back-projection techniques, by which we could constrain rupture velocity in numerous cases. Jeffrey, Emma and Marino provided us with extensive regional geodetic and seismic observations of

several earthquakes, which lead to successful study of these events. Chao An and Xiaopeng Tong are also my friends and classmates. I am glad we still keep connection and were able to collaborate on analysis of the 2010 Maule event, using a joint inversion with tsunami and geodetic datasets.

I give special acknowledgement to my parents, for their upbringing, support and love throughout my life. And also to my wife, Lian, who brings me happiness and peace to my heart all these years.

Special thanks go to our friends, who make my life so fun and colorful. Abbey Crystal is the first friend we made in the US and means so much to Lian and me. Xiaofei Pu is the one that we consider as one of the family. Jiazhong and Sai are such a cute couple that we shared lots things together with. Chia-Te Chien, Pei-Chuan Chuang and their lovely Amber also bring us so much happiness. Yingcai Zheng and Qiaoer always help us and give us suggestions as a big brother and sister to us. Thanks to my best friends, Haowen Dang, Xi Zhang, Runqiang Li, 614, Ming Chen, for their friendship and connection which means a lot to me.

I thank the staff of our department and all my colleges, e.g. Jennifer Fish, Cathy Smith, Jenna Scarpelli, Yingcai Zheng, Lingling Ye, Qingjun Meng, Abbey Crystal, Patric Fulton, Vincent Allegre, Yaofeng He, Chunhua Hu, Stephen Hernandez, Nicholas Van der Elst, Megan Avants, Esteban C. Shibaja, Jack Walter, Erin Todd, Stephanie Taylor, Stephanie Nale, and Grace Barcheck. You guys supported me a lot whenever I have had a hard time in my research or life.

I also thank my co-workers in Chinese fellowship, Hsiung Papa and Mama, Jenny

Jih, Nasya Chang, Bro. Tung and Grace and all other participants. The Chinese fellowship is an important part of my life which brings me the feeling of a family. Thanks also go to my friend that I know in ISI, Peggy and Sturt. Discussion with them is always fun.

Chapter 1

Introduction

1.1 Background

The last decade experienced a global temporal cluster of great earthquakes following the great 2004 Sumatra-Andaman earthquake. Although it is hard to prove a causal relationship between the Sumatra-Andaman event and the following global scale increase in rate of great earthquakes, the occurrence of numerous large earthquakes has provided enhanced opportunities to study the physics of the seismic cycle of inter-seismic coupling, huge seismic ruptures, and post-seismic stress release. For large earthquakes (M_w > 7.0) globally, seismologists seek to characterize the spatial distribution and temporal evolution of their rupture processes, going beyond point-source representations of the focal mechanism. Finite-fault models need to be developed for every large earthquake.

Simultaneously, during the last decade geophysicists have been able to harvest extensive observations of earthquake cycle processes from greatly expanded seismic, geodetic, gravity, and tsunami observations. Seismic observations have been used for finite-fault inversions since the 1980s [*Hartzell and Heaton,* 1983; *Ji et al.* 2002a,b], but the data density and distribution for broadband seismic recordings began to explode around 1995. GPS and InSAR techniques were developed and applied to investigate earthquake cycles and ruptures since the 1990s [*Goldstein et al.,* 1993;

Massonet et al., 1993; *Freymuller et al.,* 1994; *Burgeman et al.,* 2000; *Simons and Rosen*, 2007]. Tsunami-based finite-fault models also were first developed in the early 1990s [*Satake* 1993*; Johnson et al.* 1996], initially relying on complex tide-gauge recordings in harbors (usually analog records) and more recently with deep water ocean bottom pressure gauges that are much more robust for source investigations.

In the early days of finite-fault inversions, the quality of the results suffered from the sparse distribution of observations of different types and limited efforts to simultaneously reconcile the data from different recording systems. During the last decade though, the analysis of large earthquake rupture processes has benefitted from the dense and extensive distribution of seismic and geodetic networks, such as the EarthScope U.S. Array, Japanese F-Net, Hi-Net, Kik-Net and K-Net, and EarthScope Plate Boundary Observatory (PBO) and other UNAVCO projects. There is also valuable data resulting from the launch of several geodetic satellites, such as ALOS and Landsat 8. The NOAA deployment of Deep-ocean Assessment and Reporting of Tsunami (DART) stations has profoundly improved monitoring and analysis of tsunami waves in the Pacific, and now additional initiatives are densifying the coverage (e.g., Chilean DART deployments) and expanding the coverage (e.g., German/Indonesian DART deployments in the Indian Ocean).

Hundred of studies have now been conducted to investigate finite-fault models for large earthquakes, and routine solutions are being posted by USGS NEIC, Japan Earthquake Research Institute, and other programs around the world. Generally, for every great event, e.g., 2004 Sumatra-Andaman, 2008 Wenchuan, China, 2010 Maule,

Chile, and 2011 Tohoku, Japan, tens of finite-fault models have been developed using various subsets of the mentioned observations jointly or separately. There are some similarities, but also substantial differences amongst the resulting models, even for those obtained using similar observations. Such discrepancies result from different inversion approaches, as well as the intrinsic resolution associated with each dataset. Pursuing a Ph.D. amidst this flourishing torrent of activity is rather daunting, as one does not want to simply produce yet another finite-source model amongst many. The strategy I have adopted is to exploit specific attributes of newly acquired datasets in joint inversions that result in improved finite-fault representations due to complementary resolution of different data sets.

1.2 Resolution of Finite-Fault Models

Generally, spatial resolution, temporal resolution and moment resolution are the three basic factors that geophysicists want to resolve robustly in a finite-fault model.

Spatial resolution measures how well the slip distribution is resolved in an absolute sense. Factors influencing spatial resolution include the spatial extent of the rupture and heterogeneities of slip distribution. This is the basic information about the rupture finiteness. Some aspects of rupture finiteness can be inferred from aftershocks and afterslip distribution, inter-seismic locking patterns and other observations, but the primary information about spatial finiteness must be inferred from dynamic and static deformations of the ground recorded by seismic, geodetic, gravity and tsunami

observations. Robust characterization of spatial finiteness is central to investigations of the earthquake cycle.

Temporal resolution characterizes the evolution of moment release during the fault sliding. The overall moment release process can be described to first-order with a source time function. For a discretized finite-fault model, this is related to how fast and how far rupture propagates over the fault plane and the local slip evolution at each subfault. Rupture propagation is an important factor for estimating space-time rupture release rate. Generally, higher rupture velocity results in more intense seismic energy radiation. An extreme case is called super-shear rupture, for which the rupture velocity is higher than the shear velocity. This can cause intense directionality of ground shaking that causes increased hazards in the rupture direction and that may activate seismicity on splay faults [*Bouchon and Harabulut,* 2008]. Details of the source time function are intrinsically related to the local frictional properties and are the primary information we have about how ruptures actually progress. Systematic depth variations in seismic radiation for megathrust events, with the shallow regions tending to preferentially release low frequency seismic energy, while relatively enhanced levels of high frequency energy release down-dip [*Koper et al.,* 2011; *Lay et al.,* 2012] provide one type of source time function detail that has only recently begun to be resolved. Such frequency dependent energy release is important for anticipating ground shaking hazards from thrust events, along with revealing aspects of the frictional/sliding heterogeneity under varying pressure and temperature

conditions on the megathrust. Details of the temporal rupture energy release can also potentially reveal information about the rate-state friction law distribution with depth.

In a general sense, moment resolution means the resolution of the total seismic moment release for the event, which is a model-dependent estimate; while in a specific sense, moment resolution refers to resolution of the local moment release at each subfault. Moment resolution is related to the slip and its spatial distribution during an earthquake, and good resolution is crucial for accurately calculating stress drop and other integrative measures of stress release. Reliable estimates of total moment and slip are also important for estimating the time interval of earthquake repeat cycles.

Spatial, temporal and moment resolution are provided to some degree by each dataset mentioned above, with each data type having variable intrinsic sensitivity to these factors. Inversions that are based on a single dataset tend to fail to predict some aspects sensed by other datasets, so combining the data in strategic ways to optimize resolution appears to be a key strategy.

1.3 Resolution of each dataset.

Resolution of Teleseismic Data

Teleseismic datasets were the first to be used to investigate rupture process and source finiteness, due to the global deployment first World-Wide Standardized Seismological Network (WWSSN) and then Federation of Digital Seismic Networks (FDSN) stations. These provided accessible teleseismic ground motion records for

all large earthquakes with fairly extensive epicentral distance and azimuthal distributions. Having openly available global network data provides a stable research and monitoring environment for seismologists to study all large earthquakes. Teleseismic P and S body-waves are most commonly used to invert for finite-rupture models. Popular inversion algorithms include a linear kinematic inversion technique, the so-called multi-time-window inversion [*Hartzel and Heaton, 1973*] and non-linear simulated annealing inversion [*Ji et al. 2002a,b*]. The simulated annealing technique has been adopted by the USGS-NEIC to routinely perform finite-fault model inversions for all magnitude >6.5 earthquakes since 2004. Both inversion methods show comparable resolution and inversion stability, and the general issue of teleseismic inversion now lies in the intrinsic limitations of teleseismic records to resolve fault finiteness. Inversions with only teleseismic body waves often fail to predict the total seismic moment, depending on the parameters used in inversion. Thus, surface waves are also used in seismic inversions like the simulated annealing procedure, because the low-frequency energy content of surface waves is more sensitive to the total moment.

It is also known that teleseismic body waves have quite limited spatial resolution, even for large earthquakes. For the multi-time-window inversion approach, the rupture pattern is strongly controlled by the assumed rupture velocity [*Lay et al.,* 2010], which is because the kinematic constraint has an important influence on the intrinsic space-time tradeoff in the rupture imaging. Teleseismic P waves travel with high apparent horizontal velocity (~ 20 km/s), due to having steep incident angles.

This results in low spatial resolution when using only P waves in finite-fault model inversion. The dominant frequency content of teleseismic P waves is 0.01-1 Hz, which leads to estimated spatial resolution of >50 km. The compensating benefit of data with steep incidence angle is that they provide high temporal resolution, so that the source time function in the NEIC finite-fault model and other studies is generally well-resolved by the seismic signals.

Generally teleseismic body waves provide good temporal resolution but limited spatial and moment resolution. Adding surface waves can help to constrain the total moment, and for very large events they provide constraints on source directivity as well.

Resolution of Geodetic Data

Campaign GPS and InSAR observations are now key geodetic observations used in finite-fault model inversions. GPS data provide 3 component ground displacement observations, with horizontal accuracy of centimeters. InSAR data constrains the displacement in a Line of Sight (LOS) direction, with an accuracy of around ten centimeters. Both data types are influenced by vegetation and satellite configurations. Geodetic data tends to be ideal for resolving shallow earthquakes in arid continental regions, e.g., the 1992 Landers [*Massonet et al.* 1993], 2008 Wenchuan [*Shen et al.* 2009], and 2010 Baja California [*Wei et al.* 2011] earthquakes. The dense sampling of InSAR can cover the entire fault region, providing good constraints on the along strike rupture distribution and faulting geometry.

Most large thrust earthquakes are located in subduction zones, so that geodetic observations usually only constrain the on-land displacement field, located far from the main slip zone. Inversion with geodetic observations has strong trade-offs between rupture location and amplitude, which make it very hard to determine exact rupture distribution in the along-dip direction. In many/most cases, geodetic-based inversions relying only on static ground motions on-land fail to resolve significant slip near the trench.

Generally, for continental earthquakes, geodetic observations provide very good spatial and moment resolution. However, for off-shore earthquakes, geodetic observations tend to only provide good along-strike spatial resolution, but not good along-dip resolution. In this case, the moment resolution also trades off with the along-dip slip distribution. There are no timing information for static geodetic observations, so temporal resolution is only provided for high-rate GPS ground motions.

Resolution of Tsunami Data

Many large megathrust events generate significant tsunami waves, which is not only the main hazard, but also an important approach to quantifying the co-seismic rupture. Tsunami waves can be observed by deep ocean bottom pressure gauges, tide-gauge recordings, and on land inundation and run-up measurements. Modeling of tsunami waves can be realized by solving shallow water wave equations with bathymetry structure. It is easier to model tsunami waves in the deep ocean because they are less impacted by accuracy of the bathymetry model. Thus DART

observations are preferred for tsunami modeling now that the NOAA DART buoy system has expanded to 39 stations. Modeling tsunami waves in coastal area requires very detailed near coast bathymetry and harbor models and non-linear algorithms to calculate the tsunami waves precisely. The intrinsic non-linear wave propagation near the coast also makes it hard to adopt tsunami waves to any linear finite-fault inversion [*Satake et al.,* 2013]. Modeling tsunami inundation and run-up is very complex and non-linear and relies on detailed bathymetry and topography models (and built-infrastructure models in some cases), thus inundation observations have only been used to test finite-fault model effectiveness with forward modeling, and not yet incorporated in inversions.

Tsunami waves propagate at very low velocity (~200 m/s) compared with seismic waves (5-20 km/s apparent horizontal velocity). Such slow wave velocities provide good spatial resolution for tsunami waves, despite the long-wavelengths involved. In particular, the excitation of tsunami waves is very depth dependent, as shallow rupture tends to produce large ocean floor displacement and to excite high frequency, large amplitude tsunami. Tsunami signal thus provide significantly improved spatial resolution for both along-strike and along-dip directions, extending to near the trench.

In my early exploration of finite-fault model inversions, we iteratively modify inversion parameters to make forward-model predictions match tsunami observations. Such an iteration process generally takes several months to obtain an acceptable joint model [*Yue et al.,* 2014; *Yamazaki et al.,* 2011]. Inversions with tsunami waves can be performed with linear algorithms, as long as care is taken to use wavelengths and data

configurations that are not overwhelmed by non-linear effects [*Satake,* 1993; *Satake et al.,* 2013].

1.4 Developments of Joint Inversion Approaches

Adopting multiple datasets in joint inversions is clearly realizable if each dataset can be inverted separately. Conceptually, since each dataset has specific resolution of source spatial, temporal and moment characteristics, joint inversion can potentially exploit complementary information from each dataset to obtain a reliable finite-fault model with improved spatial, temporal and moment resolution. A major challenge in such joint inversions is the need to understand underlying limitations and physical aspects of seismology, geodesy, tsunami modeling and inversion techniques to be able to incorporate the disparate data properly in a joint inversion. This is achieved by collaboration with experts in relevant fields. The technical data processing and Green function computation has been done by collaborators: Luis Rivera, Yoshiki Yamazaki, Chao An, Susan Owen, Emma Hill, Jeffrey Freymuller, and Xiaopeng Tong. With reliably processed data, it is relatively straightforward to merge datasets in an inversion process, where the focus tends to be on relative weighting and regularization of the different data types.

In this thesis I present 7 studies that demonstrate our evolving approach to adopting different datasets into a joint inversion algorithm.

Chapter 2 is my first rupture model inversion for the 2011, M_w = 9.0 Tohoku earthquake. The novelty of this study is that I use regional hr-GPS observations from

Japanese stations to solve for the slip distribution of the Tohoku event. These are 1-s sampled solutions, professionally processed, that contain the complete dynamic and static ground displacement time histories. This exploits the seismic wave energy along with the conventional static offsets, gaining temporal and spatial resolution from the former that overcomes trade-offs of the solution for the latter. By inversion of a high quality regional hr-GPS dataset [*Yue and Lay,* 2011], we obtained a stable rupture model that is not dependent on some key inversion parameters, such as rupture velocity. This demonstrates the benefit of simultaneous fitting of the dynamic and static parts of the near-field ground displacements.

Chapter 3 presents a joint inversion approach that follows up on the intial hr-GPS inversion work of the 2011 Tohoku earthquake. I incorporate teleseismic body waves and R1 and G1 Source Time Functions (STFs) in a joint inversion with the hr-GPS and offshore static GPS measures [Yue and Lay, 2013]. Combining the datasets does not reduce the data fitting of the hr-GPS dataset, but does improve the spatial and temporal resolution of the rupture model.

Chapter 4 is a study of the 2012 M_w 8.6 Indo-Australia intraplate earthquake which struck the area off-shore of the Sunda trench along Sumatra. This is the largest strike slip event ever recorded. The rupture process is very complex and can not be sufficiently represented with a single fault plane. We used teleseismic body and surfaces waves to image the rupture process, and found that at least 4 fault segments ruptured in this event. I modified my algorithm to include multiple fault segments in a single source model inversion that fits the teleseismic body waves and R1 and G1

STFs simultaneously [Yue et al., 2012]. Sub-events, ruptured on multiple orthogonal and sub-parallel fault geometries, were resolved in the rupture model, with the magnitude of subevents ranging from M_w 8.0-8.5. This complex model result still holds up in following studies, and I have collaborated with researchers in Singapore on subsequent incorporation of hr-GPS data in the source inversion (paper in preparation, not shown in this thesis).

Chapter 5 details a source inversion for the 2012 M_w 7.6 Costa Rica earthquake, which is the best resolved fault model in my thesis (and likely the best resolved interplate thrust event ever). For this event, the seaward protrusion of the Nicoya peninsula provides dense observation of hr-GPS, campaign GPS and strong ground motion observations right above the shallow fault rupture. The extensive near-field observations provide very good constraints on the co-seismic rupture, and we resolved a stable and detailed rupture model that matches the geodetically determined pre-seismic locking pattern very well [Yue et al., 2013a]. The co-seismic rupture area is surrounded by other deformations such as aftershocks, low-frequency earthquakes, slow-slip events, and tremor.

Chapter 6 concerns my research on the 2013 Craig, Alaska M_w 7.5 earthquake, which is a strike slip event located on the boundary between the Pacific and North America plates. Joint inversions of regional hr-GPS and teleseismic observations were used to resolve super-shear rupture process for this event. I also developed a linear fault model inversion technique, using corrected empirical Green functions for each

node of a linear fault, in which I also resolved super-shear rupture velocity [Yue et al., 2013b].

Chapter 7 summarizes my research on the 2010 M_w 7.8 Mentawai tsunami earthquake, which caused a devastating tsunami inundation and hundreds of fatalities. By joint inversion of hr-GPS and teleseismic datasets, we infer large slip located near the trench, which is iteratively constrained by modeling tsunami recordings at two buoys and two well-calibrated tide-gauge stations [Yue et al., 2014a]. The Mentawai earthquake ruptured up-dip from the 2007 M_w 8.5 Bengkulu event, for which the rupture did not reach the trench. This event is of great interest in that many other great earthquakes may not have ruptured to the trench, leaving the possibility of a shallow tsunami earthquake.

Chapter 8 presents my study of the 2010 Maule, Chile M_w 8.8 earthquake. Earlier studies of the 2010 Maule earthquake have not provided clear evidence for co-seismic rupture reaching the trench, and it is generally asserted that there was no slip to the trench even though the data may not be able to rule this out. By joint inversion of hr-GPS, teleseismic, InSAR, and tsunami datasets, we obtained a model with very good resolution across the entire megathrust from up-dip to down-dip [Yue et al., 2014b]. Our finite-fault model indicates strong (~10 m) slip near the trench up-dip of two rupture large-slip patches along a bi-lateral rupture distribution. This rupture pattern shows a clear complementary pattern with aftershock activity.

The case studies I have analyzed and the corresponding datatypes used in my analyses are summarized in Table 1.1

Table 1.1.

Earthquake	Year	Used Dataset						Publications
		Hr-GPS	Teleseismic	STF/surface waves	Static GPS	InSAR /Landsat	Tsunami	
Tohoku	2011	√	√	√			○	*Yue and Lay, 2011,2013* *Yamazaki et al, 2011*
Indo-Australia	2012	√	√	√				*Yue et al, 2012;* *Hill et al, in prep*
Costa Rica	2012	√	√	√	√			*Yue et al, 2013a*
Craig	2013	√	√	√				*Yue et al, 2013b*
Mentawai	2010	√	√				○	*Yue et al, 2014*
Iquique	2014		√				√	*Lay et al, 2014*
Maule	2010	√	√			√	√	*Yue et al, 2014a*
Pakistan	2013		√			√		*Sun et al, in prep*

Note: √ presents datasets used in inversion
○ presents dataset compared with forward modeling

These studies all demonstrate improvements in the determination of finite-fault models by use of novel data types such as hr-GPS observations and joint inversion of multiple datasets with complementary sensitivity to the source. A reliable finite-fault model allows us to better understand the locking-releasing behavior of the fault plane, the frictional processes that lead to heterogeneity of slip, and the detailed nature of the seismic cycle. We are also able to better evaluate the seismic and tsunami hazard of large earthquakes.

1.5 References

Bouchon, M., and Karabulut, H. (2008). The aftershock signature of supershear earthquakes. *Science, 320*(5881), 1323-1325.

Bürgmann, R., Rosen, P. A., and Fielding, E. J. (2000). Synthetic aperture radar interferometry to measure Earth's surface topography and its deformation. *Annual Review of Earth and Planetary Sciences, 28*(1), 169-209.

Freymueller, J., King, N. E., and Segall, P. (1994). The co-seismic slip distribution of the Landers earthquake. Bulletin of the Seismological Society of America, 84(3), 646-659.

Goldstein, R. M., Engelhardt, H., Kamb, B., and Frolich, R. M. (1993). Satellite radar interferometry for monitoring ice sheet motion: Application to an Antarctic ice stream. *Science 262*, 1525–1530.

Hartzell, S. H., and Heaton, T. H. (1983). Inversion of strong ground motion and teleseismic waveform data for the fault rupture history of the 1979 Imperial Valley, California, earthquake. *Bulletin Seismological Society of America, 73*(6A), 1553-1583.

Ji, C., Wald, D. J., and Helmberger, D. V. (2002). Source description of the 1999 Hector Mine, California, earthquake, part I: Wavelet domain inversion theory and resolution analysis. *Bulletin of the Seismological Society of America, 92*(4), 1192-1207.

Ji, C., Wald, D. J., and Helmberger, D. V. (2002). Source description of the 1999

Hector Mine, California, earthquake, part II: Complexity of slip history. *Bulletin of the Seismological Society of America, 92*(4), 1208-1226.

Johnson, J. M., Satake, K., Holdahl, S. R., and Sauber, J. (1996). The 1964 Prince William Sound earthquake: Joint inversion of tsunami and geodetic data. *J. of Geophys. Res.*,*101*(B1), 523-532.

Koper, K. D., A. R. Hutko, and T. Lay (2011). Along-dip variation of teleseismic short-period radiation from the 11 March 2011 Tohoku Earthquake (M_w 9.0), *Geophys. Res. Lett., 38*, L21309, doi:10.1029/2011GL049689.

Lay, T., H. Kanamori, C. J. Ammon, K. D. Koper, A. R. Hutko, L. Ye, H. Yue, and T. M. Rushing (2012). Depth-varying rupture properties of subduction zone megathrust faults, *J. Geophys. Res., 117*, B04311, doi:10.1029/2011JB009133.

Lay, T., C. J. Ammon, A. R. Hutko, and H. Kanamori (2010). Effects of kinematic constraints on teleseismic finite-source rupture inversions: Great Peruvian earthquakes of 23 June 2001 and 15 August 2007, *Bull. Seism. Soc. Am., 100*, 969-994, doi:10.1785/0120090274

Lay, T., Yue, H., Brodsky, E., and An, C. (2014). The April 1, 2014 Iquique, Chile M_w 8.1 earthquake rupture sequence. *Geophys. Res. Lett*.,(in revision)

Massonnet D, Rossi M, Carmona C, et al. (1993) The displacement field of the Landers earthquake mapped by radar interferometry. *Nature, 364*, 138–142.

Satake, K. (1993). Depth distribution of coseismic slip along the Nankai Trough, Japan, from joint inversion of geodetic and tsunami data. *J. Geophys. Res., 98*(B3), 4553-4565.

Satake, K., Fujii, Y., Harada, T., and Namegaya, Y. (2013). Time and space distribution of coseismic slip of the 2011 Tohoku earthquake as inferred from tsunami waveform data. *Bull. Seism. Soc. Amer.,103*(2B), 1473-1492.

Shen, Z. K., Sun, J., Zhang, P., Wan, Y., Wang, M., Bürgmann, R., ... and Wang, Q. (2009). Slip maxima at fault junctions and rupturing of barriers during the 2008 Wenchuan earthquake. *Nature Geoscience, 2*(10), 718-724.

Simons, M., and Rosen, P. A. (2007). Interferometric synthetic aperture radar geodesy. 391-446.

Wei, S., Fielding, E., Leprince, S., Sladen, A., Avouac, J. P., Helmberger, D., ... & Briggs, R. (2011). Superficial simplicity of the 2010 El Mayor-Cucapah earthquake of Baja California in Mexico. *Nature Geoscience, 4*(9), 615-618.

Yamazaki, Y., Lay, T., Cheung, K. F., Yue, H., & Kanamori, H. (2011). Modeling near‐field tsunami observations to improve finite‐fault slip models for the 11 March 2011 Tohoku earthquake. *Geophys. Res. Lett., 38*(7).

Yue, H., and T. Lay (2011). Inversion of high-rate (1 sps) GPS data for rupture process of the 11 March 2011 Tohoku earthquake (M_w 9.1), *Geophys. Res. Lett., 38*, L00G09, doi:10.1029/2011GL048700.

Yue, H, T. Lay and K. D. Koper (2012). En Echelon and Orthogonal Fault Ruptures of the 11 April 2012 Great Intraplate Earthquakes. *Nature, 490*, 245-249, doi:10.1038/nature11492.

Yue, H. and T. Lay (2013). Source Rupture Models for the M_w 9.0 2011 Tohoku Earthquake from Joint Inversions of High-Rate Geodetic and Seismic Data. *Bull.*

Seis. Soc. Amer., 103. 1242-1255; doi:10.1785/0120120119.

Yue, H., T. Lay, S. Y. Schwartz, L. Rivera, M. Protti, T. H. Dixon, S. Owen and A. V. Newman, (2013a). The 5 September 2012 Nicoya, Costa Rica M_w 7.6 earthquake rupture process from joint inversion of high-rate GPS, strong-motion, and teleseismic P wave data and its relationship to adjacent plate boundary interface properties. *J. Geophys. Res*., 118, 5453-5466, doi:10.1002/jgrb.50379.

Yue, H., T. Lay, J. T. Freymueller, K. Ding, L. Rivera, N. A. Ruppert, and K. D. Koper (2013b). Supershear rupture of the 5 January 2013 Craig, Alaska (M_w 7.5) earthquake, *J. Geophys. Res., 118*(11), 5903-5919, doi:10.1002/2013JB010594.

Yue, H., T. Lay, L. Rivera, C. An, C.Vigny, and X. Tong (2014a). Fault slip to the trench in the M_w = 8.8 2010 Maule, Chile earthquake from joint inversion of hr-GPS, teleseismic, InSAR and tsunami observations. *J. Geophys. Res*., (submitted)

Yue, H., T. Lay, L. Rivera, Y. Bai, Y. Yamazaki, K. F. Cheung, E. M. Hill, K. Sieh, W. Konko, and A. Muhari (2014b). Rupture process of the 2010 M_w 7.8 Mentawai tsunami earthquake from joint inversion of near-field hr-GPS and teleseismic body wave recordings constrained by tsunami observations. *J. Geophys. Res*., (in revision)

Chapter 2

Inversion of high-rate (1 sps) GPS data for rupture process of the 11 March 2011 Tohoku earthquake (Mw 9.1)

Abstract

The space-time fault displacement history of the 11 March 2011 Tohoku (M_w 9.1) megathrust earthquake is obtained by least-squares inversion of high-rate (1-sps) GPS ground motions recorded in Japan. Complete near-source seismic and static ground motions are fit in the inversion using a normal mode formalism to compute the Green functions. The basic rupture pattern is stable for various choices of model parameters and solution smoothing, and excellent fits to the complete seismo-geodetic ground motions are obtained. The preferred solution has concentrations of slip near the trench and hypocenter, with subfault source time function durations of ~30-70 s and maximum slip of ~60 m. Down-dip slip spreads over a wider area with smaller maximum slip (< ~10-15 m). Inversion of the high-rate GPS data exploits both the timing and total displacement information in the ground motions, yielding stable estimates of the seismic moment (~4.8 x 10^{22} Nm; M_w = 9.1) and slip distribution for ground motion periods > 25 s.

2.1 Introduction

Seismic, geodetic and tsunami observations are now commonly used to estimate finite-fault slip distribution models for large earthquakes either by separate or joint

inversion procedures [e.g., *Ji et al.*, 2004; *Delouis et al.,* 2010*; Konca et al.,* 2010; and many others]. There are advantages and limitations associated with each type of data, and development of unified models that exploit the collective advantages is a long-term goal. To date, most joint inversions of seismic and geodetic observations involve modeling of seismic waves together with static ground motion displacements using separate wave propagation and static motion algorithms, and there is uncertainty in weighting of the distinct information from each data type. With the advent of high-rate GPS recordings, the distinctions between seismic and geodetic observations and modeling have become blurred, as recordings close to an event contain the progression of all seismic arrivals accompanied by near-field terms that evolve into the static offsets. By computing complete ground motion Green functions accounting for all of these contributions, the high-rate GPS time series can essentially be treated like seismograms including any detectable static offsets. This has been the case for analysis of recordings from twice-integrated strong motion accelerometers for decades, but thus far there have been relatively few inversions of time-varying high-rate GPS observations for finite-faulting models [e.g., *Ammon et al*., 2011; *Vigny et al*., 2011].

The great 11 March 2011 Tohoku earthquake was recorded by over 1200 continuously recorded GPS sensors in Japan, and ground position solutions with 1 s sampling have been made available to the research community for hundreds of these stations. We develop an inversion algorithm that constrains the rupture process for the Tohoku event using three-component 1 sps high-rate GPS ground position solutions The simultaneous inversion of the time-varying GPS recordings of seismic and static

motions provides a well-resolved rupture model for the earthquake, and the formalism can readily be extended to incorporate teleseismic observations for all seismic arrivals.

2.2. 2011 Tohoku Earthquake Observations

The 11 March 2011 Tohoku earthquake ruptured the entire width of the megathrust offshore of northeastern Japan, producing many geophysical observations that have been rapidly analyzed to constrain the rupture process. Direct measures of bathymetric motions of the seafloor resolve seaward displacements of the upper plate by ~24 m above the hypocenter [*Sato et al.*, 2011] and ~50 m near the trench [http://www.jamstec.go.jp/j/about/press_release/20110428/]. Finite-fault rupture models inverted from teleseismic and low-pass filtered strong-motion data indicate that the largest fault displacements are located up-dip of the hypocenter with slip of 40-60 m extending to the trench [e.g., *Ammon et al.*, 2011; *Hayes*, 2011; *Ide et al.*, 2011; *Lay et al.*, 2011b; *Simons et al.*, 2011; *Yoshida et al.*, 2011]. Modeling and inversions of tsunami data support large near-trench slip [e.g., *Lay et al.*, 2011a; *Fujii et al.*, 2011; *Maeda et al.*, 2011] Geodetic inversions of static GPS coseismic offsets tend to concentrate large slip in the central region of the rupture zone, near the hypocenter [e.g., *Iinuma et al.*, 2011; *Ozawa et al.*, 2011; *Simons et al.*, 2011], although it seems likely they have limited resolution of more seaward slip. On the other hand, back-projections of teleseismic short-period seismic wave energy indicate source locations primarily in the down-dip portion of the megathrust below the coast, not in

the up-dip regions of large slip [*Koper et al.*, 2011; *Simons et al*., 2011; *Wang and Mori*, 2011].

The Tohoku earthquake was recorded by over 1,200 densely deployed continuously recording GPS stations, most of which have been processed for high-rate (1-sps) position solutions. These signals are free of the bandwidth and clipping limitations of regional broadband seismometers for resolving the dynamic displacements and do not require unstable double integration as is the case for strong motion recordings in order to resolve the co-seismic static displacements. The timing information and wide range of apparent velocities from P wave to little-dispersed Rayleigh wave arrivals in the regional high-rate GPS recordings provides good spatial resolution of the faulting process, while the explicit inclusion of static deformations bounds the total seismic moment and slip distribution. Inversion of the complete ground motion recordings requires computation of Green functions including all dynamic and static terms. The simultaneous inversion of the time-varying GPS recordings of seismic and static motions provides a well-resolved rupture model for the earthquake, and the formalism can readily be extended to incorporate teleseismic observations for all seismic arrivals.

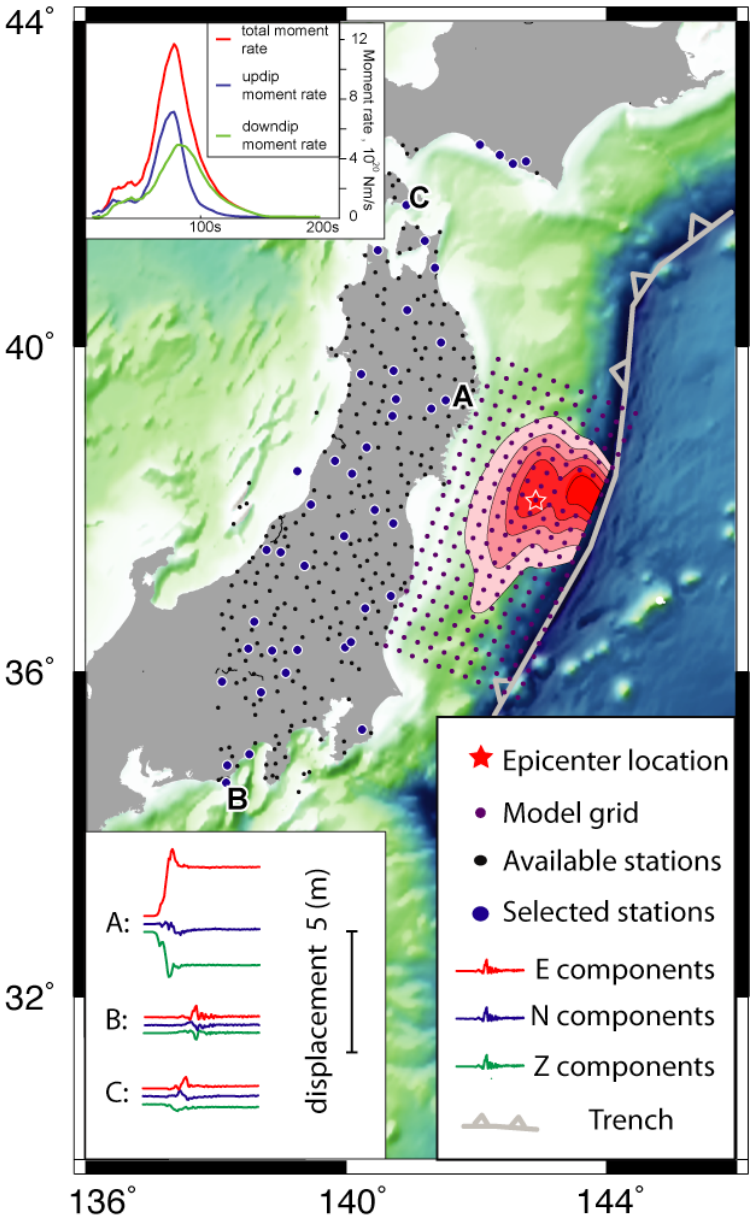

Figure 2.1. Station distribution and model grid positions (purple spots). Available and selected stations are marked as black and larger blue spots, respectively. The red star marks the epicenter. The preferred slip distribution is shown on the grid. The trench is marked with a gray toothed line. Example three-component high-rate GPS ground motions of three stations (A, B and C on the map), are plotted on the bottom. Moment rate functions for the whole fault plane, up-dip and down-dip of hypocenter portions of the fault are shown on the top left.

2.3. Model parameters and inversion

Over 400 high-rate three-component GPS time series were made available courtesy

of GPS-Solutions, and we chose various distributed subsets of 43 high signal-to-noise ratio stations to invert for the slip-distribution. We selected stations to provide good location constraints parallel to the Honshu coast (Figure 2.1), and present results here for one subset, although different groups of stations were used to evaluate stability of the solutions. The fault model (Figure 2.1) has eleven 20 x 20 km^2 subfaults along dip and 22 along a strike of 202°. The dip of the rupture plane for the model presented here has varies with 2 segments; a dip of 10° for the fault less than 27 km beneath sea level and a dip of 22° below 27 km, approximated from the seismic reflection model of *Miura et al.* (2005). Inversions for various constant dip values and 3-segment models with a shallow segment dipping only 5° were performed, with generally consistent results to the model presented here. The source time function of each sub-fault is parameterized by 6 triangles with 10 s half-time durations shifted by 10 s each, giving total subfault durations of up to 70 s. The rake is allowed to vary between subevents for each subfault. The hypocenter location is at the 9th grid point along strike (counting from northeast) and 5th grid along dip (counting from up-dip position near the trench). We use the relocated epicenter from *Zhao et al.* (2011) (38.11°E, 142.92°N), an initial depth of 20 km beneath sea level, and an origin time of 14:46:18.14 UTC. Ground motion time windows 600 s long starting at the origin time were inverted, eliminating any need to pick first arrival times for the very emergent signal onsets. The preferred initial rupture expansion velocity is 1.5 km/s out to a distance of 100 km from the hypocenter, and then increases to 2.5 km/s, based on back-projection imaging [*Koper et al.*, 2011] and finite-fault modeling of teleseismic signals [*Ammon et al.*, 2011; *Lay et*

al., 2011].

Normal mode summation of all modes for PREM [*Dziewonski and Anderson*, 1981] up to 80 mHz were used to generate Green functions, using a mode set provided by L. Rivera, accounting for all seismic and static ground motions with intrinsically balanced weighting of information.. To reduce the computational effort, we obtain the Green functions for each subfault-station pair using a pre-calculated database with 10 km epicentral spacing and 1 km source depth spacing. We use the Green's function for the nearest node from the database for each station, incurring minor errors (< 5 km) in propagation distance, insignificant for the 80 mHz limit of the signal spectrum. We apply a low-pass filter to the data and the Green functions to ensure common spectral content and to eliminate mode truncation ringing. PREM has a simple 1D structure so the low-pass filtering also suppresses short-period signals that are poorly predicted by the model. On the other hand, filtering reduces time resolution and some seismic wave features, so the low-pass filter is selected carefully to balance the trade-off between the time resolution and the model effectiveness. We present results for a low-pass corner at 25 s, but very similar results are found using corners of 20 s to 40 s. Green functions for rakes of 45°and 135° for each subfault are used in a non-negative least square inversion [*Lawson and Hanson*, 1995], constraining each subfault rake to within that range.

We add a smoothing weight matrix to the Green's function matrix to constrain the simultaneously activated triangle subevents of adjacent subfaults: $\beta\times(m_i - m_{i-1})=0$. No smoothing in time was applied to the different subevents for the same segment. In our calculation, β is calculated by $\beta_i = \frac{\beta_0\sqrt{\sum_{j=1}^{n} G_{ij}^2}}{(dx^2+dy^2)}$, where G_{ij} is the Green's function, i is

the number of parameters and j is the number of data, dx and dy are the segment dimensions for each subfault. The physical significance of this algorithm is that subfaults with higher Green function amplitudes (closer to stations) are more constrained and if grid size is decreased we smooth the solution more spatially. Many smoothing approaches were tested, and as for all finite source inversions, smoothing has significant effect. Our preferred model is representative of the solutions we found to be stable.

2.4. Discussion and Conclusions

Our preferred model (Figure 2.2) has a seismic moment distribution near the hypocenter generally consistent with a previous combined inversion of teleseismic body waves, surface waves, and low-sample rate (30 s) GPS data [*Ammon et al.*, 2005], although the mapping to slip using variable source rigidity from the PREM layered structure enhances up-dip slip similar to inversions of teleseismic P waves [*Lay et al.*, 2011b]. The area for the main rupture spans ~200 km along strike and ~200 km along dip, with a rupture asymmetry to the south. The maximum model slip is ~60 m near the trench and the seismic moment is ~4.8×10^{22} Nm (M_w 9.1). Excellent matches to the recordings were obtained (Figure 2.3; all data and synthetics are shown in Auxiliary Figure 2.A1)[1].

[1]Auxiliary materials are available in the HTML. Doi:10.1029/2011GLxxxxxx.

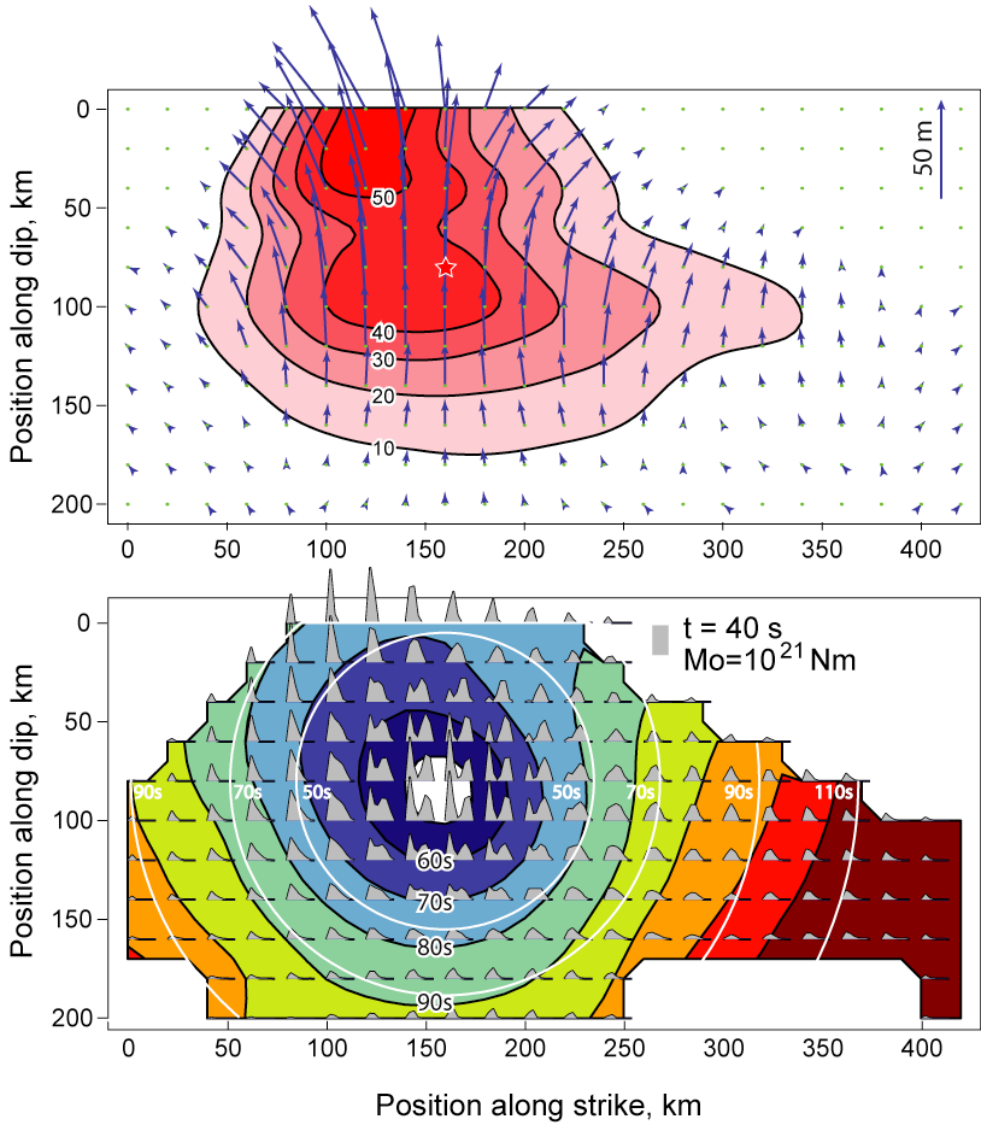

Figure 2.2. Preferred model slip distribution is plotted in the upper panel, with the maximum slip value of ~60 m at the top center grid and total seismic moment of ~4.8 × 10^{22} Nm. In the lower panel the source time functions for all subfaults are shown as gray polygons, with the subfault source function centroid time shown as colored background. A rectangle with the area of seismic moment of 10^{21} Nm and time duration of 40 s is plotted as a reference for the subfault source time functions. Rupture expansion time counters are marked as white concentric circles.

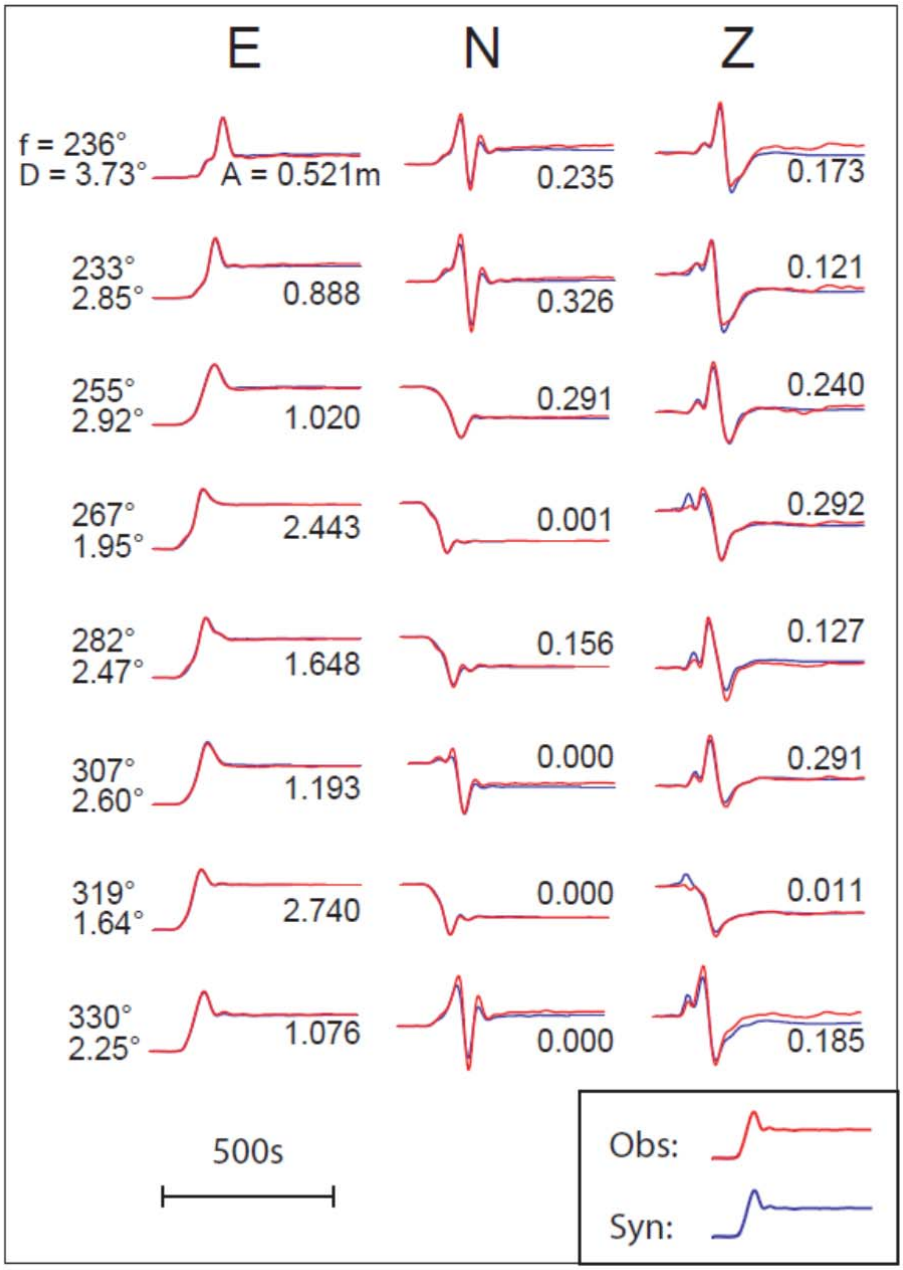

Figure 2.3. Three-component (E – east; N – north; Z – vertical) high-rate GPS ground motion observations (red curves) and preferred model predictions (blue curves) for 8 of the 40 stations used in the inversion (all station data and predictions are shown in Figure 2.A1). Station number, azimuth (ϕ) and epicentral distance (Δ) are shown for each waveform.

Many parameters influence finite-source inversions, including the station distribution, fault geometry, signal window, rupture velocity, low-pass filter corner frequency, parameterization of the subfault source time functions, and smoothing design. We explored the influence of all of these parameters, finding that the first order pattern shown in Figure 2.2 is relatively stable, but most influenced by choice of rupture velocity and smoothing weight, which we discuss below.

For teleseismic inversions, rupture velocity has particularly strong influence on slip patterns, with severe trade-off due to intrinsic lack of spatial resolution. Slip near the rupture front where the number of parameters is a maximum tends to be preferred by teleseismic least square inversions. For our high-rate GPS inversions, the slip pattern is not as strongly affected by the choice of rupture velocity due to having relatively good spatial resolution (Figure 2.4, Figure 2.A2). When choosing an appropriate rupture velocity (not too high or too low) with a subfault source time function long enough to span the real rupture time, the inversion uses more of the degrees of freedom of each subfault source function to fit the data (Figure 2.4). In our inversion, the centroid time of each subfault source functions proves quite stable for different choice of rupture velocity ranging from 1.5 km/s to 3.0 km/s (Figure 2.2 and 2.4). The up-dip region has a broad region of slip with a moment rate centroid time of around 60-80s (Figure 2.1), with subfault source time functions being single broad peaks. The down-dip region has a moment rate centroid time of between 70-90 s. There is a southerly lobe with a centroid time of 90-110 s. The central portion of the fault has double peaked subfault source time functions. The roughness of the subfault source functions is

dependent on the smoothing, so we prefer not to interpret the complexity as multiple slip fronts as invoked by *Ide et al*. [2011]. Large area ruptured at the same time up-dip, suggesting that the rupture was not predominantly slip pulse in nature.

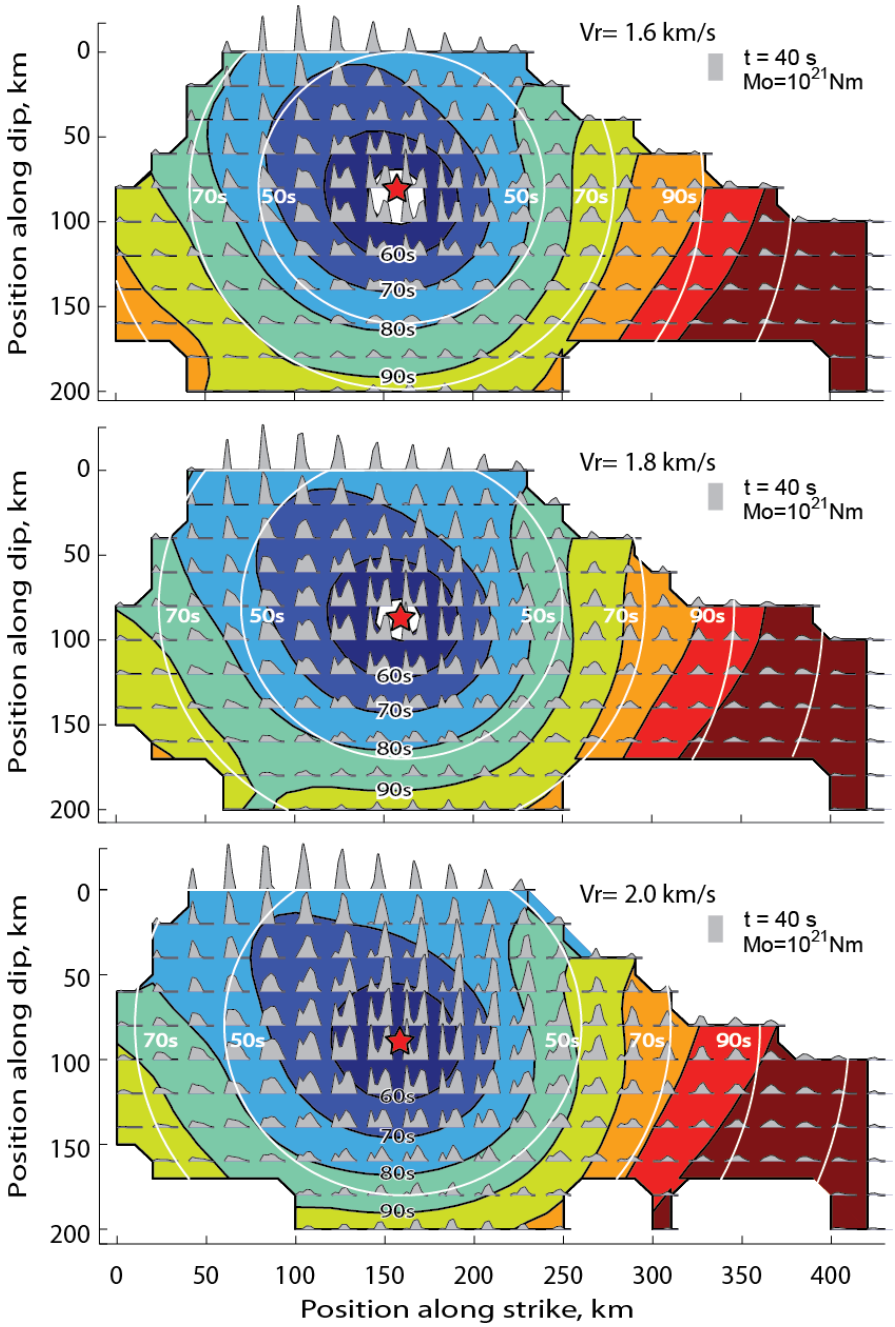

Figure 2.4. Comparison of subfault source function centroid time for inversion results with different rupture velocities of 1.6, 1.8 and 2.0 km/s. Symbols are the same as in Figure 2.2.

Choosing a suitable smoothing weight usually involves balancing the trade-off between data fit and model roughness. However, our inversions always fit the data with about 97% variance reduction due to the smooth signals and many finite-fault parameters. On the other hand, the smoothing weight directly influences the maximum slip estimate. Varying the smoothing weight of β_0 between 0.5 to 1.5 results in estimates of maximum slip between 80 m and 58 m (after scaling by the PREM rigidity structure). Our preferred smoothing weight was selected by requiring the maximum slip amount to be around ~60 m, as observed near the toe of the upper wedge.

Inversions for potency rather than seismic moment were also performed. With no smoothing, identical slip results are obtained from seismic moment and potency inversions, but some smoothing is required for sensible model behavior. We find basically similar models in slip distribution for potency inversions despite the effects of smoothing interacting with the different Green function amplitudes (Figure 2.A3).

The availability of dense, high-rate GPS observations for the great 2011 Tohoku earthquake enables self-consistent, balanced seismo-geodetic inversions, and stable rupture models are obtained, with complete ground motions longer than 25 s being well-modeled using a simple 1D structure. The complete fitting of the dynamic and static terms (Figures 2.A4) provides obtain good spatial and temporal resolution of the faulting process and constraints on the seismic moment. The inverted slip pattern is stable for moderate changes in model parameters. The slip in the up-dip segment largely occurs over a large area with long source time function simultaneously,

consistent with crack-like rupture. Slip in the down-dip segments propagates more as slip-pulses, which may be related to stronger short-period radiation observed from the deeper region.

2.5 Acknowledgments. This work made use of GMT and SAC software. We thank L. Rivera for providing the normal mode data set. We thank for K. Larson for helping us to locate high-rate GPS data. Our data, generously made available by C. Rocken of GPS Solutions, Inc. originated with efforts by GSI, NGDS, Hitz, GPSS, and VERIPOS. C. J. Ammon and H. Kanamori provided helpful discussions of potency inversion, smoothing, and modeling of high rate GPS recordings using the normal mode approach, which was suggested by C. J. Ammon, and helpful comments on the manuscript. This work was supported by NSF grants EAR0635570.

2.6 References.

Ammon, C. J., T. Lay, H. Kanamori, and M. Cleveland (2011), A rupture model of the great 2011 Tohoku earthquake, *Earth Planets Space*, in press.

Delouis, B., J.-M. Nocquet, and M. Vallée (2010), Slip distribution of the February 27, 2010 Mw = 8.8 Maule earthquake, central Chile, from static and high-rate GPS, InSAR, and broadband teleseismic data, *Geophys. Res. Lett., 37*, L17305, doi:10.1029/2010GL043899.

Dziewonski, A. M., and D. L. Anderson (1981), Preliminary reference Earth model 1, *Physics of the Earth and Planetary Interiors*, *25*(4), 297-356.

Fujii, Y., K. Satake, S. Sakai, M.Shinohara, and T. Kanazawa (2011), Tsunami source of the 2011 off the Pacific coast of Tohoku, Japan earthquake, *Earth Planets Space*, in press.

Hayes, G. (2011), Rapid source characterization of the 03-11-2011 M_W 9.0 Off the Pacific Coast of Tohoku earthquake, *Earth Planets Space*, in press.

Ide, S., A. Baltay, and G. C. Beroza (2011), Shallow dynamic overshoot and energetic deep rupture in the 2011 Mw 9.0 Tohoku-oki earthquake, *Science*, *332*, 1426-1429.

Iinuma, T., M. Ohzono, Y. Ohta, and S. Miura (2011), Coseismic slip distribution of the 2011 off the Pacific coast of Tohoku erthquake (M9.0) estimated based on GPS data – Was the asperity in Miyagi-oki ruptured? *Earth Planets Space*, in press.

Ji, C., K. M. Larson, Y. Tan, K. W. Hudnut, and K. Choi (2004), Slip history of the 2003 San Simeon earthquake constrained by combining 1-Hz GPS, strong motion, and teleseismic data, *Geophysical research letters*, *31*(17), Art. No. L17608.

Lawson, C. L., and R. J. Hanson (1995), *Solving least squares problems*, Society for Industrial Mathematics.

Konca, A. O., S. Leprince, J.-Ph. Avouac, and D. V. Helmberger (2010), Rupture process of the 1999 M_w 7.1 Duzce earthquake from joint analysis of SPOT, GPS, InSAR, Strong-Motion, and teleseismic data: A supershear rupture with variable rupture velocity, *Bull. Seism. Soc. Am., 100*, 267-288.

Koper, K. D., A. R. Hutko, T. Lay, C. J. Ammon, and H. Kanamori (2011), Frequency-dependent rupture process of the 11 March 2011 M_W 9.0 Tohoku earthquake: Comparison of short-period *P* wave backprojection images and broadband seismic rupture models, *Earth Planets Space*, in press.

Lay, T., Y. Yamazaki, C. J. Ammon, K. F. Cheung, and H. Kanamori (2011a), The great 2011 of

the Pacific coast of Tohoku (M_W 9.0) earthquake: Comparison of deep-water tsunami signals with finite-fault rupture model predictions, *Earth Planets Space*, in press.

Lay, T., C. J. Ammon, H. Kanamori, L. Xue, and M. J. Kim (2011b), Possible large near-trench slip during the great 2011 Tohoku (M_W 9.0) earthquake, *Earth Planets Space*, in press.

Maeda, T., T. Furumura, S. Sakai, and M. Shinohara (2011), Significant tsunami observed at the ocean-bottom pressure gauges at 2011 off the Pacific coast of Tohoku earthquake, *Earth Planets Space*, in press.

Miura, S., et al. (2005), Structural characteristics off Miyagi forearc region, the Japan Trench seismogenic zone, deduced from a wide-angle reflection and refraction study, *Tectonophys.*, *407*, 165-188.

Ozawa, S., T. Nishimura, H. Suito, T. Kobayahi, M. Tobita, and T. Imakiire (2011), Coseismic and postseismic slip of the 2011 magnitude-9 Tohoku-oki earthquake, *Nature*, doi:10.1038/nature10227.

Sato, M., et al. (2011), Displacement above the hypocenter of the 2011 Tohoku-oki earthquake, *Science*, *332*, 1395.

Simons, M., et al. (2011), The 2011 magnitude 9.0 Tohoku-oki earthquake: Mosaicking the megathrust from seconds to centuries, *Science*, *332*, 1421-1425.

Wang, D. and J. Mori (2011), Rupture process of the 2011 off the Pacific coast of Tohoku Earthquake (M_w 9.0) as imaged with back-projection of teleseismic *P*-waves, *Earth Planets Space*, in press.

Yoshida, Y., H. Ueno, D.Muto, and S. Aoki (2011), Source process of the 2011 Off the Pacific Coast of Tohoku earthquake with the combination of teleseismic and strong motion data, *Earth Planets Space*, in press.

Zhao, D., Z. Huang, N. Umino, A. Hasegawa, and H. Kanamori (2011), Structural heterogeneity in the megathrust zone and mechanism of the 2011 Tohoku-oki earthquake (M_w 9.0), *Geophys. Res. Lett.*, in press.

2.7 Auxiliary figures

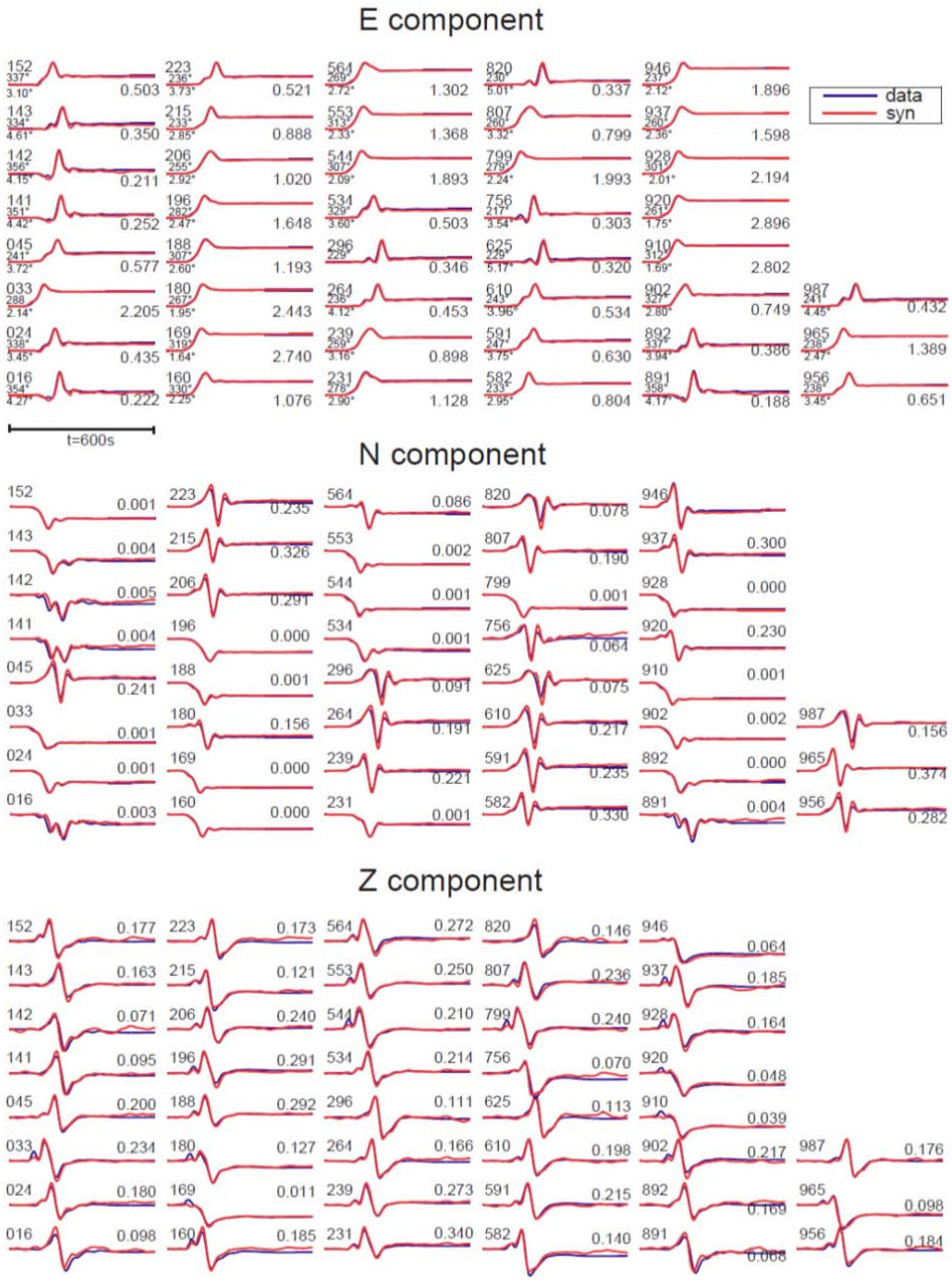

Figure 2.A1. Comparison of observed high-rate GPS signals (red curves) and predicted displacements (blue curves) waveforms for all stations with three components used in the preferred finite-fault inversion. Station number, azimuth, and epicentral distance are shown at the left side of each east-west component. Maximum displacements (m) are shown toward the right of each wave-form.

-

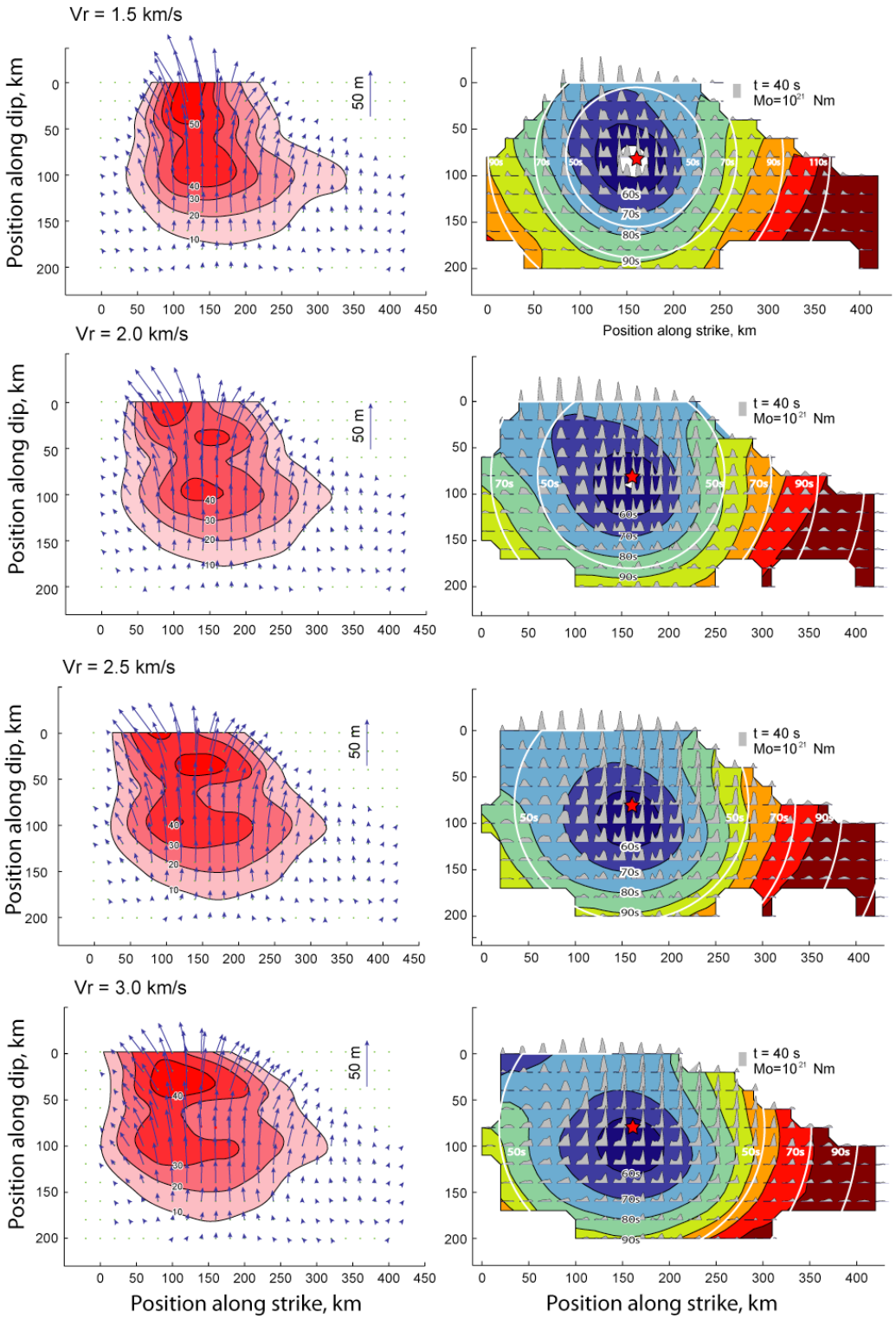

Figure 2.A2. Comparison of slip distribution (left panels) and subfault source time functions (right panels) for inversions with different rupture velocity, Vr = 1.5, 2.0, 2.5, and 3 km/s. The markers and legend are the same as in Figure 2.2.

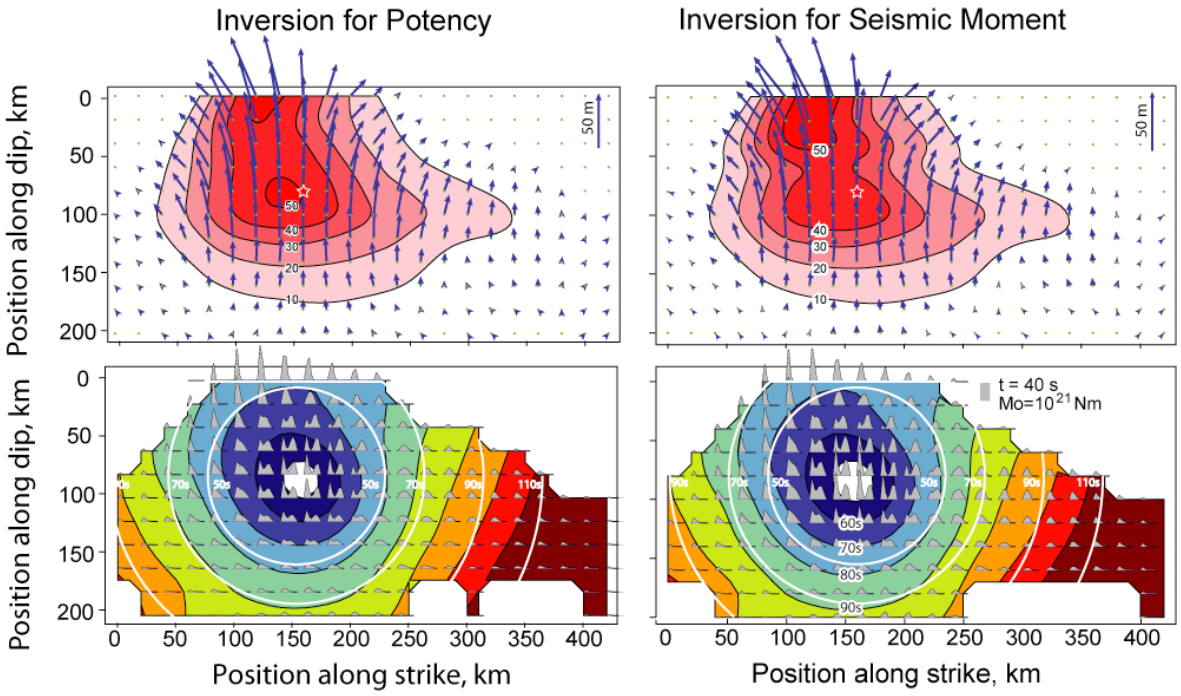

Figure 2.A3. Comparison between inversion for potency and inversion for seismic moment. All markers and legends are the same as Figure 2.2. The maximum slip for the potency inversion is ~55 m and the total seismic moment is 4.8×10^{22} Nm.

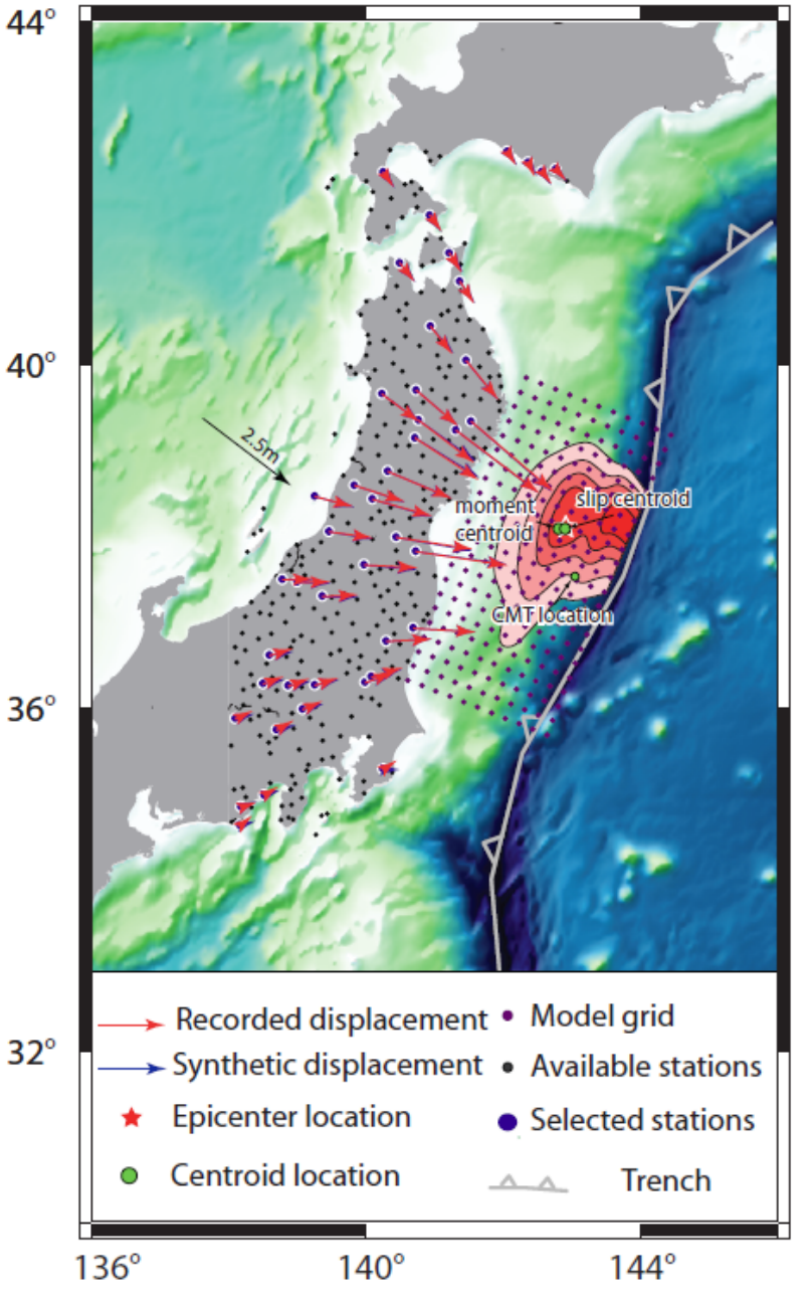

Figure 2.A4. Map-view of the recorded static coseismic horizontal ground displacements (red arrows) and predicted static ground displacements (blue arrows) for our preferred model from inversion of the high-rate GPS data. _Available and selected stations are marked as black and blue spots respectively. Epicenter position is marked by the red star and the grids are marked as purple spots with our preferred slip distribution as background. The trench is marked with gray toothed line. Seismic moment centroid and slip centroid for our preferred model are located near the epicenter, which is ~70 km north of the CMT centroid location.

Chapter 3

Source Rupture Models for the 2011 Tohoku-Oki Mw 9.0 Earthquake From Joint Inversions of High-Rate Geodetic and Seismic Data

Abstract The space-time history of fault slip during the 11 March 2011 Tohoku earthquake (M_w 9.0) is determined using high sample rate (1 sample/sec) three-component GPS recordings (hr-GPS) from regional stations across Japan, teleseismic broadband P-waves, global R_1 source time functions (STFs) determined by empirical Green's function deconvolutions of short-arc Rayleigh waves and ocean bottom deformation observations (OBGPS). Least-squares inversions are performed for models with prescribed rupture front expansion. Joint inversion yields improved resolution comparing to inversions with a single data type in checker-board test, and joint inversion keeps inversion stability to some key parameters, such as the rupture front velocity and the subfault duration. In our preferred model, the joint inversions yield consistent seismic moment estimates of 4.2×10^{22} Nm (M_w 9.0), and this model shows dispersed slip near the hypocenter and maximum slip (~60m) up-dip on the megathrust along the trench. A minor down-dip rupture extension further to the south is also resolved with centroid source time later than 110 sec. The joint inversion models appear to reconcile conflicting results from separate dataset inversions, which tend to concentrate slip either up-dip or down-dip.

3.1 Introduction

The M_w 9.0 2011 Tohoku-Oki earthquake is the best-recorded great earthquake to date. Extensive coseismic observations were provided by dense near-field strong ground motion and GPS networks, teleseismic body and surface wave recordings from global seismic networks, deep-water and near-coastal tsunami observations from buoys and pressure gauges, and tsunami run-up and inundation measurements (e.g., Lay and Kanamori, 2011; Mori *et al*., 2011). These data allow characterization of the rupture process of this huge megathrust event with an unprecedented level of detail. Numerous finite-fault models, capturing aspects of the spatio-temporal evolution of the rupture, have been determined by modeling or inversion of the seismic, geodetic and tsunami observations both separately and, in some cases, jointly. The focus is now on evaluating intrinsic resolution of different data sets and reconciling differences between the various models. In general, finite-fault models inverted with similar datasets usually yield fairly similar rupture patterns, indicating that the results are not exclusively controlled by the specific inversion techniques and parameterizations, although those can have important effects.

Seismic waves, including teleseismic body waves and surface waves and near-field strong ground motion signals, have been analyzed to determine the overall 2011 Tohoku-Oki source rupture process. Many of the seismic wave inversions obtain a consistent large-scale large slip region up-dip, east of the epicenter and close to the trench (e.g., Hayes, 2011; Ide *et al.*, 2011; Lay *et al.,* 2011a; Shao *et al*., 2011; Yoshida *et al*., 2011a,b). However, some seismic wave inversions place the large

slip patch closer to the hypocenter (e.g., Koketsu *et al.*, 2011), with the reasons for the differences not being very clear. Factors such as the assumed fault model geometry (dip and depth), choice of hypocenter, assumed rupture expansion parameters, and source region velocity structure (particularly the rigidity structure used to map inverted subfault seismic moment estimates to slip) all appear to contribute to the differences between the seismic finite-fault models.

Back-projection methods applied to teleseismic short-period seismic network data indicate locations of coherent radiation from localized regions of the megathrust down-dip, west of the epicenter (Ishii, 2011; Koper *et al.,* 2011a,b; Meng *et al.*, 2011; Wang and Mori, 2011; Yao *et al*., 2011; Zhang *et al.*, 2011). These back-projections do not directly image slip on the fault, but very few localized sources of coherent short-period radiation appear in the large slip area extending from the hypocenter to the trench. The difference in location between areas of large slip shallower on the megathrust and the deeper high-frequency source radiation patches is also indicated by near-field strong ground motion data (e.g., Kurahashi and Irikura, 2011; Yoshida *et al.*, 2011a). Varying frequency-dependent seismic radiation between up-dip and down-dip has been observed for other subduction zone megathrusts and appears to involve widespread depth-dependent behavior (Lay *et al.,* 2012).

Geodetic inversions using the huge data set from regional GPS static displacement measurements to estimate the spatial slip distribution on the fault plane provide unprecedented sampling of the deformation, but no temporal information about the rupture evolution. For the 2011 Tohoku-Oki earthquake, the GPS stations all locate

westward from the rupture plane, and there is a tendency for these inversions to place the maximum slip west of or centered beneath the epicenter (Iinuma *et al.,* 2011; Koketsu *et al*., 2011; Miyazaki *et al.,* 2011; Ozawa *et al*., 2011; Simons *et al.,* 2011), although not in every case (e.g., Ito *et al*., 2011a). Offshore observations of seafloor motions from shifts in locations of GPS and OBS stations, and offsets in multi-channel reflection profiles (e.g., Fujiwara *et al*., 2011; Ito *et al*., 2011b; Sato *et al.*, 2011) provide static displacement information right above the epicenter and near the toe of the sedimentary wedge. Inclusion of these observations, treated as elastic deformations, in geodetic inversions tends to shift the maximum slip up-dip toward the trench, similar to many seismic models (e.g., Ito *et al*., 2011b).

Tsunami observations provide good spatial resolution of the seafloor deformation due to the relatively low propagation velocity of tsunami waves. Inversion of tsunami observations requires linearization of the non-linear tsunami wave equations (Saito *et al.,* 2010). Finite-fault models inverted from tsunami observations consistently locate a large slip patch up-dip on the fault, very close to the trench (Fujii *et al*., 2011; Koketsu *et al*., 2011; Maeda *et al*., 2011; Saito *et al.,* 2011). Iterative forward modeling of tsunami observations using finite fault models obtained from seismic observations (Lay *et al*., 2011c; Yamazaki *et al.,* 2011, 2012) achieves good fits to both the tsunami recordings and teleseismic P waves.

Each available dataset provides limited resolution of inverted slip models, as discussed by Yokota *et al*. (2011), Koketsu *et al.* (2011) and Wei *et al.* (2012). Joint inversions of diverse datasets may overcome the limitations of separate inversions,

ideally achieving good resolution across the entire fault model, but joint inversion presents challenges in information weighting and self-consistent modeling. Several joint inversions have been performed for the 2011 Tohoku event, with the maximum slip patches tending to locate somewhat up-dip, east of the epicenter, but usually not reaching as far as the trench (Ammon *et al.,* 2011; Lee, 2011; Koketsu *et al.,* 2011; Yokota *et al.,* 2011).

The near-field ground displacements produced by the 2011 Tohoku earthquake were recorded by a dense geodetic network (GEONET), comprised of ~1200 GPS stations deployed across Japan (Grapenthin *et al.,* 2011). Time-varying solutions for ground position with high-rate (1 sample/sec) calculation (hr-GPS) record both the transient motions produced by seismic waves and the time evolution of the static offsets. Inversion of hr-GPS data is thus inherently a joint inversion of geodetic and seismic data, requires complete Green's functions for all motions, and has been found to provide stable slip patterns relatively independent of key inversion parameters such as rupture velocity (Yue and Lay, 2011) and consistent with joint inversions of other datasets (Ammon *et al*., 2011; Yokota *et al*., 2011). This paper extends the hr-GPS inversions conducted by Ammon *et al*. (2011) and Yue and Lay (2011) and discusses the resolution and stability of hr-GPS inversion and the advantage of joint inversion with additional seismic data to achieve a well-resolved rupture model for the 2011 Tohoku-Oki earthquake.

3.2 Data and Methods

3.2.1 Fault parameterization

Our source model (Figure 3.1) is parameterized with 16 subfaults along strike and 8 along dip on a fault plane with dip that progressively increases with depth from 4.8° to 23°. The dimension of each sub-fault is 30 km × 30 km, and the total fault dimensions are 480 km × 240 km. The geometry of the varying fault dip (Figure 3.1d) was estimated from an east-west seismic reflection profile through the source region near the hypocenter (Miura *et al.,* 2005). We use a one-dimensional layered source structure in the modeling, and have to make some approximations to map the true three-dimensional ocean/wedge/slab geometry into a radially stratified velocity model. The depth below seafloor of each grid point at the center of a subfault in the reflection profile geometry was set equal to the overlying sedimentary prism thickness (Figure 3.1d) to give an approximately correct localized depth phase delay time for the teleseismic P-wave Green's functions, while the fault dip was preserved to give correct radiation patterns. The epicenter (38.107°E, 142.916°N) determined by the mainshock relocation of Zhao *et al.* (2011) (Figure 3.1a), is associated with the 6th node along strike, and 4th node along dip (at a depth below seafloor of 17 km (2011)), defining the geographic location of the fault plane. We reference distance along-strike from the northeastern corner of the model and along-dip down from the trench side of the model.

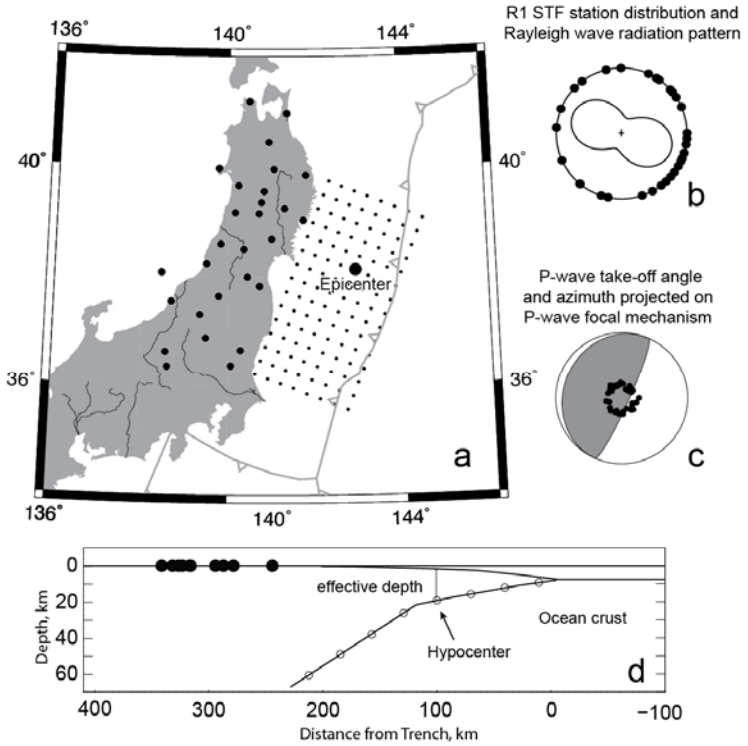

Figure 3.1. a) The locations of 30 hr-GPS stations on Honshu are shown as black-filled circles. The 15 × 8 model grid of the central positions of 30 km × 30 km subfaults is shown with small black dots. The epicenter is indicated by the large black-filled circle. The trench is marked with a gray barbed line. b) Azimuthal directions of 31 R1 STF observations are shown by black filled circles relative to the 250 s period Rayleigh wave radiation pattern for the average fault model shown in the center. c) 38 teleseismic P-wave take-off angles and azimuths are projected on the lower hemisphere of the average mechanism P wave focal mechanism and shown as black filled circles. d) Cross-section of the fault model indicating the fault geometry and ocean bottom geometry. The node depth in the flat PREM reference model was taken as the effective sedimentary prism thickness plus 3 km water. The dip used for each subfault is preserved as the dip of the actual megathrust. The detailed geometry of the prism is shown in Table A1. The hypocenter is located at the 4th node from trench.

For each sub-fault, the source time function is parameterized with 10 symmetric triangles with 5 sec half-durations staggered by 5 sec each. The seismic moment of each triangle for each subfault is an inversion parameter, allowing complex subfault source time functions with up to 55 sec long total duration. Parameterizing for such relatively long subfault rupture durations reduces kinematic constraints on the rupture that result from specified rupture velocity and shorter subfault rupture durations (e.g.,

Lay *et al*., 2010). We assume an initial rupture expansion velocity of V_r = 1.5 km/sec outward on the fault plane from the hypocenter to a distance of 100 km, and then increase V_r to 2.5 km/sec, based on prior back-projection imaging (Koper *et al.,* 2011a,b) and finite-fault modeling of teleseismic signals (Ammon *et al.,* 2011; Lay *et al.*, 2011b). In our previous work, we used two slip-vectors to parameterize a rake-varying slip on each subfault and applied a non-negative least square inversion (Lawson and Hanson, 1995), however, the stacking of the source time functions of two orthogonal slips into the total source time functions (STFs) could not be applied in a linear inversion algorithm. In our inversion with STFs dataset, we fixed the rake angle at 90° referencing to the focal mechanism solution of the Tohoku event. In joint inversions using hr-GPS and teleseismic P-wave data, Green functions for rakes of 45° and 135° on each sub-fault are used in the inversion, allowing variable rake within that range for each subfault.

3.2.2 hr-GPS data

About 1200 high-rate three-component GPS ground motion time series have been processed for the 2011 Tohoku-Oki earthquake. We obtained hr-GPS ground motion records from 1Hz GEONET data, provided by the Geospatial Information Authority of Japan (GSI). The estimated detection level for co-seismic surface displacements is 1 cm horizontal and 2.5 cm vertical, and favorable comparisons with Bernese processing are documented on the GPS-Solutions website where the 1 sample/sec data were distributed. Estimated standard deviations of the horizontal component signals are ~0.02 m, and for vertical components the standard deviations are ~0.04 m. For the

characteristic horizontal peak displacements of several meters for the 2011 event, these random errors are only a few percent, which is small relative to uncertainties related to model parameters for our inversions. We did not reprocess the raw GPS data, but compared the ground motion estimates for nearby stations with independently-processed ARIA data (with 30 sec sampling) to ensure reliability and freedom from multipath contamination (Yue and Lay, 2011).

From the full set of hr-GPS time series, we selected 57 stations with 3-component displacement records for inversion, taking into consideration the signal-to-noise ratios and the azimuthal coverage (Figure 3.1). We extracted 500-sec-long time windows from the high-rate data, starting at the earthquake origin time (05:46:18 UTC) determined by the mainshock relocation of Zhao *et al.* (2011). Normal mode summation of all modes for PREM (Dziewonski and Anderson, 1981) up to 80 mHz was used to generate hr-GPS Green's functions, using a mode set provided by Luis Rivera. These mode sums account for all seismic and static ground motions at regional distances for a spherical, layered, anelastic Earth model with intrinsically balanced weighting of dynamic and static ground motion information. To reduce the computational effort, we specify the Green's functions for each sub-fault-station pair using a pre-calculated database with 10 km epicentral spacing and 1 km source depth spacing. We use the Green's function for the nearest node from the database for each station, incurring minor errors (<5 km) in propagation distance, which are insignificant for the 80 mHz (12.5s) limit of the signal spectrum. We applied a fourth-order low-pass Butterworth filter with a corner at 25 sec to both the raw data

and the Green's functions to eliminate noise in the processed data and mode sum truncation ringing, respectively. The parameters used in this study are the same as used by Yue and Lay (2011), who found stability in hr-GPS-only inversions using many permutations of station subsets from the large number of hr-GPS stations that are available. The results we show here are not significantly dependent on the precise choice of stations as long as similar azimuthal and spatial distributions are used.

3.2.3 Teleseismic P-wave data

The teleseismic P-wave data set is comprised of 38 broadband ground motions from stations of the Federation of Digital Seismic Networks (FDSN), accessed through the Incorporated Research Institutions for Seismology (IRIS) data center. The data were selected from hundreds of available FDSN seismograms to have good azimuthal coverage (Figure 3.1c) and high signal-to-noise ratio. A 200-sec-long time window was extracted from the raw data, starting 10 sec prior to the arrival of the P waves. The initial motions of the P waves were aligned manually, relative to the USGS-NEIC reported origin time (05:46:24 UTC). The USGS origin time is 5-6 sec later than local determinations, primarily due to existence of a very weak initial seismic energy release that can only be seen in local high frequency stations. We shifted the teleseismic P-wave data first arrival alignments by a corresponding amount to ensure consistency with the hr-GPS reference origin time from Zhao *et al*. (2011). Because the grid spacing is 30 km and the rupture velocity is low (initially 1.5 km/sec), the hypocentral subfault will still capture the P-wave onsets even if there is a delayed onset of visible far-field ground displacement.

Teleseismic P-wave Green's functions were generated using the layered propagator matrix code of Kikuchi and Kanamori (1991) for the PREM velocity structure, again ensuring consistency with the source structure used for the hr-GPS Green's function. This choice of PREM velocity structure is significant in that the near-surface crustal layer in PREM does not have as low of a rigidity as assumed in some P-wave inversion studies for this event (e.g., Lay *et al*., 2011a), which can lead to differences in slip estimates near the trench. The Green's functions and data were both filtered by a Butterworth low-pass filter with a corner at 1 sec and the seismograms were decimated to 0.5 sec time sampling. Considering the relatively long source duration of ~150 sec for the Tohoku-Oki event (Yue and Lay, 2011), the teleseismic P-waves windows can have some contamination from PP-wave arrivals for stations at shorter epicentral distances. The contaminated tail energy of these P-wave traces was manually cut and given zero out, so was the Green's function, such that joint inversions will only use hr-GPS, more distant P-wave data, and surface wave data for constraining later parts of the source solution.

3.2.4 R1 STF data

725 short-arc Rayleigh wave (R_1) relative source time functions (STFs) were estimated from the main shock observations by deconvolving empirical Green's functions (EGFs) (e.g., Ammon *et al.,* 1993) given by signals at the same station for the 9 March 2011 M_w 7.3 foreshock. The R_1 signals were isolated using a wide group velocity window, and the deconvolutions used an iterative time-domain procedure with positivity constraint, based on the method of Kikuchi and Kanamori (1982). A

low-pass Gaussian filter (α = 0.1 Hz) was applied to the deconvolved signals to reduce short-period noise in the resulting time series. These relative R_1 STFs isolate the differential source effects of the larger and EGF events, with accurate estimation of the larger event properties for periods longer than about 30 sec. All STFs were bin-stacked, reference to their azimuth, into 29 traces with a 10° increment, and these stacked R_1 STFs were used in inversion to improve data quality and reducing data scale. Although the Mw = 7.3 foreshock, used as the EGF, has a relatively short source time duration (~30s) to the main event (~140s), the time finiteness could not be neglected in STFs calculation, because 30s long source duration is longer than the applied low-pass filter. We convolved a 30s long symmetric triangle to the stacked R_1 STFs to remove the source finiteness effect of the EGFs. A 400-sec-long time window was extracted from the STFs, and the data were decimated to 5 sec sampling. The processing of the R_1 STFs presents some challenges for joint inversion. By deconvolving an EGF, the STFs are affected by any differences in the faulting geometry (dip and/or rake) for the larger event's rupture relative to the smaller event. For finite-fault inversion with a model that varies in dip, δ, we apply subfault moment corrections proportional to $\sin(\delta_{EGF} \times 2)/\sin(\delta_{SUBFAULT} \times 2)$ to account for varying subfault contribution to the overall synthetic STFs.

3.2.5 Ocean bottom GPS data

Co-seismic displacement on the ocean floor of 5 stations near the epicenter was determined using a GPS/acoustic combination technique (Sato *et al. 2011).* It is shown that the maximum horizontal slip near the hypocenter is ~25m, and the

maximum vertical displacement near the hypocenter is ~3m. The 3-components displacements of these 5 OBGPS stations were used in our joint inversion. Static displacements obtained from stacking the normal mode, the same as used by hr-GPS Green's functions, were used as the Green's function for inversion of the OBGPS data.

We ran two basic sets of inversions with different combinations of datasets: joint inversion with hr-GPS data, teleseismic P-wave data, R_1 STFs and OBGPS data, using a constant rake of 90°, is designated the GTS inversion; joint inversion with hr-GPS data and teleseismic P-wave data, allowing variable rake on the subfaults, is designated the GT inversion.

3.3 Results and discussion

3.3.1 Checkerboard tests and stability test

Before showing results of data inversions, we demonstrate the generic resolution of single and joint dataset inversions for simple slip model distributions. Checkerboard tests provide a convenient visualization of relative resolution and stability, but have to be used cautiously as there are many parameters that can trade-off in finite-source models. The synthetic data for our checkerboard tests were computed using the actual station distributions and the same Green's functions as used in the data inversions shown later. When no damping is applied and no noise is added, each inversion resolves exactly the same slip distribution as the input model, because the inversion matrix is fully-ranked. However, when applying any regularization technique, even for noise-free data, slip locations and magnitudes with intrinsically

low spatial resolution for the data and model configuration will be smeared out by the regularization effect. For most inversion problems, resolution and stability are controlled by the degree of similarity of the eigenvectors of the inversion matrix, described as its associated covariance matrix. Essentially, if the eigenvectors are similar between two parameters and they contribute to the fit to the same data, the two parameters cannot be differentiated by the inversion. For the specific case of finite-fault model inversions, the similarity between the Green's functions of difference subfaults determines their relative resolution.

Regularization is necessary to ensure inversion stability for most finite-fault source model inversions. We applied a Laplacian regularization, which constrains the second order gradient for each parameter to be zero. The strength of regularization influences the slip expansion and peak slip amplitude, and our selection of a preferred regularization parameter is based on two factors: the maximum slip amount near the up-dip limit of the fault should not exceed the ocean floor displacement (~60-80 m) observed at the toe of the upper wedge; and the rupture distribution should be compatible with the resolution shown in the checkerboard tests.

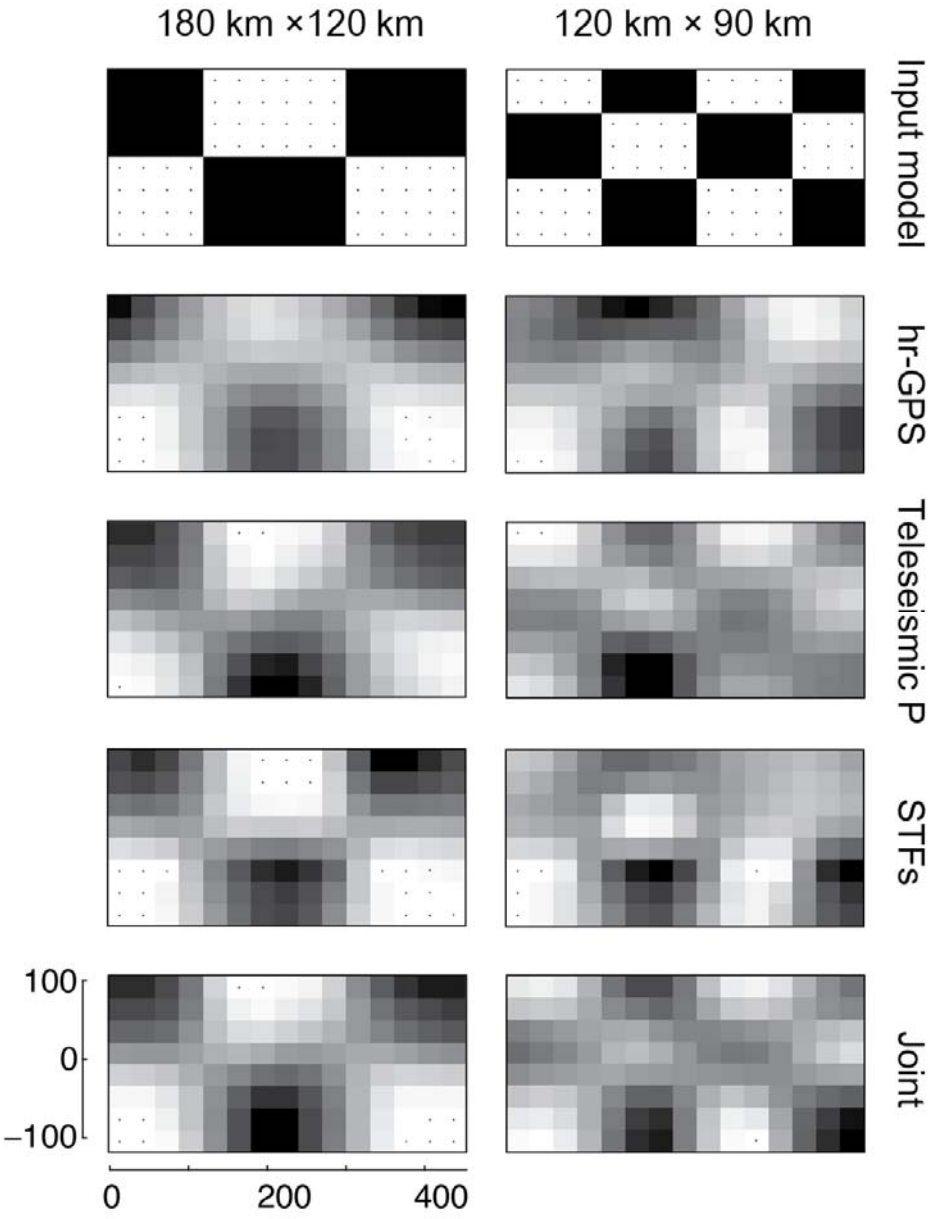

Figure 3.2. Examples of checkerboard tests for synthetic slip distributions larger than the model discretization (covering up to 6 × 4 nodes and 4 × 3 nodes in these cases). These indicate the relative resolution for fixed-rake inversions with hr-GPS, teleseismic P-waves and R1 STFs separately and jointly. These apply the same regularization and weighting between different datasets as used in the inversion of real data. The hr-GPS inversion has good resolution down-dip but poor resolution up-dip, especially toward the along-strike (horizontal) limits of the fault model. Teleseismic P-wave inversion has fair resolution across the fault plane. R1 STFs provide good resolution for the sparse checkerboard test but poor resolution for the finer checkerboard test due to the lack of high frequency content. The joint inversion has improved resolution across the fault plane, exploiting the relative strengths of the different data sets.

Figure 3.2 shows results for representative checkerboard inversions with relatively large-scale slip patterns with dimensions larger than the model parameterization. The rupture velocity for the synthetics and the model are the same, and the smoothing regularization is the same as used in the data inversions. The rake is constant in this case. The hr-GPS dataset, for which the primary time-varying signal involves the time growth of the static offset and the arrival of the little-dispersed surface wave motions with relatively low horizontal velocities (~4 km). The timing information (which is not included in geodetic static offset inversions) should provide high resolution; however, for the Tohoku-Oki earthquake, all hr-GPS stations are located on one side of the hypocenter, which leads to a trade-off between the subfault slip time and the slip location. The vertical displacement for a thrust event changes sign with epicentral distance, while the horizontal displacement does not. For the Tohoku-Oki event GPS station distribution, the up-dip and down-dip regions of slip on the megathrust produce opposing vertical displacements that interfere to shape the weak overall vertical ground motion, while the larger eastward component displacement results from constructive interference of all fault motions. The advantage of three-component GPS signal inversion is the slip of the up-dip and the down-dip needs to contribute together to fit the large eastward displacement and interfering to fit the relatively minor vertical displacement. Inversion with three-component displacements thus provides more sensitivity to the slip distribution along dip than inversion with only horizontal component. Generally the resolution of hr-GPS data comes from both the interfering of three-component ground displacement and the timing information of the

time-varying signals. The hr-GPS checkerboard tests recover the input patterns well on the down-dip part of the fault model, but the up-dip slip pattern is smeared along strike direction in finer checker-board test (Figure 3.2). It was well established that the static displacement with observations on one side of the fault has limited resolution to the near trench displacement, (Wei *et al. 2012*; Yokota *et al. 2011*). In our test, the resolution of the hr-GPS data is much improved than the static GPS data, especially in the along dip direction; the along strike resolution is limited due to the absence of stations to the north and south side of the fault plane. For teleseismic P-wave inversions, directivity effects are relatively minor due to the high apparent velocity of teleseismic P-waves (~20 km/sec). The checkerboard tests of teleseismic P-wave inversions still show fairly good resolution throughout the whole fault planes (Figure 3.2); however, for very shallow regions of the fault plane the interference between P and pP depth phases produces low amplitude Green's functions that can give rise to instability in the slip resolution, particularly if the fault geometry (dip) is inaccurately specified. For the azimuthally well-distributed R_1 STF data inversion, which emphasizes long-period Rayleigh wave energy with low phase velocity (~4 km/sec), the spatial resolution is quite good, in principle. While the EGF technique accounts for overall dispersion, attenuation and aspherical effects effectively, actual variations in excitation due to curved fault plane and depth distribution of the source will degrade the ideal resolution (Figure 3.2 ideally uses consistent Green's functions for the synthetics and inversions through the fault plane, which is not realistic). The checkerboard test for joint inversion of the different datasets using the actual relative

weighting applied to the data provides better resolution than any individual dataset (Figure 3.2). The complementary sensitivity of the different data sets is exploited in the joint inversions, with the good up-dip resolution provided by the P-waves offsetting the weak up-dip resolution from the hr-GPS data.

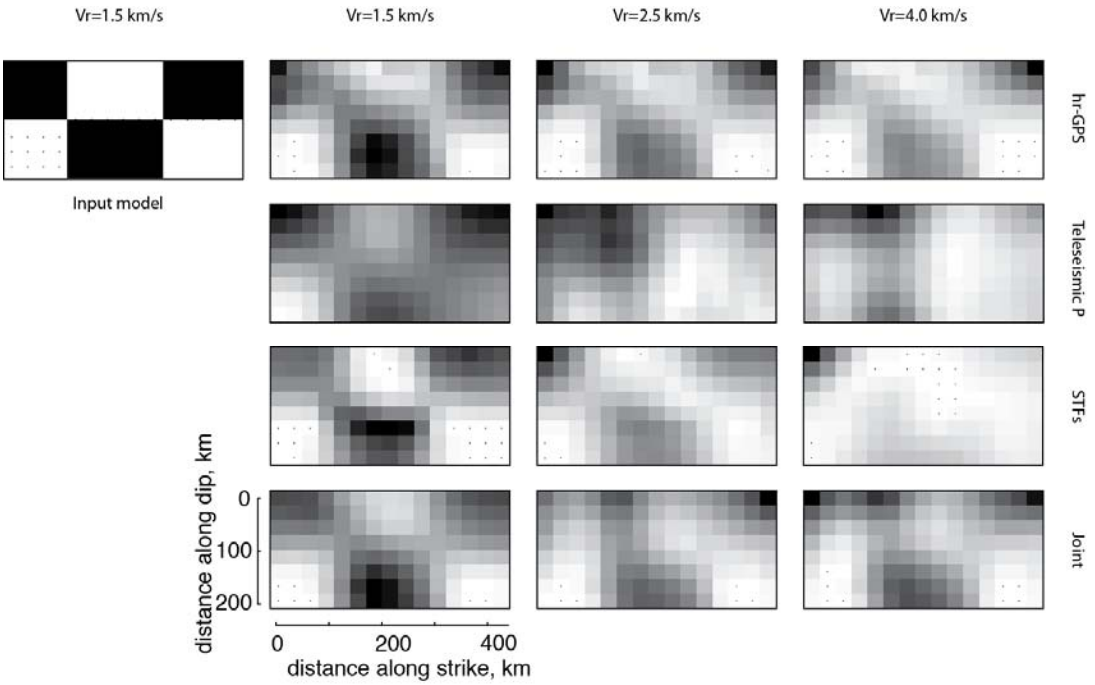

Figure 3.3. Examples of checkerboard tests for a synthetic slip distribution for a rupture velocity, Vr = 1.5 km/s. Inversions for various assumed values of Vr for fixed-rake inversions with hr-GPS, teleseismic P-waves and R1 STFs separately and jointly are shown. These apply the same regularization and weighting between different datasets as used in the inversion of real data. The hr-GPS inversions have the best resolution of slip for incorrect assumed rupture velocity. Teleseismic P-wave and R1 STF inversions have poor resolution when the wrong rupture velocity is assumed. The joint inversion performs slightly better than the hr-GPS inversion for the wrong rupture velocity.

Figure 3.3 provides checkerboard tests for a simple slip distribution for which a rupture velocity of 1.5 km/sec was used in the simulations, with either correct or overestimated rupture velocities used in the inversions. This is a particularly important test, as teleseismic P-wave data are well-known to have limited resolution

of rupture velocity, and errors in the assumed value can completely control the inferred spatial distribution of slip (e.g., Lay *et al*., 2010). In this case, the hr-GPS data have intrinsically good spatial resolution that largely stabilizes the solution even for very inaccurate choice of rupture velocity, as long as the source time function durations are sufficiently long-lasting for each subfault such that the slip distribution is not kinematically constrained to expand outward as a rupture annulus prematurely. The pronounced deterioration of the recovered images for the teleseismic P-waves and R_1 STFs occurs despite having the long subfault duration flexibility because these data simply have lower intrinsic resolution. The joint inversions strongly resemble the hr-GPS inversion alone due to the high spatial resolution intrinsic to the regional seismo-geodetic information in the hr-GPS signals, as discussed by Yue and Lay (2011).

It is apparent and convenient to show the inversion resolution using checker-board, however in checkerboard test we apply the same Green's function for generating synthetic data and inversion matrix, for which the effect of the Green's function discrepancy will not be tested. The fault geometry is a key parameter to determine the Green's function, for which radiation pattern and depth phase varies with different fault geometry, and may impact our inversion result. To test the inversion stability with different fault model, we applied three set of parameterization to the fault model: single dip (10°) fault model as used by Lay *et al. (2011)*, multi-dip fault model without correcting for the effective depth, and our updated muti-dip fault model with corrected effective depth. All the other inversion parameters were applied the same to

the three joint inversions with all dataset, and the results are plotted in Figure 3.A1. The differences in slip pattern between these models are subtle, implying the impact of slightly fault geometry change to joint inversion are not significant.

We also tested the inversion stability by varying source duration of each subfault. In this test, we used 5, 10 and 15 symmetric triangles each with 5s rising time and 5s shift time to parameterize each subfault source time function, simulating a 30s, 55s and 80s long source time function respectively. The inversion result, including the slip distribution and each source time function, are shown in Figure 3.A2. It is demonstrated when source time is long enough, longer than 50s probably longer than the true source duration, inversion will not use the tail of each source time function, and the inversion results of 55s and 80s long source duration are almost identical to each other.

We now move on to actual data inversions for which the results can be appraised in the context of these model tests. We first consider the overall slip distributions and then address the time evolution of slip in the preferred models. We use the rupture front expansion parameters and smoothing parameters described earlier for all of the models.

3.3.2 GTS inversion slip pattern

Separate inversions of hr-GPS, teleseismic P-waves, R_1 STF datasets and joint inversion results with hr-GPS, teleseismic P-wave, R_1 STFs and OBGPS dataset for

constant rake models (λ = 90°) are shown in Figure 3.4. In hr-GPS inversion, two slip

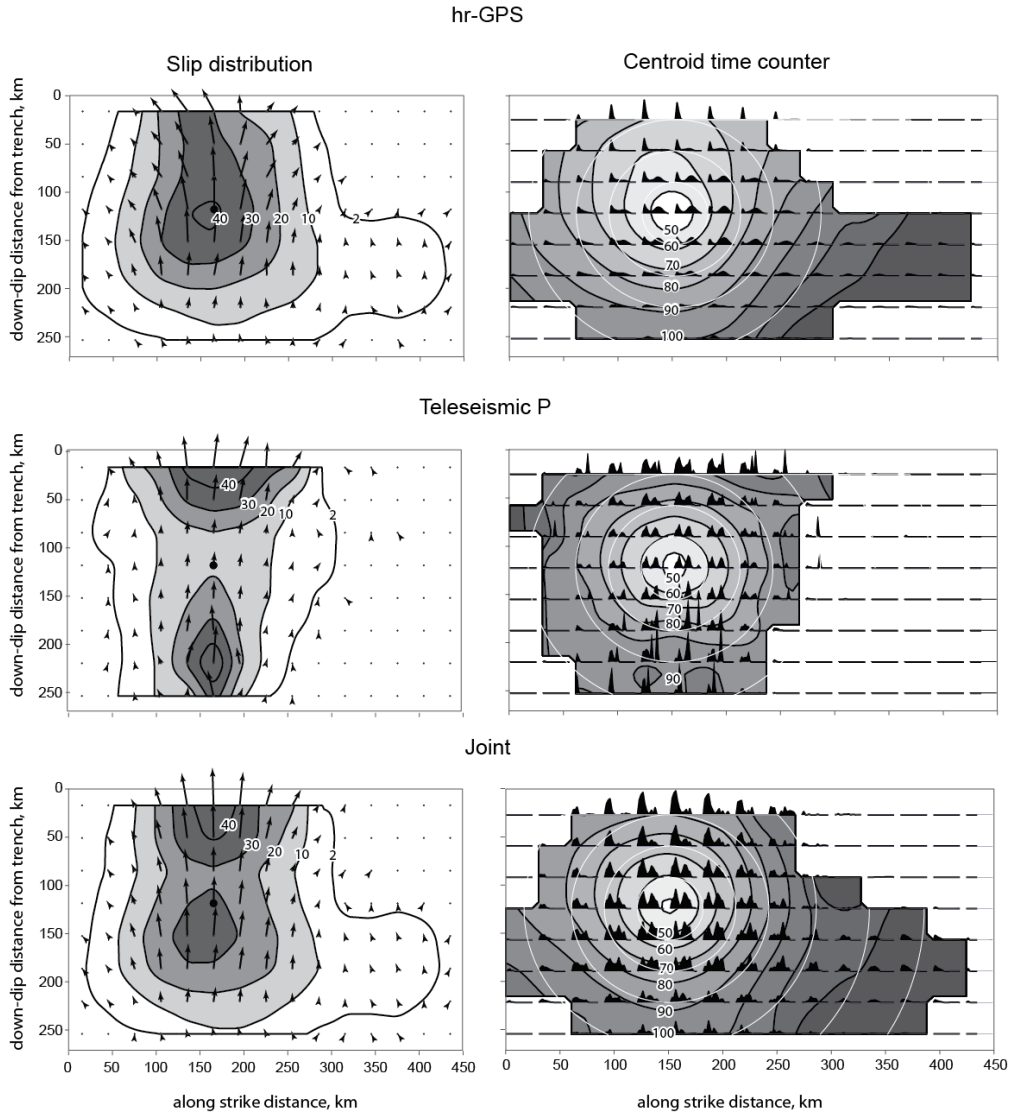

Figure 3.4. (left) Model slip distributions for inversions with variable rake for separate hr-GPS and teleseismic P inversions, and for joint inversion. For each sub-fault, two slip vectors with rakes of 45° and 135° were allowed in a non-negative inversion that constrains the rake to the intervening range of angles. For separate hr-GPS inversion, the maximum slip is located near the hypocentral region, but slip extends up to the trench. For separate teleseismic inversion, two regions of larger slip (~50m) locate near the trench and down-dip from the hypocenter. The joint inversion retains a weak two-patch pattern but the overall slip is similar to the hr-GPS inversion result. (right) For each of the inversion models, the source time functions for all sub-faults are shown as black polygons, with the sub-fault source function centroid times contoured by the gray-scale background with black contours labeled by the black filled numbers. For each sub-fault, the total possible rupture duration is 75 s. Model rupture front expansion is indicated by the white concentric circles which have

20 s intervals.

patches are resolved, one concentrated patch near the trench with maximum slip of ~60 m, and spreading ~300km along strike direction; the other slip patch locates near the hypocenter and down-dip spreading to a larger area than up-dip slip patch.

The hr-GPS data also resolve a down-dip low-slip region that extends along strike to the south. Teleseismic P-wave data resolve a more extended slip pattern with the maximum slip locating near the trench and decrease smoothly to down-dip direction. This model has similarities with other teleseismic inversions, but it is important to recognize that the absolute values of slip are constrained by using of PREM rigidity structure compared to, for example, the slip distribution of Lay *et al*. (2011a), which used lower rigidities at shallow depth and inferred larger peak slip. The minor slip region to the south indicated by the hr-GPS inversion is not resolved by the P-wave dataset. There is substantial variability in finite-fault model in the southern part of the megathrust amongst the published body wave inversions, some of which may be attributed to contamination from PP phases that we have suppressed explicitly. Inversion with R_1 STFs separately resolved similar up-dip rupture pattern as hr-GPS inversion, with maximum slip of ~60m and spreading ~300 km along strike direction. Down-dip slip patch is shown in STFs inversion result but not as significant as hr-GPS inversion. The slip patch extended to the south was also resolved in STFs inversion, although the location between these two slip patches varies slightly. Joint inversion kept the common features of each separate inversion result, and resolved a maximum slip near the trench with ~ 50m slip, extended slip near the hypocenter and

a slip patch extended to the south. Considering the common feature of all three separate inversions, the blank zone between up-dip and down-dip slip patches in hr-GPS inversion may not be realistic and the slip is most probably continuous from up-dip to down-dip. This artifact in hr-GPS inversion, which is not shown in our previous work (Yue and Lay, *2011*) may be attributed to a sparse grid points and low-grade regularization applied. Comparing with other finite fault models, seismic observations tends to resolve large slip near the trench, (e.g., Hayes, 2011; Lay *et al.,* 2011a; Shao *et al*., 2011; Yoshida *et al*., 2011a,b) with maximum slip of ~60m. This rupture feature is consistent with the large horizontal slip observed near the toe of the upper wedge. This feature is quite consistent with the maximum slip near the trench resolved in our work. Extended rupture near the hypocenter was always resolved by geodetic based inversions, (Iinuma *et al.,* 2011; Miyazaki *et al.,* 2011; Simons *et al.,* 2011), with maximum slip amount varies from 35m to 60m. Including OBGPS data in geodetic based inversion tends to improve the result resolution and put slip to the east side (Ito *et al. 2011*; Wei *et al. 2012*). In our inversion result, the down-dip slip pattern is significant and extended to a larger area than the up-dip slip patch, which is a main difference between our result and most seismic based inversion results. Comparisons between inversion with or without OBGPS data are shown in Figure 3.A4. It is shown the maximum slip and detailed slip pattern are influenced by the OBGPS data, especially from the hypocenter to the up-dip, but the overall slip patterns are consistent with or without OBGPS dataset. The southern propagating slip patch is widely observed in high-frequency back-projection results, and a depth-frequency

dependent radiation behavior were used to interpret the discrepancy of long-period and short-period back-projection result (Koper *et al. 2011a,b*). The down-dip southern extended slip patch is also resolved by near-field strong motion inversion works (e.g., Kurahashi and Irikura, 2011; Yoshida *et al.*, 2011a). In our result, this slip pattern is robust in both hr-GPS and R_1 STF inversion results. A similar down-dip southern extended slip patch was resolved by most joint inversion works (Ammon *et al.,* 2011; Koketsu *et al.,* 2011; Yokota *et al.,* 2011). However in a recent joint inversion work by Wei *et al.* (2012), using static GPS and OBGPS observations together with near field strong ground motion observations, this patch locates up-dip more close to the trench.

The joint inversion combines the basic characteristic of the individual inversions, but still fits all the data quite well Figure 3.5 (all waveform fits for the joint inversion and separate inversions are shown in Figure 3.A5 and A6). The degree of waveform recovery could be expressed by the power of waveform fitting residual, which only have relative but not absolute significance: a decrease of waveform fitting residual means the data are fitted better, but a small number of the residual power does not necessarily mean the waveform are fitted very well. The power of the waveform fitting residual of the separate inversions of hr-GPS, teleseismic P waves and R_1 STFs are 0.6%, 6% and 2% respectively, and the waveform fitting residual power of the joint inversion of for hr-GPS, teleseismic P waves, R_1 STFs and OBGPS data are 2%, 11%, 11% and 2%. Although waveform fitting residual is elevated by several percent in joint inversion than inversion with each dataset separately, the waveforms are still

well fitted Figure 3.A5 and A6.

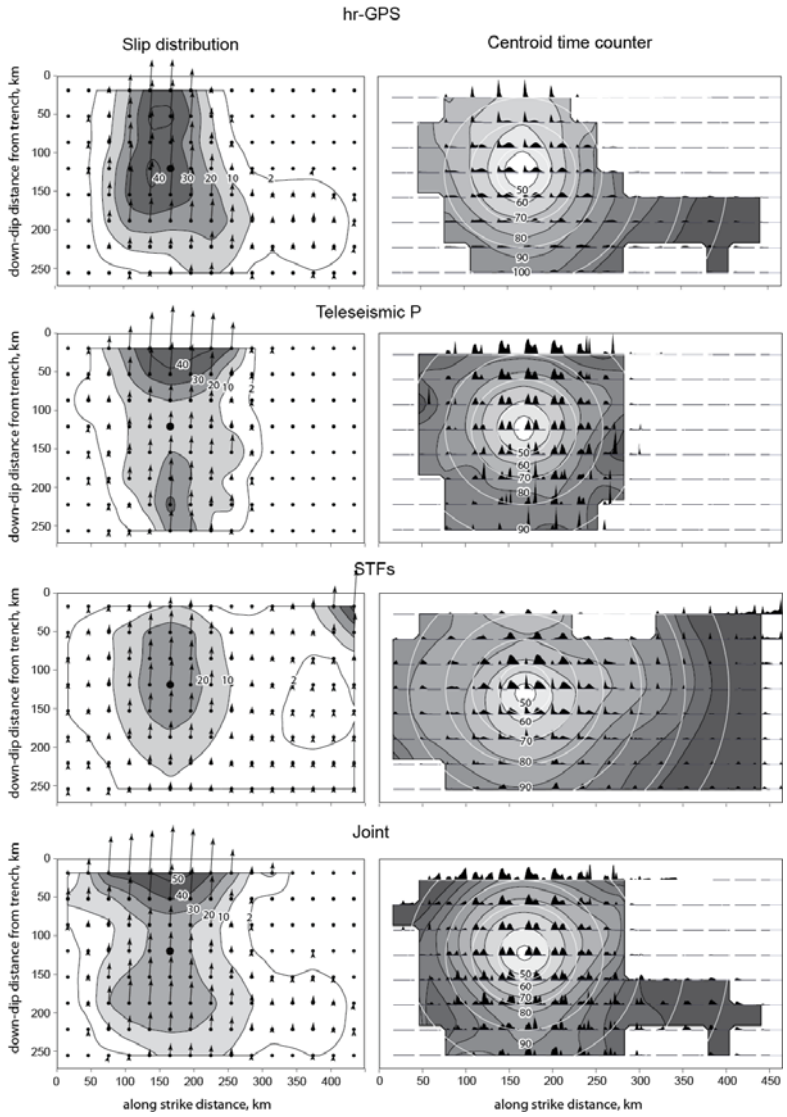

Figure 3.5. (left) Model slip distributions for fixed-rake inversions. For each subfault, one slip vector with the rake fixed at 85° was used in a non-negative inversion. The hr-GPS data, teleseismic P-wave data, and R1 STF data were inverted separately and jointly. All three data sets resolve similar rupture locations along strike, but vary in slip distribution along dip. The hr-GPS and teleseismic inversions results are similar to the variable-rake inversions summarized in Figure 3.4. Inversion of R1 STFs finds the main slip near the hypocenter and a late slip up-dip to the south, which appears to be an instability from the end of the STFs due to their positivity constraint. The joint inversion slip pattern is quite similar to the variable-rake solution in Figure 3.4. (right) For each of the inversion models, the source time functions for all sub-faults are shown as black polygons, with the sub-fault source function centroid value time shown as gray scaled background with black contours labeled by the black-filled numbers. For each subfault, the total allowed rupture duration is 75s. Model rupture

front expansion is indicated by the white concentric circles which have 20 s intervals.

3.3.3 GT inversion slip pattern

The overall slip pattern resolved by GT inversion is quite similar to the slip pattern of GTS inversion Figure 3.A3. In the hr-GPS separate inversion and GT joint inversion, the maximum slip amount is smaller than fix-rake hr-GPS separate inversion and GTS joint inversion. It is probably resulted by the effective regularization factor. The summed power of Green's function differs between fix-rake and vary-rake inversion, so even we applied the same regularization factor to the data, the effective regularization applied to Green's functions scaled by the Green's function scale of each parameter also differs. Then the effect of different regularization will either extend the rupture area giving a low slip amount, or focusing slip into concentrated large maximum slip. But the regularization will not change the power of the Green's function matrix, so the average slip or summed seismic moment will be kept. The seismic moment resolved by vary-rake GT joint inversion is 4.6×10^{22} Nm, comparing with a seismic moment resolved by the fix-rake GTS joint inversion of 4.2×10^{22} Nm. Although we allowed a rake variation in the GT inversion, the rake change is not obvious in separate teleseismic P wave inversion result. In separate hr-GPS inversion and GT joint inversion results, the resolved slip vector seems like radiated from the hypocenter, which is probably an artifact in geodetic inversion when all GPS slip vectors focusing to the hypocenter, Figure 3.6. So the rake change should not be significant as resolved by teleseismic inversions, and a fix-rake assumption used in GTS inversion is a credible assumption in Tohoku

earthquake.

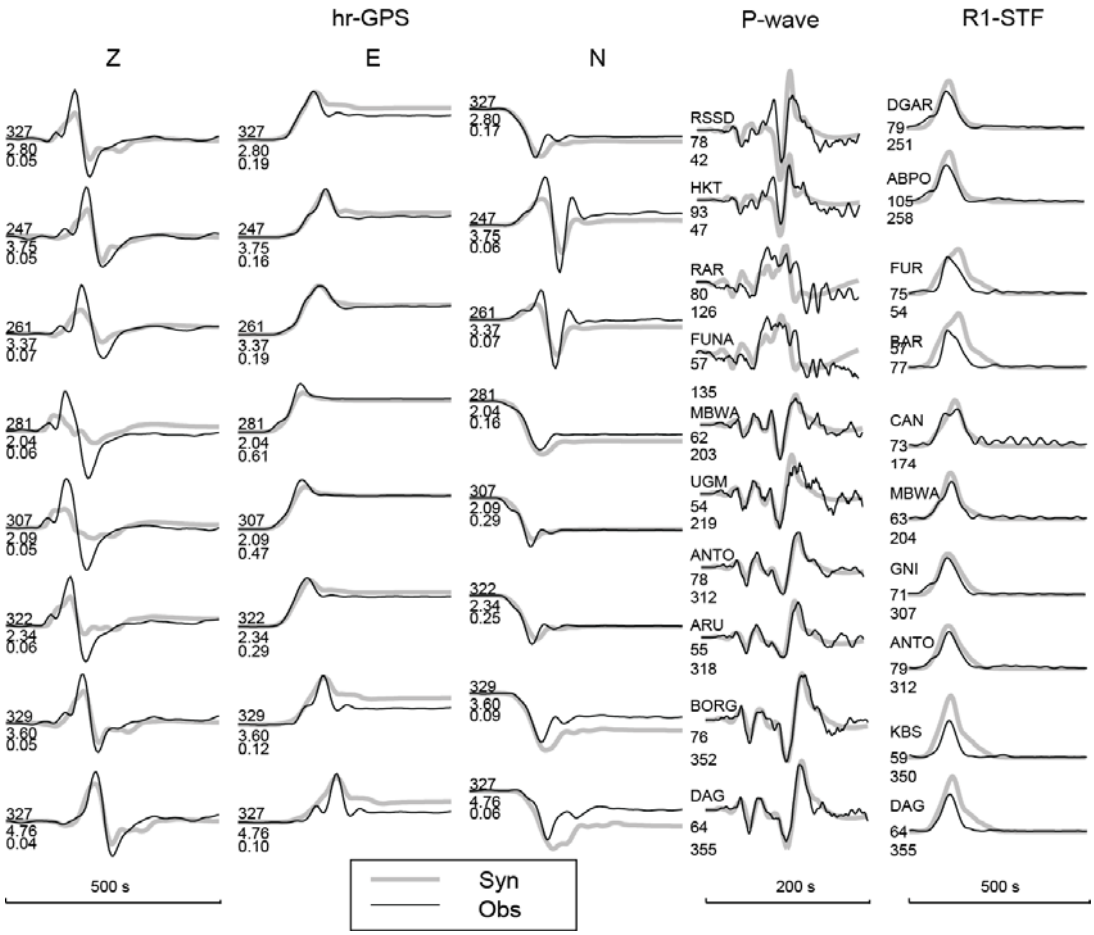

Figure 3.6. Comparison of observed (thin black lines) and predicted (thick gray lines) waveforms for the preferred fixed-rake joint inversion model in Figure 3.5 using hr-GPS, teleseismic P-wave and R1 STFs. For the three-component hr-GPS data, station names, epicentral distances, and peak amplitude (in m) are labeled. For teleseismic P-waves and R1-STFs, stations names, epicentral distances and azimuth are labeled. The time windows used for each data set were 500 s (hr-GPS), 200 s (P-waves) and 500 s (R1 STFs).

3.3.4 Source time functions

The source time functions for each subfault differ systematically between up-dip and down-dip regions for these inversions, particularly clearly for the hr-GPS inversions (Figures 3.4 and 3.A3) and the R_1 STF inversion (Figure 3.4). The shallowest two rows of subfaults tend to be dominated by a single source function

pulse with a lower amplitude secondary pulse spread over about 40 sec, whereas near the hypocenter (3rd to 5th rows of nodes along dip) most subfaults show more balanced double source function pulses, for both individual and joint inversions (Figures 3.4 and 3.A3). Similar source time function complexity was resolved by the teleseismic data inversions of Ide *et al*. (2011) and Lee *et al.* (2011), who interpreted this as a two stage rupture, with the second stage being driven by the very large slip up-dip. This is plausible for our model, given the maximum slip up-dip is ~50 m, but resolving slip front behavior is constrained by the smoothing in the inversions.

The down-dip subfaults (6th to 8th rows of nodes along dip) source time functions exhibit multiple pulses with shorter durations (10-20 sec) that are more variable between individual and joint inversions. These complex time function pulses could be interpreted as either several spatially limited asperities rupturing at slightly different times, or several re-rupturing patches in the down-dip region driven by surrounding quasi-static slip. The kinematic model is too limited to resolve this issue, but we prefer the first notion, as it is consistent with interpretations that have been advanced to explain the concentration of sources of coherent short-period radiation from the deeper part of the megathrust detected by back-projection of short-period signals (e.g., Ishii, 2011; Koper *et al.,* 2011a,b; Meng *et al*., 2011; Wang and Mori, 2011; Yao *et al*., 2011; Zhang et al., 2011). It is plausible that there are coherent bursts of short-period radiation from failure of small asperities at depth (e.g., Lay *et al*., 2012). Our finite-fault models do not resolve comparable scale structures, but are consistent with features comparable to the down-dip ruptures in the 1978 and 2005 Miyagi-Oki

earthquakes, with M_w ~ 7.2-7.4. This is clearly on a spatial scale smaller than the larger uniform slip regions at shallower depths.

For hr-GPS inversions, the source time function centroid time contours are somewhat more wide-spread up-dip and more spatially concentrated down-dip. This is not apparent in teleseismic P-wave inversions and is suppressed in the joint inversions (Figures 3.4, 3.5). Widely spread contours indicate that the rupture has slip occurring over the same time frame over a large area. If this is the case, it is plausible that short-period radiation emanates from a corresponding large rupture front, and will not be imaged by the back-projection method, which seeks point-wise coherent alignment of intervals of short-period signal. This may explain why the back-projections do not find concentrated sources of short-period radiation from the up-dip region.

3.3.5 Waveform fitting and relative weighting between datasets

Joint inversions always present challenges for relative weighting of different datasets. Some inversions use proportionate weighting after normalizing the data (e.g., Koketsu *et al.* 2011), but this may fail to account for relative modeling error for each dataset. For our joint inversions, we preferred to give more weight to datasets with less expected modeling error. The error of hr-GPS Green's functions comes primarily from the 1-D reference model inaccuracy, which is reduced by using a low-pass filter that suppresses periods shorter than 25 sec. Although the estimated data error of vertical displacements (~0.04 m) is larger than for horizontal displacements (~0.02 m), these values are still on the same scale, so our 3-component hr-GPS waveforms are

equally weighted. Teleseismic P-waves have higher frequency content, which improves resolution of the source radiation details, but reference model inaccuracy increases for shorter period signals as well. The R_1 STF dataset has errors stemming from the EGF deconvolution technique being applied to a rupture with a large span of source depths and possible rake variations. GPS/acoustic (OBGPS) data present significant slip amount near the epicenter and will give import constrains to the slip amount on the fault plane. The coseismic slip of these stations were obtained from 28th March to 5th April, which is 17-25 days after the earthquake, and the displacement measurement may be contaminated by the after-slip, aftershocks or ocean bottom land-slide. Meanwhile, only 5 stations are available for these ocean bottom displacements each with one static displacement, comparing with more observations for hr-GPS, P-wave and STFs data, the scale of the OBGPS displacements will be extremely large after normalized by the sample point number. If we apply the same weighting to the OBGPS dataset, the inversion will mostly fit the OBGPS data, given 10^{-5} residual to the OBGPS data but tens of percent residual to the other dataset. So we applied a much lower weighting to the OBGPS datasets. In our GTS joint inversions, the weights used in merging hr-GPS, teleseismic P-waves, R_1 STFs and OBGPS datasets are 1, 0.2, 2 and 0.01, respectively. We applied this relatively weighting to each dataset to achieve balanced data fitting residual ranging from several percent to around ten percent: ~2% for hr-GPS and OBGPS and ~10% for teleseismic P-waves and STFs. Our preferred weighting comes from performing dozens of test to evaluate the waveform fits for each dataset, but there is typical

subjectivity in deciding what weights are optimal. For our chosen weighting, the rupture area is mainly controlled by the low frequency content of the hr-GPS and the R_1 STFs, with the short-wavelength details are mainly contributed by the teleseismic P-wave dataset and OBGPS dataset. The weighting directly influences how well each data set is matched. For our preferred weights, we fit the P-waves quite well in general without sacrificing the match to the waveform information of both the dynamic and static part of the hr-GPS data (Figure 3.5, A5 and A6). The shape of the R_1 STFs iswell fitted but not to the detailed waveforms, which reflects our caution about the dependence on the EGF procedure (Figure 3.5).

The preferred GTS joint inversion model is plotted in map view in Figure 3.7, along with observed and predicted horizontal ground motion statics from the GPS stations and OBGPS stations. The direction and magnitude of static motions is well matched, as expected from the time-varying comparisons in Figure 3.5. The fits indicate that the assumption of uniform rake is acceptable for this model representation. The large near-trench slip is located where there is a seaward bulge in the upper wedge, and this is the area where large seafloor motions have been inferred.

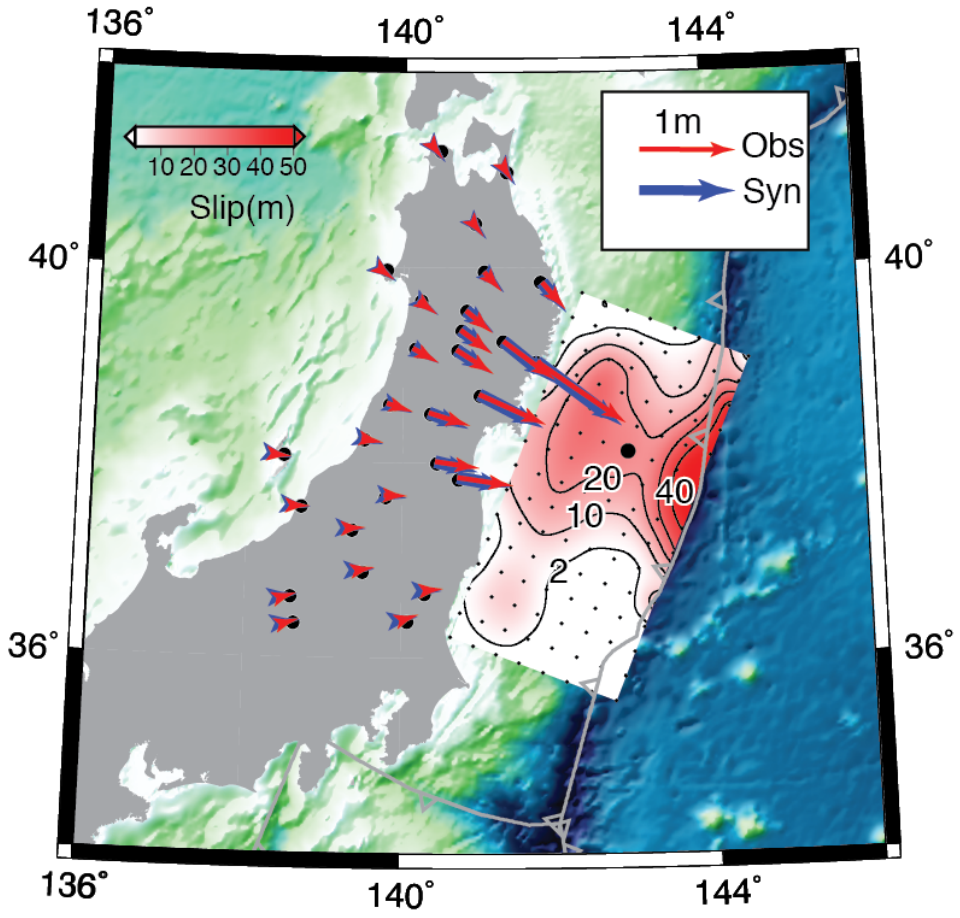

Figure 3.7. Slip distribution for the preferred joint fixed-rake model in map view. Observed and predicted horizontal static displacements after 500 s for the hr-GPS stations used in the inversion are plotted with red and blue arrows, respectively.

3.4 Conclusions

Using joint least-squares inversions of hr-GPS data, teleseismic P-wave data, R_1 STF data and OBGPS data, we obtain slip models for the 2011 Tohoku-Oki event consistent with the time-varying and static data sets. The joint inversions tend to compensate for limitations of each dataset, yielding good combined resolution of slip on the fault plane. The Tohoku-Oki event has large-scale regions of large slip (~50 m) up-dip near the trench and down-dip near the hypocenter, and a minor extension of

down-dip slip to the south. Subfault source time functions in the up-dip region show a dominant early pulse with a weaker secondary shoulder and a spatially wide-spread centroid time contour, suggestive of slip occurring over a large area simultaneously. The central portion of the megathrust has two distinct moment rate pulses, each with about 25 sec duration. This may represent repeated slip of the subfaults driven by very large slip up-dip, or some other rupture irregularity. Source time functions for the down-dip subfaults have multiple shorter duration pulses, possibly related to the region having medium to small-scale fault heterogeneities that generate spatially coherent short-period seismic wave radiation when patches fail in either isolated moderate size events or as part of a great rupture like the 2011 event. The joint inversion results appear to reconcile differences in slip models between seismic-wave-based models, which tend to have most slip up-dip, and geodetic-static-offset-based models, which tend to have most slip near the hypocenter. The added information from the time-varying components of the hr-GPS plays the primary role in resolving the slip distribution.

3.5 Acknowledgements. This work made use of GMT and SAC software. Federation of Digital Seismic Networks (FDSN) teleseismic data were obtained from the Incorporated Research Institutions for Seismology (IRIS) Data Management System (DMS). We thank L. Rivera for providing the normal mode data set. Our hr-GPS data, generously made available by C. Rocken of GPS Solutions, Inc., originated with efforts by GSI, NGDS, Hitz, GPSS, and VERIPOS. Modeling of high-rate GPS recordings using the normal mode approach was suggested by C. J.

Ammon. We also support our associate editor Mark Simons and two anonymous reviewers for their valuable suggestions. This work was supported by NSF grant EAR0635570.

3.6 References

Ammon, C. J., T. Lay, H. Kanamori, and M. Cleveland (2011). A rupture model of the 2011 off the Pacific coast of Tohoku Earthquake, *Earth Planets Space* **63** 693-696, doi:10.5047/eps.2011.05.015.

Ammon, C. J., A. A. Velasco, and T. Lay (1993). Rapid estimation of rupture directivity: Application to the 1992 Landers (M_S = 7.4) and Cape Mendocino (M_S = 7.2), California earthquakes, *Geophys. Res. Lett.* **20**(2) 97–100, doi:10.1029/92GL03032.

Dziewonski, A. M., and D. L. Anderson (1981). Preliminary reference Earth model 1, *Phys. Earth Planet. Inter*. **25**(4) 297–356, doi:10.1016/0031-9201(81)90046-7

Fujii, Y., K. Satake, S. Sakai, M. Shinohara, and T. Kanazawa (2011). Tsunami source of the 2011 off the Pacific coast of Tohoku, Japan earthquake, *Earth Planets Space* **63**(7) 815–820, doi: 10.5047/eps.2011.06.010.

Fujiwara, T., S. Kodaira, T. No, Y. Kaiho, N. Takahashi, and Y. Kaneda (2011). The 2011 Tohoku-Oki earthquake: Displacement reaching the trench axis, *Science* **334** 1240, doi:10.1126/science.1211554.

Grapenthin, R., and J. T. Freymueller (2011). The dynamics of a seismic wave field: Animation and analysis of kinematic GPS data recorded during the 2011 Tohoku - oki earthquake, Japan, *Geophys. Res. Lett.* **38** L18308,

doi:10.1029/2011GL048405.

Hayes, G. (2011). Rapid source characterization of the 03-11-2011 M_w 9.0 Off the Pacific Coast of Tohoku earthquake, *Earth Planets Space* **63** 529-534, doi:10.5047/eps.2011.05.012.

Ide, S., A. Baltay, and G. C. Beroza (2011). Shallow dynamic overshoot and energetic deep rupture in the 2011 Mw 9.0 Tohoku-oki earthquake, *Science* **332** 1426-1429.

Iinuma, T., M. Ohzono, Y. Ohta, and S. Miura (2011). Coseismic slip distribution of the 2011 off the Pacific coast of Tohoku Earthquake (*M* 9.0) estimated based on GPS data – Was the asperity in Miyagi-oki ruptured?, *Earth Planets Space* **63** 643-648.

Ishii, M. (2011). High-frequency rupture properties of the M_w 9.0 off the Pacific coast of Tohoku earthquake, *Earth Planets Space* **63** 609-614, doi: 10.5047/eps.2011.07.009.

Ito, T., K. Ozawa, T. Watanabe, and T. Sagiya (2011a). Slip distribution of the 2011 off the Pacific coast of Tohoku Earthquake inferred from geodetic data, Earth Plaets Spac 63 627-630, doi:10.504/eps.2011.06.023.

Ito, Y., T. Tsuji, Y. Osada, M. Kido, D. Inazu, Y. Hayashi, H. Tsushima, R. Hino, and H. Fujimoto (2011b). Frontal wedge deformation near the source region of the 2011 Tohoku - Oki earthquake, *Geophys. Res. Lett*. **38** L00G05, doi: 10.1029/2011GL048355.

Kikuchi, M. and H. Kanamori, (1982). Inversion of complex body waves, *Bull.*

Seismol. Soc. Am. **72** 491–506.

Kikuchi, M., and H. Kanamori (1991). Inversion of complex body waves−III. *Bull. Seismol. Soc. Am.* **81** 2335 – 2350.

Koketsu, K., Y. Yokota, N. Nishimura, Y. Yagi, S. Miyazaki, K. Satake, Y. Fujii, H. Miyake, S. Sakai, Y. Yamanaka, and T. Okada (2011). A unified source model for the 2011 Tohoku earthquake, *Earth Planet. Sci. Lett*. **310**(3–4) 480-487.

Koper, K. D., A. R. Hutko, and T. Lay (2011a). Along-dip variation of teleseismic short-period radiation from the 11 March 2011 Tohoku Earthquake (M_w 9.0), *Geophys. Res. Lett.* **38** L21309, doi:10.1029/2011GL049689.

Koper, K. D., A. R. Hutko, T. Lay, C. J. Ammon, and H. Kanamori (2011b). Frequency-dependent rupture process of the 2011 M_w 9.0 Tohoku Earthquake: Comparison of short-period P wave back-projection images and broadband seismic rupture models, *Earth Planets Space* **63** 599-602, doi:10.5047/eps.2011.05.026.

Kurahashi, S., and K. Irikura (2011). Source model for generating strong ground motions during the 2011 off the Pacific coast of Tohoku Earthquake, *Earth Planets Space* **63** 571-576, doi:10.5047/eps.2011.06.044.

Lawson, C. L., and R. J. Hanson (1995). *Solving Least Squares Problems*, Soc. for Ind. Appl. Math., Philadelphia, Pa.

Lay, T., C. J. Ammon, A. R. Hutko, and H. Kanamori (2010). Effects of kinematic constraints on teleseismic finite-source rupture inversions: Great Peruvian earthquakes of 23 June 2001 and 15 August 2007, *Bull. Seism. Soc. Am*. **100** 969-994, doi:10.1785/0120090274.

Lay, T., and H. Kanamori (2011). Insights from the great 2011 Japan earthquake, *Physics Today* **64** 33-39.

Lay, T., C. J. Ammon, H. Kanamori, L. Xue, and M. J. Kim (2011a). Possible large near-trench slip during the 2011 M_w 9.0 off the Pacific coast of Tohoku earthquake, *Earth Planets Space* **63** 687-692, doi:10.5047/eps.2011.05.033.

Lay, T., C. J. Ammon, H. Kanamori, M. J. Kim, and L. Xue (2011b). Outer trench-slope faulting and the 2011 M_w 9.0 off the Pacific coast of Tohoku Earthquake, *Earth Planets Space* **63**(7) doi:10.5047/eps.2011.05.006, 713-718.

Lay, T., Y. Yamazaki, C. J. Ammon, K. F. Cheung, and H. Kanamori (2011c). The 2011 M_w 9.0 off the Pacific coast of Tohoku Earthquake: Comparison of deep-water tsunami signals with finite-fault rupture model predictions, *Earth Planets Space* **63**(7) doi:10.5047/eps.2011.05.030, 797-801.

Lay, T., H. Kanamori, C. J. Ammon, K. D. Koper, A. R. Hutko, L. Ye, H. Yue, and T. M. Rushing (2012). Depth-varying rupture properties of subduction zone megathrust faults, *J. Geophys. Res.*, in press.

Lee, S.-J. (2011). Rupture process of the 2011 Tohoku-Oki earthquake based upon joint source inversion of teleseismic and GPS data, Terr. Atmos. Ocean. Sci. 23, 1-7.

Lee, S.-J., B.-S.Huang, M. Ando, H.-C. Chiu, and J.-H. Wang (2011). Evidence of large scale repeating slip during the 2011 Tohoku-Oki earthquake, *Geophys. Res. Lett*. **38** L19306, doi:10.1029/2011GL049580.

Maeda, T., T. Furumura, S. Sakai, and M. Shinohara (2011). Significant tsunami observed at ocean-bottom pressure gauges during the 2011 off the Pacific coast of Tohoku earthquake, *Earth Planets Space* **63** 803-808, doi:10.5047/eps.2011.06.005.

Meng, L., A. Inbal, and J. - P. Ampuero (2011). A window into the complexity of the dynamic rupture of the 2011 M_w 9 Tohoku-oki earthquake, *Geophys. Res. Lett.* **38** L00G07, doi:10.1029/2011GL048118.

Miura, S., N. Takahashi, A. Nakanishi, T. Tsuru, S. Kodaira, and Y. Kaneda (2005). Structural characteristics off Miyagi forearc region, the Japan Trench seismogenic zone, deduced from a wide-angle reflection and refraction study, *Tectonophysics* **407**(3–4) 165-188.

Miyazaki S, J. J. McGuire, and P. Segall, (2011). Seismic and aseismic fault slip before and during the 2011 off the Pacific coast of Tohoku Earthquake, *Earth Planets Space* **63**(7) 637-642, doi:10.5047/eps.2011.07.001

Mori, N., T. Takahashi, T. Yasuda, and H. Yanagisawa (2011). Survey of 2011 Tohoku earthquake tsunami inundation and run-up, *Geophys. Res. Lett.*, *38*, L00G14, doi: 10.1029/2011GL049210

Ozawa, S., T. Nishimura, H. Suito, T. Kobayahi, M. Tobita, and T. Imakiire (2011). Coseismic and postseismic slip of the 2011 magnitude-9 Tohoku-oki earthquake, *Nature* **475** 373-376 doi:10.1038/nature10227.

Pollitz, F., R. Bürgmann, and P. Banerjee (2011). Geodetic slip model of the 2011

M9.0 Tohoku earthquake, *Geophys. Res. Lett.* **38** L00G08, doi:10.1029/2011GL048632.

Saito, T., K. Satake, and T. Furumura (2010). Tsunami waveform inversion including dispersive waves: the 2004 earthquake off Kii Peninsula, Japan, *J. Geophys. Res*. **115** B06303, doi:10.1029/2009JB006884.

Saito, T., Y. Ito, D. Inazu, and R. Hino (2011). Tsunami source of the 2011 Tohoku‐Oki earthquake, Japan: Inversion analysis based on dispersive tsunami simulations, *Geophys. Res. Lett*. **38** L00G19, doi:10.1029/2011GL049089.

Sato, M., T. Ishikawa, N. Ujihara, S. Yoshida, M. Fujita, M. Mochizuki, and A. Asada (2011). Displacement above the hypocenter of the 2011 Tohoku-Oki earthquake, *Science* **332**(6036), 1395. doi:10.1126/science.1207401

Shao, G., X. Li, C. Ji, and T. Maeda (2011). Focal mechanism and slip history of the 2011 Mw 9.1 off the Pacific coast of Tohoku Earthquake, constrained with teleseismic body and surface waves, *Earth Planets Space* **63** 559-564, doi:10.5047/eps.2011.06.028.

Simons, M., S. E. Minson, A. Sladen, F. Ortega, J. Jiang, S. E. Owen, L. Meng, J.-P. Ampuero, S. Wei, R. Chu, *et al*. (2011). The 2011 magnitude 9.0 Tohoku-oki earthquake: Mosaicking the megathrust from seconds to centuries, *Science* **332** 1421-1425.

Wang, D., and J. Mori (2011). Rupture process of the 2011 off the Pacific coast of Tohoku earthquake (M_w 9.0) as imaged with back-projection of teleseismic P

waves, Earth Planets Space 63 603-607, doi:10.5047/eps.2011.05.029.

Shengji Wei, Robert Graves, Don Helmberger, Jean-Philippe Avouac, Junle Jiang (2012). Sources of shaking and flooding during the Tohoku-Oki earthquake: A mixture of rupture styles, Earth and Planetary Science Letters, Volumes 333–334, 91-100, doi: 0012-821X, 10.1016/j.epsl.2012.04.006.

Yamazaki, Y., T. Lay, K. F. Cheung, H. Yue, and H. Kanamori (2011). Modeling near-field tsunami observations to improve finite-fault slip models for the 11 March 2011 Tohoku earthquake, *Geophys. Res. Lett*. **38** L00G15, doi:10.1029/2011GL049130.

Yamazaki, Y., K. F. Cheung, and T. Lay (2012). Generation mechanism and near-field dynamics of the 2011 Tohoku tsunami, *Bull. Seism. Soc. Am*., this volume.

Yao, H., P. Gerstoft, and P. M. Shearer (2011). Compressive sensing of the Tohoku-Oki M_w 9.0 earthquake: Freqeuency-dependent rupture modes, *Geophys. Res. Lett*. **38** L20310, doi:10.1029/2011GL049223.

Yokota, Y., K. Koketsu, Y. Fujii, K. Satake, S. Sakai, M. Shinohara, and T. Kanazawa (2011). Joint inversion of strong motion, teleseismic, geodetic, and tsunami datasets for the rupture process of the 2011 Tohoku earthquake, *Geophys. Res. Lett*. **38** L00G21, doi:10.1029/2011GL050098.

Yoshida, K., K. Miyakoshi, and K. Irikura (2011a). Source process of the 2011 off the Pacific coast of Tohoku Earthquake inferred from waveform inversion with long-period

strong-motion records, *Earth Planets Space* **63**(7) 577–582, doi:10.5047/eps.2011.06.050

Yoshida, Y., H. Ueno, D. Muto, and S. Aoki (2011b). Source process of the 2011 off the Pacific coast of Tohoku earthquake with the combination of teleseismic and strong motion data, *Earth Planets Space* **63**(7) 565-569, doi:10.5047/eps.2011.05.011.

Yue, H., and T. Lay (2011). Inversion of high-rate (1-sps) GPS data for rupture .process of the 11 March 2011 Tohoku earthquake (M_w 9.1), *Geophys. Res. Lett*. **38** L00G09, doi:10.1029/2011GL048700.

Zhang, H., Z. Ge, and L. Ding (2011). Three sub-events composing the 2011 off the Pacific coast of Tohoku earthquake (M_w 9.0) inferred from rupture imaging by back-projecting teleseismic P waves, *Earth Planets Space* **63** 595-598, doi:10.5047/eps.2011.06.021.

Zhao, D., Z. Huang, N. Umino, A. Hasegawa, and H. Kanamori (2011). Structural heterogeneity in the megathrust zone and mechanism of the 2011 Tohoku-oki earthquake (M_w 9.0), *Geophys. Res. Lett*. **38** L17308, doi:10.1029/2011GL048408.

3.7 Auxiliary figures

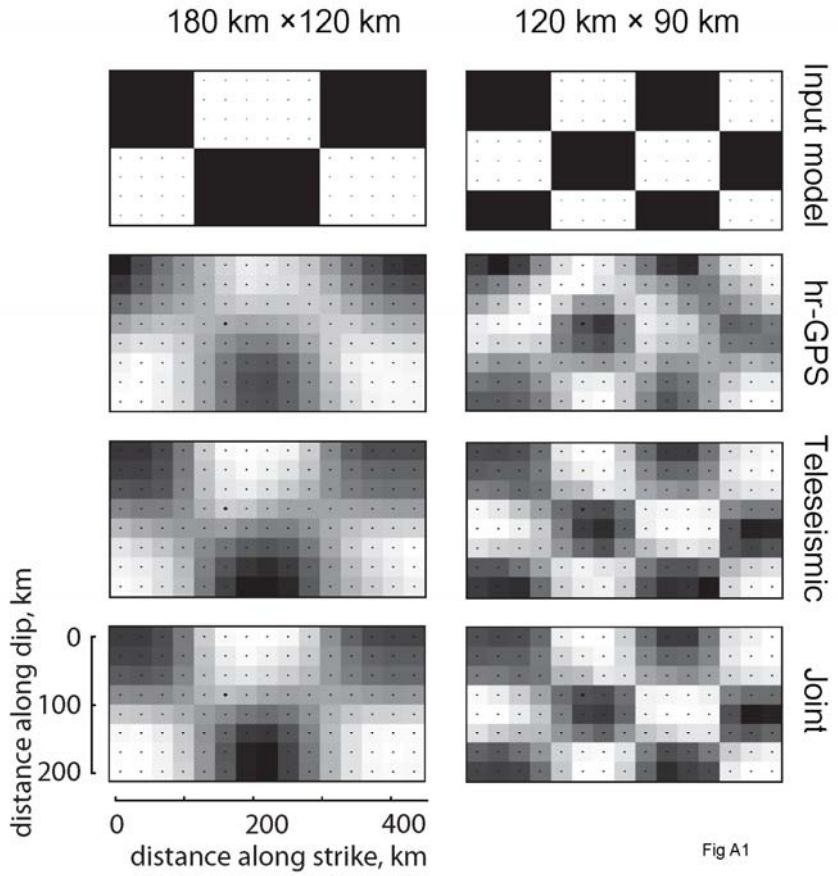

Figure 3.A1. Examples of checkerboard tests for synthetic slip distributions larger than the model discretization (covering up to 6 × 4 nodes and 4 × 3 nodes in these cases). These indicate the relative resolution for variable-rake inversions using hr-GPS and teleseismic P-waves separately and jointly. These apply the same regularization and weighting between different datasets as used in the inversion of real data. The hr-GPS inversion has good resolution down-dip but poor resolution up-dip, especially toward the along-strike (horizontal) limits of the fault model. Teleseismic P-wave inversion has good resolution up-dip and reduced resolution down-dip. The joint inversion has improved resolution across the fault plane, exploiting the relative strengths of the different data sets.

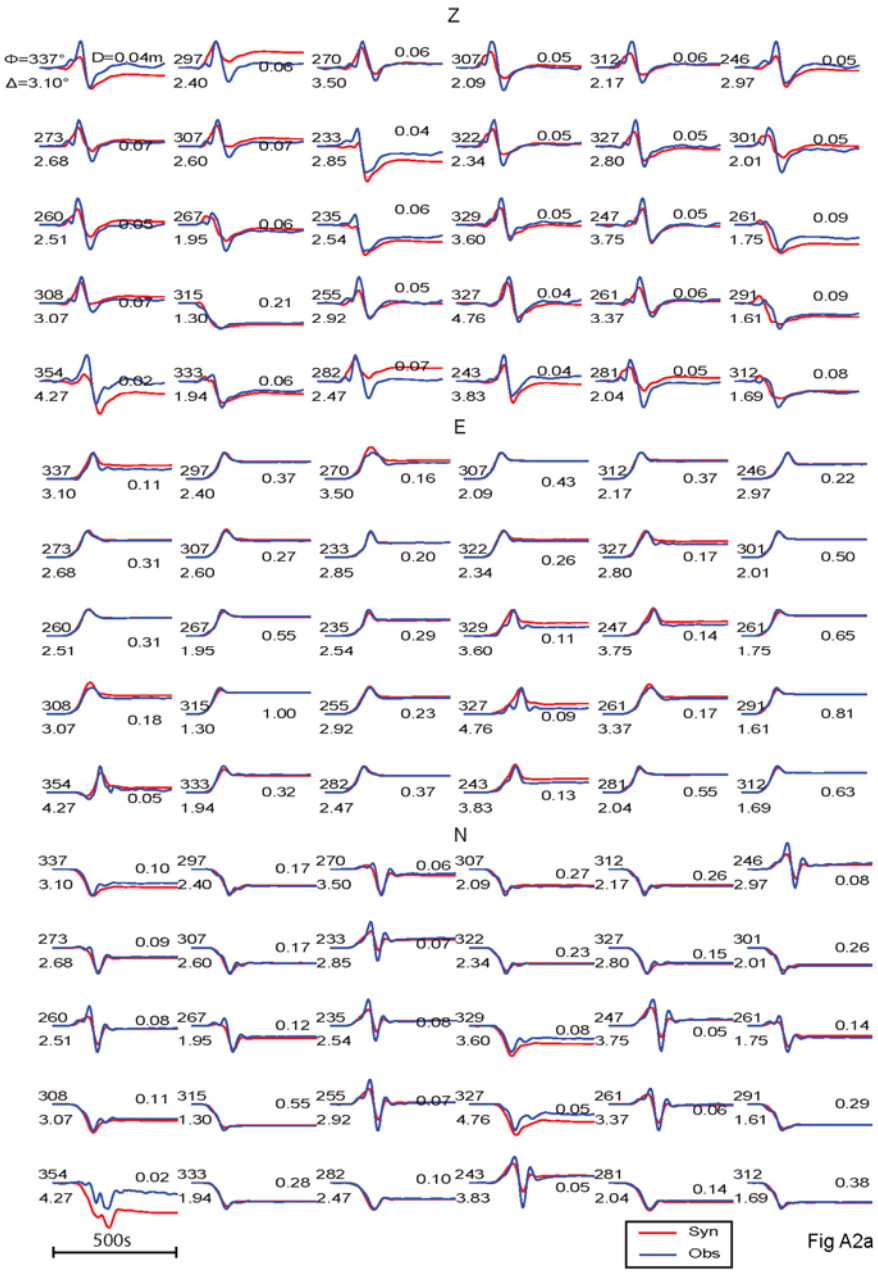

Figure 3.A2. (a) Comparison of all observed (blue lines) and predicted (red lines) 3-component hr-GPS waveforms for the variable-rake joint inversion with hr-GPS and teleseismic P-wave datasets (Figure 3.3). Station azimuths and epicentral distances are shown on the left of each record. Maximum slip amplitudes in m are shown on the right of each record. (b) Comparison of all observed (blue lines) and predicted (red lines) teleseismic P-wave waveforms for the variable-rake joint inversion. Station names, azimuths and epicentral distances are labeled on the left of each record.

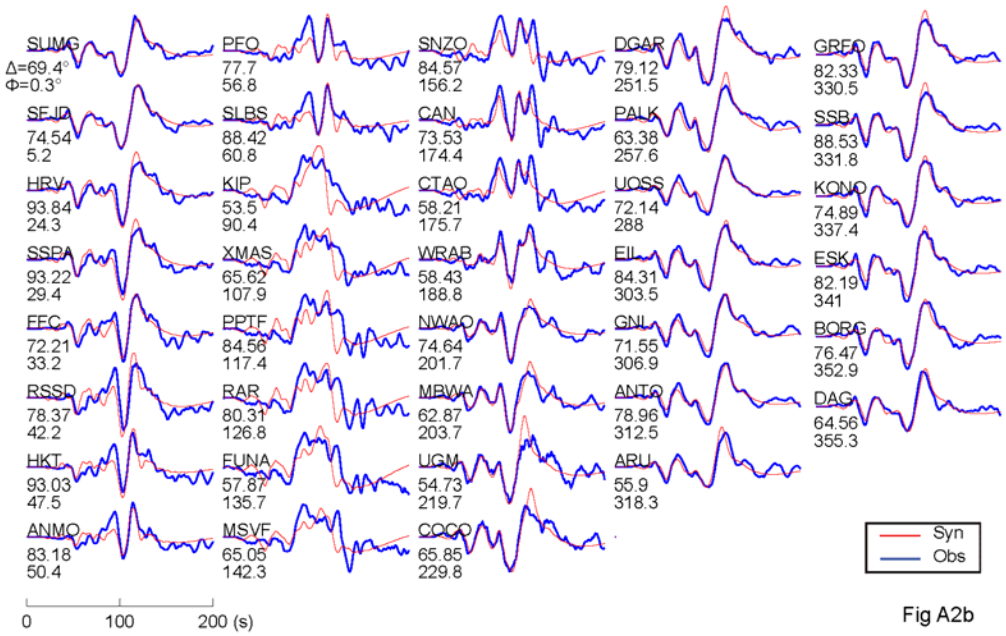
SUMG
Δ=69.4°
Φ=0.3°
PFO
77.7
56.8
SNZO
84.57
156.2
DGAR
79.12
251.5
GRFO
82.33
330.5
SFJD
74.54
5.2
SLBS
88.42
60.8
CAN
73.53
174.4
PALK
63.38
257.6
SSB
88.53
331.8
HRV
93.84
24.3
KIP
53.5
90.4
CTAO
58.21
175.7
UOSS
72.14
288
KONO
74.89
337.4
SSPA
93.22
29.4
XMAS
65.62
107.9
WRAB
58.43
188.8
EIL
84.31
303.5
ESK
82.19
341
FFC
72.21
33.2
PPTF
84.56
117.4
NWAO
74.64
201.7
GNL
71.55
306.9
BORG
76.47
352.9
RSSD
78.37
42.2
RAR
80.31
126.8
MBWA
62.87
203.7
ANTO
78.96
312.5
DAG
64.56
355.3
HKT
93.03
47.5
FUNA
57.87
135.7
UGM
54.73
219.7
ARU
55.9
318.3
ANMO
83.18
50.4
MSVF
65.05
142.3
COCO
65.85
229.8
Syn
Obs
0
100
200 (s)
Fig A2b

Figure 3.A2b.

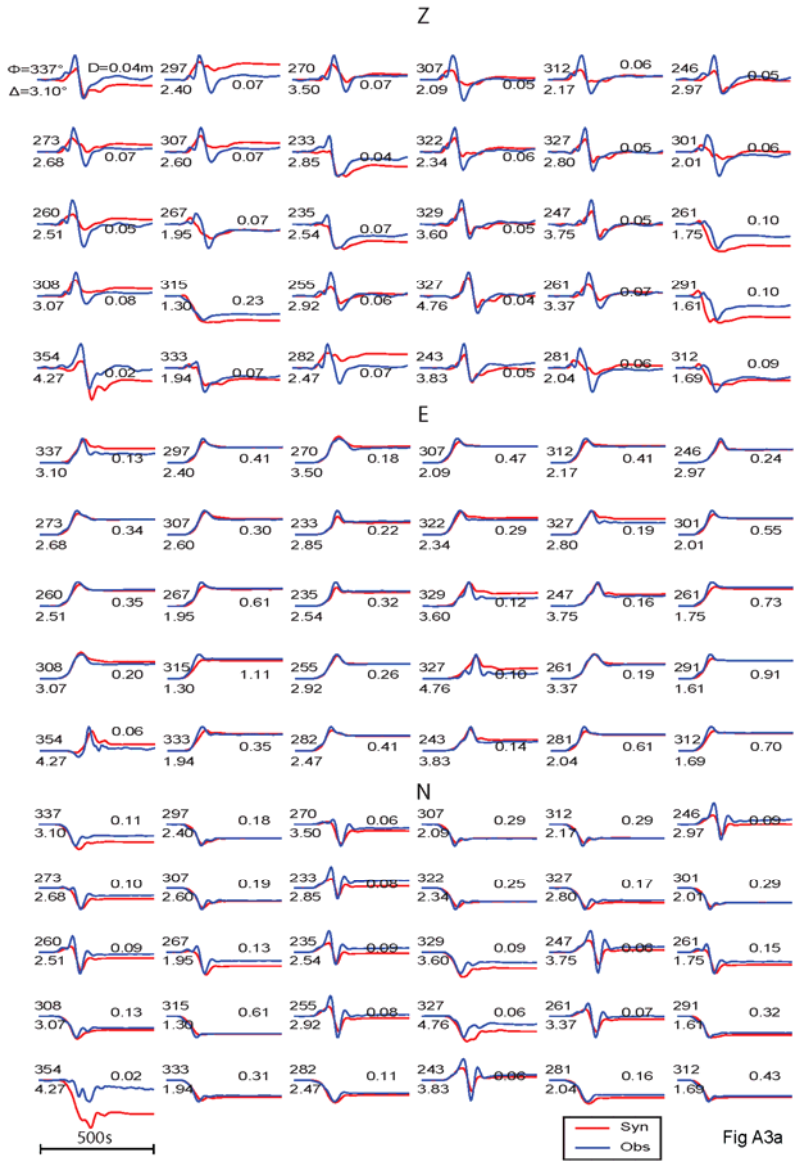

Figure 3.A3. (a) Comparison of all observed (blue lines) and predicted (red lines) 3-component hr-GPS waveforms for the constant-rake joint inversion with hr-GPS, teleseismic P-waves, and R1 STFs (Figure 3.4). Station azimuths and epicentral distances are shown on the left of each record. Maximum slip amplitudes in m are shown on the right of each record. (b) Comparison of all observed (blue lines) and predicted (red lines) teleseismic P-wave waveforms for the constant-rake joint inversion model. Station names, azimuths and epicentral distances are labeled on the left of each record. (c) Comparison of all observed (blue lines) and predicted (red lines) R1 STF waveforms for the constant-rake joint inversion model. Stations names, epicentral distances and azimuths are labeled on the right of each record.


SUMG
Δ=69.4°
Φ=0.3°
PFO
77.7
56.8
SNZO
84.57
156.2
DGAR
79.12
251.5
GRFO
82.33
330.5
SFJD
74.54
5.2
SLBS
88.42
60.8
CAN
73.53
174.4
PALK
63.38
257.6
SSB
88.53
331.8
HRV
93.84
24.3
KIP
53.5
90.4
CTAO
58.21
175.7
UOSS
72.14
288
KONO
74.89
337.4
SSPA
93.22
29.4
XMAS
65.62
107.9
WRAB
58.43
188.8
EIL
84.31
303.5
ESK
82.19
341
FFC
72.21
33.2
PPTF
84.56
117.4
NWAO
74.64
201.7
GNI
71.55
306.9
BORG
76.47
352.9
RSSD
78.37
42.2
RAR
80.31
126.8
MBWA
62.87
203.7
ANTO
78.96
312.5
DAG
64.56
355.3
HKT
93.03
47.5
FUNA
57.87
135.7
UGM
54.73
219.7
ARU
55.9
318.3
ANMO
83.18
50.4
MSVF
65.05
142.3
COCO
65.85
229.8
Syn
Obs
0
100
200 (s)
Fig A3b

Figure 3.A3 (b)

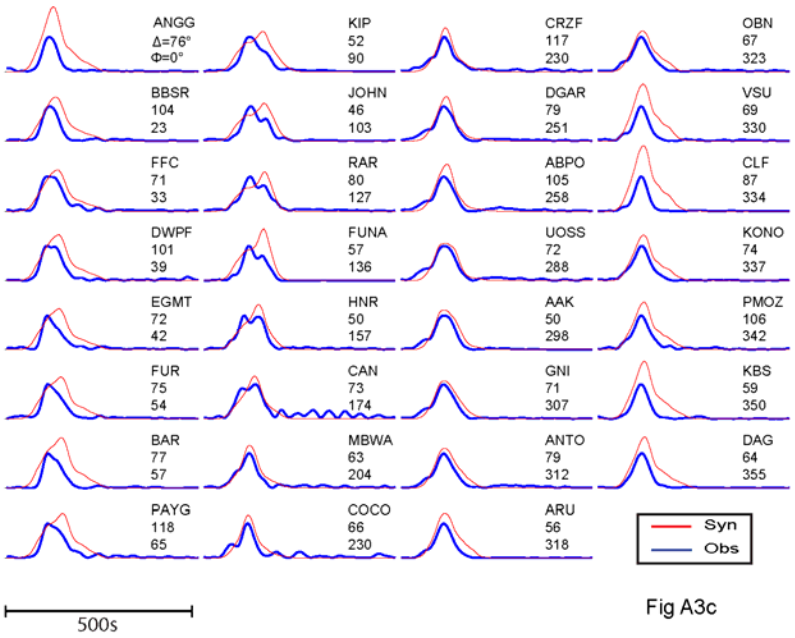
ANGG
Δ=76°
Φ=0°
KIP
52
90
CRZF
117
230
OBN
67
323
BBSR
104
23
JOHN
46
103
DGAR
79
251
VSU
69
330
FFC
71
33
RAR
80
127
ABPO
105
258
CLF
87
334
DWPF
101
39
FUNA
57
136
UOSS
72
288
KONO
74
337
EGMT
72
42
HNR
50
157
AAK
50
298
PMOZ
106
342
FUR
75
54
CAN
73
174
GNI
71
307
KBS
59
350
BAR
77
57
MBWA
63
204
ANTO
79
312
DAG
64
355
PAYG
118
65
COCO
66
230
ARU
56
318
Syn
Obs
500s
Fig A3c

Figure 3.A3 (c)

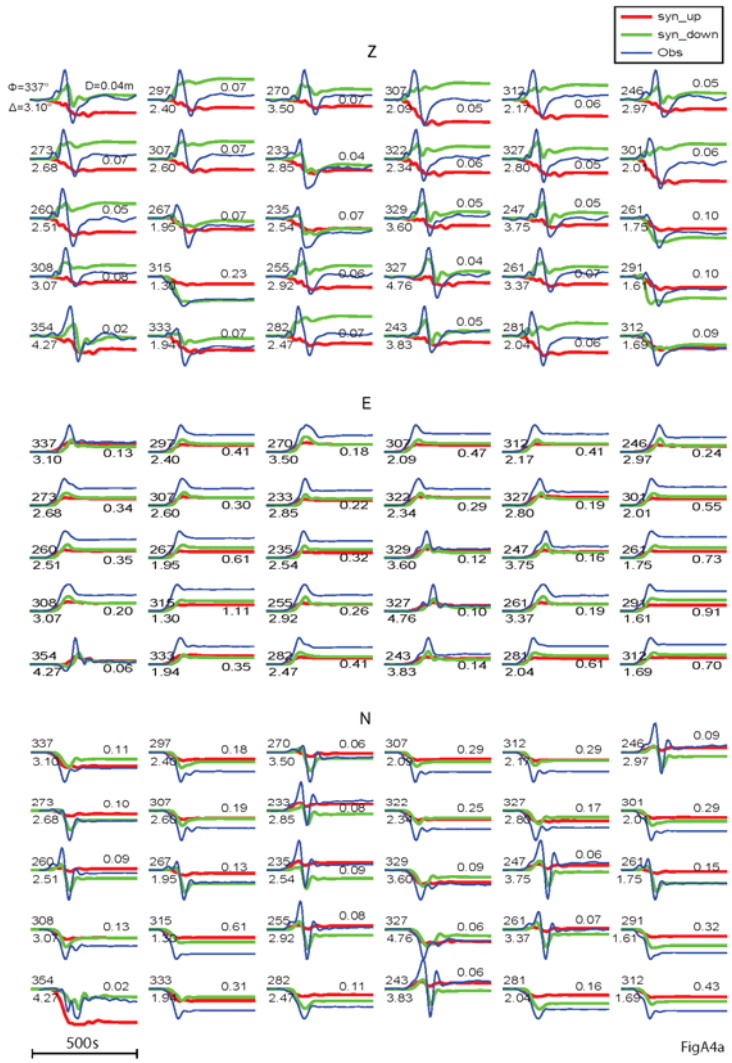

Figure 3.A4. (a) Comparison of all observed waveforms (blue lines) for the 3-component hr-GPS data with contributions of the up-dip (red lines) and down-dip (green lines) sub-faults for the joint constant-rake inversion. Station azimuths, epicentral distances and peak amplitudes are labeled. For the vertical Z component, the contributions from the up-dip and down-dip parts of the megathrust can have opposite signs, whereas for the E and N components, the contribution from the up-dip and down-dip part of the megathrust are similar in sign. (b) Similar comparison for all observed waveforms (blue lines) for the P waves, with contributions of the up-dip (red lines) and down-dip (green lines) subfaults for the joint constant-rake inversion. Energy arriving earlier than 80 s in the waveforms originates mainly from up-dip on the megathrust, while the energy coming after 80 s mainly originates from down-dip. (c) Similar comparison for all observed waveforms (blue lines) for the R1 STFs, with contributions of the up-dip (red lines) and down-dip (green lines) subfaults for the joint constant-rake inversion.

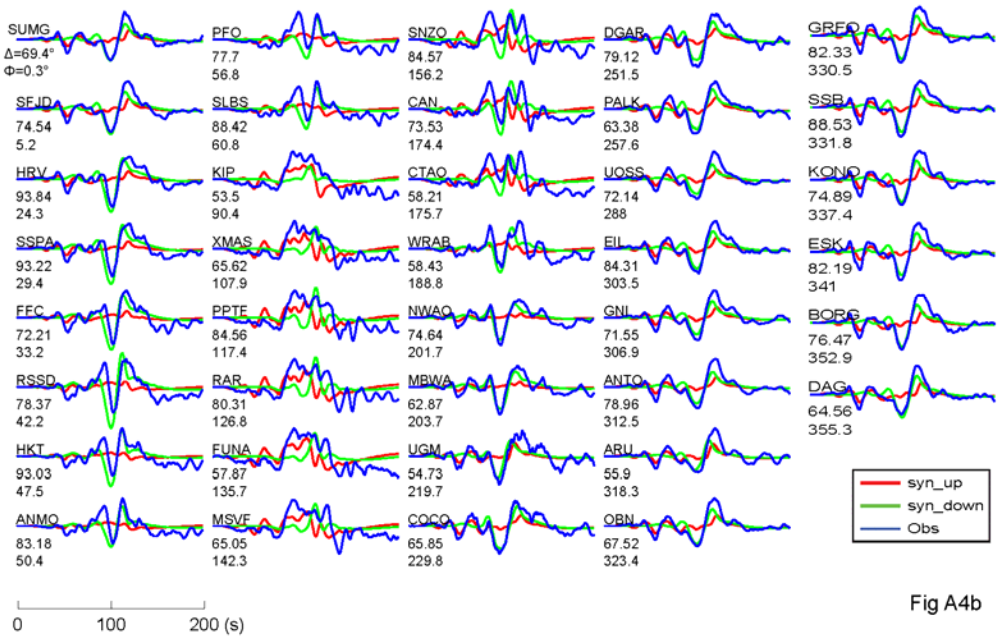

Fig A4b

Figure 3.A4 (b)

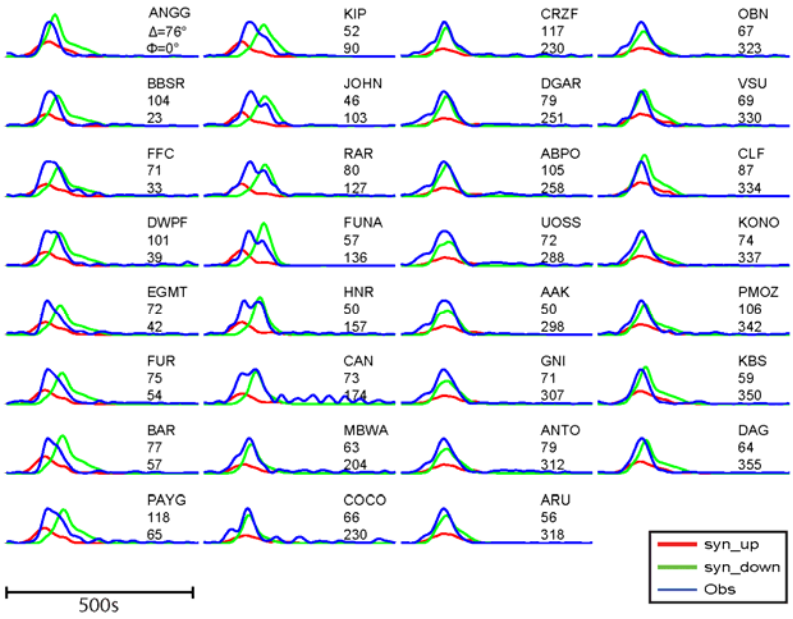

Fig A4c

Figure 3.A4 (c)

Chapter 4

The Great Intraplate Earthquakes of 11 April 2012: En Echelon and Conjugate Fault Ruptures on an Emerging Indian-Australian Plate Boundary

Abstract

The Indo-Australian plate is undergoing distributed internal deformation caused by the lateral transition along its northern boundary from continental collision to island arc subduction zone. On 11 April 2012, one of the largest strike-slip earthquakes ever recorded (seismic moment magnitude, Mw 8.6) occurred ~100-200 km southwest of the Sumatra subduction zone. The unusual intraplate strike-slip faulting located seaward of a subduction zone results from NW-SE compression within the plate caused by the India-Eurasia continental collision to the northwest and NE-SW extension associated with slab pull stresses as the plate underthrusts Sumatra to the northeast. Seismic wave analyses reveal that the 11 April 2012 event had an extraordinarily complex rupture lasting ~160 s, followed ~2 hours later by a great (Mw 8.2) aftershock. The main event ruptured on a WNW-ESE trend fault plane, followed by two aftershocks happened on an perpendicular (NNE-SSW) fault plane cutting the main fault plane and an subprallel fault plane (WNW-ESE trending) ~150km to the south, respectively. A secondary erupture happened either on another en echelon faults or conjugates faults as far as 400 km west to the epicenter right on

the nightyeast ridge. Rupture extended 50-60 km deep into the oceanic lithosphere and peak slip on the first segment approached 90 m. The great aftershock, with an epicenter located 185 km to the SSW of the mainshock epicenter, ruptured bilaterally on a NNE-SSW fault. These great ruptures on a lattice of strike-slip faults represent lithospheric deformation that may eventually lead to a localized boundary between the Indian and Australian plates.

4.1 Introduction

It has long been recognized from relative plate motions that the Indo-Australian plate is not behaving as a rigid unit1. Earthquake focal mechanisms, plate spreading rates inferred from magnetic lineations, fracture zone orientations, seismic stratigraphy, folds and sedimentary unconformities, and geodetic observations indicate diffuse internal deformation of the plate over a broad equatorial region (Figure 4.1) extending from the central Indian Ridge near the Chagos Bank eastward past the Ninetyeast Ridge to the Sumatra Trench2-5, southward along the Ninetyeast Ridge, and southeastward throughout the Wharton Basin5-6. The southwestern part of the plate appears to have already fragmented to produce the Capricorn subplate5,7-8, which has a diffuse border with the Australian plate along the southern Ninetyeast Ridge. The NNE-SSW trends of the Ninetyeast Ridge and fracture zones in the Wharton Basin, together with aligned left-lateral strike-slip faulting mechanisms in both areas, may lead one to anticipate a similar orientation for any great rupture in the intraplate deformation zone. For example, the large 18 June 2000 (13.87°S, 97.3°E, Mw 7.9)

earthquake in the Wharton Basin appears to have involved predominantly left-lateral strike-slip faulting along the expected NNE-SSW orientation, although a second fault orientation was also activated during the 34 s long rupture9-10. However, the east-west trend of the equatorial deformation zone raises the possibility of right-lateral faulting with that orientation for intraplate events further north.

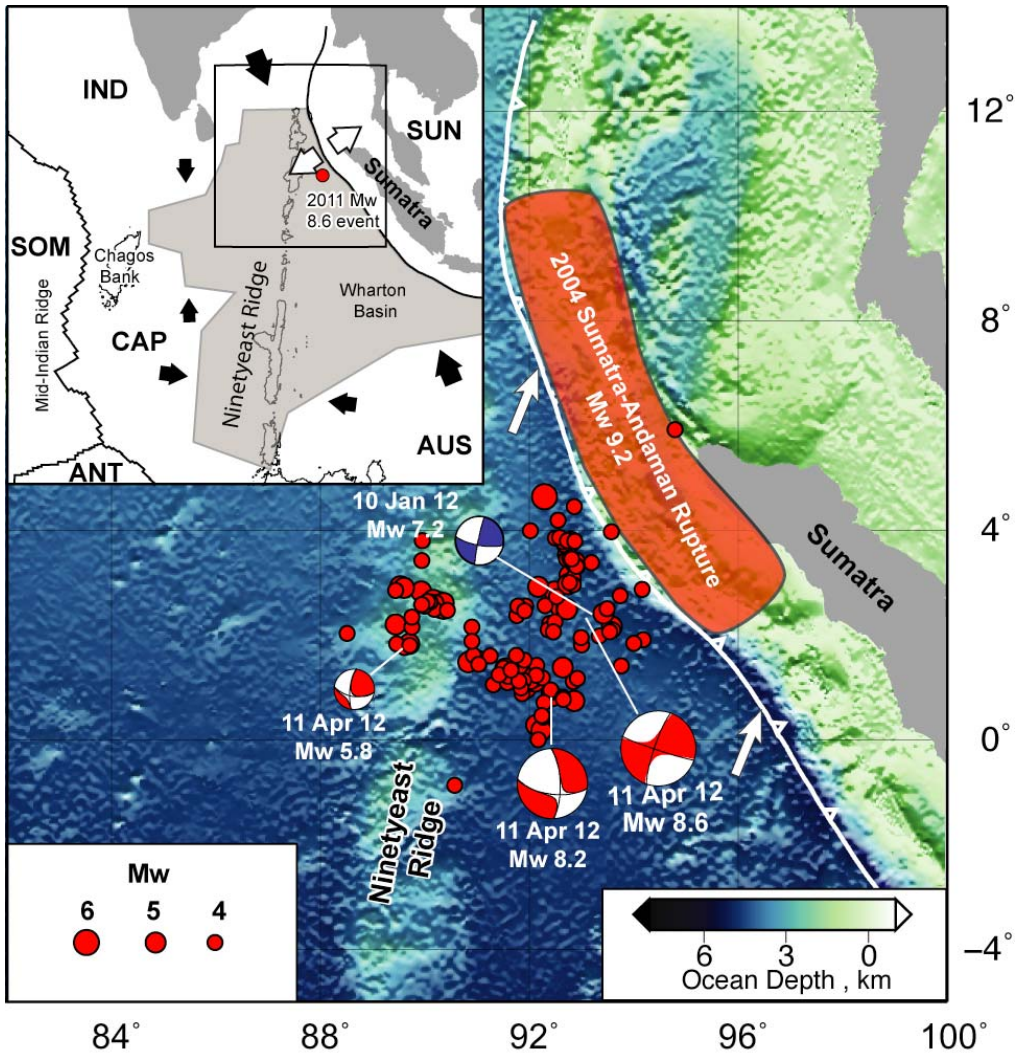

Figure 4.1 | **The 11 April 2012 Rupture Sequence**. The inset map shows the regional plate tectonic setting with the Indo-Australian plate being segmented into three subplates: India (IND); Australian (AUS); and Capricorn (CAP), and the adjacent Somalian (SOM), Antarctic (ANT) and Sunda (SUN) plates. The transparent gray zone is a region of intraplate deformation between the subplates with black arrows indicating directions of intraplate compression and white arrows showing extension from subduction [5]. Major bathymetric features like the Chagos Bank,

Ninetyeast Ridge and Wharton Basin are indicated. The large map shows the USGS W-phase moment tensor solutions for the M_w 8.6 and 8.2, events of 11 April, 2012, USGS one-week aftershock locations, and location and focal mechanism for the 10 January 2012 (M_w 7.2) event used as empirical Green functions in the surface wave analysis, and a M_w 5.8 aftershock on the Ninetyeast Ridge. The barbed line indicates the Sumatra trench, and the rupture zone of the M_w 9.2 Sumatra-Andaman underthrusting event is shown. White arrows indicate the direction of motion of the Indo-Australian composite plate relative to the Sunda plate.

On 11 April 2012 a great intraplate earthquake (Mw 8.6) initiated at 2.31°N, 93.06°E at 08:38:37 UTC, followed by a great aftershock (Mw 8.2) at 0.77°N, 92.45°E at 10:43:09 UTC (Figure 4.1). The overall faulting geometries of both events inferred from point-source moment tensor representations are similar (Figure 4.1), with steeply dipping strike-slip orientations having either left-lateral slip on NNE-SSW faults or right-lateral slip on WNW-ESE faults, either of which would be consistent with the pervasive NW-SE compressional stress orientation throughout the region6. The first event is possibly the largest strike-slip earthquake ever seismically recorded (the 15 August 1950 Assam (Mw 8.6) interplate earthquake in the eastern Himalayas is of comparable size11, but uncertain in faulting mechanism12-14), and it is probably the largest intraplate earthquake ever seismically recorded (the 1933 Sanriku (Mw ~8.4-8.6) outer rise normal faulting event could be of comparable size). The 2012 events are located 100-200 km seaward of the Sumatra subduction zone in which the Indo-Australian plate is underthrusting the Sunda plate, offshore of the epicentral region of the 26 December 2004 Sumatra-Andaman (Mw 9.2) interplate earthquake rupture (Figure 4.1), which involved 15 to 30 m of trench-perpendicular coseismic displacement on the plate boundary15.

The relative epicentral locations of the two great events on 11 April 2012 immediately

suggest rupture on a NNE-SSW striking fault, and numerous rapid analyses of the seismic waves performed to characterize the space-time faulting history made this assumption; however, as more aftershock locations were determined, clear trends along parallel WNW-ESE lineations offset in latitude by ~150 km became apparent (Figure 4.1). A robust seismic method for identifying fault planes and rupture finiteness is by stacking short-period P-wave signals from groups of seismic stations at teleseismic distances corrected for propagation from a grid of possible source locations16-19. Within a few hours of the events, such semi-automated back-projections of short-period P waves from the mainshock recorded by networks of stations in Europe, China, Japan, and Australia showed that pulses of coherent short-period seismic energy release appeared to illuminate both WNW aftershock trends, as well as additional loci of seismic radiation that were clearly not on a single NNE-SSW oriented fault20.

4.2 Back-projection of teleseismic P waves.

A summary of our own back-projections of short-period teleseismic P waves recorded by stations around Europe is presented in Figure 4.2 (a time-varying animation is provided in the Supplemental Information Movie S1). These images are obtained using 85 ground velocity recordings at distances of 55°-95° from the source region filtered in the passband 0.5-2.0 Hz. Coherent sources of short-period seismic energy radiation are imaged for over 160 s and display a close correspondence with the regional distribution of epicenters of early (first-week) aftershocks, which are clearly on multiple faults. The initial rupture on the northeastern WNW-ESE fault appears to

expand bilaterally, with stronger radiation in the western part of the fault. After about 50 s the WNW rupture propagation ends, with a total fault length of about 150 km and a low overall rupture velocity of about 1.5 km/s. Beginning around 40 s into the rupture, seismic radiation begins to be emitted from a perpendicular, presumably left-lateral conjugate plane that first ruptures 50-100 km in the SSW direction (from 30 to 60 s), then 50-100 km in the NNE direction (from 55 to 80 s). After about 75 s, seismic radiation continues on a second WNW-ESE fault that is roughly parallel to the first and separated by ~150 km to the southwest. This rupture propagates to the WNW, perhaps discontinuously, until about 145 s, at which time seismic radiation initiates on a fourth distinct fault further to the west and persists until ~160 s. Also shown in Figure 4.2 are back-projection results for the Mw 8.2 aftershock that commences 2 hours later. The region of short-period energy release is much more compact than that of the mainshock, and the duration is roughly half as long (~80-85 s). The short-period energy release indicates bilateral rupture on a NNE-SSW plane with dominant propagation initially from the epicenter toward the NNE, consistent with the locations of early aftershocks, and weaker late energy release to the SSW.

Similar patterns of short-period radiation are observed for arrays of stations in Japan (see Figure 4.S1 and Movies S1 and S2 and by other investigators who have posted preliminary solutions on-line20-22. Using a lower frequency passband of 0.1-0.5 Hz for the European P wave observations smears the energy more broadly in space and accentuates the late energy in the mainshock rupture that occurs near longitudes of 89.5°-90.5° E, but otherwise gives results very similar to those in Figure 4.2 (Movies

S1 and S2).

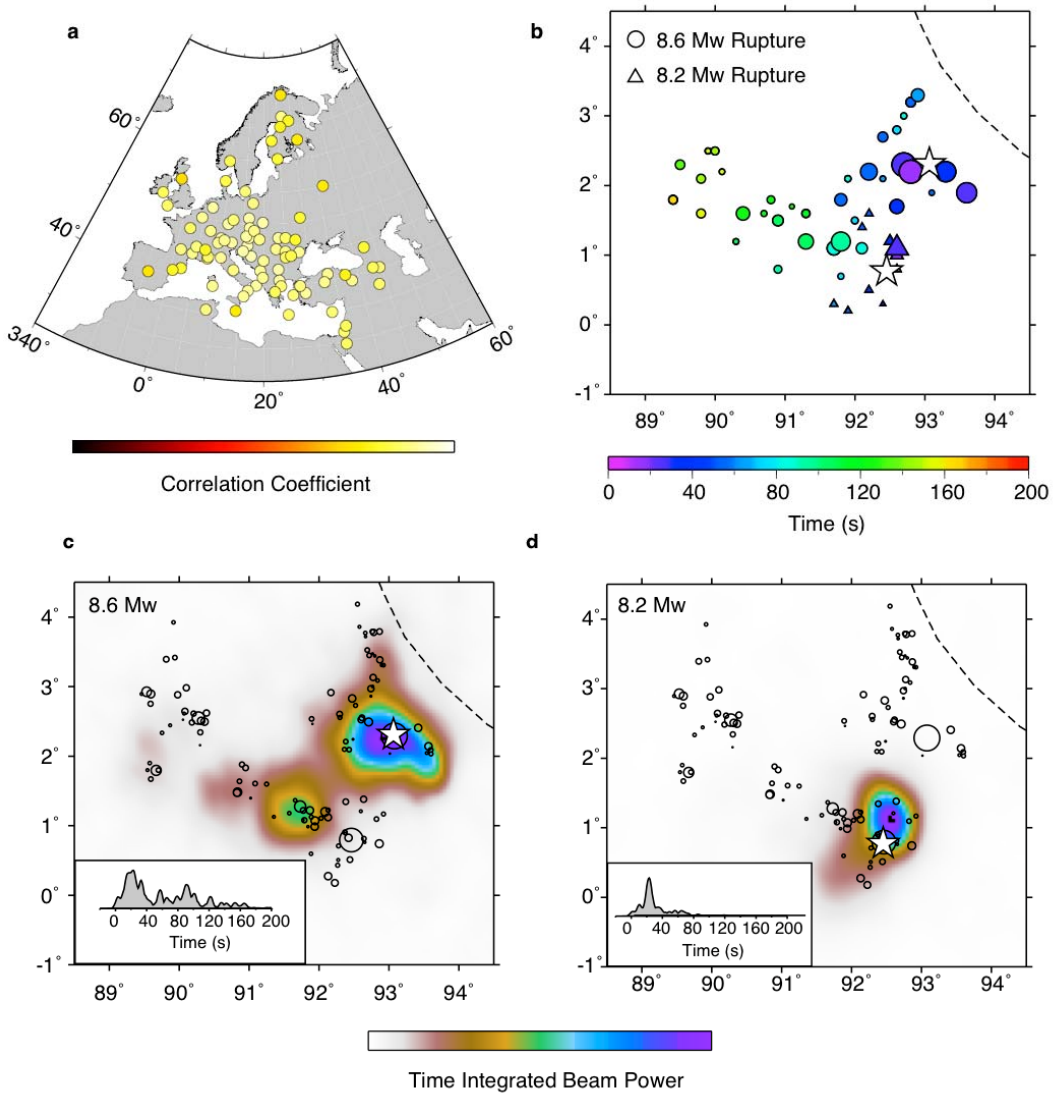

Figure 4.2 | **Short-period Seismic Energy Release Pattern**. **a,** Seismograph stations in Europe that were used for the 0.5-2.0 Hz back-projection of the M_w 8.6 and M_w 8.2 Sumatra earthquakes. Stations were selected for high P wave similarity and a broad geographical distribution. **b,** Local beam power maxima during the back-projections, with color indicating time after the nominal origin time. Symbol size is proportional to beam power. **c,** Time integrated beam power for the M_w 8.6 back-projection. The circles are early NEIC aftershocks with symbol size proportional to magnitude, and the dashed line is the Sumatra trench. The inset shows peak beam power as a function of time. **d,** same as panel **c,** but for the M_w 8.2 aftershock. The time-dependent behavior is best evaluated by viewing Supplemental Movies S1 and S2.

An important limitation of these and other short-period back-projections is that they

are not directly sensitive to magnitude of fault slip18-19,23. Thus, while the short-period results indicate multiple potential activated faults, the relative seismic moments of the fault segments are not resolved (short-period seismic radiation is more sensitive to slip-rate variations, and back-projection methods depend critically on wave field coherency, which can be very high for spatially concentrated radiation from a small event and low for diffuse radiation from a large event).

4.3 Back-projection of R1/G1 STFs

To overcome this deficiency, we used broadband surface waves to image spatial variations in seismic moment release, again allowing for the possibility of multiple fault segments. To account for complex surface wave propagation effects, we use global seismic recordings of short-arc Rayleigh waves (R1) and Love waves (G1) for a moderate size (Mw 7.2) event on 10 January 2012 with a source location (2.45°N, 93.21°E; 18:36:59 UTC) about 20 km northeast of the mainshock epicenter, and a similar strike-slip focal mechanism. These signals are deconvolved from the corresponding Mw 8.6 and 8.2 great event recordings using an iterative deconvolution procedure with a positivity constraint24, thus removing most dispersion, attenuation, and focusing effects. The resulting time series are called relative source time functions24-25 (STFs) and large earthquake rupture properties can be inferred by projecting the STFs into a space-time history of seismic radiation essentially the same way as is done in short-period back-projections.

The spatial distribution of long-period seismic wave radiation imaged over a gridded region around the Mw 8.6 and 8.2 earthquake epicenters is shown in Figure 4.3. The

STFs, which have timing relative to the EGF epicenter locatio, are linearly stacked at each possible position on the map using propagation phase velocities of 4.0 km/s and 4.5 km/s for R1 and G1 signals, respectively. These phase velocities are appropriate for the central period range of the dominant periods of the surface waves (20 s – 200 s), and comparable values have been used in imaging finite source ruptures in previous studies24-25. The data were averaged over 10° azimuthal windows prior to back-projection, and relative weighting proportional to R1 and G1 source radiation patterns were applied so as to down-weight STFs near radiation nodes. The peak amplitude of stacked energy at each grid location is shown in Figure 4.3. Darker colors indicate stronger long-period source radiation, which tracks the aftershock distribution. There is some intrinsic smearing of the images due to the non-uniform and incomplete azimuthal coverage, and the spatial resolution is lower than for the short-period back-projections because we are dealing with one-sided moment rate functions; however, this method provides a better indication of seismic moment distribution. Plots of this imaging with R1 and G1 separately are shown in Figure 4.S2.

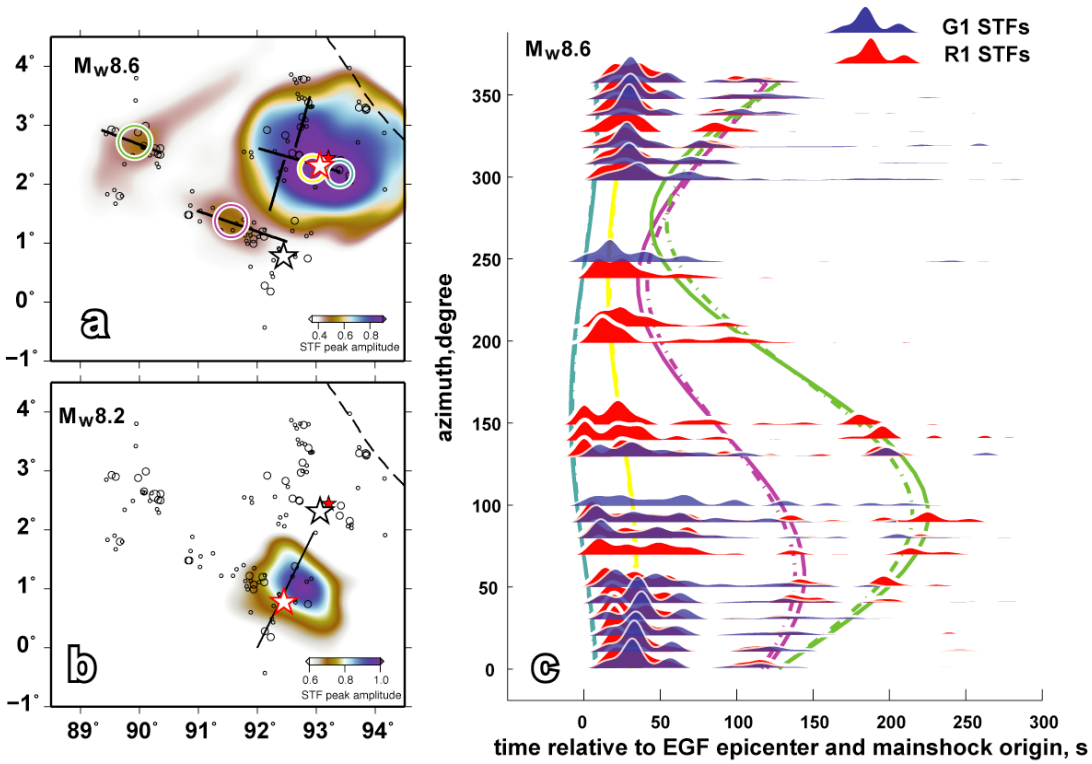

Figure 4.3 | Long-period Seismic Energy Release Pattern. The maps show the spatial patterns of long-period surface wave energy sources for the 11 April 2012 (M_w 8.6) mainshock (epicenter indicated with a red outlined star in (a)) and the large (M_w 8.2) aftershock 2 hours later (epicenter indicated with a red outlined star in (b)). The one-week aftershock distribution is shown by small circles with radii proportional to seismic magnitude. The color images indicate the peak stacked energy at each position from combined R1 source time functions (STFs) and G1 STFs back-projected relative to the epicentral location of the 10 January 2012 (M_w 7.2) event (majenta asterisks) which was used for empirical Green functions (EGFs). Solid lines indicate the orientations of likely subfaults that ruptured during each event. Snapshots that indicate the time history of energy release are shown in Figure 4.S3. Colored circles in the mainshock image indicate specific locations of energy release that produce arrivals considered in panel (c), which shows the azimuthally binned and stacked R1 (red) and G1 (blue) STFs plotted in time relative to the EGF epicenter. These represent seismic moment as a function of time observed at different azimuths. The colored curves correspond to the colored circles in (a), showing the predicted arrival times of energy from each location, with "S-curve" patterns due to relative propagation times toward different azimuths. The solid curves are for R1 waves using a velocity of 4.0 km/s and the dashed curves are for G1 waves using a velocity of 4.5 km/s. The features aligned on such curves form the corresponding images in (a), although images formed after 60 s of delay from the STF onsets have the first 60 s of the STFs masked out to avoid contamination. A corresponding profile of STFs for the M_w 8.2 aftershock is shown in Figure 4.S4.

For the Mw 8.6 event, the largest long-period source energy is concentrated near the

epicenter, but there is significant source energy along both ESE-WNW aftershock trends, indicating either continuous rupture on corresponding faults or a sequence of discrete triggered 'early' aftershocks. The secondary features have peak amplitudes from 20-30% of the largest features, indicative of significant relative seismic moment. Snapshots of the reconstructed long-period radiation as a function of time are shown in Figure 4.S3, and these reveal rupture propagation in the WNW direction on both faults, and that the concentration of radiation almost 400 km west of the epicenter occurs at about 120 s. The relative source time functions for the Mw 8.2 aftershock were similarly processed (Figure 4.S4), and indicate source radiation concentrated near the hypocenter with rupture propagation toward the NNE. Comparison with Figure 4.2 shows good agreement in source radiation locations for ~1 s period energy and ~20-200 s period energy, bolstering the interpretation that multiple faults with significant slip were activated during the main rupture.

4.4 Segmented Finite Fault Model Inversion

To resolve the spatial slip distribution, broadband teleseismic P and SH waves were inverted for finite-faulting models using multiple distinct fault segments inferred from the back-projections of short- and long-period seismic energy. While single-fault inversions allow basic waveform features in the first 60 s to be fairly well fitted, later parts of the rupture can be fit better with additional fault complexity (and more parameters). Finite-fault inversions require specification of substantial a priori information about faulting geometry, rupture initiation time, rupture velocity, and discretization of the fault surface and subfault source time functions. We use the

consistency of the short-period and long-period imaging approaches in conjunction with the dominant aftershock trends to specify 4 fault segments for the mainshock and 1 for the largest aftershock, with locations and timing of rupture initiation guided by the high-resolution short-period back-projections.

Figure 4.4 shows the fault model geometry and the slip distributions obtained by least squares inversion of P and SH waves using 200 s long time windows of the seismograms (with some being truncated early to avoid contamination from PP and SS phases). Guided by the short-period back-projections, we specified the initial rupture velocity as 1.5 km/s on the first plane, 2.5 km/s on the conjugate NNE-SSW planes, and 2.0 km/s on the southern and western segments. There is uncertainty in the kinematic parameters, but the collective information from aftershock locations and P wave and surface wave back-projections does provide first-order constraints.

Each fault segment has its rupture initiate at 30 km depth, with 10-km wide by 20-km long subfaults extending from the ocean floor (below a 5 km thick ocean layer) to 55-km depth. Resolution of hypocentral depths is poor, but the choice was made based on the 30-50 km centroid depths found in very long-period point-source inversions for this event, suggestive of rupture extending throughout the oceanic lithosphere. Subfaults were parameterized to have rupture durations of up to 15 to 17.5 s based on initial inversions with single fault orientations being used for the entire rupture, but the complexity of slip does not provide tight constraints on the subfault durations. Fault dip for the initial rupture was specified as 76° (toward the

northeast) based on single fault modeling, and the dips of other segments were constrained to match those of aftershock focal mechanisms or by performing inversions for a range of values. For most fault segments the body wave inversion concentrates seismic moment and, hence, slip in the upper three rows of each fault model (depths of 5-35 km below ocean surface), spanning the thin oceanic crust and uppermost mantle layer, but deeper slip is found on several of the segments, notably segment (c).

Our results show that the great events of 11 April 2012 involve rupture of a very complex network of faults, for which we have no documented precedent in recorded seismic history. Good fits are found for the large P and SH wave data set (see Figure 4.S5), but some secondary features are not fully accounted for. The failure process can be summarized as initial large moment release during a predominantly WNW-propagating low rupture velocity (1.5 km/s) asymmetric bilateral strike-slip rupture with large peak slip (~88 m) and about 150 km total rupture length with seismic moment corresponding to Mw ~8.5 that then triggered bilateral failure of a crossing conjugate fault that had a seismic moment corresponding to Mw ~8.3, with subsequent rupture occurring to the south on an en echelon ESE-WNW fault that expanded in the WNW direction with a seismic moment of Mw ~8.4, culminating with a fourth activated fault segment about 300 km west of the epicenter that ruptured on either a WNW-ESE or NNE-SSW fault (or both) with Mw ~8.1 (Figure 4.S6 shows the inversion results assuming the NNE-SSW orientation). The cumulative moment of these ruptures is about a factor of two higher than point-source seismic

moment estimates for the Mw 8.6 event (our composite faulting gives Mw 8.76 and likely the total size is overestimated due to limited resolution of the very long-period energy in the body waves and slight errors in the fault geometries (seismic moment estimates for strike-slip events from body waves tend to be unstable due to the weak down-going radiation patterns). However, single point-source seismic moment estimates tend to underestimate total moment for complex events, and allowing two-sources in W-phase inversions for the main event is reported to give about 50% higher estimates of total seismic moment (Z. Duputel, personal communication).

Figure 4.4a–f (next page), Slip distributions on each subfault; g, map showing locations of subfaults. Map shows fault segments activated during the 11 April 2012 Mw 8.7 mainshock, specified for finite-fault slip model inversion of teleseismic broadband P and SH waves and R1 and G1 STFs. The faulting complexity is guided by the short-period and long-period source imaging in Figs 2 and 3 (and associated animations and time snapshots in the Supplementary Information) along with the one-week aftershock distribution. The red star indicates the epicentral location, and red dots indicate the placement of hypocentres (all at 30 km depth) on each fault segment. The rectangles indicate the subfault strikes and dips (shallow edge is on the green side, deeper edge on the black side. We use four subfaults (two of the subfaults are further subdivided) with onset times (T0) constrained by the short-period back-projections. Slip distributions on each subfault (arrows indicate the relative size and direction of slip, with slip size colour contoured using the colour scale at right; green dots indicate the grid) are shown in a–f, with the subfault grids having 20 km spacing along-strike and 10 km spacing along-dip. The peak slip and Mw of each subfault is indicated, as is the position of the hypocentre on each subfault from which the rupture expands. The rupture velocity is 2.0 km s−1 for all subfaults. The Mw 8.2 event (epicentre given by black star) is not inverted because the broadband P and SH waves are obscured from surface waves from the first event, but it appears to involve bilateral rupture on a fifth fault, trending NNE–SSW. δ, dip; λ, rake; φ, strike.

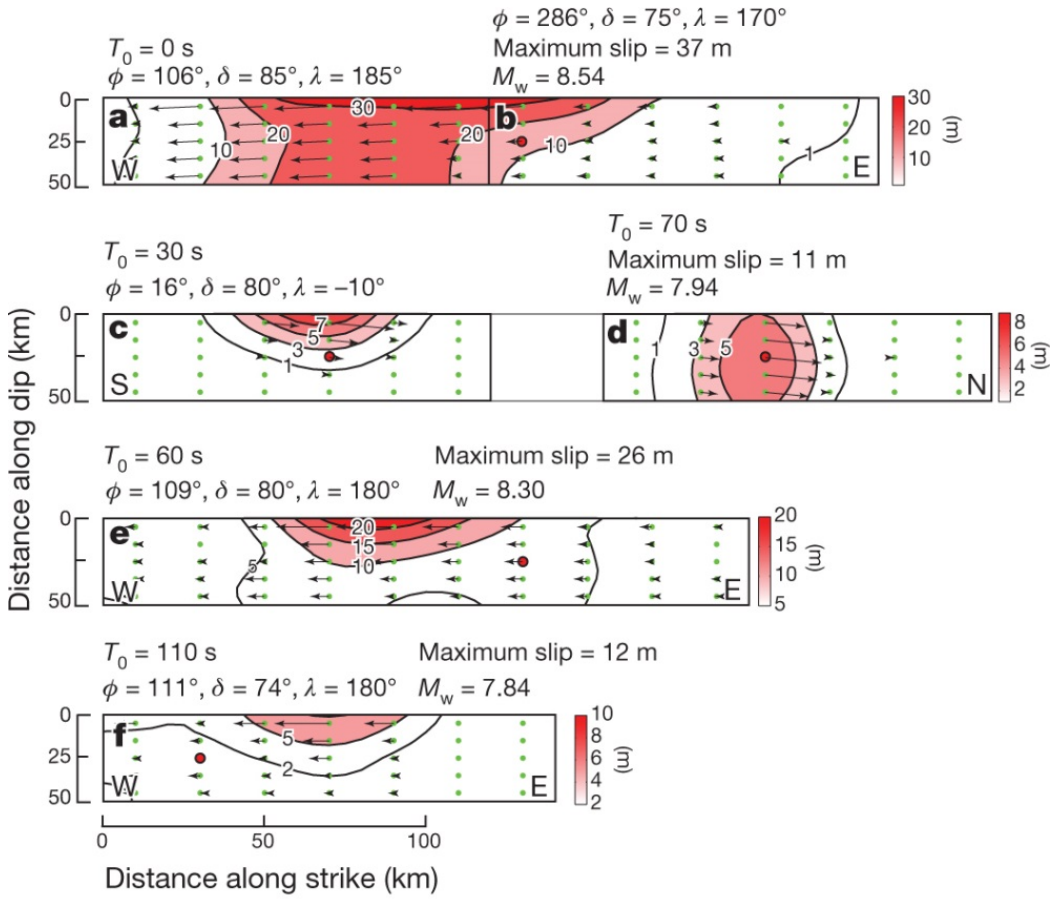
T_0 = 0 s
ϕ = 106°, δ = 85°, λ = 185°
ϕ = 286°, δ = 75°, λ = 170°
Maximum slip = 37 m
M_w = 8.54
T_0 = 30 s
ϕ = 16°, δ = 80°, λ = −10°
T_0 = 70 s
Maximum slip = 11 m
M_w = 7.94
T_0 = 60 s
ϕ = 109°, δ = 80°, λ = 180°
Maximum slip = 26 m
M_w = 8.30
T_0 = 110 s
ϕ = 111°, δ = 74°, λ = 180°
Maximum slip = 12 m
M_w = 7.84
Distance along dip (km)
Distance along strike (km)
(m)

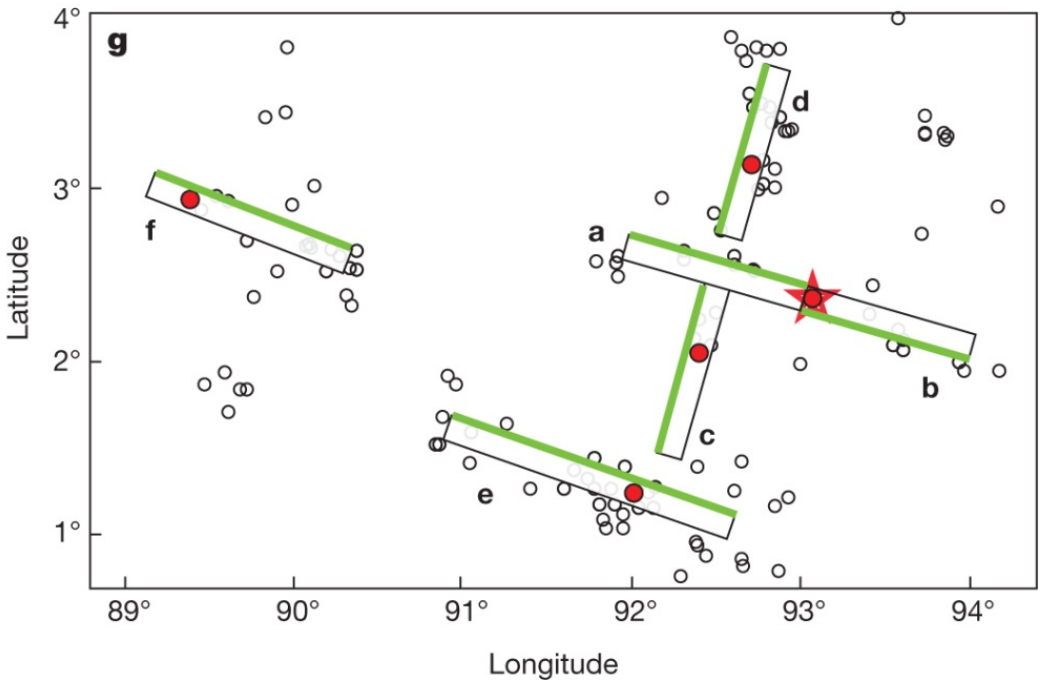
Latitude
Longitude

Even allowing for the trade-offs and non-uniqueness of the very complex model description, it is well-established that this event activated a complex lattice of faults in the deformation zone between the India and Australia subplates, with the deep centroid depths, large estimated fault displacements, and large extent of faulting of the sequence suggesting localization of deformation in the region extending westward from Sumatra to the Ninetyeast ridge. The shortening between the India and Australia subplates that is being accommodated across this deformation zone is mainly being distributed onto strike-slip faults rather than thrust faults, and the ultimate configuration of the plate boundary that will develop is difficult to anticipate. The failure process appears to be influenced by the plate fabric, with NNE-SSW trending structures embedded in the plate from its earlier formation likely providing zones of weakness that can fail in strike-slip event. However, the primary seismic moment is on WNW-ESE features, cross-cutting the grain of the Ninetyeast ridge (high resolution bathymetry swaths along the ridge have revealed many WNW-ESE fractures in the seafloor prior to this sequence, as communicated to us by JoAnn Stock). Many more large fracturing events will be needed to evolve a localized plate boundary, so future extraordinary ruptures in the region may well occur, but this event currently stands as the greatest intraplate strike-slip earthquake geophysicists have yet recorded.

4.5 Methods Summary

Short-period back-projection imaging. Two large aperture arrays of broadband seismic stations in Europe and Japn that record coherent P wave arrivals were used to image locations of source radiation during the Mw 8.6 and Mw 8.2 events without a priori assumption about any fault orientations. The teleseismic P waves are narrow-band filtered and aligned by a multi-channel cross-correlation method to suppress travel time effects of three-dimensional Earth structure, with arrival onsets aligned for the epicentral location. For a gridded distribution of possible source locations at a fixed depth (there is very little depth resolution), predictions are made of the travel time variations expected across the array relative to the initial alignment and the seismograms are shifted corresponding amounts and summed using fourth-root stacking. Higher stack amplitudes at certain times are found for source locations that produce coherent arrivals in the P-wave signals. The space-time variations of coherent short-period source radiation for the two great events events are inferred from the locations and timing of large stack amplitudes the time-varying images.

Surface wave source time function imaging. Surface waves that travel along the short great-circle arc (R1 Rayleigh waves and G1 Love waves) from the source region to broadband seismic stations around the world are used to image the space-time locations of long-period seismic radiation from the Mw 8.6 and Mw 8.2 events. To remove the complex dispersion effects of surface wave propagation, R1 and G1 recordings from an Mw 7.2 earthquake that occurred on January 10, 2012 with very similar location and focal mechanism to the Mw 8.6 mainshock are used as empirical

Green functions (EGFs). These signals are deconvolved from the corresponding records of the large events, eliminating long-range propagation effects and giving relative source time functions (STFs), which indicate the difference in overall source radiation for the large events compared to the EGF. The source functions, are then back-projected over a source grid similar to the short-period P wave procedure, but using an average phase velocity for R1 (4.0 km/s) and for G1 (4.5 km/s), with STF features that are coherent at azimuthally distributed stations stacked up at corresponding space-time locations. This provides images of where long-period radiation emanated from the source region independent of assumption of a particular fault geometry.

Finite fault slip model inversion. Given the complex space-time distributions of source radiation indicated by the short-period P wave and long-period R1 and G1 STF back-projections, along with the correlated aftershock distribution, we specify a set of fault segments comprised of multiple 10 km wide by 20 km long subfaults that activate at prescribed times (based on the short-period imaging), and invert broadband teleseismic P and SH waves for finite fault slip distributions. The geometries of the segments are constrained by aftershock distribution and focal mechanisms, back-projections, and suites of inversions with varying parameters. We specify rupture velocity on each segment guided by the back-projections, and allow a flexible parameterization of the source functions on each subfault. The inversion is linear, allows rake to vary within 90 degree on each subfault. The final result is a model of

time-varying slip on each fault segment consistent with the back-projection imaging, aftershocks, and broadband teleseismic signals. The many parameters in such a complex model make the finite-source kinematic slip inversion even more non-unique than for single fault models, so it is best viewed as a plausible realization of overall rupture process for the event.

Full Methods and any associated references are available in the online version of the paper at www.nature.com/nature.

4.6 Acknowledgements

We thank Hiroo Kanamori, Zacharie Duputel, and Gavin Hayes for discussions and exchanges of information about this event. Alexander Hutko provided early short-period back-projection results. This work made use of GMT and SAC software and Federation of Digital Seismic Networks (FDSN) seismic data. The Incorporated Research Institutions for Seismology (IRIS) Data Management System (DMS), the European ORFEUS data center, and the NIED F-net data center were used to access the data. This work was supported by NSF grant EAR0635570 (T.L.) and EAR0951558 (K.D.K.).

4.7 References

1. Minster, J.B. & Jordan, T. H. Present day plate motions. J. Geophys. Res. 83,

5331-5354 (1978).

2. Wiens, D. et al. A diffuse plate boundary model for Indian Ocean tectonics. Geophys. Res. Lett. 12, 429-432 (1985).

3. Gordon, R. G., DeMets, C. & Argus, D. F. Kinematic constraints on distributed lithospheric deformation in the equatorial Indian Ocean from present motions between the Australian and Indian plates. Tectonics 9, 409-422 (1990).

4. Gordon, R. G. DeMets, C., & Royer, J.-Y. Evidence for long-term diffuse deformation of the lithosphere of the equatorial Indian Ocean, Nature 395, 370-373 (1998).

5. Royer, J.-Y. & Gordon, R. G. The motion and boundary between the Capricorn and Australian plates. Science 277, 1268-1274 (1997).

6. Delescluse, M. & Chamot-Rooke, N. Instantaneous deformation and kinematics of the India-Australia plate. Geophys. J. Int. 168, 818-842 (2007).

7. Royer, J.-Y. & Chang, T. Evidence for relative motions between the Indian and Australian plates during the last 20 Myr from plate tectonics reconstructions: Implications for the deformation of the Indo-Australian plate. J. Geophys. Res. 96 11,779-11,802 (1991).

8. DeMets, C. & Royer, J.-Y. A new high-resolution model for India-Capricorn motion since 20 Ma: Implications for the chronology and magnitude of distributed crustal deformation in the Central Indian Basin. Current Science 85, 339-345 (2003).

9. Robinson, D. P., Henry, C., Das, S. & Woodhouse, H. H. Simultaneous rupture along two conjugate planes of the Wharton Basin earthquake. Science 292, 1145-1148

(2001).

10. Abercrombie, R. E., Antolik, M. & Ekström, G. The June 2000 Mw 7.9 earthquakes south of Sumatra: Deformation in the India-Australia Plate. J. Geophys. Res. 108, No.B1, 2018, doi:10.1029/2001JB000674 (2003).

11. Kanamori, H. The energy release in great earthquakes. J. Geophys. Res. 82, 2981-2987 (1977).

12. Ben-Menahem, A., Aboodi, E. & Schild, R. The source of the great Assam earthquake - an interplate wedge motion. Phys. Earth Planet. Inter. 9, 265-289 (1974).

13. Chen, W.-P. & Molnar, P. Seismic moments of major earthquakes and the average rate of slip in Central Eurasia. J. Geophys. Res. 82, 2945-2969 (1977).

14. Molnar, P. A review of the seismicity and the rates of active underthrusting and deformation at the Himalayas. J. Himalayan Geology 1, 131-154 (1990).

15. Ammon, C. J., et al. Rupture process of the 2004 Sumatra-Andaman earthquake. Science 308, 1133-1139 (2005).

16. Ishii, M., Shearer, P. M., Houston, H. & Vidale, J. E. Extent, duration and speed of the 2004 Sumatra-Andaman earthquake imaged by the Hi-net array. Nature 435, 933-936 (2005).

17. Krüger, F. & Ohrnberger, M. Tracking the rupture of the Mw 9.3 Sumatra earthquake over 1,150 km at teleseismic distance. Nature 435, 937-939 (2005).

18. Koper, K. D., Hutko, A. R., Lay, T. & Sufri, O. Imaging short-period seismic radiation from the 27 February 2010 Chile (Mw 8.8) earthquake by back-projection of P, PP, and PKIKP waves, J. Geophys. Res. 117, B02308, doi:10.1029/2011J B008576

(2012).

19. Koper, K. D., Hutko, A. R. & Lay, T. Along-dip variation of teleseismic short-period radiation from the 11 March 2011 Tohoku Earthquake (Mw 9.0). Geophysical Res. Lett. 38, L21309, doi:10.1029/2011GL049689 (2011).

20. Incorporated Research Institutions for Seismology. Back Projections for Mw 8.7 off W Coast of Northern Sumatera http://www.iris.edu/spud/backprojection/118733, (2012).

21. Meng, L., Ampuero, J.-P. & Luo, Y. Back-projection Results, 4/11/2012 (Mw8.6) offshore Sumatra, Indonesia. http://www.tectonics.caltech.edu/slip_history/2012_Sumatra/back_projection/

22. Kiser, E. Preliminary rupture modeling of the April 11, 2012 Sumatran earthquakes. http://www.seismology.harvard.edu/research_sumatra2012.html

23. Lay, T. et al. Depth-varying rupture properties of subduction zone megathrust faults. J. Geophys. Res. 117, B04311, doi:10.1029/2011JB009133 (2012).

24. Ammon, C. J., Kanamori, H. & Lay, T. A great earthquake doublet and seismic stress transfer cycles in the Central Kuril Islands. Nature 451, 561-565 (2008).

25. Lay, T., Kanamori, H., Ammon, C. J., Hutko, A. R., Furlong, K. & Rivera, L. The 2006-2007 Kuril Islands great earthquake sequence. J. Geophys. Res. 114, B11308, doi:10.1029/2008JB006280 (2009).

Supplementary Information is linked to the online version of the paper at

www.nature.com/nature.

4.8 Auxiliary Figures

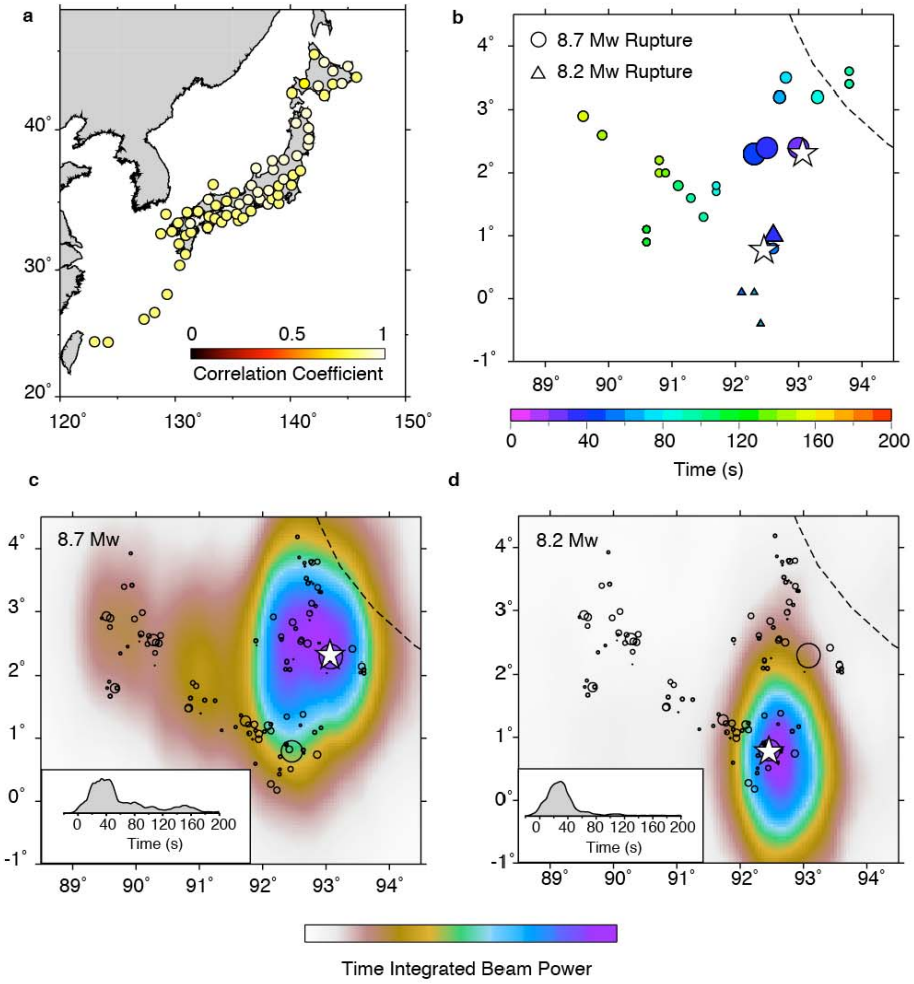

Figure S1 | Short-period Seismic Energy Release Pattern Imaged by F-net. (**a**) Locations of broadband seismograph stations in Japanese F-net used for the 0.5-2.0 Hz P wave back-projection of the M_w 8.7 and M_w 8.2 Indo-Australia earthquakes. Stations were selected for high P wave similarity. (**b**) Local beam power maxima during the back-projections, with color indicating time after the nominal origin time. Symbol size is proportional to beam power. (**c**) Time integrated beam power for the M_w 8.7 back-projection. The circles are early NEIC aftershocks with symbol size proportional to magnitude, and the dashed line is the Sumatra trench. The inset shows peak beam power as a function of time. (**d**) same as panel (**c**), but for the M_w 8.2 aftershock. The time-dependent evolution is best evaluated by viewing Movie S2.

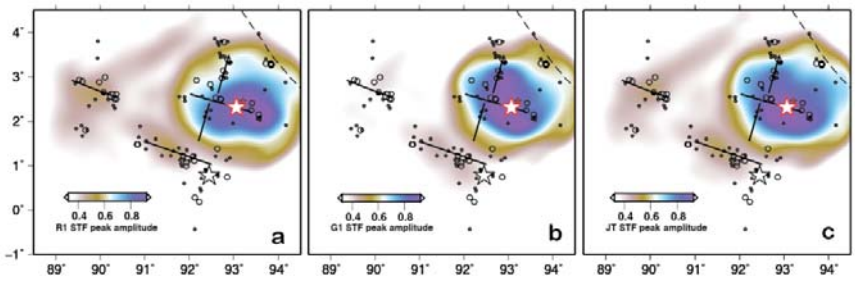

Figure S2 | Long-period Seismic Energy Release Pattern. Maps showing the spatial patterns of long-period surface wave energy sources for the 11 April 2012 (M_w 8.7) mainshock (epicenter indicated with a red outlined star) imaged using (a) R1 source time functions (STFs) only, (b) G1 STFs only, and (c) joint R1 and G1 STFs. Azimuthal weighting proportional to the R1 or G1 radiation patterns is used for each case to suppress instabilities near radiation nodes.

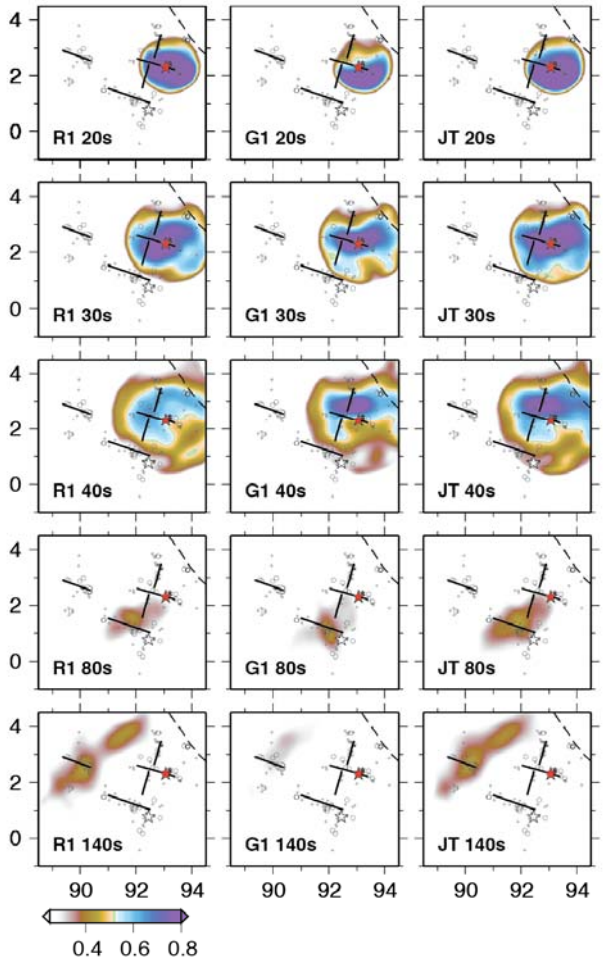

Figure S3 | Time-varying Images of the Long-Period R1 and G1 Back-projection for the Mainshock. The back-projections of R1 and G1 source time functions (STFs) over the source region grid are shown for the indicated times, with the color image indicating locations of source radiation at long-period. The left column shows the images from just R1 STFs, the middle column shows the images from just G1 STFs, and the right column shows the images from joint R1+G1 imaging (as in Figure 3), where weighting proportional to radiation pattern coefficient has been applied. Linear stacking is used in each case. The secondary sources to the SW at 80s and to the west at 130 s have amplitudes about 20-30% of the peak near the hypocenter, consistent with seismic moment for M_w 8.0-8.3 subevents.

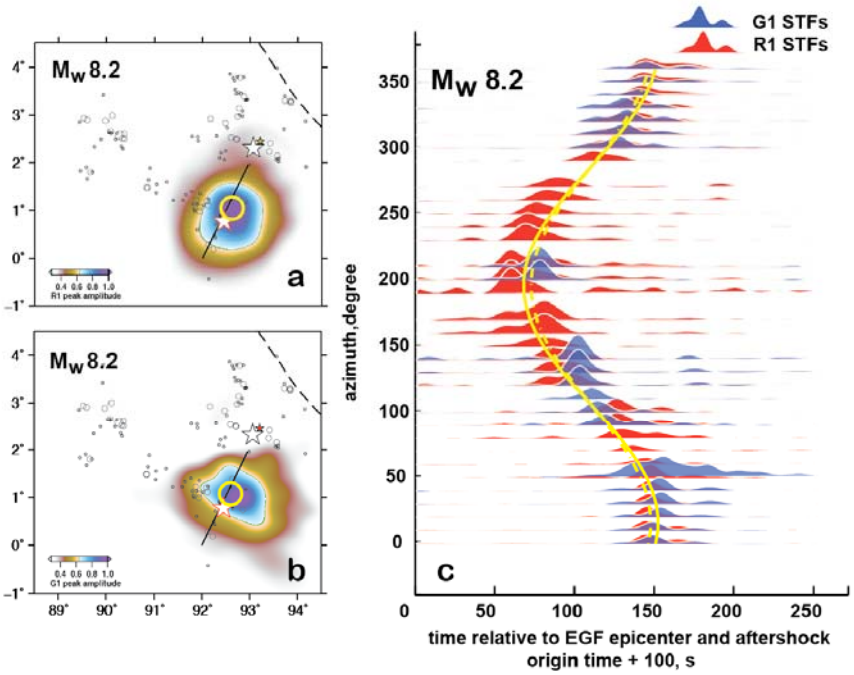

Figure S4 | Long-period Seismic Energy Release Pattern for the M_w 8.2 Aftershock. The maps show the spatial pattern of long-period surface wave energy release for the large aftershock on 11 April 2012 (M_w 8.2) for which the red-outlined star indicates the epicenter, as imaged from (a) R1 source time functions (STFs) and (b) G1 STFs. The one-week aftershock distribution is shown by small circles with radii proportional to seismic magnitude. The color image indicates the peak stacked energy from the STFs back-projected relative to the epicentral location of the 10 January 2012 (M_w 7.2) event (orange stars) which was used for empirical Green functions (EGFs). The star with black outline indicates the mainshock epicenter. The yellow circle in the images indicates a reference location of energy release that gives the move-out of R1 and G1 STF arrivals. The straight lines indicate the probable orientation of the fault that ruptured in the event. Panel (c) shows the azimuthally binned and stacked R1 (red) and G1 (blue) STFs plotted as functions of time relative to the EGF epicenter with a 100 s time shift from the aftershock origin time. These STFs represent seismic moment as a function of time observed in surface waves at different azimuths. The yellow curves correspond to the yellow circles in (a) and (b), showing the predicted arrival times of energy from that location, with the "S-curve" pattern caused by the relative propagation times toward different azimuths. The solid curve is for R1 waves using a velocity of 4.0 km/s and the dashed curve is for G1 waves using a velocity of 4.5 km/s. The STF signals aligned on such curves for each position in the map form the corresponding images in (a) and (b).

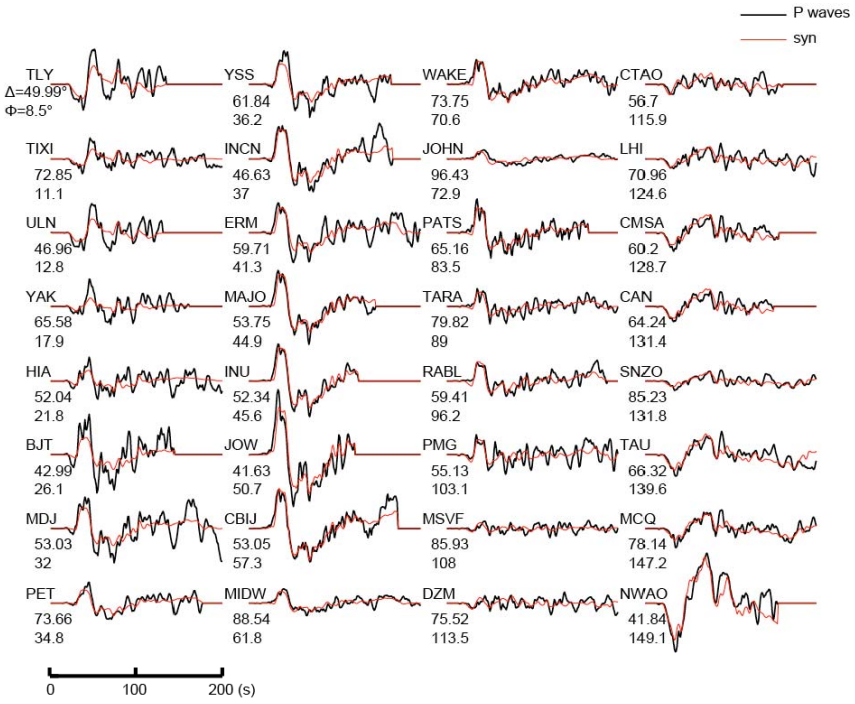

Figure S5a | Observed and Predicted Broadband Waveforms for the 11 April 2012 M_w 8.7 Mainshock. Broadband P wave ground displacement data filtered in the passband 1-200 s are shown with black lines. The station name, angular distance, Δ, and azimuth from the source, ϕ, are shown. Similarly filtered synthetics for the preferred fault model in Figure 4 are shown with red traces. Some traces are truncated to avoid contamination from PP arrivals. All of these traces are vertical component P waves.

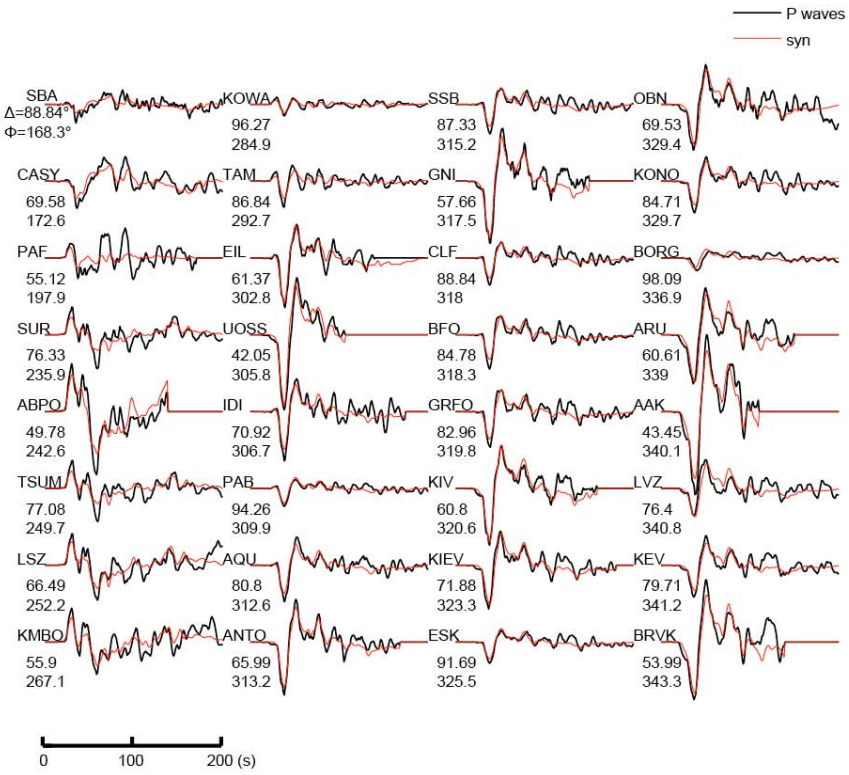

Figure S5b | Observed and Predicted Broadband Waveforms for the 11 April 2012 M_w 8.7 Mainshock. Broadband P wave ground displacement data filtered in the passband 1-200 s are shown with black lines. The station name, angular distance, Δ, and azimuth from the source, ϕ, are shown. Similarly filtered synthetics for the preferred fault model in Figure 4 are shown with red traces. Some traces are truncated to avoid contamination from PP arrivals. All of these traces are vertical component P waves.

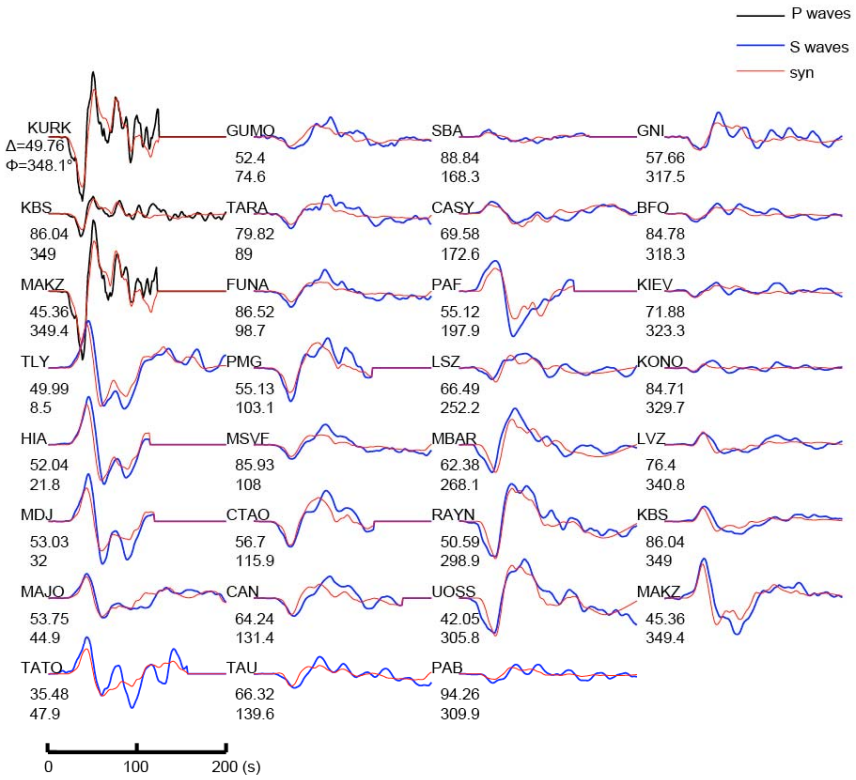

Figure S5c | Observed and Predicted Broadband Waveforms for the 11 April 2012 M_w 8.7 Mainshock. Broadband ground displacement data filtered in the passband 1-200 s are shown with black (vertical component P waves) or blue (tangential component SH waves) lines. The station name, angular distance, Δ, and azimuth from the source, ϕ, are shown. Similarly filtered synthetics for the preferred fault model in Figure 4 are shown with red traces. Some traces are truncated to avoid contamination from PP or SS arrivals.

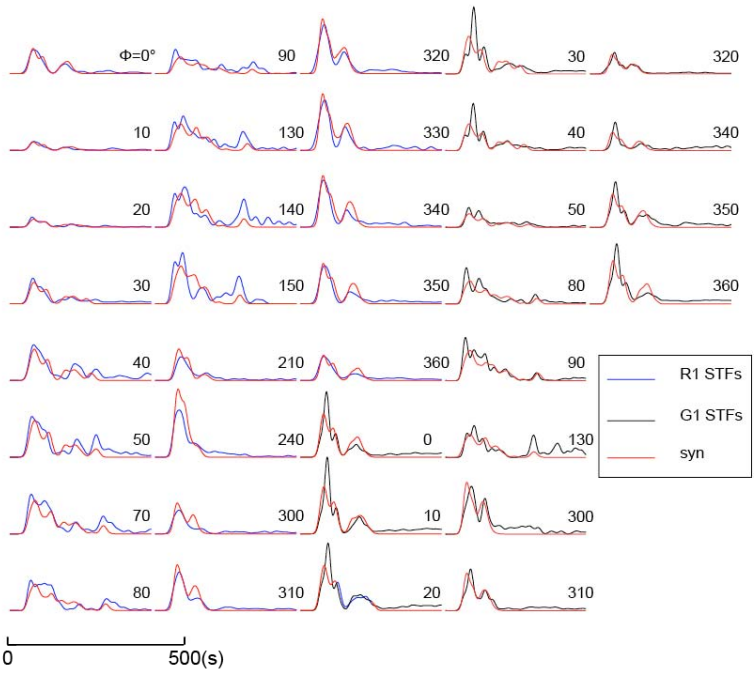

Figure S5d | Observed and Predicted Broadband Waveforms for the 11 April 2012 M_w 8.7 Mainshock. Broadband surface wave STF data stacked in 10° azimuthal bins are shown with blue lines (R1 STFs) and black lines (G1 STFs). The central azimuths from the source for each stacking bin, ϕ, are shown. Corresponding synthetics for the preferred fault model in Figure 4 are shown with red traces.

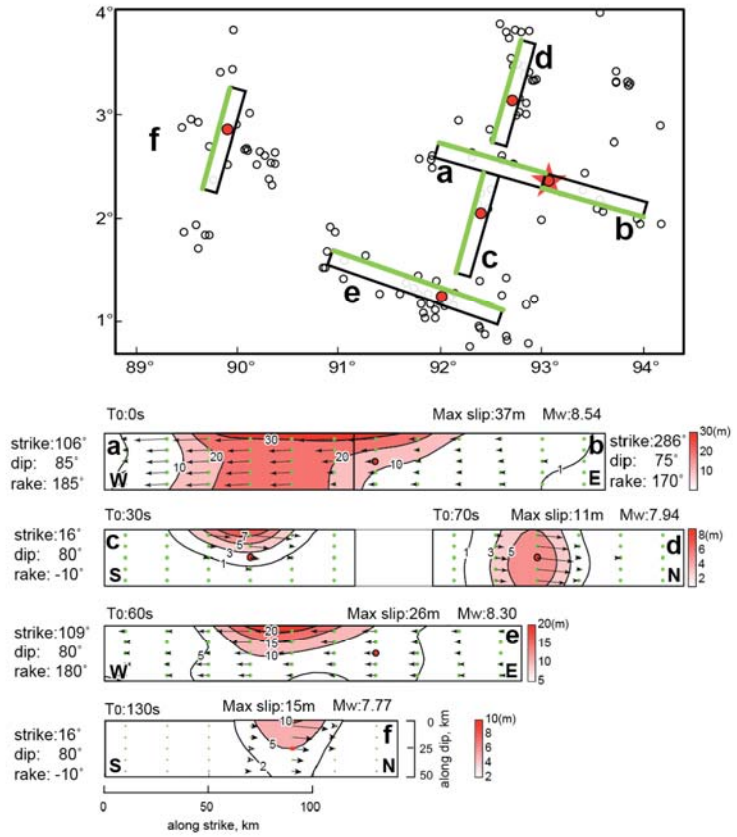

Figure S6 | Finite-Fault Inversion For Choice of NNE-SSW Fault on Ninetyeast Ridge. The map shows fault segments activated during the 11 April 2012 M_w 8.7 mainshock, specified for finite-fault slip model inversion of teleseismic broadband P and SH waves and G1 and R1 STFs. In this case, we choose the NNE-SSW orientation for segment f, with rupture trending along the Ninetyeast ridge. The red star indicates the epicentral location, and red dots indicate the placement of hypocenters (all at 30 km deep) on each fault segment. The time at which each segment begins to rupture is indicated by T0.The rectangles indicate the subfault strikes and dips (shallow edge is on the green side, deeper edge on the black side. We use 4 subfaults, two of which are subdivided, with onset times constrained by the short-period back-projections. The corresponding slip distributions on each subfault are shown below, with the subfault grids having 20 km spacing along strike and 10 km spacing along dip. The peak slip and M_w of each subfault is indicated, as is the position of the hypocenter on each subfault from which the rupture expands. The rupture velocity is 2.0 km/s on all subfaults. This solution can be compared with that in Figure 4.

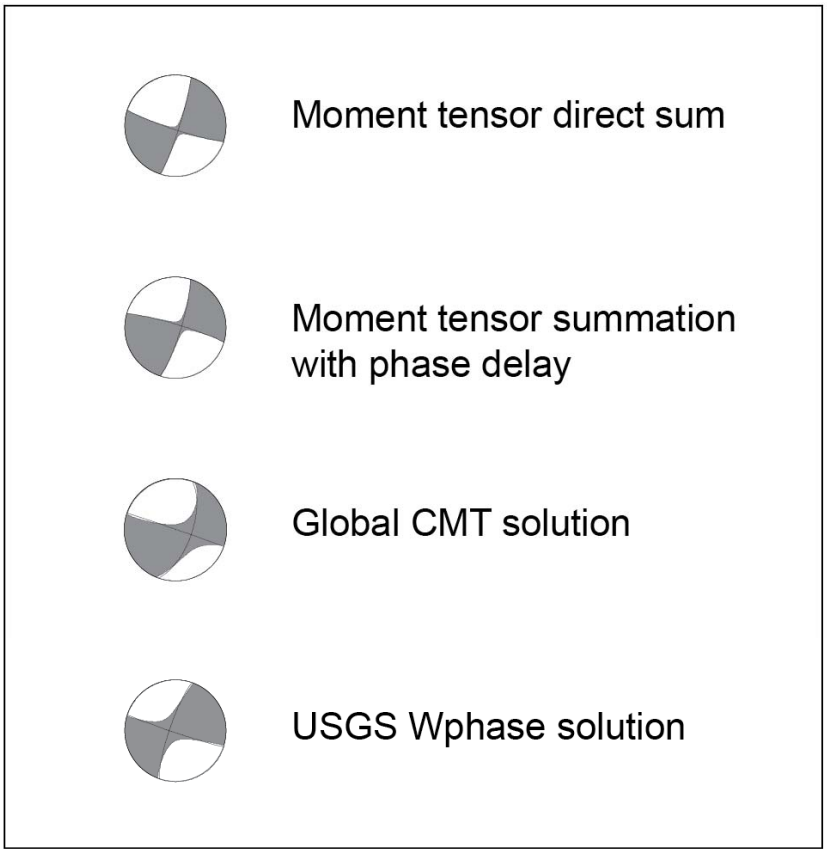

Figure S7 | Point source moment tensor representations for the 8.7 event. The top solution is the direct sum of all subfault moment tensors from the model in Figure 4, with no allowance for space-time variations. The second solution is the sum allowing for phase delay. The lower two are actual data inversions by the Global CMT and W-phase methods. The fault model solution produces only minor non-double couple component, although a complete calculation with the spatial effects will increase it, possibly to the level of the observed solutions.

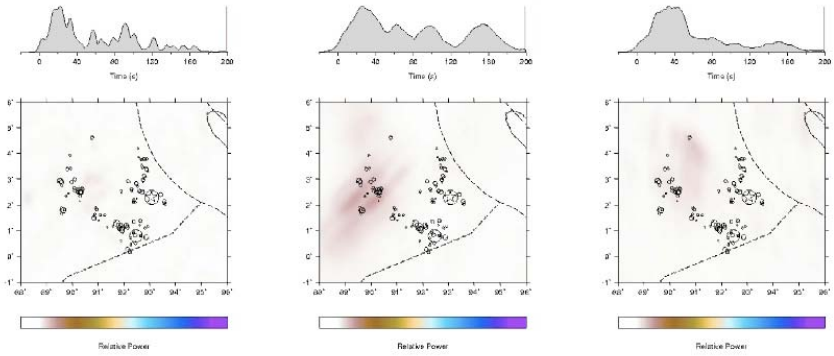

Movie S1 | QuickTime (.mov) animations of short-period P wave back-projections for the 11 April 2012 M_w 8.7 event using stations in Europe and Japan. The left panel is for European recordings filtered in the 0.5-2.0 Hz band. This corresponds to the information in Figure 2b,c. The middle panel is for the same European recordings filtered in the 0.1-0.5 Hz band. The right panel is for the F-net broadband recordings in Japan filtered in the 0.5-2.0 Hz band.

The movie is also available at:
http://es.ucsc.edu/~thorne/NATURE_SUMATRA/YLK_SI_Movies.html

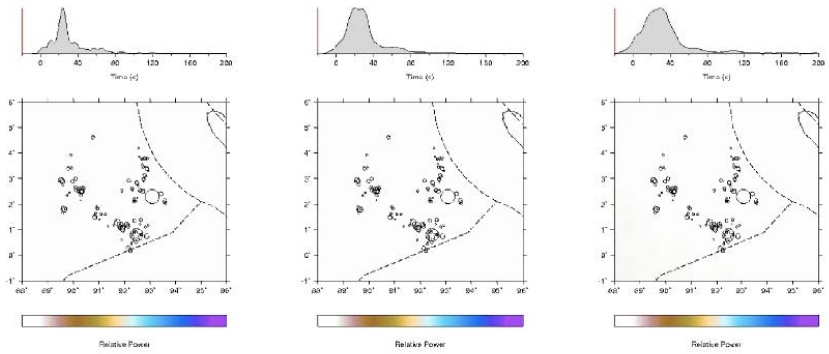

Movie S2 | QuickTime (.mov) animations of short-period P wave back-projections for the 11 April 2012 M_w 8.2 event using stations in Europe and Japan. The left panel is for European recordings filtered in the 0.5-2.0 Hz band. This corresponds to the information in Figure 2d. The middle panel is for the same European recordings filtered in the 0.1-0.5 Hz band. The right panel is for the F-net broadband recordings in Japan filtered in the 0.5-2.0 Hz band.

The movie is also available at:
http://es.ucsc.edu/~thorne/NATURE_SUMATRA/YLK_SI_Movies.html

Chapter 5

The 5 September 2012 Nicoya, Costa Rica Mw 7.6 earthquake rupture process from joint inversion of high-rate GPS, strong-motion, and teleseismic P wave data and its relationship to adjacent plate boundary interface properties

Abstract

On 5 September 2012, a large thrust earthquake (M_w 7.6) ruptured a densely-instrumented seismic gap on the shallow-dipping plate boundary beneath the Nicoya Peninsula, Costa Rica. Ground motion recordings directly above the rupture zone provide a unique opportunity to study the detailed source process of a large shallow megathrust earthquake using very nearby land observations. Hypocenter relocation using local seismic network data indicates that the event initiated with small emergent seismic waves from a hypocenter ~10 km offshore, 13 km deep on the megathrust. A joint finite-fault inversion using high-rate GPS, strong-motion ground velocity recordings, GPS static offsets, and teleseismic P waves reveals that the primary slip zone (slip > 1 m) is located beneath the peninsula. The rupture propagated down-dip from the hypocenter with a rupture velocity of ~3.0 km/s. The primary slip zone extends ~70 km along strike and ~30 km along dip, with an average slip of ~2 m. The associated static stress drop is ~3 MPa. The seismic moment is 3.5 x 10^{20} Nm, giving M_w = 7.6. The co-seismic large-slip patch directly overlaps an

onshore inter-seismic locked region indicated by geodetic observations, and extends down-dip to the intersection with the upper plate Moho. At deeper depths, below the upper plate Moho, seismic tremor and low frequency earthquakes have been observed. Most tremor locates in adjacent areas of the megathrust that have little co-seismic slip; a region of prior slow slip deformation to the southeast also has no significant co-seismic slip or aftershocks. An offshore locked patch indicated by geodetic observations does not appear to have experienced co-seismic slip, and aftershocks do not overlap this region, allowing the potential for a comparable size rupture offshore in the future.

5.1. Introduction

On 5 September 2012, a large shallow-dipping thrust event (M_w 7.6) partially ruptured the plate boundary megathrust fault beneath the Nicoya Peninsula, Costa Rica (Figure 5.1). An inland and relatively deep hypocenter was reported by the USGS (10.085°N, 85.315°W, 35 km, 14:42:07 UTC, http://comcat.cr.usgs.gov/earthquakes/eventpage/pde20120905144207800_35#summary), as shown in Figure 5.1. Teleseismic W-phase inversions also indicate a relatively deep (30-40 km) centroid depth (USGS, *Ye et al*. [2013]), and the global CMT (G-CMT) depth was ~30 km (http://www.globalcmt.org/CMTsearch.html). Given the relatively well-constrained regional plate boundary geometry [e.g., *DeShon et al*., 2006], these depth estimates suggest rupture under the northeastern part of the peninsula, which is somewhat at odds with the strongest shaking (Modified Mercalli Scale Intensity X) being felt in the

town of Nosara, 6 km from the Pacific coast.

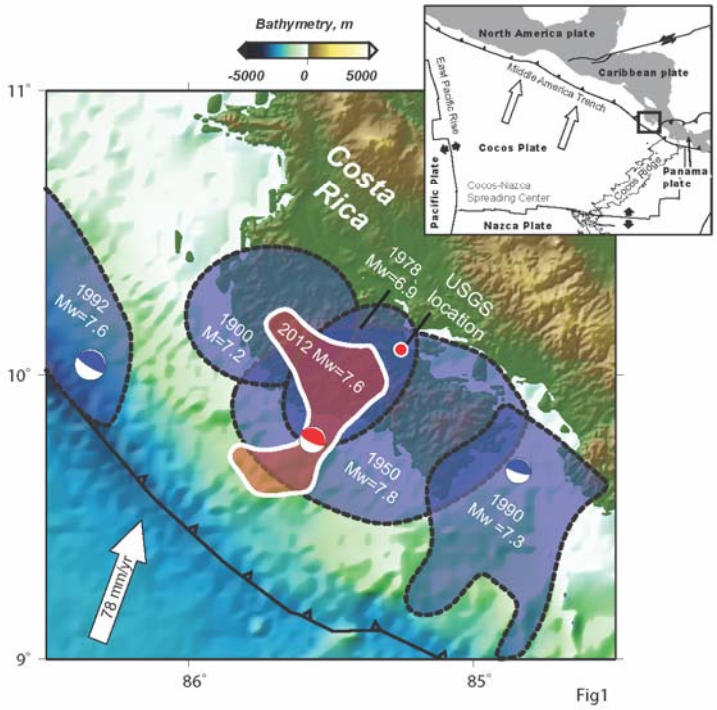

Figure 5.1. Maps of the study area and regional plate tectonic setting. The inset map locates the Cocos Plate which subducts beneath the North America, Caribbean and Panama plates along the Middle America Trench. Spreading and transform plate boundaries are marked by solid lines with black arrows indicating relative plate motion. Trenches are marked with barbed solid lines. The Cocos Plate motion relative to the North American and Caribbean Plates is indicated by white arrows. The box identifies the Nicoya peninsula of Costa Rica that is enlarged in the main map. Global centroid-moment tensor solutions are shown for the September 5, 2012 Nicoya, Costa Rica M_w 7.6 event (red filled beach ball) and the 1992 M_w=7.6 and 1990 M_w=7.3 events (blue filled beach balls). The co-seismic region of the 2012 event is indicated with the red-filled patches. The co-seismic slip > 1.2 m regions are outlined with solid white curves. Aftershock areas of 1992, 1990, 1978 and 1950 events are indicated with blue-filled patches. Estimated rupture area of 1900 event is also indicated with blue filled patches. The relative plate motion direction and rate of the Cocos plate is indicated by the white arrow.

Numerous deployments of seismic and geodetic instruments have been conducted over the entire Nicoya Peninsula during the last decade [e.g., *Norabuena et*

al., 2004; *Outerbridge et al.,* 2010] motivated by both the unusual opportunity to place stations on land above a relatively shallow megathrust and by concerns about the regional seismic hazard. The last major earthquake in the Nicoya region was in 1950 (M_S 7.7, M_w ~ 7.8), implying that up to 5 m of slip deficit may have accumulated. Many stations were operating during the 2012 earthquake including high-rate GPS (hr-GPS) with ground position solutions computed at 5 samples per second (sps), and low-rate (1 sample per 15 seconds) GPS (lr-GPS), strong ground motion, broadband and short-period seismic networks [*Dixon et al.,* 2013]. We utilize these regional observations along with teleseismic body waves to study the mainshock rupture process and to compare the slip distribution to prior characterizations of megathrust failure processes.

With steadily improving accuracy over the last decade, hr-GPS time-series allow inversion of the space-time rupture history of large earthquakes [e.g., *Miyazaki et al.*, 2004; *Ji et al.,* 2004; *Yue and Lay*, 2011]. The main advantage is that both time-varying (seismic wave motions) and static ground deformations can be modeled in a self-consistent fashion, which yields improved inversion stability compared to teleseismic-signal-only inversions. However, prior hr-GPS finite-fault inversion studies for large megathrust events have been constrained by having one-sided (land side only) station distributions, relatively far from offshore rupture zones, reducing the along-dip slip resolution. This limitation can be partly compensated by joint inversion with teleseismic datasets, with improved resolution achieved by combining the relative advantages of both near-field and teleseismic observations [*Ammon et al.*,

2011; *Yue and Lay*, 2013; *Wei et al.*, 2012; *Koketsu et al.*, 2011]. However, substantial uncertainty in coseismic slip location remains. For the Nicoya Peninsula, geodetic and seismic networks are directly above and around the main rupture area of the 2012 Costa Rica event (Figure 5.1) offering unusually good resolution of the space-time history of the rupture process. Comparable resolution has been obtained for earlier megathrust deformation processes around the Nicoya Peninsula, including accumulation of seismic slip deficits, seismic tremor, slow slip events, and microseismic and aftershock distributions, as summarized in the next section.

5.2 Regional tectonic setting and megathrust observations

The Nicoya Peninsula protrudes about 60 km seaward over the megathrust plate boundary, where the Cocos plate underthrusts the Caribbean plate at a convergence rate of ~78 ± 1 mm/yr (Figure 5.1) [*DeMets et al.*, 2010; *Protti et al.* 2012]. There are only a few other subduction zones where peninsulas or forearc islands (e.g., the Mentawai Islands offshore of Sumatra) provide land access as close as 50-60 km to a deep trench. Beneath the Nicoya Peninsula there is an along-strike change in the origin of the subducting Cocos plate lithosphere. Lithosphere subducting beneath northwestern Nicoya was formed at the East Pacific Rise (EPR), while lithosphere subducting beneath southeastern Nicoya was formed at the Cocos Nazca spreading center (CNS). Sea floor magnetic anomalies suggest a young age for both lithospheres at the trench: ~24 myr for EPR, and decreasing from 22 to 15 myr southeast toward the Cocos Ridge for CNS [*Barckhausen et al.*, 2001; *LaFemina et al*., 2009]. There is a strong variation in heat flux across this lithospheric boundary, from 20–40 mW/m^2

in EPR crust, to 105–115 mW/m^2 in CNS crust. This heat flux as well as an upper plate seismic velocity contrast across the EPR-CNS lithospheric boundary [*Audet and Schwartz*, 2013] may influence frictional properties along the megathrust near the peninsula [e.g., *Harris and Wang*, 2002; *Newman et al*., 2002; *Spinelli and Saffer*, 2004].

Several large historic earthquakes have ruptured the megathrust near the Nicoya Peninsula. The 25 March 1990 M_w 7.3 (CMT) earthquake ruptured the off-shore region southeast of the Nicoya Peninsula [*Protti et al.*, 1995], and the 2 September 1992 shallow M_w 7.6 Nicaragua tsunami earthquake ruptured along the subduction zone northwest of the Nicoya Peninsula [*Kanamori and Kikuchi*, 1993; *Ihmlé*, 1996]. These events bracketed a seismic gap beneath the Nicoya Peninsula ~150 km wide (Figure 5.1). The 1990 rupture zone may have previously ruptured in 1939 in an M_S 7.3 event. Three recorded large earthquakes ruptured beneath the Nicoya Peninsula in the 20th century: the 21 June 1900 M ~7.2 event, the 5 October 1950 M_S 7.7, M_w ~7.8 event and the 23 August 1978 M_w = 6.9 event (Figure 5.1) [*Pacheco and Sykes*, 1992; *Protti et al.*, 2001; *Avants et al.*, 2001; *Norabuena et al.,* 2004; *Allen et al*., 2009]. The large 1900 and 1950 events have very uncertain rupture zones, which may overlap beneath the central Nicoya Peninsula, with the smaller 1978 event also located in the corresponding region (Figure 5.1). *Nishenko* [1991] notes other large events likely located under Nicoya in 1827, 1853, 1863, and 1916, and infers that this is one of the most active seismic regions of Costa Rica. Large events under Nicoya have a recurrence time of ~28-50 yr, depending on assumptions about rupture overlap.

Warnings about the increasing risk of a large megathrust earthquake striking Nicoya have been issued for more than two decades [e.g., *Gonzalez and Protti,* 2005; *Lundgren et al* 1999； *Nishenko,* 1991; *Protti et al.,* 1995; *Protti et al* 2001; *Pacheco and Sykes,* 1992; *Iinuma et al., 2004*； *Feng et al* 2012].

Regional seismicity beneath the Nicoya Peninsula has been examined using a local on-land and off-shore combined broadband/short-period seismic network [e.g., *Newman et al.*, 2002; *DeShon et al., 2005*], and suggests an up-dip limit of the seismogenic zone that deepens from near 15 km depth in the south to 20 km in the north. *Newman et al.* [2002] suggest that this is related to the thermal contrast of the underthrust CNS versus EPR oceanic crust. Other types of deformation are also reported around the Nicoya Peninsula, including transient slow-slip events [*Outerbridge et al.*, 2010; *Jiang et al.*, 2012], deep low-frequency [*Brown et al.*, 2009] and very low frequency [*Walter et al*., 2011] earthquakes, and non-volcanic tremor [*Outerbridge et al.*, 2010; *Walter et al.*, 2011]. This background activity is not releasing all strain in the subduction zone; geodetic observations indicate spatially varying inter-seismic coupling, with a concentrated slip-deficit area under the coastal region of central Nicoya Peninsula [e.g., *Iinuma et al.,* 2004; *Lundgren et al.* 1999*; Norabuena et al*., 2004; *Feng et al.,* 2012]. The most recent of these studies suggests total locking was present below the central Nicoya Peninsula for at least a decade prior to 2012. Assuming this behavior characterized earlier periods, at least 3 m of slip could have accumulated since 1978 and even more in the surrounding region that ruptured in 1950.

It is generally accepted that large interplate events are likely to rupture previously locked sections of the megathrust, thus it is reasonable to anticipate that the 2012 Costa Rica event should have ruptured the slip-deficit region imaged by *Feng et al.* [2012]. Initially, it was surprising to note that the inland, relatively deep hypocenter reported by the USGS appeared to be distinct from the locked patch, co-locating with a down-dip region of low-frequency earthquakes and tremor which is assumed to be weakly seismically coupled. We exploit the high quality data from the Nicoya Peninsula to evaluate just how close the correspondence is between the prior slip-deficit and co-seismic regions and the relationship of the co-seismic slip region to regions of tremor and slow slip. Slip zones of recent large earthquakes such as the 2010 Chile (M_w 8.8) and 2011 Tohoku earthquakes (M_w 9.0) have been compared with prior estimates of slip-deficit patterns, but the offshore spatial resolution of the latter is limited; the Nicoya Peninsula configuration enables a much more detailed comparison.

5.3. Data and method

5.3.1 Hypocenter relocation

An accurate hypocenter is important for finite-fault inversions as it influences the faulting kinematics. For most large earthquakes near-field or regional recordings are not available, so the hypocenter reported by the USGS is commonly used in finite-fault inversion. In the case of the 2012 Costa Rica event, the seismic stations on the Nicoya Peninsula, comprising 13 broadband seismic stations and 10 strong ground motion stations, enable a more accurate hypocenter determination (Figure 5.2). The

broadband stations are maintained by UC Santa Cruz, Georgia Institute of Technology and Observatorio Vulcanologico y Sismologico de Costa Roca (OVSICORI-UNA) and the strong ground motion stations are maintained and distributed by Laboratorio de Ingenieria Sismica at Universidad de Costa Rica. All broadband stations went off-scale for the mainshock when the large seismic waves arrived, however, the timing of initial P arrivals is still available for locating the initial seismic radiation.

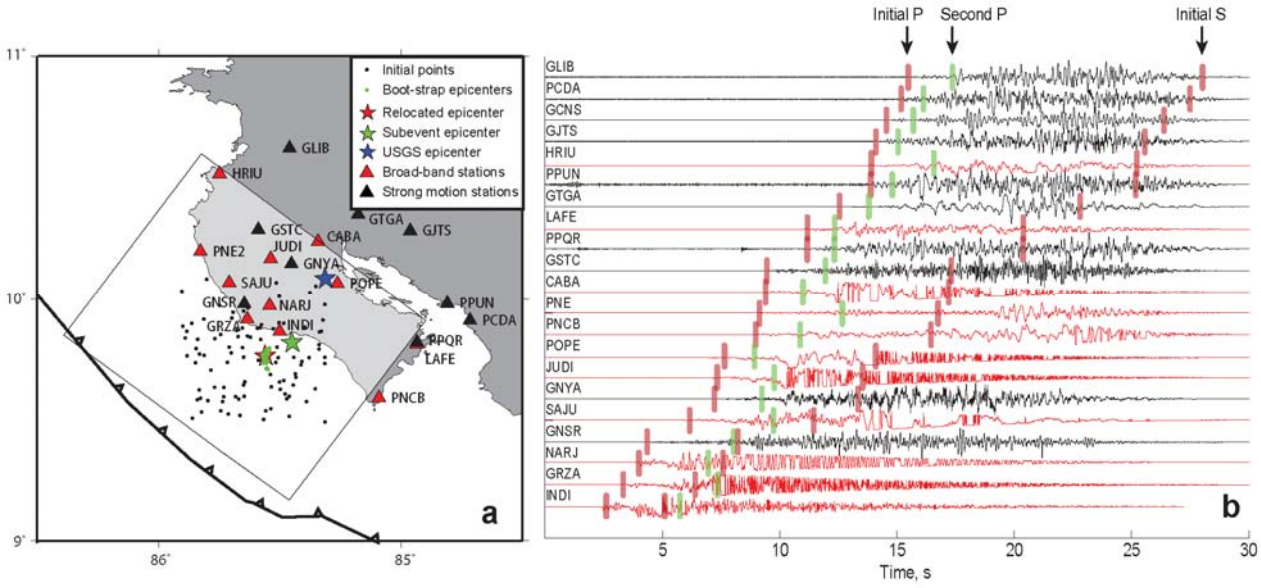

Figure 5.2. a) The relocated epicenter of the 2012 Nicoya, Costa Rica event based on local seismic observations is indicated with a red-filled star, and the USGS epicenter from teleseismic data is marked with a blue-filled star. The epicenter of a strong-onset subevent in the local data is indicated with a green-filled star. Initial positions of each assumed hypocenter used in the location process are indicated by black dots to indicate the inversion stability. Hypocenters located by 40 boot-strap realizations are plotted with green filled circles to evaluate relocation uncertainty. Local seismic stations are marked by red and black triangles for broadband and strong ground motion stations, respectively. The Middle America Trench is indicated by the barbed curve and the rupture model area is marked by the rectangle. **b**) Vertical component records from regional broad-band and strong ground motion stations are shown by red and black waveforms, respectively, ordered by epicentral distance. Predicted P arrival times for the hypocenter and large subevent are marked by red and green bars respectively. Predicted S wave arrival times of the hypocenter are also marked by the later red bars. A linear taper was applied to each trace after the initial P wave motion to emphasize the initial amplitudes.

To relocate the hypocenter, we picked 21 arrival times from 3 component records checking for reliable initial motions. A 1D P-wave velocity model from a local tomography study [*Deshon et al.*, 2005] was used for ray-tracing. We assume the hypocenter is located on the megathrust with geometry defined from a seismic reflection profile [*Christeson et al.*, 1999]. The same fault geometry is used in our finite fault model parameterization (Figure 5.3). The along-strike and along-dip position of the hypocenter and its origin time are inverted for using a classical Newton-Gaussian inversion technique. Stations within 100 km from the preliminary hypocenter are used to guarantee that the first motions are from the Pg phases. To test dependence on the initial position, 50 relocations were performed with different initial positions within a 60 km x 60 km area, centered near the preliminary hypocenter. All inversions give relocated hypocenters within ~1 km horizontal distance, indicating a stable inversion. The preferred hypocenter is 9.76°N, 85.56°W at depth of 13.1 km below sea level, which is ~10 km off the coast. The initial time is at 14:42:04.4 UTC, 2.6 s earlier than the USGS origin time for a source depth of 35 km. The averaged absolute value of the predicted initial time residual is ~0.23 s, which is close to the error of the manually picked initial arrivals. Assuming the rays are close to horizontal and a typical P wave velocity of ~5 km/s, then the associated epicenter location error is approximately 1.5 km.

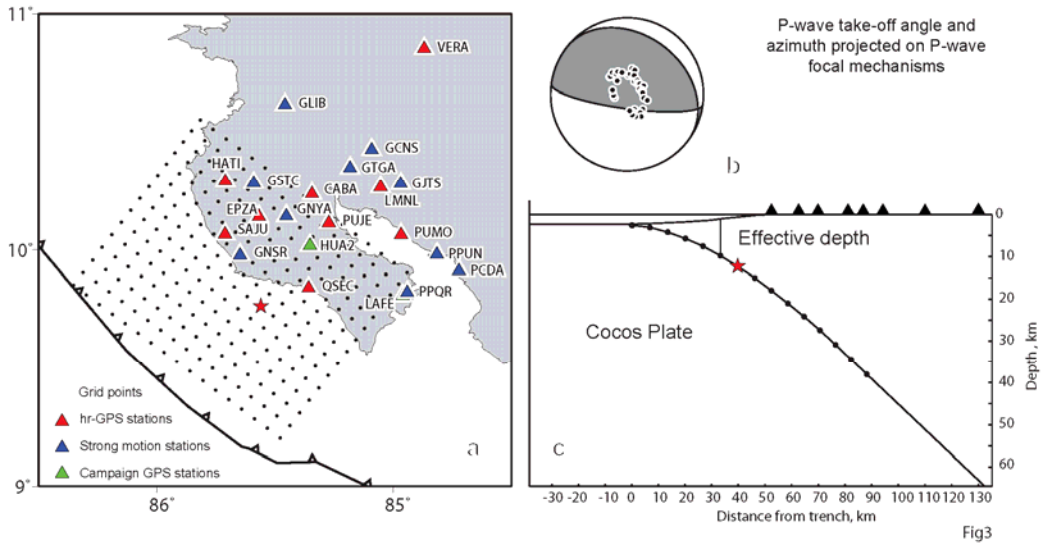

Figure 5.3. Rupture model parameterization. **a**) Map of the rupture model grid, parameterized with 17 and 15 nodes, with 7.5-km spacing along strike and dip, respectively. The relocated epicenter is indicated by a red-filled star. The locations of local stations used in the inversion are marked by red-, blue-, and green-filled triangles for hr-GPS stations, strong ground motion stations, and lr-GPS stations respectively. **b**) The azimuths and take-off angles of teleseismic P wave recordings used in our inversion are projected onto the lower hemisphere focal mechanism of the 2012 Nicoya, Costa Rica event. **c**) Cross-section indicating the fault model and ocean bottom geometry. The node depth in the flat 1D model was taken as the effective prism thickness with dip used for each subfault preserved to correspond to the dip of the actual megathrust.

When considering the predicted S wave arrivals in the near-field seismic traces, we found the broadband stations are off-scale after the initial S arrival, but there are some secondary phases between the initial P and S arrivals (Figure 5.2), which are probably P waves from rupture subevents. A consistent secondary P wave arrival, stronger than the first very emergent P arrival, could be identified around 2-3 s after the initial motion. By picking corresponding arrival times, we located a subevent hypocenter at 9.82°N, 85.47°W, at a depth of 17.2 km on the megathrust (Figure 5.2a). The origin time of this subevent is 14:42:07.7 UTC. Stations with epicenter distances from 20-100 km are used for this location, to exclude the influence of the S wave

energy from the hypocenter in the very close stations. We used the differential arrival time between the initial motion and the subevent P wave motion to make a relative relocation, given the relocated hypocenter as a reference point. The subevent locates ~12 km down-dip of the hypocenter, and is delayed by ~3.4 s from the initial rupture, which suggests initial down-dip rupture propagation at a velocity of ~3.5 km/s. The relative relocation is not strongly influenced by the uncertainty of the reference model and is sensitive to the relative location between the hypocenter and subevent location. The arrival time picking of the subevent has more uncertainty than the initial motion, which introduces larger errors in the location and initial time. The estimated location and initial time of the subevent indicate down-dip rupture propagation, which is a stable pattern that got proved in boot-strap algorithm, but may not be used to prescribe the rupture velocity precisely.

In earthquake location procedures errors are introduced by using a reference 1-D velocity model, which does not account for actual 3-D heterogeneities. Such error will tend to increase with propagation distance. For the 2012 Nicoya, Costa Rica event, we have 21 stations within 100 km epicentral distance and 4 stations within 30 km epicentral distance. For these data reference model error that accumulates with distance will be small. To test the inversion stability, we adopted a boot-strap algorithm, in which we randomly selected half the stations for relocation in each boot-strap realization. 40 boot-strap realizations are made; the location results fall within 5 km from the preferred hypocenter location, suggesting a maximum location error of 5 km (Fig. 2). The boot-strap algorithm samples different stations in each

realization, varying the effects of 3-D heterogeneity. The relatively concentrated location of the boot-strap results, with standard deviation of 1.4 km and maximum of 5 km, indicates that 3-D heterogeneity does not impact our location significantly.

Another concern about the location uncertainty comes from the one-sided station distribution, in which the origin time trades-off with the off-shore distance of the epicenter. In our tests, location excluding the 4 closest stations moves the epicenter 5 km closer to the coast line and delays the initial time by ~0.5 s. This is consistent with the boot-strap location uncertainties. We use the location from the complete data set as our final hypocenter.

Considering the weak amplitude of the initial local P wave motion, which may not be observable in the teleseismic records, it is unclear exactly what feature in the near-field signals corresponds to the teleseismic first-motions (the teleseismic waves also have weak initial motions in the first few seconds). It seems likely that the USGS location has substantial uncertainty due to both the emergent onset of the P wave radiation during the first few seconds of this event and due to possible biases by slab heterogeneity for paths to North American and European stations. We will use the locally determined hypocenter in the finite-fault modeling as it is well-constrained and compatible with the near-field ground deformations.

5.3.2 Fault parameterization

For the finite-fault inversion, the fault plane is parameterized with 17 and 15 subfaults along strike (307°) and dip, respectively, with 7.5-km spacing (Figure 5.3a). The total fault model area is 128 x 113 km^2. The 2D fault geometry is the same as that

used in the hypocenter relocation [*Christeson et al.*, 1999], with the ocean bathymetry removed and the offshore subfault depth in the flat 1D model taken as the effective prism thickness with the depth-varying dip for each subfault preserved to correspond to the dip of the actual megathrust (Figure 5.3c). We adopt a multi-time window inversion [*Hartzell and Heaton*, 1983], in which the source time function of each subfault is parameterized with 8 symmetric triangles with 2 s rise times and 2 s shifts, which allow up to a 18 s long source time function for each subfault. We use two components of the slip-vector to parameterize a rake-varying slip on each subfault and apply a non-negative least square inversion [*Lawson and Hanson*, 1995], in which the rake of each subfault is allowed to vary between 45° and 135°. We apply a Laplacian regularization [*Hartzell and Heaton*, 1983], which constrains the second order gradient for each parameter to be zero.

5.3.3 High-rate GPS signals

We obtained 3 component ground motion solutions for 9 high-rate (5 sps) GPS stations, which are maintained by the University of South Florida, and OVSICORI-UNA and distributed by UNAVCO (Figure 5.3a). The high-rate positions were processed using single station bias fixing [*Bertiger et al.,* 2010] and point-positioning [*Zumberge et al*., 1997] with JPL's GIPSY-OASIS software. For these rapid deformations, the station position is estimated as a stochastic parameter, and we use high-rate (30-s) satellite clock and orbit files provided by JPL [*Desai et al.,* 2011]. The tropospheric parameters are fixed to the values estimated from a prior processing run where the positions are held fixed. The estimated standard deviation

for these GPS signals is ~1.6 cm. These random errors are only a few percent of the characteristic peak displacements (~60 cm) for the 2012 Nicoya, Costa Rica event, which is small relative to uncertainties related to model parameters for our inversions. Separate processing of the data using GIPSY and GAMIT algorithms gives only a few percent differences in time series.

To model the near-field ground displacements recorded by hr-GPS, Green functions for the full dynamic and static elastic deformation field must be used. For modeling hr-GPS data for the 2011 Tohoku earthquake, we used Green functions calculated by summing all normal modes up to 80 mHz for the PREM velocity structure. Those Green functions are reliable for long period (> 20 s) signals and epicentral distances larger than 100 km [*Yue and Lay*, 2011; 2013]. However, for the Nicoya, Costa Rica event we have observations at epicentral distances less than 50 km from many of the subfaults with stable signals down to periods of a few seconds. To exploit the short-period information for very near-field displacements, we applied a frequency-wavenumber (F-K) integration method including all near-field terms (Computer Programs in Seismology, Robert Herrmann). The F-K method accounts for both dynamic and static near-field ground displacements, and its static displacement predictions agree well with analytical results, such as the half-space Okada model [*Okada*, 1992]. The same 1-D velocity model used in the hypocenter relocation is used in the F-K integration. The model parameters are listed in supplementary materials.

We calculated a dense Green function database for epicentral distances of 0-500

km and source depths of 0-50 km with 1 km increment for distance and depth. We use the nearest Green functions for each source grid node for each station, incurring minor errors (<0.5 km) in propagation distance, which are insignificant compared to the model grid spacing of 6 km. In our inversion for all datasets, the Green functions of each node are convolved with the subfault source time functions, and both Green functions and data are low-pass filtered at a corner frequency of 0.2 Hz, to eliminate any short-period multi-pathing artifacts in the data processing and any short-period propagation effects not accounted for by the 1-D velocity structure. The Green functions and hr-GPS data are down-sampled to 1 sps after low-pass filtering. Each trace has an 80-s long time window, starting at the origin time of the relocated hypocenter.

5.3.4 Low-rate GPS signals

Two GPS stations on Nicoya Peninsula, HUA2 and LAFE (Figure 5.3), record low-rate data only (1 sample per 15 s). These two stations are located above the down-dip edge of the mega-thrust, where there are no hr-GPS stations. Although dynamic rupture process information is not provided by the lr-GPS records, the co-seismic static displacement are useful, and help to constrain the slip in the southeastern region of the fault plane. The values may be affected somewhat by any afterslip occurring during the time window of the solutions. We model these static offsets using the same Green function database as used in the hr-GPS inversion, by considering only the static off-set after the time-varying motions have passed. For a joint inversion, the static displacements only contribute to the accumulated seismic

moment and its spatial distribution, with time-varying rupture expansion information controlled by the dynamic signals of hr-GPS and seismic recordings.

5.3.5 Strong ground motion records

The 2012 Nicoya, Costa Rica event was recorded by ~40 accelerometers across Costa Rica, out of which 10 were located within 100 km from the hypocenter (Figure 5.3a). These strong ground motion sensors have a flat instrument response to ground acceleration from 0.1 Hz to 40 Hz, with a sample rate of 200 sps. The lower frequency response of the strong motion sensors is not well-resolved. To minimize accumulated scattering effects over long propagation distances, we only used the stations within 100-km epicentral distance for inversion. To model the strong ground motion data, we use the same Green function dataset as used for modeling the hr-GPS data. The 1-D model is not expected to be valid for periods shorter than a few seconds, so we utilize only the low frequency portion of the acceleration recordings. Double integration of the data to ground displacement was not very stable, so we use integrations to ground velocity in the inversion. Three component ground accelerations from the 10 stations were demeaned, detrended, tapered, and integrated to ground velocity. The Green functions were differentiated to ground velocities. A bandpass filter with corner frequencies of 0.1 to 0.3 Hz was applied to limit the signals to the range of validity of the 1-D velocity model and the data. All strong motion records were cut with a 80 s long time window, starting at the origin time of the relocated hypocenter.

5.3.6 Teleseismic records

To ensure compatibility of the near-field source model and teleseismic observations we include high quality P-wave observations in the joint inversion for a finite-fault model. The teleseismic P-wave dataset is comprised of 33 broadband ground displacements from stations of the Federation of Digital Seismic Networks (FDSN), accessed through the Incorporated Research Institutions for Seismology (IRIS) data center. The data were selected from hundreds of available FDSN seismograms to have good azimuthal coverage (Figure 5.3b) and high signal-to-noise ratios, for epicentral distances from 40° to 90°. Instrument responses were removed to reconstitute ground displacement with a bandpass filter with corner frequencies of 0.005 to 0.9 Hz. A 90-s-long time window was extracted from the raw data, starting 10 s prior to the clearest first arrival of the P waves. Unlike the near-field data, which use absolute time, the arrival times of teleseismic waves are influenced by remote path structures, and in our inversion the P wave initial motions were aligned manually. The teleseismic P waves have emergent initial arrivals, consistent with what we observed in the near-field data. The ambiguous initial arrivals raise some uncertainty of how to align the teleseismic dataset with the locate dataset that uses absolute time. Considering it likely that the very weak initial P waves from the hypocenter seen in the near-field data are missed from the teleseismic P wave onsets, we assume that the teleseismic initial motion is actually associated with the strong subevent ~3 s after the hypocentral time. To align with the absolute time of the local data, the aligned teleseismic P wave records were shifted by 3 s. Such a shifted alignment is suggested by inversion results when the teleseismic data are given very small weight and the

inversion is mainly controlled by the local hr-GPS data. Those inversions produce uniform delays in the teleseismic data fitting when the teleseismic dataset is aligned with the rupture initial. Inversions with a 3 s alignment shift match the early portions of both local and teleseismic data. The teleseismic Green functions are generated with a reflectivity method which accounts for interaction in 1-D layered structures on both the source and receiver sides [*Kikuchi et al.*, 1993]. The local 1-D layered model is used for the source side and a typical continental model is used for the receiver side. The same bandpass filter used for the data is applied to the Green functions.

5.3.7 Weighting between datasets

Joint inversions always present challenges in relative weighting between different datasets. In our joint inversion, we are combining near-field displacement field, velocity field and teleseismic displacement field in one joint inversion, for which the optimal relative weighting is hard to determine quantitatively. Our choice of weighting between datasets comes from evaluation of attributes of the different datasets. In our joint inversion, the most reliable information comes from the hr-GPS observations, which provides stable ground displacement information that covers a wide frequency band. Teleseismic P and SH data have limited spatial resolution due to high apparent velocities, and are down-weighted in the joint inversion. Regional strong ground motion data suffer from unknown receiver structure, in which the sediment effect can be significant. Also, we invert ground velocities, which involves error introduced by data integration and Green's function differentiation. The band-pass spanned by the strong ground motion data is also limited at low frequency,

so the weighting given to the strong ground motions is the lowest. Our preferred weighting between hr-GPS lr-GPS / teleseismic / strong ground motion data are 1/0.2/0.1 after normalization by the mean data value and sample points. We explored ranges of relative weights finding stable results for moderate deviations about these preferred choices.

5.4. Results and Discussion

5.4.1 Rupture velocity

In linear finite-fault model inversions, rupture velocity plays an important role in the kinematic expansion and accumulation of slip. Teleseismic P wave data have limited resolution of rupture velocity and it is often necessary to draw upon constraints from other methods, such as back-projections, and to allow relatively long subfault rupture durations to avoid imposing a tight expanding rupture annulus [*Lay et al.*, 2010]. However, well-distributed near-field data, particularly hr-GPS data, exhibit less sensitivity to the initial rupture velocity because they have intrinsic sensitivity to the spatial slip distribution [*Yue and Lay*, 2011; 2013]. With the constraints from both static displacement and dynamic waveform fitting, inversions with hr-GPS tend to yield stable rupture models as long as the input rupture velocity is high enough to capture the real rupture front and the source time duration is long enough to cover the whole rupture duration. Although the basic rupture model from hr-GPS inversion will not be greatly impacted by the input rupture velocity, the data-misfit residual will be partially influenced by the rupture velocity. If the rupture velocity is less than the real rupture velocity, the initial motion in the data may not be well modeled although the

static displacements may be well fit; if the rupture velocity is at least as high as the real rupture velocity, we do not expect significant waveform misfit residual for increasing rupture velocity. We can exploit the trade-off curve of rupture velocity and waveform misfit residual to define an appropriate model rupture velocity.

Trade-off curves of rupture velocity versus normalized waveform mismatch residual, for joint inversions with constant rupture velocity ranging from 2.0 km/s to 6.0 km/s, are shown in Figure 5.4. A rupture velocity of 3.0 km/s gives a turning point in the trade-off curve for hr-GPS data, suggesting that is a sufficiently high rupture velocity to account for the data onsets. In our joint inversions, the rupture space-time pattern is mainly controlled by the hr-GPS data because they provide the best resolution with the maximum weighting, the teleseismic data and strong ground motion data contribute to details of the slip-expansion, constrained to the model space compatible with the hr-GPS signals. A rupture velocity of 3.0 km/s also gives a minimum residual mismatch for the static lr-GPS data. Static GPS data have no resolution of rupture propagation; however, in the joint inversion the alignment for the hr-GPS data allows all of the static signals to be matched simultaneously. The teleseismic P wave data show a broad residual minimum between rupture velocities of 3.5 km/s to 4.0 km/s, with only a small increase in misfit for a rupture velocity of 3.0 km/s. For the teleseismic dataset, the maximum misfit residual at rupture velocity of 2.0 km/s is no more than two times the minimum residual at rupture velocity of 6.0 km/s, indicating the limited teleseismic resolution of rupture velocity. The strong ground motion data have some resolution of rupture locations and rupture velocity,

but higher rupture velocity is intrinsically preferred by the more distant short-period strong ground motion data because it allows for a larger rupture front and more associated inversion parameters to try to fit the data complexity. The trade-off curve for strong ground motion data suggests a preferred rupture velocity between 3.5 km/s and 4.0 km/s, which is similar to that for the teleseismic dataset. Overall, the behavior for the hr-GPS data leads us to prefer models using a rupture velocity of 3.0 km/s, but we include relatively long subfault source time functions to ensure that the final model is not excessively controlled by the imposed rupture kinematics.

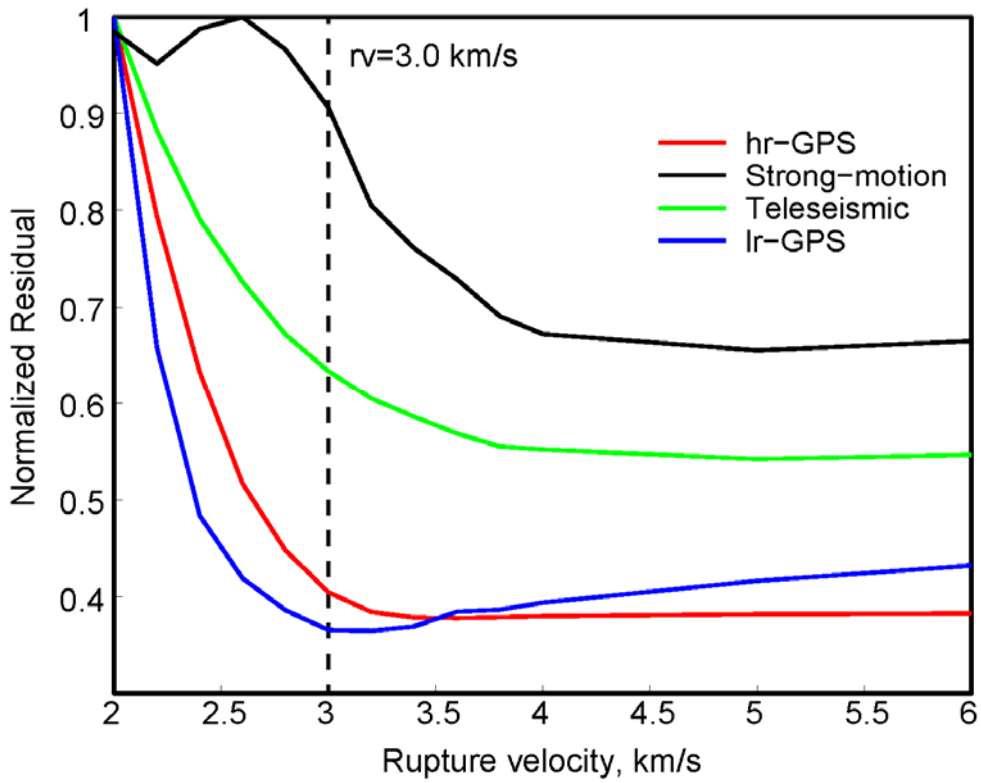

Figure 5.4. Trade-off curves indicating normalized inversion residual versus rupture velocity for each dataset. Red, black, green and blue curves indicate hr-GPS, strong ground motion, lr-GPS and teleseismic datasets, respectively. Joint inversions were made using constant rupture velocities varying from 2 km/s to 6 km/s. A rupture velocity of 3.0 km/s was used for the final preferred model.

5.4.2 Preferred rupture model

The slip distribution, subfault source time functions, and space-time rupture evolution of our preferred model are shown in Figure 5.5. The overall rupture propagation direction is from up-dip to down-dip, which is consistent with the relative locations between the relocated hypocenter and the 3-s later subevent. The main large-slip patch locates beneath the peninsula, spanning ~30 km along dip and ~70 km along strike. The average slip of the well-resolved primary slip region (slip > 1m) is ~2 m, indicating an average static stress drop of ~3 MPa. The total seismic moment of our preferred model is 3.5×10^{20} Nm, which gives $M_w = 7.6$. The peak slip amplitude in the model is ~4.4 m, located down-dip from the hypocenter. The centroid depth of the slip distribution is ~21 km, which is shallower than the GCMT centroid (30 km) and W-phase centroid estimates (30 to 40km). The centroid location is at 9.91°N and 85.54°W, which is ~14 km to the north of the GCMT centroid location and ~ 44 km to the west of the W-phase centroid location. The dominant slip direction is at 90° rake, with minor right-lateral component, which is consistent with the 118° rake of the GCMT solution, as well as the slightly oblique subduction direction.

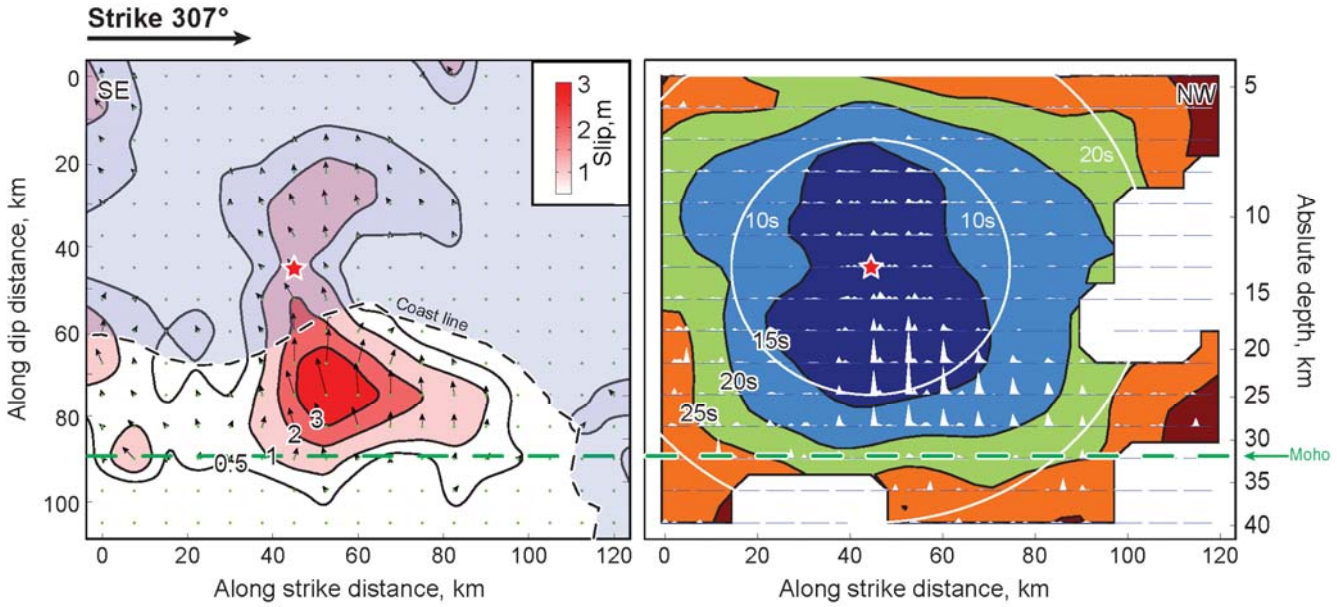

Fig. 5

Figure 5.5. a) Rupture-plane view of the slip distribution for our preferred model with a rupture velocity of 3.0 km/s. The absolute depths of the nodes for the varying-dip model are shown on the right. The maximum slip is ~4.4 m located near the center of the main slip patch at around 25 km depth. The total seismic moment is 3.51 x 10^{20} Nm, which gives an M =7.63 earthquake. The hypocenter on the fault plane is marked with a red-filled star. Only nodes with a slip larger than 0.5 m are contoured and the slip directions at each node are indicated with black arrows. The coastline is marked by the dashed curve with the offshore region shaded blue. The Moho interface at ~32 km depth is projected onto the fault plane and indicated with a dashed green line. **b**) Source time functions of each subfault node are shown as white polygons. The centroid time of each node is contoured as the background colored map. Constant rupture velocity expansion time counters are marked as white concentric circles.

There is a secondary slip patch located up-dip off-shore and to the north-west of the hypocenter, which is a stable feature of many inversions we conducted. However, the moment of this off-shore rupture patch is approximately 13% of the total moment, and the waveform contributions from this patch are too weak to be confidently isolated in the various data signals. The seismic moment of the up-dip slip patch is ~4.5 $\times 10^{19}$ Nm, corresponding to an M_w 7.0 earthquake. Because of its offshore

location, it is difficult to constrain the precise moment (and existence) of this secondary slip-patch and the moment and location of such a patch varies with different selection of inversion parameters, but there is some increase in waveform mismatch if we truncate the offshore grid, so it appears to be a minor part of the coseismic rupture.

For the main slip patch beneath the Nicoya peninsula, the source time duration is ~10 s for most subfaults, with a sharp initial energy release and slow decay. Such a moment rate shape is consistent with a crack model. Secondary pulses or multiple peaks are present on a few subfaults, which may present repeated slip events or effects of our regularization. For FFM inversion such details are not usually very stable. Given the uncertainty in the Green's functions we do not try to interpret all of the subfault complexity, noting that the basic pattern is quite uniform and simple.

The rupture evolution is most clearly depicted with snap-shots of the space-time history of slip velocity (Figure 5.6). The rupture initiated near the hypocenter, and expanded up-dip and down-dip slowly within 5 s; the main slip patch started to rupture at 7 s, and continuously propagated down-dip. At 15 s, the main rupture front reached its down-dip limit and began to extend bilaterally along strike, with the north-west propagation dominating. Around 15-17 s, the rupture reached its peak moment release, which covers a length of ~60 km along strike. The slip of the main rupture area ended at ~21 s. The rupture of the isolated up-dip slip patch starts at 11 s and lasts to 19 s, giving a subsource duration of 8 s. Finite fault model details are provided in the supplementary materials. .

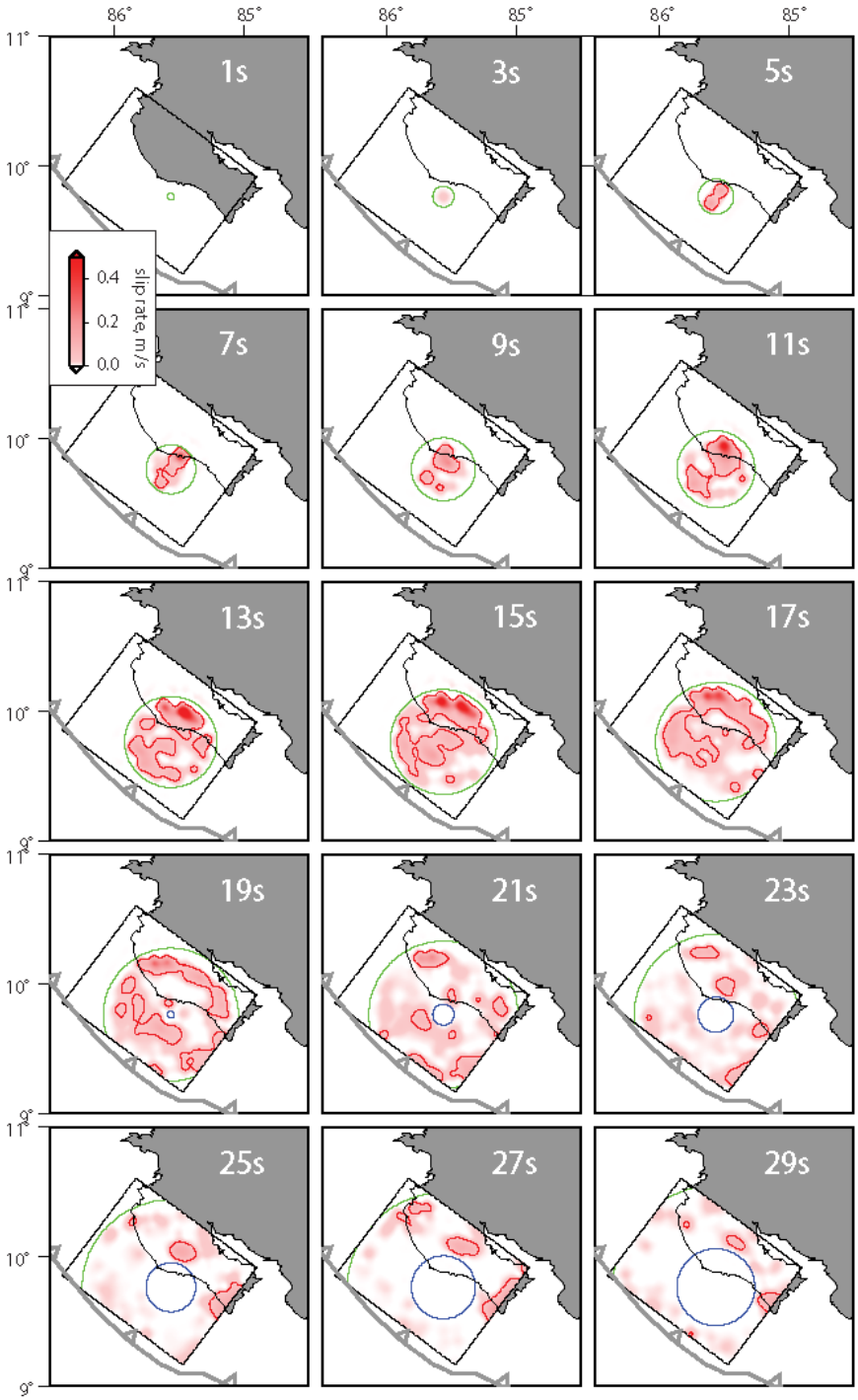

Fig.6

Figure 5.6. Snapshots of the space-time history of slip velocity during the 2012 Nicoya, Costa Rica earthquake for our preferred rupture model are shown in 2 s intervals. Particle motion velocity is shown with a red scale. The kinematic expanding rupture annulus is indicated by the green (rupture front) and blue (healing front) circles.

5.4.3 Data fits

The waveform and static displacement fits of all datasets are shown in Figure 5.7a-e. Generally for finite-fault inversions, the quality of waveform fits depends on the fault parameterization, Green's function adequacy and inversion regularization. It always presents a challenge to optimize the model parameters and waveform mismatch residuals. This is particularly true for waveform fits in joint inversions because how the residuals distribute across different datasets strongly depends on the relative weighting used. Because the relative weighting between GPS/teleseismic/strong ground motion data is 1/0.2/0.1, the inversion tends to fit the data in order from highly weighted to lowly weighted datasets. Thus, the GPS data are best fit in our joint inversion, and the strong ground motion data are least fit.

Figure 5.7 demonstrates that both static displacements and dynamic waves are well fit for the hr-GPS dataset (Figure 5.7a,d,e) and lr-GPS data (Figure 5.7d,e). The teleseismic dataset are satisfactorily modeled including the first peak, indicating acceptable time coordination with the local absolute time signals. The strong ground motion data are generally matched in phase, but the amplitude of larger arrivals at several stations are underestimated. Stations with significantly under-predicted waveforms, such as GTGA and GCNS, are at locations which are described to be "very soft" in their logging information, consequently sediment amplification effects may be significant. Overall, this joint inversion achieved good waveform fits to the various datasets, which suggests that the inversion model is a reasonable first-order representation of the broadband source. As with all such finite-fault models, it is

challenging to prescribe uncertainties, and as we proceed to compare the model with other observations we will emphasize those aspects of the model that are most stable for a wide range of permutations of data sets, relative weights, rupture velocity, and other model parameters.

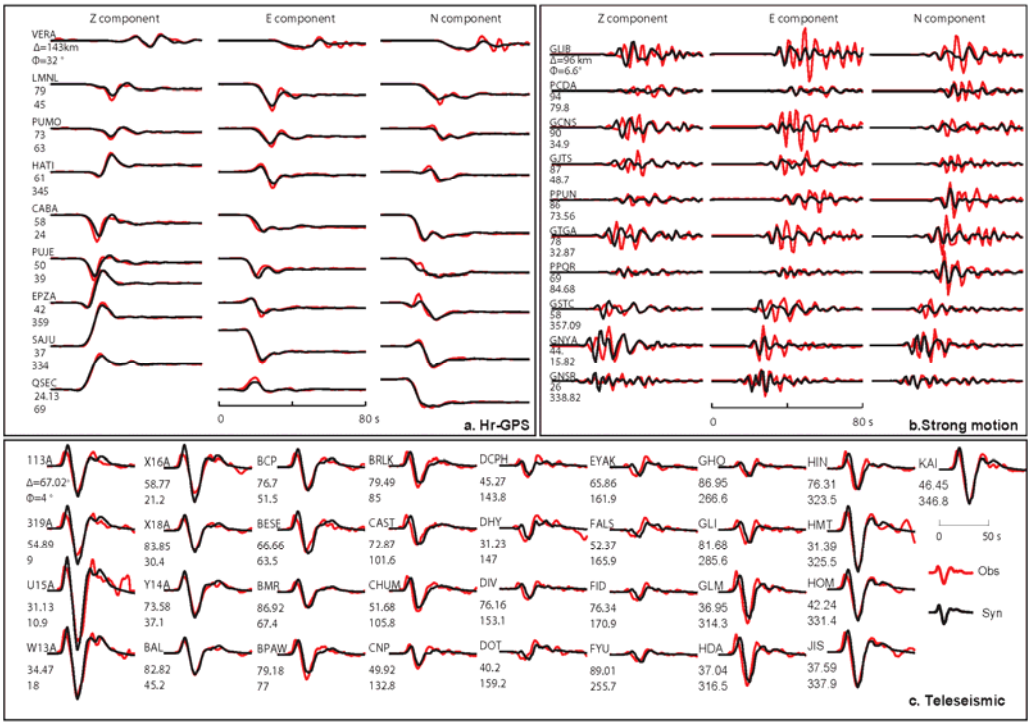

Fig 7 a-c

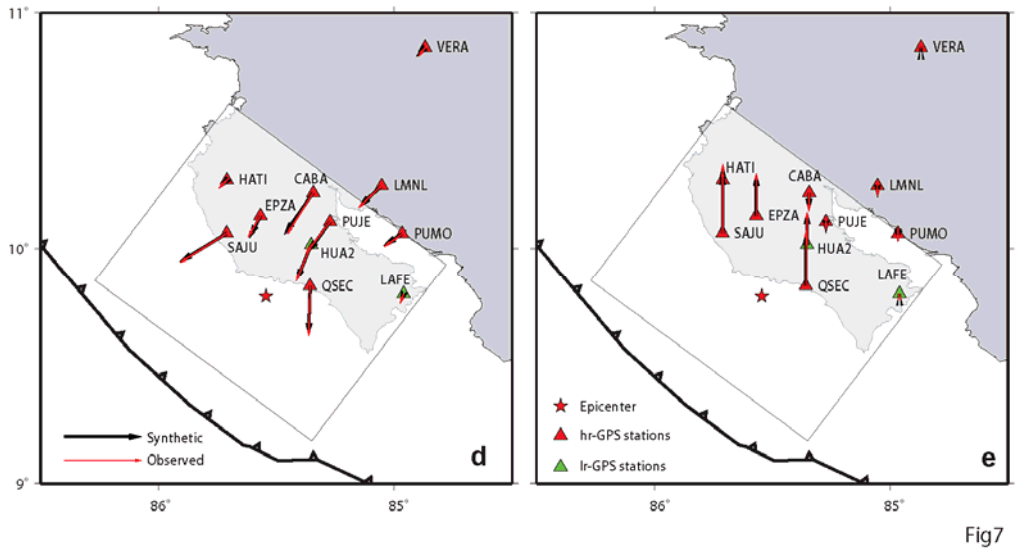

Figure 5.7. Observed (red) and modeled (black) waveforms for **a**) hr-GPS, **b**) strong ground motion and **c**) teleseismic P-wave data for the preferred joint inversion. Three-component hr-GPS and strong ground motion records and vertical teleseismic P wave records are used in the inversion. Hr-GPS and strong ground motion are ordered by epicentral distance; teleseismic P wave data are ordered by azimuth. Station names, epicentral distances and azimuths are shown by each trace. Observed and modeled co-seismic static displacements for 9, hr-GPS stations and 2 lr-GPS stations are plotted with red and black arrows, respectively for **d**) horizontal motions, and **e**) vertical motions. Stations locations of hr-GPS and lr-GPS stations are plotted with red- and green-filled triangles, respectively.

5.4.4 Comparison with other megathrust deformation observations

Figure 5.8 compares our preferred slip model for the 2012 Nicoya, Costa Rica event with other characterizations of megathrust deformation around the Nicoya Peninsula. The inter-seismic locking pattern inverted by *Feng et al.* [2012] using the daily solution of continuous and campaign GPS data with an averaged time span of ~8 years, has an extended pattern below both land and ocean areas. In their results, two locked patches are resolved, with one located up-dip off-shore and the other located

inland (black outlines in Figure 5.8), separated by ~30 km, and embedded within a larger region of at least 80% locking. The down-dip slip deficit patch is consistent with the co-seismic rupture area having slip amplitude larger than 2 m in the 2012 event. The average slip amount in this area is ~ 3 m. For an average plate convergence rate of 78 mm/yr [*Protti et al. 2012*] and a fore-arc motion rate of 10 mm/yr [*LaFemina et al.*, 2009], the projected slip accumulation rate in the trench-normal direction is ~77 mm/yr. Thus ~3 m average slip released in this region could have accumulated over ~40 yr, which is compatible, given the uncertainties, with the ~60 years since the 1950 rupture under the Nicoya Peninsula.

If the slip distribution were known for the 1950 and 1900 events, then a slip versus time interval analysis could provide insight into the inter-seismic cycle beneath the Nicoya peninsula [*Shimazaki and Nakata*, 1980], however, there is no knowledge of the slip distributions for the 1950 and 1900 events, apart from their estimated magnitude and general location (Fig. 1). Any estimation of slip amount for these two older events requires assumptions about stress drop or rupture scale, as well as location of the slip.

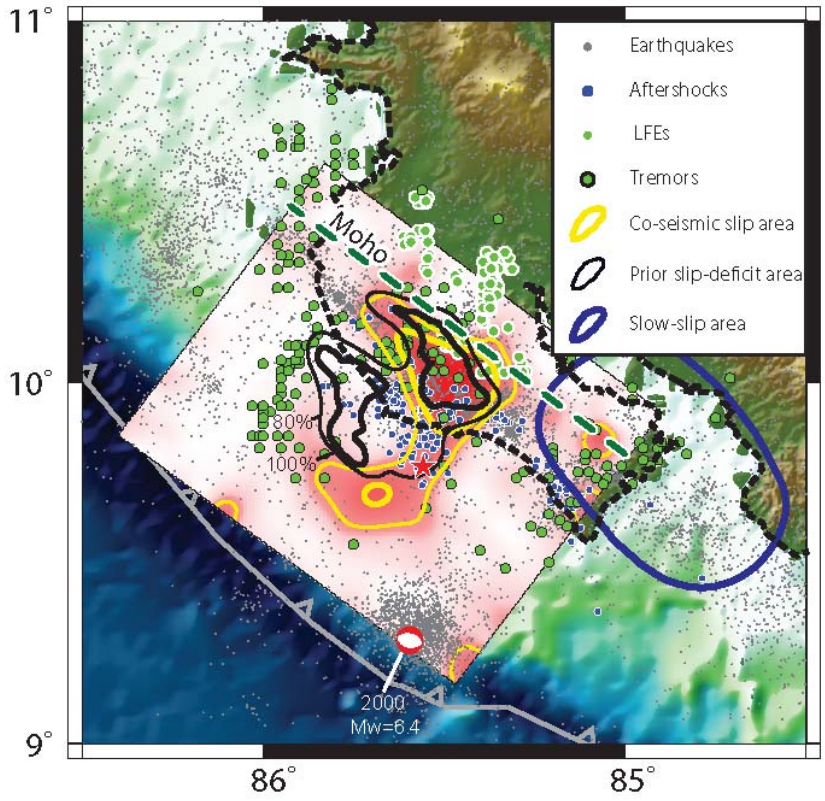

Figure 5.8. Summary map of the 2012 Nicoya, Costa Rica rupture model and surrounding fault zone observations. The co-seismic slip distribution for our preferred rupture model is mapped with red-white color scale, with regions of coseismic slip > 1.2 m outlined in thin yellow and slip > 2.0 m outlined with thick yellow. The epicenter is shown with a red star. The inter-seismic locked region is outlined in thick/thin black counters for > 80% and 100% slip-deficit [*Feng et al.,* 2012], respectively. The slip area (slip > 70 mm) of the 2007 slow-slip event [*Outerbridge et al,* 2010] is outlined in blue. Well located background seismicity is plotted with grey-filled circles. About 10,000 of these events are from 1999-2001 [*Ghosh et al,* 2008], ~1500 events from 2007 and 4800 events from 2009. Preliminary aftershocks within a month of the 2012 main shock are plotted with blue-filled circles. Low frequency earthquakes (LFE) identified within tremor on May 17th, 2007 [*Brown et al.,* 2009] are plotted with green-filled, white-bordered circles. Tremor events from May 2007, August 2008 and April 2009 are plotted with green-filled, black-bordered circles [*Walter et al.,* 2011]. The intersection between the fault plane and the overriding plate Moho interface are project in the map as a green dashed line.

The offshore locked patch does not co-locate with the offshore slip patch in the rupture model. Given that the co-seismic slip and inter-seismic slip-deficit inversions

both have limited off-shore resolution, the regions could coincide, but the amount of slip is certainly less than that of the patch below land. If the inter-seismic slip deficit estimation is reliable in *Feng et al.* [2012], there should still be substantial strain accumulated off-shore. If we assume the 1950 M = 7.8 event ruptured both the up-dip and down-dip locked patches rather than only the down-dip one, a comparable amount of slip accumulation to that released in 2012 may exist offshore and a similar size earthquake may occur in the future.

Aftershock locations [*Newman et al.,* 2013] within 5 km from the megathrust are also shown in Figure 5.8, with most surrounding the main down-dip rupture patch and only a few locating within the region with 2 m or larger slip. Many aftershocks are found in the region with >80% locking, and low levels of coseismic slip. These aftershock locations will likely be improved by manual adjustment of P and S wave arrival times and relocation in a 3-D velocity model, but it is notable that the offshore high slip-deficit region has very few aftershocks in it. If it is correctly placed, it is plausible that this patch remains unbroken and may fail in the future in an earthquake comparable in size to the 2012 event.

Non-volcanic tremor events around Nicoya have been detected offshore as well as down-dip on the megathrust [*Walter et al.*, 2011]. Tremor location estimates are distributed on both sides along strike and down-dip of the co-seismic slip patch (Figure 5.8). A few tremor events overlap the main co-seismic slip patch, which gives some possibility that tremor may co-locate with the co-seismic rupture area or be on parallel faults. It is important to recognize that *Walter et al*. [2011] used an envelope

cross-correlation method to locate the tremor events, which may have significant location uncertainties, especially for off-shore events. In general, the tremor event distribution is adjacent to the co-seismic slip area and the inter-seismic locked areas. Tremor relocations using more advanced methods are being pursued to enable detailed comparison with the co-seismic slip distribution. It is also interesting that the tremor events co-locate with the areas that show relatively high *b* values ($b \sim 2.0$) in back-ground seismicity both northwest and southeast of the Nicoya Peninsula interpreted as relatively weak seismic coupling [*Ghosh et al.,* 2008]. The main co-seismic area ruptured during the 2012 Nicoya, Costa Rica event has an ordinary *b*-value ($b \sim 1.0$) in background seismicity. In 2007 a slow-slip event [*Outbridge et al.,* 2010] occurred southeast of the main slip patch in a region with seismic tremor that is relatively deep on the megathrust. This region may be down-dip of the 1990 earthquake rupture zone (Figure 5.1). There were few aftershocks in this region and almost no coseismic slip is imaged there.

Low frequency earthquakes (LFEs) accompanying the 2007 slow slip event were located precisely by a template matching technique [*Brown et al*., 2009] and locate down-dip of the 2012 co-seismic slip region. The down-dip limit of large co-seismic slip is near depths of 30 to 35 km, with a large slip gradient of 0.25 m/km, in contrast with the up-dip slip gradient of ~0.1 m/km (Figure 5.5a). The large slip gradient may be related to an abrupt material property change near 30-35 km depth. The Moho boundary in the overriding plate intersects with the subducting plate at a depth of ~32 km [*Deshon et al*., 2005], which may provide such a material property

change near the slip zone margin. It has been suggested that the mantle wedge beneath Costa Rica is 15-25% serpentinized [*DeShon and Schwartz,* 2004; *DeShon et al*., 2005] as a result of fluid release from the subducting plate. A transition from mafic granulite lower-crust to serpentinized mantle will lead to frictional transition from un-stable sliding to stable-sliding, with low-frequency earthquakes possibly indicating such a transition zone. Our rupture model suggests that the slip-deficit patch and coseismic slip zone only extend to the bottom of the upper plate lower crust, with the deeper megathrust strain releasing as ductile deformation with low frequency earthquakes.

Figure 5.8 reveals a complex intermingling of different megathrust deformation processes rather than a simple depth-varying segmentation between stable sliding and unstable sliding domains. The correspondence between the region of large slip-deficit and the coseismic slip in the 2012 event is particularly striking. Such a pattern is not unexpected, but this may be the best-resolved correlation for any megathrust due to the fortuitous land distribution provided by the Nicoya Peninsula. The apparent lack of large slip in the offshore locked patch raises the possibility of a comparable earthquake to rupture that region in the future. It is interesting that both the slip-deficit and coseismic slip regions are surrounded by lateral and up- and down-dip transitions to regions of slow slip, tremor and/or low frequency earthquakes. The lateral transition from strain accumulation/coseismic rupture in the northwest to slow slip and tremor in the southeast coincides with the change in underthrust Cocos plate crustal origin and the along-strike gradients in thermal structure of the subducting

plate. The moderate scale length of the locked patches and coseismic slip zone may be related to absence of much larger earthquakes in this seismically active region, as appears to be the case along much of the Middle American trench [e.g., *Ye et al*., 2013]. The existence of plate boundary parallel deformation of the fore-arc, which increases toward the north along Nicaragua and El Salvador [e.g., *LaFemina et al*., 2009] may also play a role in constraining the lateral continuity of strongly locked regions on this megathrust.

The observation of shallow tremor offshore of northwestern Nicoya Peninsula is a distinctive attribute of this megathrust. This appears to be outside of the large slip-deficit regions and coseismic slip area. The very shallow megathrust appears to have ruptured to the northwest in the 1992 Nicaragua tsunami earthquake, and the possibility of an up-dip rupture extending to the trench offshore of the Nicoya Peninsula should be considered. The 2012 coseismic slip did not appear to drive much slip offshore, other than the one patch discussed above, but it is possible that the unruptured slip-deficit region may have prevented rupture from extending into the shallow part of the wedge. The 2011 Tohoku earthquake demonstrated that with a large enough down-dip rupture of a locked patch, it is possible to drive slip all the way to the trench, but the frequent failure of a modest size locked region under the Nicoya Peninsula may reduce the likelihood of such a compound rupture in this region. The 2010 Mentawai tsunami earthquake ruptured up-dip of larger megathrust events in 2007, so it is difficult to rule out occurrence of a rare tsunami earthquake in the shallow region of the Nicoya megathrust.

The regional occurrence of low-frequency earthquakes, seismic tremor and slow-slip events, adjacent to the area of large co-seismic slip confirms prior studies indicating that the Costa Rica megathrust has very diverse frictional properties [e.g., *Schwartz and Rokosky*, 2007; *Walter et al.,* 2011], which may be related to variations in sediment composition, temperature distribution and fluid content. In the subduction zone beneath the Nicoya Peninsula, each region of the megathrust appears to have a preferred strain release mechanism, and further work is needed to constrain the total deformation budget of each process to evaluate how the overall plate convergence is being accommodated.

5.5. Conclusion

Using extensive near-field observations, comprising hr-GPS, lr-GPS and strong ground motion data, together with teleseismic P wave observations in a joint inversion we obtained a detailed and stable space-time slip model for the 5 September 2012 Nicoya, Costa Rica earthquake. The relocated hypocenter location is found to be 9.76°N, 85.56°W at depth of 13.1 km below sea level and ~ 10 km off the coast. The initial time is at 14:42:04.4 UTC, 2.6 s earlier than the USGS origin time for a source depth of 35 km. A strong subevent is located at 9.82°N, 85.47°W, at a depth of 17.2 km on the megathrust, with an initial time of 14:42:07.8, and may correspond to the detectable first-arrival teleseismically. The co-seismic rupture extends from the hypocenter down-dip with a total source duration of ~21 s, at an average rupture velocity of 3.0 km/s. The area of large slip spans ~30 km along dip and ~70 km along strike, with maximum slip of 4.4 m. The total seismic moment is 3.5×10^{20} Nm, which

gives M_w = 7.6.

The area of large co-seismic slip correlates well with a previously determined on shore region of 100% inter-seismic slip deficit or locking, with full release of strain accumulation over ~40 yrs. A small region off-shore appears to have coseismically ruptured with the equivalent of an M_w 7.0 earthquake. This slip locates adjacent to the up-dip 100% locked patch, and may have only released a small amount of the accumulated inter-seismic strain. This up-dip region appears to have the potential to rupture in the future with a magnitude comparable to the 2012 Nicoya, Costa Rica event. The mainshock slip patch is surrounded by aftershock activity, non-volcanic tremor events, low-frequency earthquakes and slow-slip events. This confirms pervious studies suggesting that the Costa Rica megathrust has very diverse frictional properties that are not simply depth-dependent, but also vary along strike. This may be related to variations in sediment composition, temperature distribution and fluid content. Each region of the megathrust appears to have a preferred strain release mechanism.

5.6 Acknowledgements

We made extensive use of the frequency-wavenumber integration code in the seismic wave simulation software made openly available by Robert Herrmann (http://www.eas.slu.edu/eqc/eqccps.html). We thank Víctor González for installing and operating the Nicoya seismic and CGPS networks, and Aaron Moya from LIS-UCR for providing the strong motion data. We thank two anonymous reviewers and the Associate Editor for their helpful reviews. This work made use of GMT and SAC software. The IRIS

DMS data center was used to access the seismic data from Global Seismic Network and Federation of Digital Seismic Network stations. This work was supported by NSF grants EAR-1245717. (T. L.) and OCE-0841061 and EAR-0842338 (S. Y. S). We thank Jake Walter for providing the aftershock catalog.

5.7 References

Allen, T. I., K. D. Marano, P. S. Earle, and D. J. Wald (2009), PAGER-CAT: A composite earthquake catalog for calibrating global fatality models, *Seism. Res. Lett.*, *80*, 57-62, doi:10.1785/gssrl.80.1.57.

Ammon, C. J., T. Lay, H. Kanamori, and M. Cleveland (2011). A rupture model of the 2011 off the Pacific coast of Tohoku Earthquake, *Earth Planets Space, 63* 693-696, doi:10.5047/eps.2011.05.015.

Audet, P. and Schwartz, S. Y. (2013), Structural and hydrologic controls of subduction zone seismogenic behavior, *Nature Geoscience*, in press.

Avants, M., S. Schwartz, A. Newman, and H. DeShon (2001), Large underthrusting earthquakes beneath the Nicoya Peninsula, *Eos Trans. AGU, 82*(46), Fall Meet. Suppl., Abstract T52E-07.

Barckhausen, U., C. R. Ranero, R. von Huene, S. C. Cande, and H. A. Roeser (2001), Revised tectonic boundaries in the Cocos Plate off Costa Rica: Implications for the segmentation of the convergent margin and for plate tectonic models, *J. Geophys. Res.*, 106(B9), 19,207–19,220, doi:10.1029/2001JB000238.

Bertiger, W., S. Desai, B. Haines, N. Harvey, A. Moore, S. Owen, and J. Weiss (2010), Single receiver phase ambiguity resolution with GPS data, *J Geod*, *84*(5), 327-337.

Brown, J. R., G. C. Beroza, S. Ide, K. Ohta, D. R. Shelly, S. Y. Schwartz, W. Rabbel, M. Thorwart, and H. Kao (2009), Deep low-frequency earthquakes in tremor localize to the plate interface in multiple subduction zones, *Geophys. Res. Lett.*, 36,

L19306, doi:10.1029/2009GL040027.

Christeson, G. L., K. D. McIntosh, T. H. Shipley, E. R. Flueh, and H. Goedde (1999), Structure of the Costa Rica convergent margin, offshore Nicoya Peninsula, *J. Geophys. Res.*, *104*(B11), 25,443–25,468, doi:10.1029/1999JB900251.

DeMets, C., R. G. Gordon, and D. F. Argus (2010), Geologically current plate motions, *Geophys. J. Int.*, *181*, 1 – 80, doi:10.1111/j.1365-246X. 2009.04491.x.

Desai, S. D., W. Bertiger, B. Haines, N. Harvey, C. Sella, A. Sibthorpe, and J. P. Weiss (2011), Results from the reanalysis of global GPS data in the IGS08 reference frame, Abstract G53B-0904 presented at 2011 Fall Meeting, AGU, San Francisco, Calif., 5–9 Dec.

DeShon, H. R., and S. Y. Schwartz (2004), Evidence for serpentinization of the forearc mantle wedge along the Nicoya Peninsula, Costa Rica, *Geophys. Res. Lett., 31*(21), L21611, doi: 10.1029/2004GL021179

DeShon, H. R., S. Y. Schwartz, A. V. Newman, V. González, M. Protti, L. M. Dorman, T. H. Dixon, D. E. Sampson, and E. R. Flueh (2006), Seismogenic zone structure beneath the Nicoya Peninsula, Costa Rica, from three-dimensional local earthquake P- and S-wave tomography, *Geophys. J. Int., 164*(1), 109-124, doi:10.1111/j.1365-246X.2005.02809.x.

Dixon, T. H., Schwartz, S., Protti, M., Gonzalez, V., Newman, A. and Marshall, J. (2013), Detailed data available for recent Costa Rica earthquake, EOS, Trans. Am. Geophys. Union, vol. 94, no. 2, p17-18.

Feng, L., A. V. Newman, M. Protti, V. González, Y. Jiang, and T. H. Dixon (2012), Active deformation near the Nicoya Peninsula, northwestern Costa Rica, between 1996 and 2010: Interseismic megathrust coupling, *J. Geophys. Res., 117*, B06407, doi:10.1029/2012JB009230.

Ghosh, A., A. V. Newman, A. M. Thomas, and G. T. Farmer (2008), Interface locking along the subduction megathrust from b-value mapping near Nicoya Peninsula, Costa Rica. *Geophys. Res. Lett., 35*(1), L01301,doi: 10.1029/2007GL031617

González-Salas, V., and J. M. Protti-Quesada (2005), Afinamiento del potencial sísmico y monitoreo de la brecha sísmica de Nicoya, *no. 147, p. 12-15*.

Harris, R. N., and K. Wang (2002), Thermal models of the Middle America Trench at the Nicoya Peninsula, Costa Rica, *Geophys. Res. Lett., 29*, doi:10.1029/2002GL015406.

Hartzell, S. H., & Heaton, T. H. (1983). Inversion of strong ground motion and teleseismic waveform data for the fault rupture history of the 1979 Imperial Valley, California, earthquake. *Bull. Seism. Soc. Amer.,73*(6A), 1553-1583.

Ihmlé, P. F. (1996). Monte Carlo slip inversion in the frequency domain: Application to the 1992 Nicaragua Slow Earthquake, *Geophys. Res. Lett.,* 23(9): 913-916, doi: 10.1111/j.1365-246X.1996.tb01536.x

Iinuma, T., M. Protti, K. Obana, V. González, R. Van der Laat, T. Kato, S. Miyazaki, Y. Kaneda, and E. Hernández (2004), Inter-plate coupling in the Nicoya Peninsula, Costa Rica, as deduced form a trans-peninsula GPS experiment, *Earth Planet. Sci. Lett.*, 223, 203-212, doi: http://dx.doi.org/10.1016/j.epsl.2004.04.016.

Ji, C., K. M. Larson, Y. Tan, K. W. Hudnut, and K. Choi (2004), Slip history of the 2003 San Simeon earthquake constrained by combining 1-Hz GPS, strong motion, and teleseismic data, *Geophysical research letters*, *31*(17), L17608.

Jiang, Y., S. Wdowinski, T. H. Dixon, M. Hackl, M. Protti, and V. González (2012), Slow slip events in Costa Rica detected by continuous GPS observations, 2002 – 2011, *Geochem., Geophys., Geosys., 13*, Q04006, doi:10.1029/2012GC004058.

Kanamori, H., and M. Kikuchi (1993), The 1992 Nicaragua earthquake: A slow tsunami earthquake associated with subducted sediments, *Nature, 361*, 714 – 716, doi:10.1038/361714a0.

Kikuchi M., H. Kanamori, and K. Satake (1993). Source complexity of the 1988 Armenian earthquake: evidence for a slow after-slip event, *J. Geophys. Res., 98*(B9), 15-797, doi:

Koketsu, K., Yokota, Y., Nishimura, N., Yagi, Y., Miyazaki, S. I., Satake, K., ... & Okada, T. (2011). A unified source model for the 2011 Tohoku earthquake, *Earth Planet. Sci. Lett., 310*(3), 480-487, doi: http://dx.doi.org/10.1016/j.epsl.2011.09.009,

LaFemina, P., T. H. Dixon, R. Govers, E. Norabuena, H. Turner, A. Saballos, et al. (2009), Fore-arc motion and Cocos Ridge collision in Central America, *Geochem. Geophys. Geosys., 10*, Q05S14, doi:10.1029/2008GC002181.

Lawson, C. L., and R. J. Hanson (1995), *Solving least squares problems*, Society for Industrial Mathematics.

Lay, T., C. J. Ammon, A. R. Hutko, and H. Kanamori (2010). Effects of kinematic

constraints on teleseismic finite-source rupture inversions: Great Peruvian earthquakes of 23 June 2001 and 15 August 2007, *Bull. Seism. Soc. Amer., 100,* 969-994, doi:10.1785/0120090274.

Lay, T., C. J. Ammon, H. Kanamori, L. Xue, and M. J. Kim (2011), Possible large near-trench slip during the 2011 M_w 9.0 off the Pacific coast of Tohoku Earthquake, *Earth, Planets and Space*, *63*(7), 687-692.

Lundgren, P., M. Protti, A. Donnellan, M. Heflin, E. Hernandez, and D. Jefferson (1999), Seismic cycle and plate margin deformation in Costa Rica: GPS observations from 1994 to 1997, *Journal of Geophysical Research: Solid Earth*, *104*(B12), 28915-28926.

Miyazaki, S., K. M. Larson, K. Choi, K. Hikima, K. Koketsu, P. Bodin, J. Haase, G. Emore, and A. Yamagiwa (2004), Modeling the rupture process of the 2003 September 25 Tokachi-Oki (Hokkaido) earthquake using 1-Hz GPS data, *Geophys. Res. Lett., 31*, L21603, doi:10.1029/2004GL021457.

Newman, A. V., J. M. Protti, V. M. Gonzalez, T. H. Dixon, S. Y. Schwartz, L. Feng, Z. Peng, J, Marshall, R. Malservisi, S. E. Owen, Success! Detailed Pre-event Analysis Identified the Slip Area and Magnitude of the Sept. 2012 MW 7.6 Nicoya Earthquake, *Abstract at the 2013 AGU Meeting of the Americas, Cancun, Mexico, 14-17 May 2013*

Newman, A.V., S. Y. Schwartz, V. Gonzáles, H. R. DeShon, J. M. Protti, and L. Dorman (2002), Along strike variability in the seismogenic zone below Nicoya Peninsula, Costa Rica, *Geophys. Res. Lett., 29*, doi:10.1029/2002GL015409.

Nishenko, S. P. (1991), Circum-Pacific seismic potential: 1989 – 1999, *Pure Appl. Geophys., 135*(2), 169 – 259, doi:10.1007/BF00880240.

Norabuena, E., T. H. Dixon, S. Schwartz, H. DeShon, A. Newman, M. Protti, M., et al. (2004). Geodetic and seismic constraints on some seismogenic zone processes in Costa Rica, *J. Geophys. Res.,109*(B11), B11403, doi:10.1029/2003JB002931.

Okada, Y. (1992). Internal deformation due to shear and tensile faults in a half-space, *Bull. Seism. Soc. Amer., 82*(2), 1018-1040.

Outerbridge, K. C., T. H. Dixon, S. Y. Schwartz, J. I. Walter, M. Protti, V. González, J. Biggs, M. Thorwart, and W. Rabbel (2010), A tremor and slip event on the Cocos-Caribbean subduction zone as measured by a global positioning system (GPS) and seismic network on the Nicoya Peninsula, Costa Rica, *J. Geophys. Res., 115*, B10408, doi:10.1029/ 2009JB006845.

Pacheco, J. F., & Sykes, L. R. (1992). Seismic moment catalog of large shallow earthquakes, 1900 to 1989, *Bull. Seism. Soc. Amer., 82*(3), 1306-1349.

Protti, M., K. McNally, J. Pacheco, V. González, C. Montero, J. Segura et al. (1995), The March 25, 1990 (M_w = 7.0, M_L = 6.8), earthquake at the entrance of the Nicoya Gulf, Costa Rica: Its prior activity, foreshocks, aftershocks, and triggered seismicity, *J. Geophys. Res., 100*(B10), 20,345 – 20,358, doi:10.1029/94JB03099.

Protti, M., M. F. Güendel, and E. Malavassi (2001), *Evaluación del potencial sísmico de la Península de Nicoya*, 1st ed., 144 pp., Ed. Fund. Univ. Nac., Heredia, Costa Rica.

Protti, M., V. González, J. Freymueller & S. Doelger, (2012), Isla del Coco, on Cocos

Plate, converges with San Andres Island, on the Caribbean Plate, at 78mm/yr. *Rev. Biol. Trop*. (*Int. J. Trop. Biol.* ISSN-0034-7744), 60(3): 33-41

Schwartz, S. Y. and Rokosky, J. M. (2007), Slow slip and seismic tremor at circum-Pacific subduction zones, Rev. of Geophys., 45, RG3004 doi: 10.1029/2006RG000208

Shimazaki, K., and T. Nakata (1980), Time-predictable recurrence model for large earthquakes, *Geophysical research letters*, *7*(4), 279-282.

Spinelli, G. A., and D. M. Saffer (2004), Along-strike variations in underthrust sediment dewatering on the Nicoya margin, Costa Rica related to the updip limit of seismicity, *Geophys. Res. Lett., 31*, L04613, doi:10.1029/2003GL018863.

Walter, J. I., S. Y. Schwartz, J. M. Protti, and V. González (2011), Persistent tremor within the northern Costa Rica seismogenic zone, *Geophys. Res. Lett.*, 38, L01307, doi:10.1029/2010GL045586.

Wei, S., R. Graves, D. Helmberger, J. P. Avouac, and J. Jiang (2012), Sources of shaking and flooding during the Tohoku-Oki earthquake: A mixture of rupture styles, *Earth Planet. Sci. Lett*., *333*, 91-100, doi: http://dx.doi.org/10.1016/j.epsl.2012.04.006.

Ye, L., T. Lay, and H. Kanamori (2013), Large earthquake rupture process variations on the Middle America megathrust, *Earth Planet. Sci. Lett.,* in review.

Yue, H., and T. Lay (2011), Inversion of high-rate (1 sps) GPS data for rupture process of the 11 March 2011 Tohoku earthquake (M_w 9.1), *Geophys. Res. Lett., 38*, L00G09, doi:10.1029/2011GL048700.

Yue, H., and T. Lay (2013), Source rupture models for the M_w 9.0 2011 Tohoku earthquake from joint inversions of high-rate geodetic and seismic data, *Bull. Seism. Soc. Am.*, *103*, no. 2b, 1242-1255, doi:10.1785/0120120119.

Zumberge, J. F., M. B. Heflin, D. C. Jefferson, M. M. Watkins, and F. H. Webb (1997), Precise point positioning for the efficient and robust analysis of GPS data from large networks, *Journal of Geophysical Research: Solid Earth*, *102*(B3), 5005-5017.

Chapter 6

Supershear Rupture of the 5 January 2013 Craig, Alaska (M_w 7.5) Earthquake

Abstract

Supershear rupture, in which a fracture's crack tip expansion velocity exceeds the elastic shear wave velocity, has been extensively investigated theoretically and experimentally, and previously inferred from seismic wave observations for six continental strike-slip earthquakes. We find extensive evidence of supershear rupture expansion of an oceanic interplate earthquake, the 5 January 2013, M_w = 7.5, Craig, Alaska earthquake. This asymmetric bilateral strike-slip rupture occurred on the Queen Charlotte Fault, offshore of southeastern Alaska. Observations of first-arriving Sn and Sg shear waves originating from positions on the fault closer than the hypocenter for several regional seismic stations, with path calibrations provided by an empirical Green's function approach, indicate a supershear rupture process. Several waveform inversion and modeling techniques were further applied to determine the rupture velocity and space-time distribution of slip using regional seismic and geodetic observations. Both theoretical and empirical Green's functions were used in the analyses, with all results being consistent with a rupture velocity of 5.5 to 6 km/s, exceeding the crustal and upper-mantle S-wave velocity and approaching the crustal P-wave velocity. Supershear rupture occurred along ~100 km of the northern portion of the rupture zone, but not along the shorter southern rupture extension. The direction in which supershear rupture developed may be related to the strong material contrast across the continental-oceanic plate boundary, as predicted theoretically and experimentally. The shear and surface wave Mach waves involve strongly enhanced ground motions at azimuths oblique to the rupture direction, emphasizing the enhanced hazard posed by supershear rupture of large strike-slip earthquakes.

6.1. Introduction

Seismological observations indicate that most earthquakes have an average rupture front expansion velocity slower than the elastic S wave velocity (subshear), typically at or below the medium Rayleigh wave velocity. However, both theoretically [*Burridge*, 1973; *Andrews*, 1976; 1985; *Burridge et al*., 1979; *Dunham et. al.,* 2003; *Dunham*, 2005; *Dunham and Bhat,* 2008] and experimentally [*Rosakis et al., 1999*; *Xia et al.,* 2004; *Xia et al.,* 2005; *Passelègue et al.,* 2013], it is established that rupture can propagate faster than the S wave velocity (supershear) for mode II fractures with rupture propagation direction parallel to the fault slip direction, as is typical of strike-slip earthquakes. Dynamical models of supershear rupture indicate that high pre-stress and low static friction may be important to the initiation of supershear rupture process [*Burridge,* 1973]. The transition from sub-shear to intersonic (between S and P wave velocities) occurs when S wave energy ahead of the rupture front is sufficient to overcome frictional resistance on a pre-existing fault surface, initiating a second rupture front ahead of a subshear front [*Andrews*, 1985; *Dunham and Bhat,* 2008; *Dunham et. al.,* 2003; *Festa and Vilotte*, 2006; *Liu and Lapusta*, 2008; *Kaneko and Lapusta,* 2010]. The supershear transition can be abetted by the existence of stress heterogeneity and by proximity to failure stress along the fault [e.g., *Day*, 1982; *Olsen et al*., 1997; *Dunham et al*., 2003; *Mena et al.*, 2012].

Geophysical inferences of supershear ruptures have been reported for six large strike-slip (mode II) earthquakes in continental crust and one strike-slip event within an oceanic plate [e.g. *Archuleta,* 1984; *Bouchon et al.,* 2001; *Bouchon and Vallée*, 2003; *Choy and Boatwright*, 2004; *Frankel*, 2004; *Dunham and Archleta*, 2004; *Robinson et al*., 2006; *Walker and Shearer,* 2009;

Wang and Mori, 2012]. The 1979 Imperial Valley M_S 6.9 earthquake was the first event for which supershear rupture was inferred [*Archuleta,* 1984]. By analyzing near-field data, an over-all rupture velocity of 2.7-3.2 km/s was estimated [*Spudich and Cranswick,* 1984] with significant rupture velocity variation that included localized supershear rupture of a fault segment transected by nearby strong motion instruments [*Archuleta,* 1984]. In 1999, two strike-slip earthquakes struck the north Anatolian fault zone, the M_w = 7.4 İzmit and M_w = 7.2 Düzce events. Strong ground motions recorded directly along the Anatolian fault were used in source analyses, which indicate that both events had bilateral ruptures with supershear only on their eastern segments. A rupture velocity of ~5 km/s was reported for both events [*Bouchon et al.,* 2001; 2002], close to the value of 1.414 times the shear velocity which is found to be a stable supershear rupture velocity in some theoretical calculations [*Freund,* 1979]. Additional studies of the Turkey events indicate a range of rupture velocity estimates, but all involve supershear rupture [e.g., *Sekiguchi and Iwata,* 2002; *Birgören et al.,* 2004; *Bouin et al.,* 2004; *Konca et al.,* 2010]. Although ground motion amplification related to Mach waves is expected for supershear ruptures, ground motion simulations for supershear rupture models of the İzmit event did not produce significant peak ground velocity enhancements [*Aochi et al.* 2011], likely because the length of supershear rupture was fairly short.

The 2001 M_w 7.8 Kokoxili (Kunlunshan), China event appears to have had a more extensive supershear rupture. Although on-fault observations are not available for the Kokoxili event, eastward rupture along a 300 km long segment produced significant directivity effects, allowing supershear rupture to be identified in seismic data collected at regional distances (< 2000 km) [*Bouchon and Vallèe,* 2003]. Mach waves produced by the supershear rupture segment have

coincident arrivals from the finite-source toward particular directions [*Vallèe and Duham,* 2012], and exhibit significant amplitude enhancement due to constructive interference. Supershear rupture of the Kokoxili event is also apparent in teleseismic P wave back-projections [*Walker and Shearer*, 2009], which indicate an initial subshear rupture velocity over a distance less than 40 km, then increase to supershear rupture velocity of ~5.6 km/s.

Using teleseismic back-projections *Walker and Shearer* [2009] also identified a similar rupture process for the 2002 M_w 7.9 Denali, Alaska event. For the Denali event, one strong motion station, deployed 3 km from the fault, recorded unusual ground motions attributed to supershear rupture based on dynamic source simulations [*Ellsworth et al.*, 2004; *Dunham and* Archuleta, 2004]. A strong Mach wave and a trailing fault surface Rayleigh wave were detected in the near-field record; this complexity has also been observed in laboratory experiments [*Mello et al.,* 2010]. The moderate size M_w 6.9 2010 Yushu, China earthquake is the smallest event interpreted as having supershear rupture, based on one near-field observation along the fault and teleseismic short-period waveform back-projections [*Wang and Mori,* 2012]. The rupture is relatively short, so teleseismic inferences of supershear rupture are marginal for events of this size.

The 2012 M_w 8.6 Indo-Australia intraplate oceanic earthquake is the largest strike-slip event yet observed [*Yue et al.*, 2012]. The rupture process of the Indo-Australia event is very complex, involving rupture of no less than 4 segments. No near-field data are available, but supershear rupture was inferred using teleseismic P wave back-projections in one study [*Wang et al.,* 2012] while other back-projections indicate relatively low rupture velocities [*Meng et al.,* 2012; *Yue et al*., 2012]. The evidence for supershear rupture of this event is marginal despite its size, mainly due to the complexity of the process. Generally, rupture velocity is easier to determine for a long

unilateral rupture like the Kokoxili event [e.g., *Bouchon* 2001; *Bouchon and Vallée*, 2003] or when near-regional ground motion recordings are located directly along the fault rupture as for the Imperial Valley, Denali, İzmit, Düzce, and Yushu events [*e.g., Bouchon et al.* 2001; *Dunham and Archleta*, 2004].

Supershear rupture produces horizontally expanding planar S and surface wave Mach waves that enhance ground shaking and damage at small oblique angles to the direction of rupture propagation, affecting wave energy distribution [*Das,* 2007; *Kaneko and Lapusta,* 2010; *Andrews,* 2010]. Near the Mach cone azimuth, which is determined by the rupture velocity, the waves from along the supershear portion of the rupture interfere constructively to resemble the plane waves, effectively spreading from a line source rather than a point source, giving significantly enhanced amplitude [*Vallèe and Duham,* 2012]. The strong directivity effect of supershear rupture may cause severe damage in the forward rupture direction [*Das*, 2007; *Wang and Mori,* 2012]. For several supershear events, aftershock distributions have been found to be absent on the supershear rupture segment but abundant in splay faults. This may be caused by nearly total stress release on the main fault plane with the branch fault being activated by significant ground shaking and static stress loading [*Bouchon and Karabulut,* 2008]. Occurrence of supershear rupture is thus important for ground shaking modeling and seismic hazard estimation, along with revealing fundamental physics of rupture initiation.

6.2. 2013 M_w 7.5 Craig, Alaska Strike-Slip Earthquake

On 5 January 2013 a large strike-slip event struck along the Queen Charlotte Fault (QCF) offshore of southeastern Alaska (55.4°N, 134.7°W, depth=10 km, 08:58:19 UTC http://comcat.cr.usgs.gov/earthquakes/eventpage/pde20130105085819330_10#summary). This is

called the Craig, Alaska earthquake. The fault is the main plate boundary between the Pacific (oceanic) and North America (continental) plates, and experiences right-lateral shearing on a steeply dipping plane at a long-term rate of about 47 mm/yr. The strike-slip focal mechanism (Figure 6.1) of the 2013 event is consistent with shallow rupture of the plate boundary. Approximately 300 aftershocks within 1 month after the mainshock were located by the Alaska Earthquake Information Center (AEIC), and are distributed ~100 km to the north and ~30 km to the south of the epicenter, indicating an asymmetric bilateral rupture with predominantly northward extension. The earthquake seismic moment is ~2.2 x 10^{20} Nm and the magnitude is M_w 7.5 [*Lay et al., 2013*]. Supershear rupture has been reported for comparable size earthquakes, such as the M_w 7.6 1999 Izmit earthquake [*Bouchon et al.,* 2001], but the offshore location of the 2013 Craig, Alaska earthquake precluded near-fault ground motion measurements. Fortunately the fault runs along the continental margin, and numerous seismic and geodetic stations in Alaska and western Canada located at near-regional (<400 km) to regional distances (<1500 km) provide >180° azimuthal coverage of seismic radiation and static ground deformation for the event.

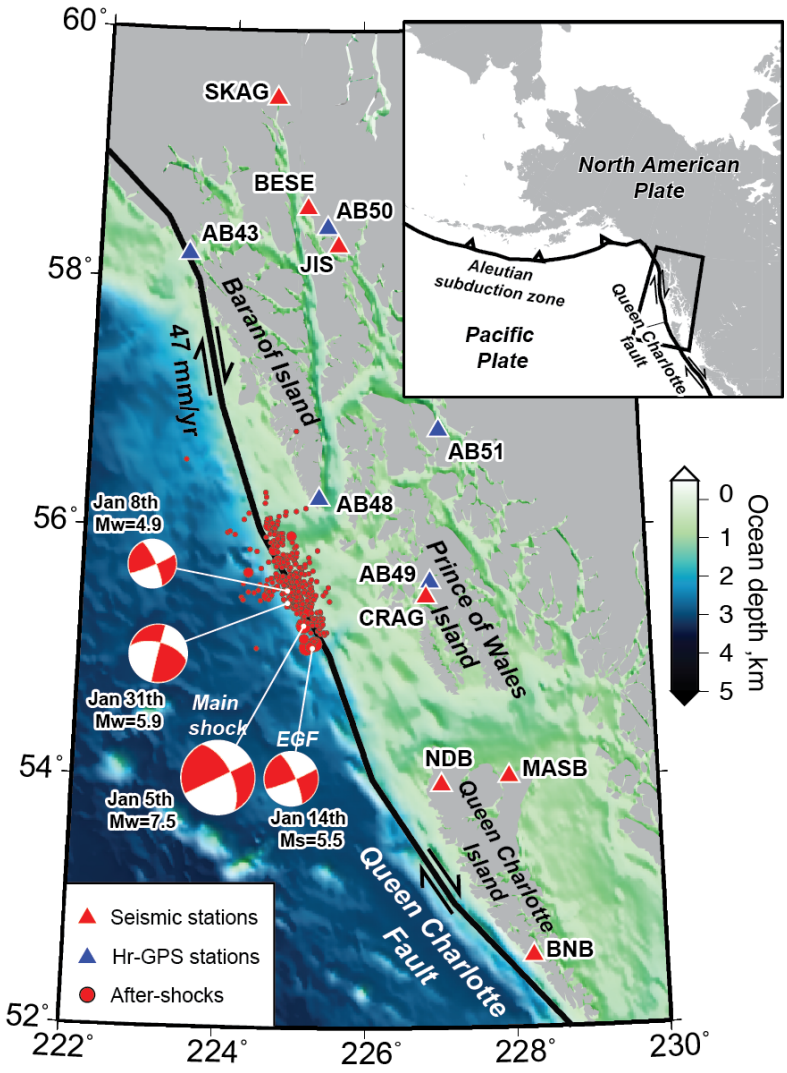

Figure 6.1. The inset indicates the regional plate tectonic setting with the Pacific and North-America plates shearing horizontally at 47 mm/yr (black arrows) along the Queen Charlotte Fault (black line) and converging along the Aleutian trench. The map shows the focal mechanism solutions of the 5 January 2013 (M_w 7.5) main event and three aftershocks. The 14 January 2013 (M_w 5.5) aftershock is used to provide empirical Green's functions (EGFs) in the pre-hypcoentral S wave and Mach wave analyses. The 31 January 2013 (M_w 5.9) event is also used as an EGF in the pre-hypocentral S wave analysis. Near-field high-rate GPS and seismic stations are shown as blue- and red-filled triangles, respectively. The locations of aftershocks in the first month following the mainshock are small red-filled circles.

6.3. Direct Supershear S wave Observations

The most straightforward evidence for a supershear rupture is observation of S waves at positions along the rupture direction that arrive earlier than the S wave from the hypocenter, with ensuing arrivals coming in reverse chronological order of the rupture process. Figure 6.2 shows that for a subshear rupture, the initial shear wavefront arriving at all directions originates from the hypocenter. For a supershear rupture, the rupture front precedes the S wavefront from the hypocenter at azimuths near the rupture direction, producing initial arrivals (designated pre-hypocentral S waves) from the end of the supershear segment at small oblique angles to the rupture propagation direction. At larger oblique angles in the forward rupture direction, the energy from the entire rupture sequence arrives together, constituting a locally planar S Mach wave. Such Mach waves are observed in supershear rupture experiments using laser image snapshots [*Rosakis et al., 1999*; *Xia et al.,* 2004; *Xia et al.,* 2005] or recorded accelerograms [*Passelègue et al.,* 2013], providing the main supershear detection criteria in experimental measurements. However, it is challenging to identify such a Mach wave for earthquakes, because the wavefront from the hypocenter is always distorted by local structure heterogeneities (Figure 6.2c), and the distribution of seismic stations is usually inadequate to resolve the continuous wavefront. The detailed velocity structure controlling the arrival times is usually not well known, therefore it is difficult to precisely calculate the hypocentral S arrival time to differentiate it from any pre-hypocentral S wave. Furthermore, regional S wave signals tend to be very complex due to crustal waveguide interactions, making it difficult to identify pre-hypocentral arrivals and Mach waves.

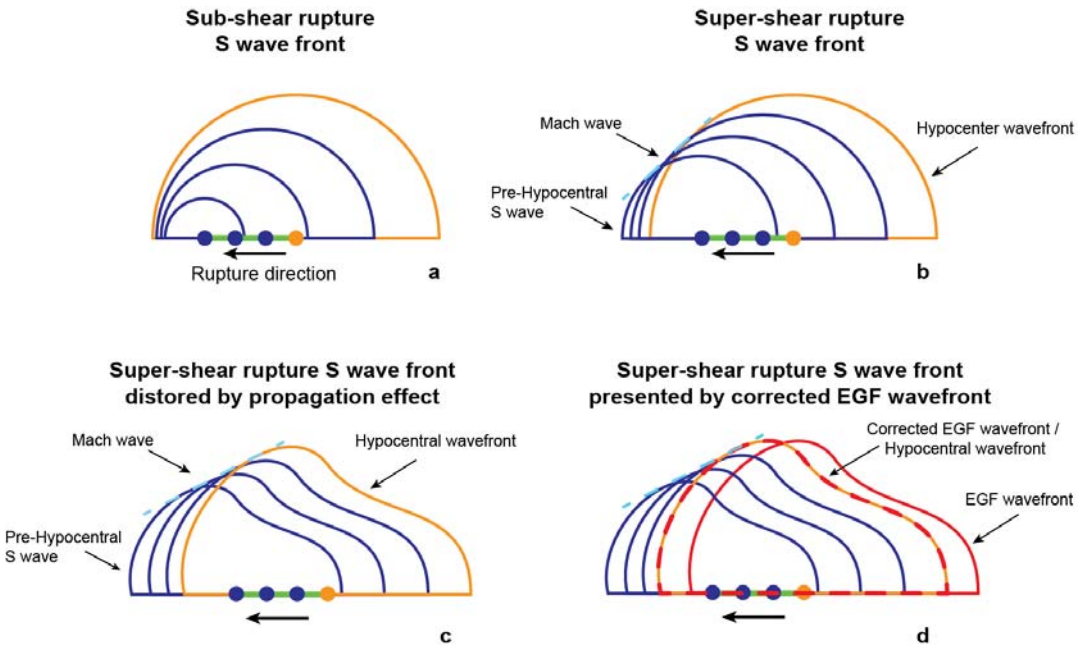

Figure 6.2. (a) The S wavefronts from the hypocenter and three locations along the leftward-propagating rupture front are indicated by orange and blue semi-circles, respectively. For subshear rupture velocity the initial S wave observed at all locations originates at the hypocenter. (b) In a supershear rupture, the S wave arrives earlier than the hypocentral wavefront along the rupture propagation direction and a Mach wave (cyan-dashed line) develops at oblique angle to the rupture direction. (c) For actual earthquakes, the rupture front is always distorted by heterogeneities, which makes it difficult to identify any pre-hypocentral arrival or a Mach wave, which will be distorted from planar by the heterogeneities. (d) The EGF wavefront (red curve) resembles the shape of the mainshock hypocentral wave front (orange curve), because the signals travel through similar structures. When corrected for the differential arrival times due to the epicentral shift for the corresponding specific phase, the EGF wavefront (red dashed curves) closely matches the mainshock hypocentral wavefront. Because the EGF wavefront is easier to identify, this operation helps to detect any pre-hypocentral S wave arrivals and Mach cone behavior for stations in the supershear rupture direction.

To address these challenges we use signals from a 14 January 2013 (M_w 5.5) aftershock (Figure 6.1) as empirical Green functions (EGFs). This small event has negligible rupture complexity and short-period regional S wave (Sg) arrivals can be picked reliably at stations that also record the mainshock. Because the EGF event locates close to the main event hypocenter, the EGF wavefront resembles the shape of main event hypocentral wavefront even though distorted

by propagation effects (Figure 6.2d). After determining the relative location of the two hypocenters, we correct for the Sg or Sn arrival time differences expected due to the differential hypocenter locations, aligning waveforms for both events, which effectively aligns the EGF Sg or Sn wavefront with the corresponding main event hypocentral wavefront (Figure 6.2d). Then, observation of any significant energy ahead of the hypocentral/EGF arrivals can be attributed to supershear rupture of the larger event.

6.3.1 EGF relocation

Precise relative locations of the EGF and mainshock hypocenters are needed for our analysis. We manually measured the initial Pn phase arrival times of both the mainshock and the EGF event at regional stations. The differential travel times from 26 stations located within 1000 km are used in our relative location determination, with both southern and northern stations being important for constraining the along-fault location (Figure 6.3). We held the mainshock location fixed at 55.2280°N, -134.8591°E, 10 km deep, as located by the AEIC using regional networks. The initial time of the mainshock is 08:58:15 in the AEIC catalog, which is 4 s earlier than the initial time reported by the USGS National Earthquake Information Center. Such an origin time discrepancy originates from differences in velocity models or differences in picking of small initial phase arrivals. The USGS location predicts ~3 s arrival time discrepancies with the closest stations, so for the regional data we prefer the AEIC parameters. Only Pn phase data are used in our relative relocation, since the shear wave phases may be influenced by supershear rupture effects.

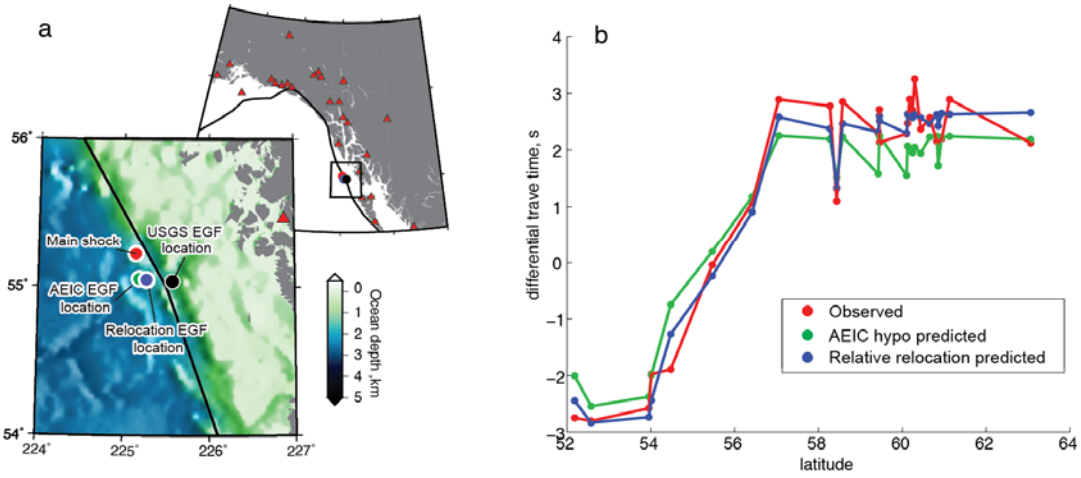

Figure 6.3. (a) In the inset, positions of stations used for relative location are shown as red-filled triangles. In the main map, the AEIC mainshock location, AEIC and USGS reported EGF locations, and our relocated relative EGF location are plotted with red-, green-, black- and blue-filled dots, respectively. The Queen Charlotte fault is plotted with a black solid line. (b) Differential Pn wave arrival times between the mainshock and the EGF event at each station sorted by their respective latitude. The curves are the observed differential arrival times (red), the predicted differential arrival times for the AEIC location (green) and for our relative relocation (blue).

The Pn differential arrival times are calculated through a 1-D layered model, extracted from a nearby active source reflection profile that includes a velocity contrast across the oceanic/continental plate boundary [*Horn et al.,* 1984]. Given that the near-field stations are all located on the landward side and the ray paths all traverse landward structure, we averaged the velocity structure on the landward side to obtain the 1D structure shown in Table 1. A Vp/Vs ratio for layered structure obtained from a nearby receiver function study [*Morozov et al.,* 1998] is used to estimate S wave velocities from the P wave velocities.

A classical Newton inversion method was applied to search for the relative location and initial time of the EGF event, avoiding local-minima effects by using multiple initial locations. The relocated EGF hypocenter is 55.0469°N, 134.7303°E, about 20 km southeast of the mainshock hypocenter. The mainshock and EGF are assumed to be at the same depth because in Pn phase

location the initial time trades-off with the hypocenter depth. The average differential time residual is <0.5 s, which indicates relative location error of <4 km (Figure 6.3). The lack of stations to the west limits resolution of the location in the EW direction, but the similarity of the focal mechanisms for the EGF and Mainshock (Figure 6.1) indicates that they are both on the Queen Charlotte Fault. A summary of mainshock and aftershock locations is shown in Table 2. We also list the AEIC location of the 31 January 2013 M_w 5.9 event, which we used as a second EGF (EGF2) for regional S wave analysis.

6.3.2 Sg wave alignment and pre-hypocentral Sg wave observations

With the relative locations between the mainshock and EGF being well determined, we can shift the Sg arrival time of the EGF signals to correspond to the mainshock hypocenter using our 1D velocity model and corresponding computed Sg raypaths. Because the distance between the relative hypocenters is small, ~20 km, the Sg travel time error produced by correcting for the differential path length to each station is < 0.5s, even allowing for 10% inaccuracy in the reference model. After correcting to a common hypocenter, the EGF waveforms identify when signals from the mainshock hypocenter should arrive in the mainshock waveforms. The arrival time of the relatively simple Sg phases for the shifted EGF waveforms are picked and both sets of signals are aligned on the hypocentral phase arrival times. The waveforms are filtered with a causal band-pass filter with corner frequencies of 1-10 Hz to remove low-frequency energy from preceding Sn phases and to emphasize the Sg arrivals.

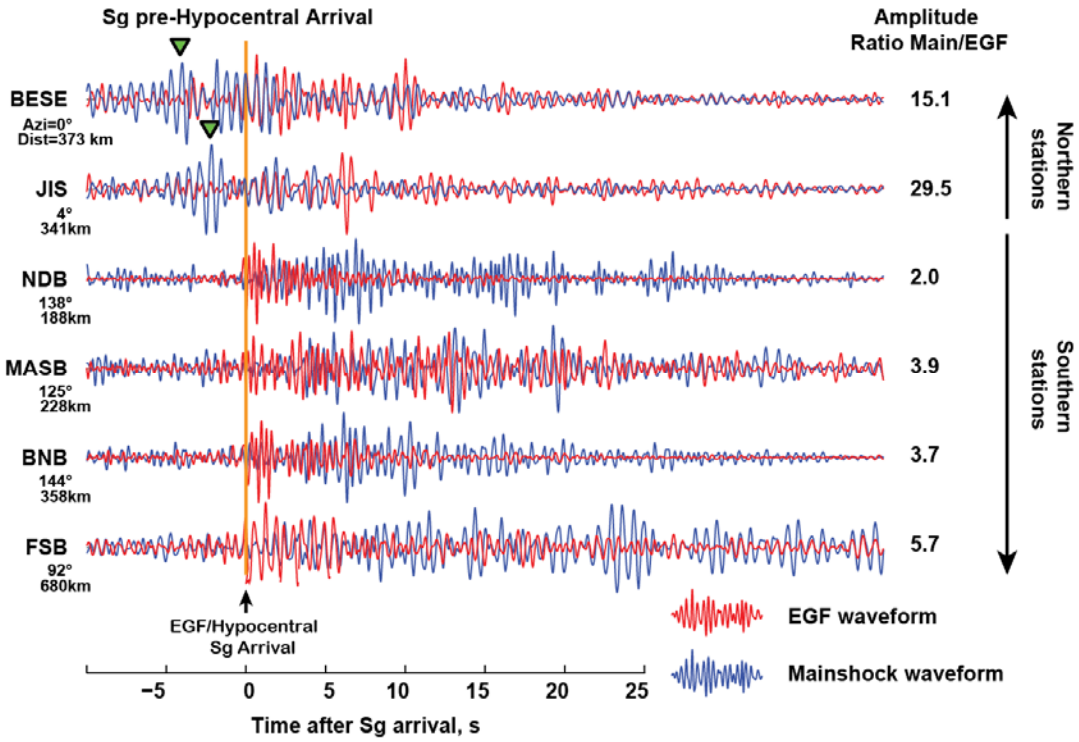

Figure 6.4. Regional vertical-component seismic records of the mainshock (blue traces) and the EGF event (red traces) aligned on the manually selected Sg arrivals from the EGF. All records are band-pass filtered between 1-10 Hz and normalized by their maximum amplitudes. Station names, azimuths and distances are indicated along with observed ratios of peak Sg amplitudes (Mainshock/EGF). For the northern stations, very large Sg arrivals for the mainshock (green-filled triangles) arrive earlier than arrivals from the hypocenter, requiring close source locations that can only be reached by supershear rupture, as in the example in Figure 6.2.

Figure 6.4 shows that the mainshock and EGF hypocentral short-period vertical component Sg arrivals are well aligned at the southern stations, FSB, BNB, MASB and NDB, but the mainshock has clear large amplitude arrivals before the hypocentral Sg arrival at the northern stations JIS and BESE. Corresponding energy is not present in the EGF waveforms, reducing the possibility of any propagation effect such as P wave scattering or multi-pathing, which should be in common for both sources. We attribute this energy to supershear rupture. For more distant northern stations, the Sg waves are not confidently identified in the EGF waveforms so this procedure cannot be applied to more data.

We also made similar Sg waveform comparisons of the mainshock and EGF recordings for various band-passes for tangential component ground displacements. Because the close southern stations on Haida Gwaii, including BNB, MASB and NDB, are all short-period (< 1 s) vertical component stations, only stations to the north are used for the tangential component analysis. A similar hypocentral-equalization process was also applied to records for EGF2, for which we corrected for the Sg arrival time caused by the differential locations reported by AEIC (Table 2). The comparison of the mainshock, EGF and EGF2 tangential displacement Sg arrivals is summarized in Figure 6.5a. The mainshock broadband tangential components at northern stations consistently show 3 to 5 s early initial Sg arrivals to the north relative to both EGF and EGF2, compatible with the results in Figure 6.4. This is apparent in all bandwidths for the tangential component signals.

The Mainshock/EGF amplitude ratios of the Sg signals in Figure 6.4 show one order of magnitude difference between the southern and northern stations, indicating a strong directivity effect of the mainshock rupture process. It proves difficult to fully model the short-period amplitude ratios because of the uncertain propagation effects, as discussed below.

6.3.3 Sn wave alignment and pre-hypocentral Sn wave observations

Sn waves refract along the continental crust-mantle (Moho) boundary, and arrive earlier than the Sg phase at regional distances, with lower frequency content (Figure 6.5). If the rupture velocity surpasses the upper mantle shear velocity (~4.5 km/s), we should also observe a pre-hypocentral Sn arrival at the northern stations. We corrected the Sn phase arrival times in EGF waveforms for the differential path lengths relative to the mainshock, using the Sn slowness for our 1D model. The waveform comparisons, again aligned on the hypocentral arrival for the

mainshock and EGF, are shown in Figure 6.5b, for two high-quality recordings. Here we use relatively broad bandpass filters to capture the low frequency content of the Sn headwaves. The mainshock has ramp-like onsets of Sn for which it is difficult to measure absolute arrival times, but the EGF signals have sharper onsets and the differential times can still be confidently measured. The mainshock Sn initial phases arrive about 5 s earlier than the hypocentral Sn time, similar to the Sg data. As tangential component Sn is the first expected arrival on the tangential components, these observations are not subject to possible contamination from earlier S arrivals (whereas Sn precedes Sg in the data in Figs. 4 and 5a).

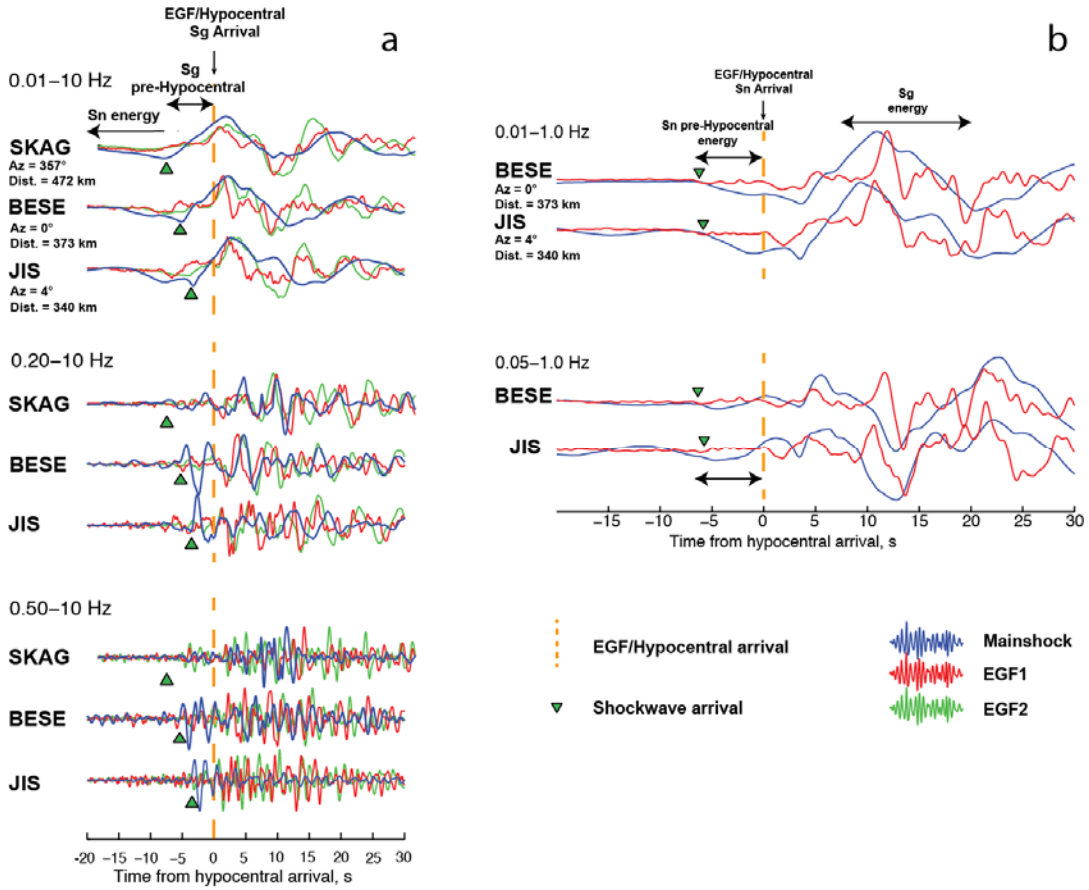

Figure 6.5. (a) Regional tangential-component ground displacement records of the mainshock (blue traces) and the two EGF events (red traces and green traces) aligned on the manually selected Sg arrivals from the EGFs for station BESE. Records are band-pass filtered between 0.01-10, 0.2-10 and 0.5-10 Hz and normalized by their maximum amplitudes. Station names, azimuths and distances are indicated. The stations shown here locate north of the hypocenter. The hypocentral/EGF Sg arrivals are aligned at 0 s and marked with an orange dashed line. The Sg pre-hypocentral arrivals for the mainshock traces are marked with green-filled triangles. (b**).** Regional tangential-component ground displacement records of the mainshock (blue traces) and the EGF1 event (red traces) aligned on the manually selected Sn arrivals from the EGF. Records are band-pass filtered between 0.01-1.0 and 0.05-1.0 Hz, and normalized by their maximum amplitudes. Station names, azimuths and distances are indicated. Stations locate to the north of the hypocenter. The hypocentral/EGF Sn arrivals are aligned at 0 s and marked with an orange dashed line. The Sn pre-hypocentral energy arrivals are marked with green-filled triangles.

With this EGF alignment technique, we have clearly identified Sn and Sg waves that arrive earlier than the hypocentral Sn and Sg shear waves. These observations clearly demonstrate the

existence of supershear rupture. Since pre-hypocentral waves are observed in both Sg and Sn phases, the rupture velocity exceeds both the crustal and upper mantle shear velocity, and thus is >4.5 km/s. The initial pre-hypocentral arrivals originate from the terminus of the supershear rupture segment, but locating that depends on the rupture expansion history of the event. Fully quantifying the rupture velocity history requires constraints on the spatio-temporal slip distribution along the fault, which must be determined using azimuthally distributed observations.

6.4. Finite Fault Model Inversion

Space-time evolution of a large earthquake rupture is usually determined by finite-fault model (FFM) inversion, quantifying the rupture velocity, *Vr*, and slip distribution. Supershear rupture velocity has been identified using FFM inversion for some previous events [*e.g., Bouchon et al.,* 2002; *Konca et al*., 2010]. Joint inversions including near-regional ground motions provide improved sensitivity to the rupture velocity compared to using only teleseismic datasets [*Yue and Lay,* 2013; *Yue et al.,* 2013]. Thus, we include both teleseismic and near-field seismic and geodetic records in our FFM inversion. Ground motion recordings at near-regional epicentral distances <400 km from the 2013 event are available from 5 high rate GPS (hr-GPS) stations and 3 broadband seismic stations (Figure 6.5). Resolving *Vr* still depends on the geometry of the station distribution, which is one-sided for the 2013 Craig, Alaska event, with most stations being located along the northern extent of the rupture. Fortunately, the rupture is predominantly toward the north. For a well-determined hypocenter and good regional velocity model, the main parameter controlling the initial S wave arrival time for any northward supershear radiation at stations along the rupture is the rupture velocity. For stations in the south the initial motion comes from the

hypocenter, so the rupture velocity does not affect the timing of the initial motion.

6.4.1 Model Parameterization

The finite-fault model is parameterized with 16 nodes along strike with 10 km increments and 3 nodes along dip with 5 km increments (Figure 6.6). The total size of the FFM is 160 km along strike and 15 km along dip. The strike is 335° and dip is 63°, given by the USGS W-phase point source focal mechanism. We found that this geometry fits the data slightly better than using the global Centroid Moment Tensor (g-CMT) solution, but using the g-CMT solution does not produce significant differences in rupture velocity or slip patterns. The hypocenter is 45 km from the southern end of the model and 115 km from the northern end. We use a multi-time-window linear inversion technique [*Hartzell and Heaton,* 1983], in which the source time function of each subfault is parameterized with 8 symmetric triangles with 2 s rise times and 2 s shifts, allowing up to 18 s long source time functions for each subfault. We use two slip-vector orientations for each subfault to allow rake-varying slip, applying a non-negative least squares inversion [*Lawson and Hanson*, 1995] in which the rake of each subfault is allowed to vary between 135° and 225°. We apply Laplacian regularization, which constrains the second order gradient for each parameter to be zero.

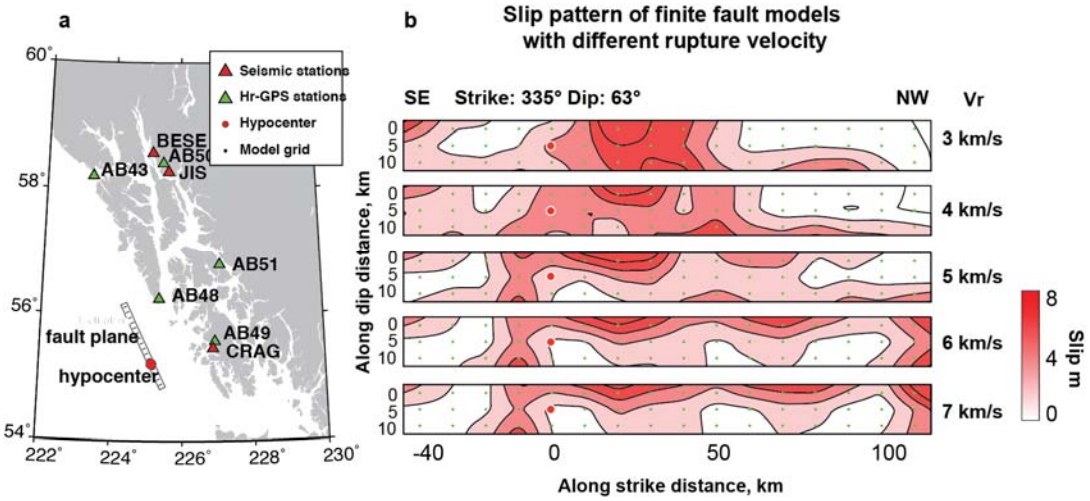

Figure 6.6. (a) Hr-GPS and seismic station locations are shown as green- and red-filled triangles. Three component ground motions from each station are inverted jointly with teleseismic P and SH waves to give finite fault models for slip distribution. The model grids are shown as black dots along the rectangle with the hypocenter location marked as a red dot. (b) Slip pattern of finite fault models inverted with different prescribed rupture velocities, *Vr*. Grid points and the hypocenter are shown as green- and red-filled dots, respectively. Magnitude of the predominantly right-lateral slip is contoured for each case.

Three datasets are used in the FFM inversions: near-regional hr-GPS, near-regional seismic, and teleseismic data. The near-regional records are all from stations located within 400 km of the hypocenter. For these we use 1D Green functions computed for our regional model.

6.4.2 Hr-GPS Dataset

We used 5 hr-GPS stations with three-component recordings of full ground displacements including time varying seismic motions and static offsets. The GPS stations are part of the Earth Scope Plate Boundary Observatory, operated by UNAVCO. We produce displacements from 1 sample per second GPS phase and pseudorange observations in a PPP solution [*Zumberge et al.* 1997] with the GIPSY software and JPL final orbits and clocks. The JPL clock estimates were linearly interpolated from 30 s to 1 s sampling. We estimate position variations using a random walk noise model in GIPSY's Kalman filter; aside from the kinematic solution approach, other

models applied were the same as those used for daily position estimates [*Fu and Freymuller,* 2012]. This process produces a position time series for each site in the ITRF2008 reference frame. A sidereal filter was applied to each record to remove the noise introduced by local multipathing, and we used the 20 minutes before the earthquake to define the zero point for the displacement seismograms.

For inversion, the hr-GPS data are filtered with a causal low-pass Butterworth filter with a corner frequency at 0.2 Hz. A 160 s time window is applied to the data spanning the dynamic waveforms and static ground displacements in all records. The same low-pass filter is applied to the Green's functions. The Green's functions are generated by a frequency-wavenumber integration method including all near-field terms (Computer Programs in Seismology, Robert Herrmann). The velocity structure is that in Table 1. We also used Green's functions for a model with a 3 km thick water layer. The latter inversion results are not significantly different and are not included in this paper. The vertical components are down-weighted by a factor of 0.2 to compensate for the higher noise level in the vertical records.

6.4.3 Near-Regional Seismic Dataset

We used 3 near-regional broadband seismic stations with three component recordings from the Alaska Regional Seismic Network (ARSN). The instrument responses were removed to recover ground displacements filtered with a causal bandpass filter in a band of 0.02 – 0.2 Hz. A 200 s long time window was used for the seismic data, spanning the main seismic energy in these records. The F-K integration algorithm was used to compute Green's functions for the seismic data. The same band-pass filter was applied to the Green's functions.

6.4.4 Teleseismic Dataset

93 teleseismic records were used in the joint inversion, including 64 P wave and 29 S wave records, from global stations of the Federation of Digital Seismic Networks (FDSN), accessed through the Incorporated Research Institutions for Seismology (IRIS) data center. The data were selected from hundreds of available FDSN seismograms to have good azimuthal coverage (Figure 6.S1) and high signal-to-noise ratios for epicentral distances from 40° to 90°. The instrument responses were removed from the raw data to recover ground displacement records. A causal bandpass filter in a band 0.005 - 0.9 Hz was applied to the data. To align with the absolute time of the local data, the teleseismic P wave onsets were shifted by 4 s, as the visible initial motion of the teleseismic records are consistent with the 4 s late initial time reported by the USGS-NEIC. The teleseismic Green's functions were generated with a reflectivity method that accounts for interactions in 1-D layered structures on both the source and receiver sides [*Kikuchi et al.,* 1993]. A 3-km-deep water layer was added to the 1D source region structure to compute the teleseismic surface reflected phases accurately. A 90 s long data window with 10 s leader before the initial motion was used. The S waves were down-weighted by a factor of 0.2 to compensate for the very large S wave amplitudes.

6.4.5 Inversion Results

In multi-time-window inversion a maximum rupture velocity (*Vr*) is imposed, so inversions were conducted for different values of *Vr*. In all cases shown here the rupture initially expands bilaterally at a subshear velocity of 3 km/s to 20 km from the hypocenter, and then *Vr* increases to a specified value, ranging from subshear to supershear (3 to 7 km/s), on the northern segment. As *Vr* on the northern segment increases, the spatial extent of the slip pattern expands (Figure 6.6),

leading to significant improvements in waveform fitting (Figure 6.7; S1). If the prescribed *Vr* exceeds the actual rupture velocity and the data are sufficient to spatially resolve the slip distribution, the slip pattern stabilizes, and the waveform fitting residual has no significant reduction with further *Vr* increase. For our FFM inversions, the slip models and waveform misfit stabilize for *Vr* = 5.5 to 6.0 km/s (Figure 6.7c), indicating that range as a reasonable upper bound on rupture expansion velocity. We find that the results do not depend strongly on the assumed initial subshear velocity or the length for the first stage of subshear rupture. The acceptable *Vr* of 5.5 to 6 km/s are supershear relative to the local crustal S wave velocity of 3.8 km/s and upper-mantle S wave velocity of 4.5 km/s [*Morozov et al.,* 1998], compatible with the Sn and Sg pre-hypocentral arrival observations. The FFM inversions indicate that the fault slip extends from the seafloor to ~15 km deeper, extending below the oceanic crust (~6 km thick) to the west but still against the continental crust (~25 km thick) to the east. For our preferred FFM rupture model (*Vr* = 6 km/s, Figure 6.6b), the slip distribution extends ~110 km to the north and ~40 km to the south of the hypocenter. The northern terminus of the rupture is not tightly constrained, and we specify it based on the aftershock distribution. Two large-slip patches locate ~20 km and ~70 km north of the hypocenter; the maximum slip of these two patches is from 8 to 10 m, varying slightly with different input parameters, but the locations of these two patches are stable. The total seismic moment is 3.2×10^{20} Nm, corresponding to M_w 7.6.

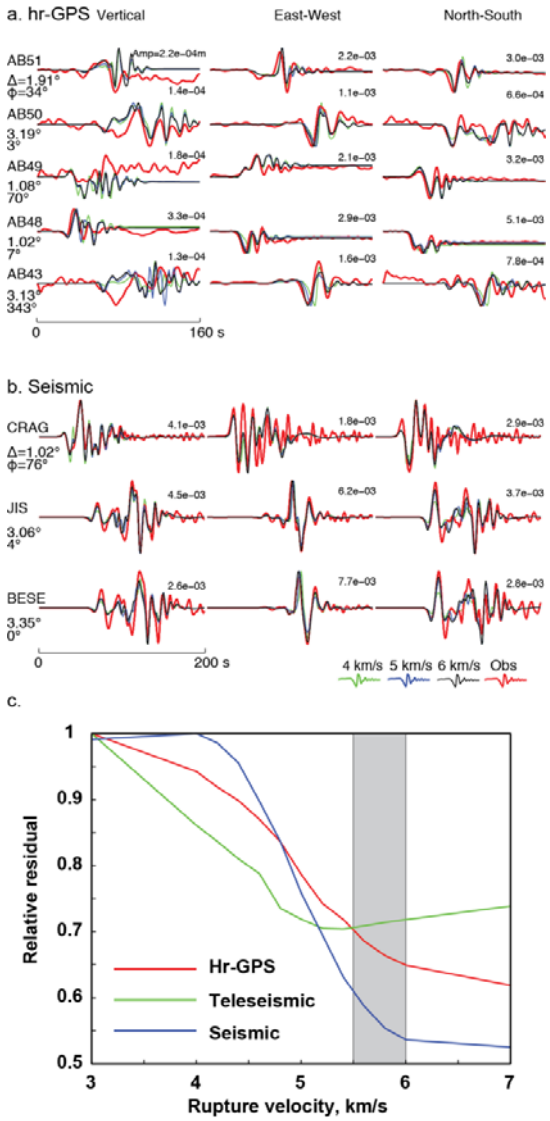

Figure 6.7. Representative observed and predicted waveforms for finite-fault models are shown for (a) hr-GPS records and (b) near-regional seismic records. Three-component records are used and shown in columns. In both cases, observed waveforms are plotted in red, and modeled waveforms for input rupture velocity of *Vr* = 4.0, 5.0, 6.0, and 7.0 km/s are plotted in green, blue, cyan and magenta, respectively. Station names, epicentral distances and azimuth of each record are labeled for each case. (c) Trade-off curves indicating normalized inversion residual versus assumed rupture velocity for each dataset for joint inversions. Red, blue, and green curves are normalized residuals of hr-GPS, seismic, and teleseismic datasets respectively. The range of preferred rupture velocity (5.5km/s- 6.0 km/s) is shaded. All observed waveforms and inversion predictions are shown in Supplementary Figure 6.S1.

6.5. Linear Fault Model Inversion

Effects of errors in the velocity structure increase as distance to a recording station increases,

making it difficult to include regional seismic data beyond 400 km distance in the FFM using theoretical Green functions. In FFM inversions the rupture velocity can trade-off with model velocity, such that apparent supershear *Vr* could be produced as an artifact of having too low of a velocity model. To overcome the uncertainty of the regional wave propagation, we use broadband Love and Rayleigh surface waves from the 14 January 2013 (M_w 5.5) aftershock as EGFs to invert for the rupture process. The EGF waveforms account for the first-order complexity of surface wave propagation along the path from the source to each regional station. EGF-based waveform inversion will diminish the potential bias caused by inaccurate wave propagation effects, enhancing sensitivity to the along-strike source rupture process.

6.5.1 Empirical Green's Function Corrections

In the EGF analysis, the path to each station for the EGF event is similar to that for each position along the mainshock rupture, except for differences in path length near the source region (Figure 6.8). Assuming that the EGF and the mainshock have the same average focal mechanism, giving identical initial phase at a particular azimuth, the phase difference between the EGF and the Green's function for any node on the mainshock model is proportional to the differential propagation distance. Assuming the heterogeneity of structure from the EGF to the mainshock nodes is small, we use the local 1D model to correct for the phase differences, giving empirical Green's function at each model node as perturbations of the EGF waveforms (Figure 6.8b,c). High frequency data may not be well corrected in this way, since at regional distances the high frequency energy involves body waves with multiple interfering phases with different slowness. But the low-frequency energy of the regional records is mainly fundamental surface waves that can be corrected with a dispersion curve.

Our phase velocity correction technique involves the following steps.

1. The spectra of the EGF waveforms are computed from the recorded waveforms.

2. A phase correction is applied to each frequency by the differential epicenter distances and the theoretical Love and Rayleigh wave fundamental mode dispersion curves.

3. An inverse Fourier transform recovers the time domain signal from the corrected spectra.

4. A geometrical spreading factor, involving the square root of the differential epicentral distance, and an azimuthal radiation ratio are applied to the corrected Green's functions to adjust the amplitudes.

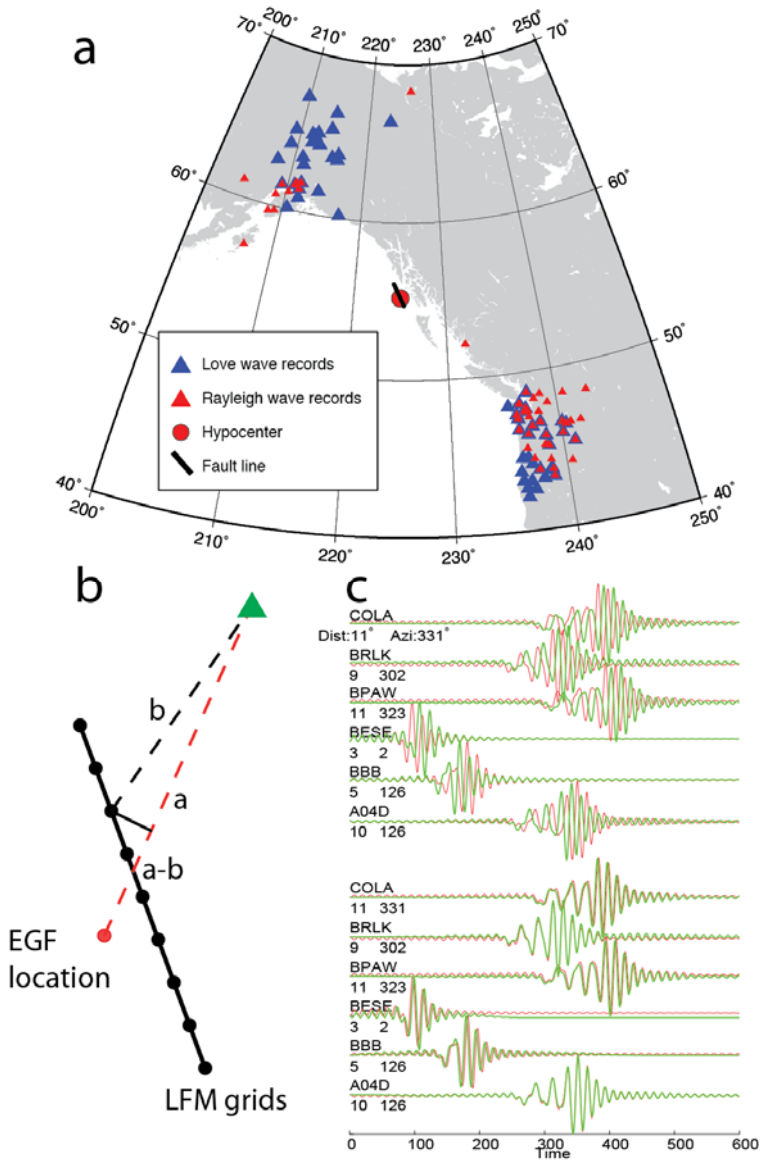

Figure 6.8 . (a) Regional distance stations used for linear-fault model inversions and forward modeling of Love and Rayleigh waves. Stations providing G1 and R1 records are shown as red and blue triangles, respectively. Stations locate within 30 degrees from the nodal directions are excluded in both datasets. The linear-fault plane is marked with a black solid line, and the hypocenter is marked with a red-filled dot. (b) For a station at regional distance, the EGF wave path length ***a,*** and the path length from a model node ***b*** differ as a function of the station location. After correcting the EGF phase spectrum at each station for the path difference, ***a-b***, we have path-specific Green's functions for each node. (c) The top panel shows the theoretical waveforms for two point sources (red for the northern node and green for the southern node) separated by 40 km and recorded at six regional distances. The lower panel shows a comparison of the theoretical Green's functions of the northern node (green waveforms) and the path-difference corrected signals (red waveforms) using the southern node as an EGF corrected to the northern node position. Stations are selected from those used in LFM inversion, with station names, azimuths and distances marked ahead of each trace.

As a test, two theoretical Green's functions were calculated for two nodes separated by 40 km. Then the waveforms for one node are corrected to the other node location using the differential path distances to several stations using the theoretical dispersion curve. The corrected Green's functions show good phase consistency with the Green's functions at the target node (Figure 6.8c). Any small amplitude discrepancies due to radiation pattern differences will not impact our conclusions about rupture velocity since the rupture velocity is mainly related to the timing or phase, in contrast with the absolute moment scale, which is more related to the waveform amplitude.

The EGF correction accounts for the propagation on the main portion of the ray-path for ~1000 km. However, a model-based correction is still needed to adjust the differential travel times near the source. One concern about the phase correction accuracy comes from uncertainty of the dispersion curves. The corrected Green's functions span 160 km along the fault strike, involving 0-135 km differential travel distances from the EGF. If our reference model is inaccurate, the northernmost node will suffer the maximum phase error. Assuming a maximum 135 km differential travel distance, the differential travel time is ~45 s at 0.05 Hz and ~30 s at 0.01 Hz. If we assume our reference model has an average error of 5%, then the travel time discrepancy introduced by the reference model uncertainty is ~2 s for 0.05 Hz and ~1.5 s for 0.01 Hz. Thus, our phase correction suffers at most 10% phase error, and will be much smaller for the dominant frequency and the majority of nodes.

6.5.2 Model parameterization

Because no depth correction is applied to the EGF (the vertical finiteness of that event is uncertain), the inversion with EGF-corrected Green's functions is constrained to a "linear" fault model (LFM), without along-dip parameterization. The LFM is parameterized with the same along-strike parameters as the FFM, with 16 nodes having increments of 10 km extending 160 km along strike. The source is again selected to be the 5th node along strike from the south, allowing for a northward-dominated rupture. The same multi-time window inversion is applied to the LFM, in which the source time function of each node is parameterized the same as in the FFM inversion.

5.3 Regional Surface wave datasets

56 Love wave (G1) records and 46 Rayleigh wave (R1) records at regional distances <1000 km, are used in a joint inversion. An azimuth window is applied to pre-select the data, to exclude stations within 30 degrees from Love or Rayleigh wave nodal directions. We do not invert the data jointly with near-regional data or teleseismic data, given the different nature of the Green functions. G1 signals are extracted from transverse components and R1 signals from vertical components for both the EGF and mainshock. A theoretical dispersion curve of the fundamental G1 and R1 modes is computed from the local 1D model. A 1000 s long time window is used to extract the raw data and Green's functions, starting from the earthquake initiation time. A group velocity window from 3-5 km/s is used to isolate the energy of the fundamental mode wave packages. Both Green's functions and data are filtered with a causal band-pass filter, with corner frequencies at 0.01 and 0.05 Hz.

For each node, the corrected Green's functions are used in a non-negative least squares inversion, which imposes the assumption that the focal mechanism produced in the mainshock

inversion is identical to that of the EGF, so no rake-variation along strike is allowed. Similar to FFM inversion, when imposing a *Vr*, the inversion is constrained to the solution space with rupture velocity no larger than that *Vr*.

6.5.4 Inversion Results

For *Vr* of 4 to 5 km/s, the source time function of each node is delimited by the specified rupture front and the length of the slip distribution increases with *Vr*, indicating underestimation of *Vr*. In contrast, for *Vr* of 6 to 7 km/s, the source functions indicate lower apparent rupture velocities in the range 5.5 to 6.0 km/s and the inversion residual waveform mismatch does not reduce much with increasing *Vr* (Figure 6.9). All waveform fits are shown in Figure 6.S2a,b. The moment distribution on the linear fault model is very similar for inversions with *Vr* = 6.0 km/s and 7.0 km/s, with strong similarity to the slip pattern of FFM inversions that used completely independent data sets for *Vr* = 6.0 km/s and 7.0 km/s. The preferred LFM model has *Vr* = 6.0 km/s, as for the FFM inversion, with rupture extending ~30 km to the south and ~100 km to the north of the hypocenter. Regions of large slip are located ~10 km and ~70 km north of the hypocenter, similar to what was found in the FFM inversions. The total seismic moment for the LFM model is 2.6×10^{20} Nm, giving a magnitude of $M_w = 7.54$.

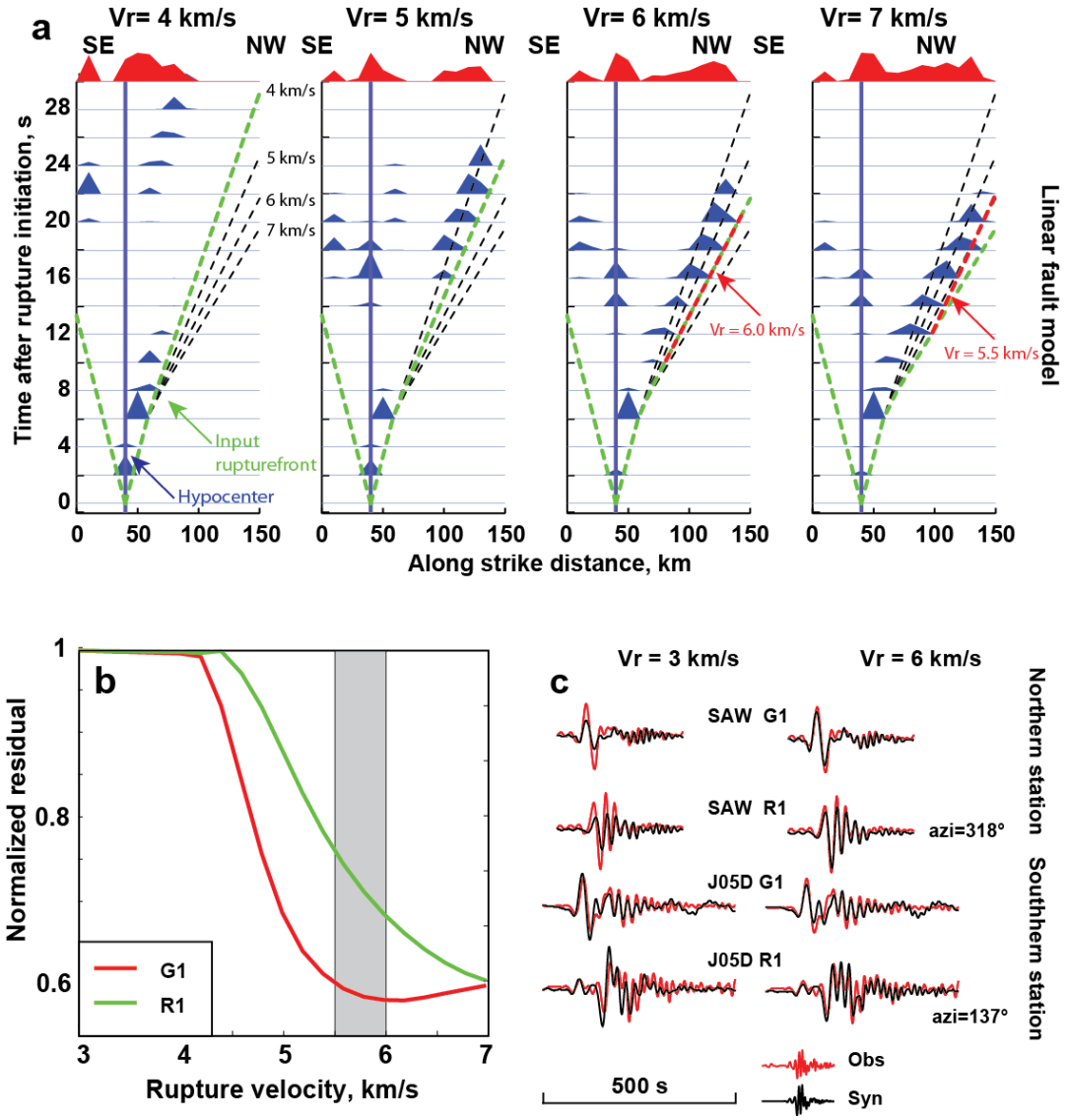

Figure 6.9. (a) Along-strike moment rate patterns for linear-fault model (LFM) inversions with different rupture velocities, *Vr*. The inversion used 46 Rayleigh wave (R1) and 56 Love wave (G1) recordings. The hypocenter is marked with a blue line. Prescribed rupture fronts are shown as green-dashed lines. Reference rupture front curves for *Vr* = 4, 5， 6 and 7 km/s are shown as black dashed lines. For the *Vr* = 6.0 km/s and 7.0 km/s cases, the inverted solutions yield effective rupture velocity of 5.5 km/s and 6.0 km/s, respectively, marked with red dashed lines. (b) Trade-off curves for normalized inversion residual versus input rupture velocity. Red and green curves are residuals of G1 and R1 waves, respectively, normalized by the maximum residual at *Vr* = 3 km/s. The range of preferred rupture velocity (5.5 km/s – 6.0 km/s) is shaded. (c) Examples of waveform fitting improvements when model rupture velocity increases from 3 km/s to 6 km/s. The observed and predicted waveforms are plotted in red and black, respectively. The complete set of waveform fits for the LFM are shown in Figures S2a, S2b.

The peak-to-peak surface wave maximum amplitude ratio between the main event and the EGF

event shows significant contrast between the northern and southern stations (Figure 6.10) due to the rupture propagation effect. At the northern stations, both Love and Rayleigh waves indicate an amplitude ratio of 800-1000, which is close to the moment ratio between the main event and the EGF event. At the southern stations, the amplitude ratio is ~300, which is 3 to 4 times smaller than for the northern stations as a consequence of the northward directivity. The amplitude ratio was also calculated between the LFM inversion synthetics and the EGF surface waves. The amplitudes are generally well matched at southern stations for different *Vr*, but the fit improved with increasing rupture velocity for the northern stations. The Love wave amplitude ratio could be fit well with a rupture velocity of 6 or 7 km/s, however these models underestimate the Rayleigh wave amplitudes by about ~20%. Part of the differential fitting behavior may be attributed to the different station distributions between Love and Rayleigh waves used in the inversion. The Love wave stations distribute along both sides of the strike direction, and are particularly sensitive to the in-plane rupture propagation, however, nodal along-strike stations are removed for the Rayleigh waves, so the Rayleigh waves are less sensitive to the rupture propagation. Only a few northern stations are used in the LFM inversions for Rayleigh waves, thus the inversion results are mainly controlled by the Love waves. The preferred rupture velocity is primarily determined from the Love wave trade-off curve. The strong amplitude variations are generally compatible with generic modeling of supershear rupture [e.g., *Bizzarri and Spudich*, 2008; *Bizzarri et al.*, 2010], and clearly demonstrate the enhanced seismic shaking hazard presented by supershear faulting of strike-slip events.

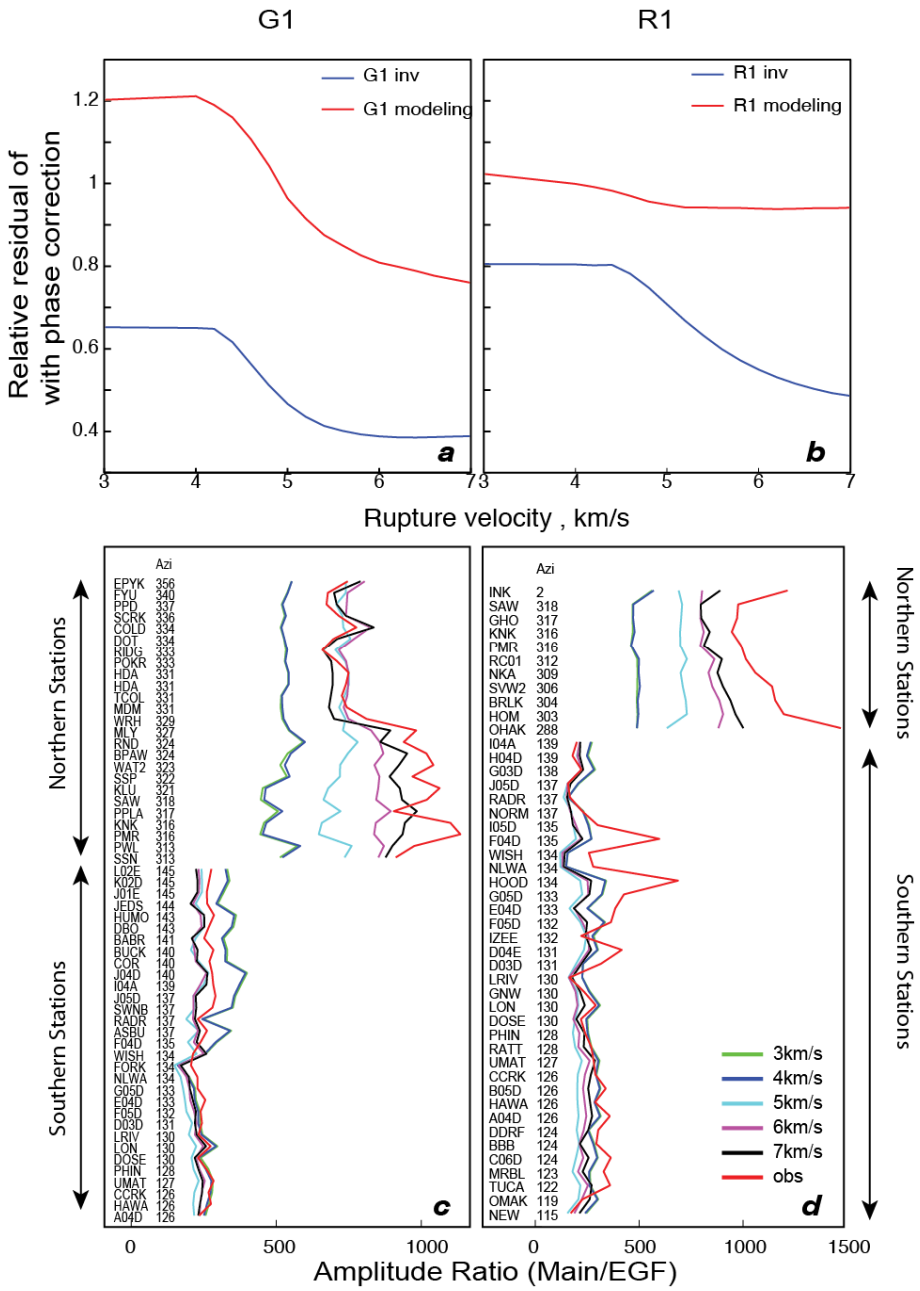

Figure 6.10. The mis-fit residual versus *Vr* trade-off curves produced by full waveform linear-fault model (LFM) inversions (blue curves) and finite-fault model (FFM) based forward predictions (red curves), using EGF signals at each station corrected for grid location using theoretical phase velocities for (a) Love waves, and (b) Rayleigh waves. Residuals are normalized by the squared norm of the waveforms. Love wave (c) and Rayleigh wave (d) peak-to-peak amplitude ratios (Main event/EGF event) at each station are plotted for synthetic and observed (red) G1 and R1 waves. Stations are sorted by their azimuths. Amplitude ratios for input rupture velocities of 3 to 7 km/s are compared with observations. Station names and azimuths are indicated to the left of the curves.

6.6. Finite Fault Model and Linear Fault Model Comparison

A forward modeling technique was applied using FFM results to predict waveforms using the phase-velocity-corrected empirical Green functions. We computed a corrected EGF (c-EGFs) database for each grid of the FFM, then the moment distribution of FFM results for a given rupture velocity are used to weight the c-EGFs and sum them to give a simulated waveform. This yields broadband waveforms for comparison with each observation that allow direct comparison between the FFM and LFM results. The waveform misfit residuals are normalized by the square norm of the observed waveforms, indicating the percentage of misfit signal (Figure 6.10a,b). The forward modeling approach gives higher residuals than the inversion because the inversion more fully explores the source parameter space, improving the waveform fitting. The Love wave modeling approach produces similar decreasing residuals as rupture velocity in the FFM increases to 5.5-6.0 km/s. The Rayleigh wave modeling residuals are less pronounced, but also decrease as *Vr* increases. In both modeling and inversion results, the residual decrease as *Vr* increases is clear, indicating consistent supershear rupture velocities.

The rupture velocity estimated from the residual trade-off curves of both the FFM and LFM inversions is in the range 5.5 – 6.0 km/s. The *Vr* could also be directly measured from the along-strike moment distributions. The along-strike moment distribution shows a similar pattern between the LFM and depth-stacked FFM results. When the input *Vr* is smaller than the real *Vr*, the moment abuts the allowed rupture front; when the input *Vr* is larger than the true *Vr*, the inversion tends to define an effective rupture velocity that is lower than the maximum allowed. For *Vr* = 6 km/s and 7 km/s, the effective rupture velocity is measured as 5.5 to 6.0 km/s from the LFM inversion results (Figure 6.9a) and the same values are found for FFM inversions. This is

consistent with the rupture velocity estimated from the waveform mismatch trade-off curves (Figs. 7c, 9b). It is important to note that minor moment still abuts the allowed rupture front for Vr = 7.0 km/s, so tracing the first non-zero moment will recover the input rupture velocity of Vr = 7.0 km/s. How to select the initial significant moment on each node presents challenges for evaluating the moment rate functions of each node objectively. Measuring the rupture velocity gives an indication of how apparent rupture velocity differs from the input rupture velocity, but may not provide a precise measurement of true rupture velocity.

Local rupture velocity varies over the northern segment, but detailed measurement for each segment does not yield consistent rupture velocity patterns for different inversions. Such rupture velocity details may not be resolved stably in either FFM or LFM inversions, but the overall supershear rupture with an average rupture velocity of 5.5 to 6.0 km/s is robust.

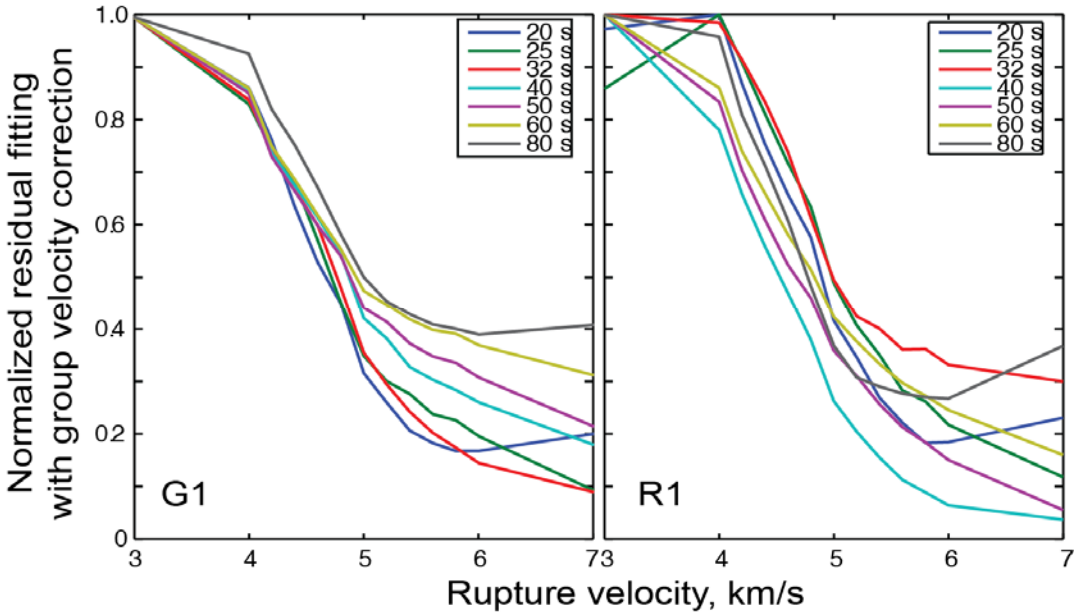

Figure 6.11 . Trade-off curves of forward modeling normalized mis-fits to narrow-band Love wave (G1) and Rayleigh wave (R1) signals for varying rupture velocities for different central period passbands, plotted with different colors. Observed average group velocity curves provide group velocity corrections for the corresponding narrow-band filtered EGF signals for differential path lengths from each grid node to each station. The finite-fault model (FFM) inversion results for each *Vr* are used to predict the narrow-band filtered mainshock waveforms with the corrected EGF signals being used as Green's functions along the fault.

Local rupture velocity varies over the northern segment, but detailed measurement on each segment doesn't yield consistent rupture velocity pattern for different inversions. Such rupture velocity details may not be resolved stably in either FFM or LFM inversions, but the overall supershear rupture with an average rupture velocity of 5.5km/s to 6.0 km/s is robust.

7. Modeling With Group Velocity Corrections

Waveform inversion of regional surface waves with the phase velocity correction may slightly suffer from reference velocity model inaccuracy since a theoretical dispersion curve is used for EGF correction. One technique that can eliminate reference model inaccuracy involves using

empirical group velocity corrections, which relies on the measured group velocity at each station to compute a group arrival time shift for different passbands. Our group velocity correction procedure follows these steps:

1. Measure the group velocity for each path using the peak amplitude arrival time of different narrow band-pass filters, obtaining group velocity dispersion curves for regional Love and Rayleigh waves. Dispersion curves are extracted from both mainshock and EGF signals, and we find good consistency.
2. Band-pass the EGF waveform with a sequence of narrow frequency windows that produce EGF wave-packets at different band-passes.
3. Apply station and wave type specific time correction to the multi-band-passed EGF wave-packets, correcting for the differential propagation lengths from each node on the mainshock model relative to the EGF path lengths.
4. Use surface wave geometric spreading factors to correct for differences in propagation length of the Green's function databases.

In this way, the EGF signals are corrected to any location in the near source region, giving a corrected EGF (c-EGF) database for a range of narrow band filtered windows. The seismic moment of the FFM results for different assumed *Vr* are then used to produce synthetics for a given passband using the c-EGF signals along the fault model. Comparison of the modeled and observed waveforms for different band-passes provides an evaluation of the FFM result reliability for an independent data set. The waveform-mismatch residual versus FFM *Vr* trade-off curves for rupture velocities from 3 to 7 km/s are computed (Figure 6.11). A consistent residual reduction

with increasing rupture velocity from *Vr* = 3 to 7 km/s, is found over all passbands from 20 s to 100 s. The minimum residual is found for *Vr* = 5 to 6 km/s, which produce an 80% - 60% residual reduction relative to the residual for *Vr* = 3 km/s.

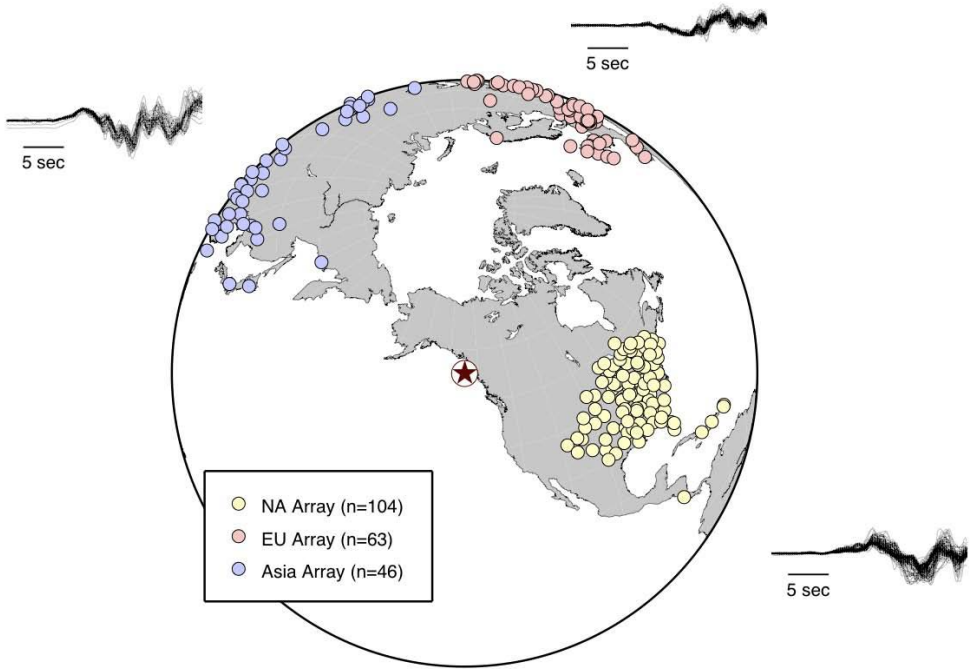

Figure 6.12. Locations of seismic stations recording teleseismic P waves used to back-project the space-time history of short-period radiation for the 2013 Craig earthquake. The stations are grouped into three arrays based on azimuth from the source and the data from each array are back-projected separately. Unfiltered, vertical component P waves from each array are shown along the plot border after being aligned and normalized with a multichannel cross-correlation algorithm. The high signal coherence of the broadband P arrivals allows stable initial alignment of the short-period arrivals.

This procedure relies only on observed information, such as the EGF waveforms and the measured group velocity dispersion curves, so it reduces uncertainty introduced by a reference model other than that affecting the FFM. The residual trade-off curve provides an independent and objective evaluation of the FFM results for a distinct data set, giving supportive evidence for a

supershear rupture velocity.

6.8. Back-Projection of Teleseismic P waves

Teleseismic P waves from three regional groupings of global broadband seismometers were back-projected to the source region [*Xu et al.,* 2009] in order to image the short-period rupture properties of the 5 January 2013 Craig, Alaska earthquake. In each case the NEIC location of 55.394° N 134.650° W, h=7.1 km, 08:58:19 (UTC) was used as a reference for aligning the waveforms. The source area was gridded in increments of 0.1° in latitude and longitude and depth was held constant at the nominal hypocentral value. Power was calculated from a 10 s long, tapered window that slides along beams created with fourth-root stacking. Traces were bandpass filtered between 0.5 and 2 s prior to being stacked, and the AK135 reference Earth model was used to calculate travel times.

All the data used in the back-projection analysis were downloaded from the IRIS DMC. A multi-channel cross correlation analysis [*VanDecar and Crosson,* 1990] was used to select similar waveforms. For the Asia array 46 traces with mean correlation coefficients above 0.85 were retained, for the North America array 104 traces with mean correlation coefficients above 0.87 were retained, and for the Europe array 63 traces with mean correlation coefficients above 0.8 were retained (Figure 6.12). The cross-correlations were performed on unfiltered, vertical component velocity waveforms using a window that started 5 s before the theoretical P arrival and extended for either 15 or 20 s.

Time-integrated images of the back-projected power for each station array are shown in Figure 6.13. Animations of the time-varying sequences are in Animation S1. Comparison of the Asian

back-projections for the mainshock and EGF event are shown in Animation S2 to convey the degree of space-time smearing of the image for a relative point-source event (the EGF), compared to the finite-rupture of the mainshock.

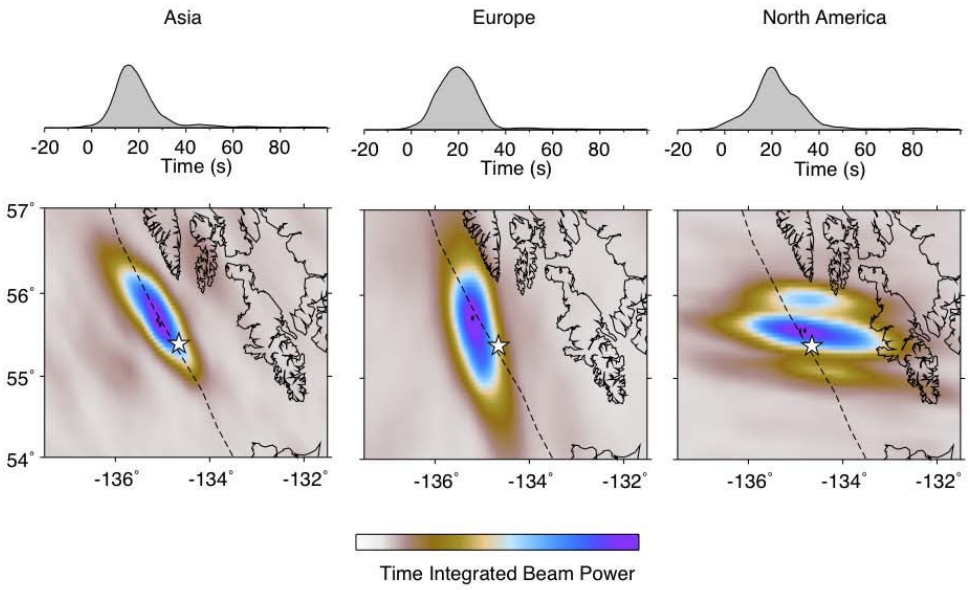

Figure 6.13. Time-integrated images from back-projection results for the three teleseismic arrays considered in this study. In each panel the star represents the epicenter and the dashed line represents the boundary between the North American and Pacific plates. All three analyses indicate a dominantly northern rupture, with energy extending at least as far north as 56° N, similar to the extent of aftershocks occurring in the first month after the mainshock (Figure 6.1). Weaker energy is observed just to the south of the epicenter. The time evolution of peak beam power shown atop the panels is influenced by a 10 s long smoothing window and the actual duration of short-period energy release is less than 40 s.

6.9. Discussion

The seismic and geodetic ground motion analyses discussed here all indicate that the 2013 Craig earthquake had supershear rupture velocity in the range 5.5 to 6.0 km/s along the northern portion of the rupture and sub-shear rupture expansion to the south. Theoretical and experimental studies of bi-material mode II ruptures, with a velocity contrast across the fault, indicate that

supershear rupture will be more likely in the direction of motion of the high seismic velocity side of the fault, with a velocity slightly lower than the P wave velocity of the slow side [*Xia et al.*, 2005; *Cochard and Rice,* 2000]. For the Queen Charlotte Fault (Figure 6.1), the fast side is the oceanic plate, which is moving northward, consistent with observed northward supershear rupture direction. Our estimates of rupture velocity, 5.5 to 6.0 km/s approach the P wave velocity of 6.6 km/s in the mid-crust (10 km) of the continental side [*Horn et al.,* 1984]

In a few previous studies of supershear rupture, aftershocks are inferred to be activated on off-fault branches, and there is relatively low aftershock production on the main fault plane as a result of large stress drop [*Bouchon and Karabulut,* 2008]. The Mach waves can also cause off-fault damage patterns that could be diagnostic of supershear rupture [*Bhat et al*., 2007], but this will not be accessible for an offshore event. For the 2013 Craig earthquake, most aftershocks locate along the plate boundary, but some are located away from the trace of the Queen Charlotte Fault. Three aftershocks with $M_w > 4.5$ have focal mechanism determinations (Figure 6.1), two of which are consistent with rupture on the Queen Charlotte Fault, whereas the largest aftershock, M_w 5.9 event on 31 January 2013 (Figure 6.1), ruptured a differently-oriented fault. It is important to notice that the previous supershear events mostly involve intraplate or continental events, where complex stress and structure heterogeneities may be present near the fault zone. For the Craig interplate event the shear-loading is released along a major plate boundary. The aftershock behavior may be affected by the strong material contrast across the ocean/continent boundary or the absence of pre-existing fault branches.

It is also indicated in previous studies that supershear rupture may be related to a full stress release that prevents aftershocks on the main fault plane [*Bouchon and Karabulut,* 2008].

Theoretically the supershear rupture may be related to a high stress drop relative to the strength drop near the crack tip [*Andrews,* 1976]. For our finite fault model of the 2013 Craig event, it is hard to resolve dynamic stress drops, but the average static stress drop is approximately 9 MPa, measured from the final rupture pattern. Such a stress drop is about three times the average stress drop of interplate events and close to typical intraplate event stress drop [*Kanamori and Anderson,* 1975]. It is hard to tell whether this slightly elevated stress drop is complete because the pre-stress state is not known. Aftershocks do occur along the primary slip area laterally, but these could locate beneath or above the co-seismic slip area given the uncertainties in depth distribution. Further relocation efforts will be needed to determine whether any aftershocks co-locate with the co-seismic slip regions. This would help to determine whether total stress drop occurred in this supershear event.

The 2013 Craig, Alaska event is the first oceanic interplate event reported to have involved supershear rupture, and it is the first offshore event for which multiple data sets independently indicate supershear rupture. Occurrence of supershear rupture has been associated with straight fault segments and termination of supershear with fault bending and splaying [*Das*, 2007; *Robinson et al*., 2010; *Bouchon et al.* 2010]. The Queen Charlotte Fault does appears to be relatively straight in the northern supershear rupture area, but the geometry is not known precisely and there is not a readily apparent explanation for the termination of rupture in the north other than it is near the southern end of the rupture zone for the 30 July 1972 Sitka, Alaska (M_w 7.6) earthquake, so the pre-stress may be low north of the rupture zone. Stress heterogeneity on the fault likely plays a role in enabling and delimiting supershear [*Schmedes et al.,* 2010], but the offshore location of the fault limits our understanding of fine structure that might be

manifestations of such stress heterogeneity. While measurements very close to the fault were not possible, the combined geodetic and seismic observations for the 2013 event still give one of the most robust characterizations of supershear rupture to date.

6.10. Conclusions

The 2013 M_w 7.5 Craig, Alaska event is found to have had a supershear rupture velocity using several independent modeling and inversion techniques.

Sg and Sn pre-hypocentral arrivals have been detected with a EGF reference time technique, and indicate that the northward rupture velocity of >4.5 km/s for the Craig event surpassed the crustal and upper-mantle shear velocity. The northward supershear rupture process produced significant short-period shaking enhancement, almost one order of magnitude larger to the north, consistent with models of *Bizzarri and Spudich* [2008].

Finite fault model inversions with regional geodetic/seismic and teleseismic observations and linear fault model inversions using regional seismic observations, indicate a rupture velocity of 5.5 to 6.0 km/s. Forward modeling procedures, using theoretical phase velocity or group velocity corrections indicate significant waveform fitting residual decreases with increasing rupture velocity. The rupture velocity is consistent with that resolved by the inversions.

The 2013 Craig, Alaska event rupture extends about 100 km northward from the hypocenter, with about 80 km of supershear rupture. Two significant energy release peaks have been identified along the strike direction located 20 km and 70 km north of the hypocenter. The rupture initially extended ~20-30 km to the north and south with subshear rupture. The northward supershear rupture direction may be related to the strong material contrast across the continental-oceanic plate

boundary.

6.11Acknowledgements. We thank Emily Brodsky and Hiroo Kanamori for exchanging ideas on supershear rupture. Eric Dunham and an anonymous reviewer provided helpful comments. We thank Charles Ammon for providing his group velocity analysis code. The Incorporated Research Institutions for Seismology data management center and the Canadian National Seismic Network data center provided seismic data seismic data from global stations and the Alaska Regional Seismic Network. GPS data were provided by the EarthScope Plate Boundary Observatory data center. This work was supported in part by NSF under grants EAR-1245717 (T.L.) and EAR-0911764 (J.F.).

6.12 References

Andrews, D. J. (1976), Rupture velocity of plane strain shear cracks, *Journal of Geophysical Research*, *81*(32), 5679-5687.

Andrews, D. J. (1985), Dynamic plane-strain shear rupture with a slip-weakening friction law calculated by a boundary integral method, *Bulletin of the Seismological Society of America*, *75*(1), 1-21.

Andrews, D. J. (2010), Ground motion hazard from supershear rupture, *Tectonophysics*, *493*(3–4), 216-221.

Aochi, H., V. Durand, and J. Douglas (2011), Influence of supershear earthquake rupture models on simulated near-source ground motion from the 1999 Izmit, Turkey, earthquake, *Bulletin of the Seismological Society of America*, *101*(2), 726-741.

Archuleta, R. J. (1984), A faulting model for the 1979 Imperial Valley earthquake, *Journal of Geophysical Research*, *89*(B6), 4559-4585.

Bhat, H. S., R. Dmowska, G. C. P. King, Y. Klinger, and J. R. Rice (2007), Off-fault damage patterns due to supershear rupture with application to the 2001 M_w 8.1 Kokoxili (Kunlun) Tibet earthquake, *Journal of Geophysical Research, 112*, B06301, doi:10.1029/2006JB004425.

Birgören, G., H. Sekiguchi, and K. Irikura (2004), Rupture model of the 1999 Düzce, Turkey, earthquake deduced from high and low frequency strong motion data, *Geophysical research letters*, *31*(5), L05610.

Bizzarri, A., and P. Spudich (2008), Effects of supershear rupture speed on the high-frequency content of S waves investigated using spontaneous dynamic rupture models and isochrones theory, *Journal of Geophysical Research, 113*, B05304, doi:10.1029/2007JB005146.

Bizzarri, A., E. M. Dunham, and P. Spudich (2010), Coherence of Mach fronts during heterogeneous supershear earthquake rupture propagation: Simulations and comparison with observations, *Journal of Geophysical Research*, *115*, B08301, doi:10.1029/2009JB006819.

Bouchon, M., and H. Karabulut (2008), The aftershock signature of supershear earthquakes, *Science*, *320*(5881), 1323-1325.

Bouchon, M., H. Karabulut, M.-P. Bouin, J. Schmittbuhl, M. Vallée, R. Archuleta, S. Das, F. Renard, and D. Marsan (2010), Faulting characteristics of supershear earthquakes, *Tectonophysics*, *493*(3–4), 244-253.

Bouchon, M., M. N. Toksöz, H. Karabulut, M.-P. Bouin, M. Dietrich, M. Aktar, and M. Edie (2002), Space and time evolution of rupture and faulting during the 1999 İzmit (Turkey) Earthquake, *Bulletin of the Seismological Society of America*, *92*(1), 256-266.

Bouchon, M., M.-P. Bouin, H. Karabulut, M. N. Toksöz, M. Dietrich, and A. J. Rosakis (2001), How fast is rupture during an earthquake? New insights from the 1999 Turkey earthquakes, *Geophysical Research Letters*, *28*(14), 2723-2726.

Bouchon, M., and M. Vallée (2003), Observation of long supershear rupture during

the magnitude 8.1 Kunlunshan earthquake, *Science*, *301*(5634), 824-826.

Bouin, M. P., M. Bouchon, H. Karabulut, and M. Aktar (2004), Rupture process of the 1999 November 12 Düzce (Turkey) earthquake deduced from strong motion and Global Positioning System measurements, *Geophysical Journal International*, *159*(1), 207-211.

Burridge, R. (1973), Admissible speeds for plane-strain self-similar shear cracks with friction but lacking cohesion, *Geophysical Journal of the Royal Astronomical Society*, *35*(4), 439-455.

Burridge, R., G. Conn, and L. B. Freund (1979), The stability of a rapid Mode II shear crack with finite cohesive traction, *Journal of Geophysical Research, 85*(B5), 2210-2222.

Choy, G. L., and J. Boatwright (2004), Radiated energy and the rupture process of the Denali Fault earthquake sequence of 2002 from broadband teleseismic body waves, *Bulletin of the Seismological Society of America, 94*(6B), S269-2S77.

Cochard, A., and J. R. Rice (2000), Fault rupture between dissimilar materials: Ill-posedness, regularization, and slip-pulse response, *Journal of Geophysical Research: Solid Earth*, *105*(B11), 25891-25907.

Das, S. (2007), The need to study speed, *Science*, *317*(5840), 905-906.

Day, S. M. (1982), Three-dimensional simulation of spontaneous rupture: The effect of nonuniform prestress, *Bulletin of the Seismological Society of America, 72*(6), 1881-1902.

Dunham, E. M. (2005), The dynamics and near-source ground motion of supershear earthquakes, Ph.D. Thesis, University of California, Santa Barbara, 225 pp.

Dunham, E. M., and H. S. Bhat (2008), Attenuation of radiated ground motion and stresses from three-dimensional supershear ruptures, *Journal of Geophysical Research: Solid Earth*, *113*(B8), B08319, doi:10.1029/2007JB005182.

Dunham, E. M., and R. J. Archuleta (2004), Evidence for a supershear transient during the 2002 Denali Fault earthquake, *Bulletin of the Seismological Society of America*, *94*(6B), S256-S268.

Dunham, E. M., P. Favreau, and J. M. Carlson (2003), A supershear transition mechanism for cracks, *Science*, *299*(5612), 1557-1559.

Ellsworth, W. L., M. Celebi, J. R. Evans, E. G. Jensen, R. Kayen, M. C. Metz, D. J.

Nyman, J. W. Roddick, P. Spudich, and C. D. Stephens (2004), Near-field ground motion of the 2002 Denali Fault, Alaska, earthquake recorded at pump station 10, *Earthquake Spectra, 20*(3), 597-615.

Festa, G., and J.-P. Vilotte (2006), Influence of the rupture initiation on the intersonic transition: Crack-like versus pulse-like modes, *Geophysical Research Letters, 33*, L15320, doi:10.1029/2006GL026378.

Frankel, A. (2004), Rupture process of the M 7.9 Denali Fault, Alasak, earthquake: Subevents, directivity, and scaling of high-frequency ground motions, *Bulletin of the Seismological Society of America, 94*(6B), S234-S255.

Freund, L. B. (1979), The mechanics of dynamic shear crack propagation, *Journal of Geophysical Research: Solid Earth*, *84*(B5), 2199-2209.

Fu, Y., and J. T. Freymueller (2012), Seasonal and long-term vertical deformation in the Nepal Himalaya constrained by GPS and GRACE measurements, *Journal of Geophysical Research: Solid Earth*, *117*(B3), B03407.

Hartzell, S. H., & Heaton, T. H. (1983). Inversion of strong ground motion and teleseismic waveform data for the fault rupture history of the 1979 Imperial Valley, California, earthquake. *Bull. Seism. Soc. Amer.,73*(6A), 1553-1583.

Horn, J. R., R. M. Clowes, R. M. Ellis, and D. N. Bird (1984), The seismic structure across an active oceanic/continental transform fault zone, *Journal of Geophysical Research: Solid Earth*, *89*(B5), 3107-3120.

Kanamori, H., and D. L. Anderson (1975), Theoretical basis of some empirical relations in seismology, *Bulletin of the Seismological Society of America*, *65*(5), 1073-1095.

Kaneko, Y., and N. Lapusta (2010), Supershear transition due to a free surface in 3-D simulations of spontaneous dynamic rupture on vertical strike-slip faults, *Tectonophysics*, *493*(3–4), 272-284.

Kikuchi, M., H. Kanamori, and K. Satake (1993), Source complexity of the 1988 Armenian earthquake: Evidence for a slow after-slip event, *Journal of Geophysical Research: Solid Earth*, *98*(B9), 15797-15808.

Konca, A. O., S. Leprince, J.-P. Avouac, and D. V. Helmberger (2010), Rupture process of the 1999 M_w 7.1 Duzce earthquake from joint analysis of SPOT, GPS, InSAR, strong-motion, and teleseismic data: A supershear rupture with variable rupture velocity, *Bulletin of the Seismological Society of America*, *100*(1), 267-288.

Lawson, C. L., and R. J. Hanson (1995), *Solving least squares problems*, Society for Industrial Mathematics.

Lay T., Ye L., Kanamori K., Yamazaki Y., Cheung K. F., Kwong K., Koper K. D., (2013), The October 28, 201 M_w 7.8 Haida Gwaii underthrusing earthquake and tsunami: Slip partitioning along the Queen Charlotte fault transpressional boundary. *Earth Planet. Sci. Lett.*, *375*, 57-70. http://dx.doi.org/10.1016/j.epsl.2013.05.005.

Liu, Y., and N. Lapusta (2008), Transition of mode II cracks from sub-Rayleigh to intersonic speeds in the presence of favorable heterogeneity, *Journal of the Mechanics and Physics of Solids*, *56*(1), 25-50.

Mello, M., H. S. Bhat, A. J. Rosakis, and H. Kanamori (2010), Identifying the unique ground motion signatures of supershear earthquakes: Theory and experiments, *Tectonophysics*, *493*(3–4), 297-326.

Mena, B., L. A. Dalguer, and P. M. Mai (2012), Pseudodynamic source characterization for strike-slip faulting including stress heterogeneity and super-shear ruptures, *Bulletin of the Seismological Society of America, 102*(4), 1654-1680, doi:10.1785/0120110111.

Meng, L., J.-P. Ampuero, J. Stock, Z. Duputel, Y. Luo, and V. C. Tsai (2012), Earthquake in a maze: Compressional rupture branching during the 2012 M_w 8.6 Sumatra earthquake, Science, 337(6095), 724–726,doi:10.1126/science.1224030.

Morozov, I. B., S. B. Smithson, L. S. Hollister, and J. B. Diebold (1998), Wide-angle seismic imaging across accreted terranes, southeastern Alaska and western British Columbia, *Tectonophysics*, *299*(4), 281-296.

Olsen, K. B., R. Madariaga, and R. J. Archuleta (1997), Three-dimensional dynamic simulation of the 1992 Landers earthquake, *Science 278*, 834-838.

Passelègue, F. X., A. Schubnel, S. Nielsen, H. S. Bhat, and R. Madariaga (2013), From sub-Rayleigh to supershear ruptures during stick-slip experiments on crustal rocks, *Science*, *340*(6137), 1208-1211.

Robinson, D. P., C. Brough, and S. Das (2006), The Mw 7.8, 2001 Kunlunshan earthquake: Extreme rupture speed variability and effect of fault geometry, *Journal of Geophysical Research, 111*, B08303, doi:10.1029/2005JB004137.

Robinson, D. P., S. Das, and M. P. Searle (2010), Earthquake fault superhighways, *Tectonophysics, 493*, 236-243.

Rosakis, A. J., O. Samudrala, and D. Coker (1999), Cracks faster than the shear wave speed, *Science*, *284*(5418), 1337-1340.

Schmedes, J., R. J. Archuleta, and D. Lavallée (2010), Dependency of supershear transition and ground motion on the autocorrelation of initial stress, *Tectonophysics*, *493*(3–4), 222-235.

Sekiguchi, H., and T. Iwata (2002), Rupture process of the 1999 Kocaeli, Turkey, earthquake estimated from strong-motion waveforms, *Bulletin of the Seismological Society of America*, *92*(1), 300-311.

Spudich, P., and E. Cranswick (1984), Direct observation of rupture propagation during the 1979 Imperial Valley earthquake using a short baseline accelerometer array, *Bulletin of the Seismological Society of America*, *74*(6), 2083-2114.

Vallée, M., and E. M. Dunham (2012), Observation of far-field Mach waves generated by the 2001 Kokoxili supershear earthquake, *Geophysical research letters*, *39*(5), L05311.

VanDecar, J. C., and R. S. Crosson (1990), Determination of teleseismic relative phase arrival times using multi-channel cross-correlation and least squares,

Bulletin of the Seismological Society of America, *80*(1), 150-169.

Walker, K. T., and P. M. Shearer (2009), Illuminating the near-sonic rupture velocities of the intracontinental Kokoxili M_w 7.8 and Denali fault M_w 7.9 strike-slip earthquakes with global P wave back projection imaging, *Journal of Geophysical Research: Solid Earth*, *114*(B2), B02304.

Wang, D., and J. Mori (2012), The 2010 Qinghai, China, earthquake: A moderate earthquake with supershear rupture, *Bulletin of the Seismological Society of America*, *102*(1), 301-308.

Wang, D., J. Mori, and T. Uchide (2012), Supershear rupture on multiple faults for the M_w 8.6 Off Northern Sumatra, Indonesia earthquake of April 11, 2012, *Geophysical Research Letters*, *39*(21), L21307.

Xia, K., A. J. Rosakis, and H. Kanamori (2004), Laboratory earthquakes: The sub-Rayleigh-to-supershear rupture transition, *Science*, *303*(5665), 1859-1861.

Xia, K., A. J. Rosakis, H. Kanamori, and J. R. Rice (2005), Laboratory earthquakes along inhomogeneous faults: Directionality and supershear, *Science*, *308*(5722), 681-684.

Xu, Y., K. D. Koper, O. Sufri, L. Zhu, and A. R. Hutko (2009), Rupture imaging of the Mw 7.9 12 May 2008 Wenchuan earthquake from back projection of teleseismic P waves, *Geochemistry, Geophysics, Geosystems*, *10*(4), Q04006.

Yue, H., T. Lay, and K. Koper (2012), En échelon and orthogonal fault ruptures of the 11 April 2012 great intraplate earthquakes, *Nature*, 490, 245–249, doi:10.1038/nature11492.

Yue, H., and T. Lay (2013), Source rupture models for the M_w 9.0 2011 Tohoku earthquake from joint inversions of high rate geodetic and seismic data, *Bulletin of the Seismological Society of America*, *103*(2B), 1242-1255.

Yue H., T. Lay, S. Schwartz, L. Rivera, M. Protti, T. H. Dixon, S. Owen, and A. V. Newman (2013) The 5 September 2012 Costa Rica M_w 7.6 earthquake rupture process from joint inversion of high-rate GPS, strong-motion, and teleseismic P wave data and its relationship to adjacent plate boundary interface properties. *Journal of Geophysical Research*, submitted.

Zumberge, J. F., M. B. Heflin, D. C. Jefferson, M. M. Watkins, and F. H. Webb (1997), Precise point positioning for the efficient and robust analysis of GPS data from large networks, *Journal of Geophysical Research: Solid Earth*, *102*(B3), 5005-5017.

6.13 Auxiliary Figures

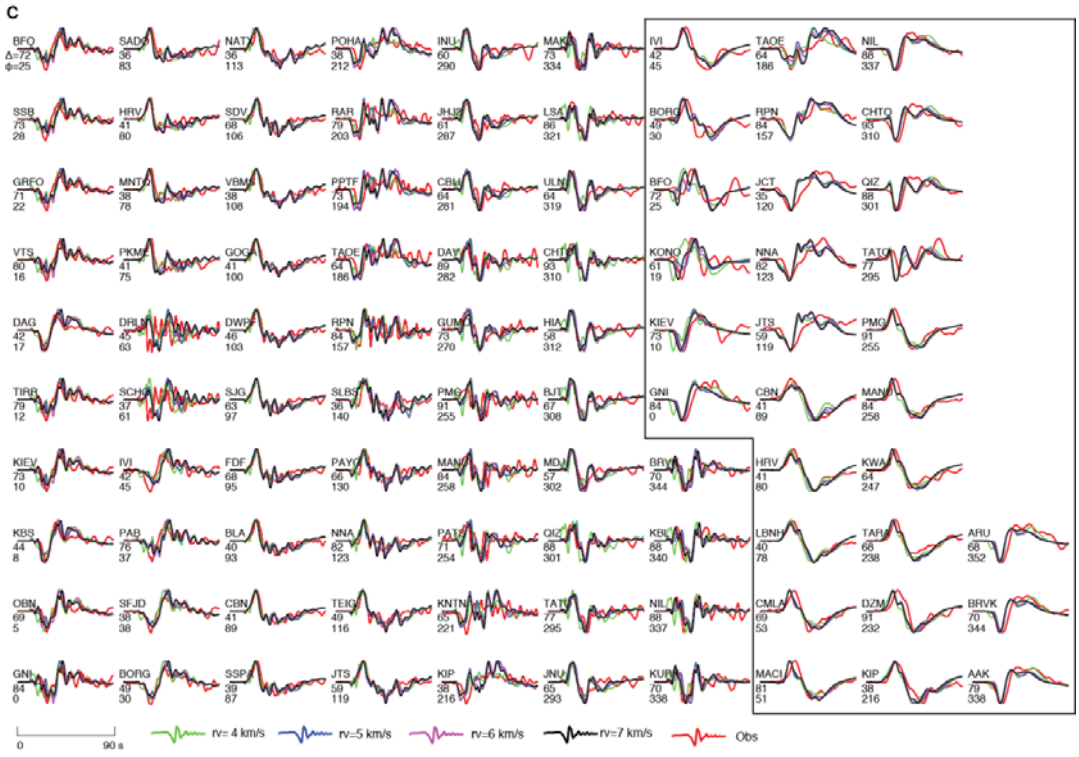

Figure 6.S1. Observed and computed waveforms for teleseismic P and SH signals used in the finite-source inversions. 64 P and 29 SH waves are used. The SH wave records are bounded with a black polygon. Observed waveforms are plotted in red, and modeled waveforms for input rupture velocity of 4.0, 5.0, 6.0, and 7.0 km/s are plotted in green, blue, cyan and magenta, respectively. Station name, epicentral distance ( ) and azimuth ( ) are labeled for each signal.

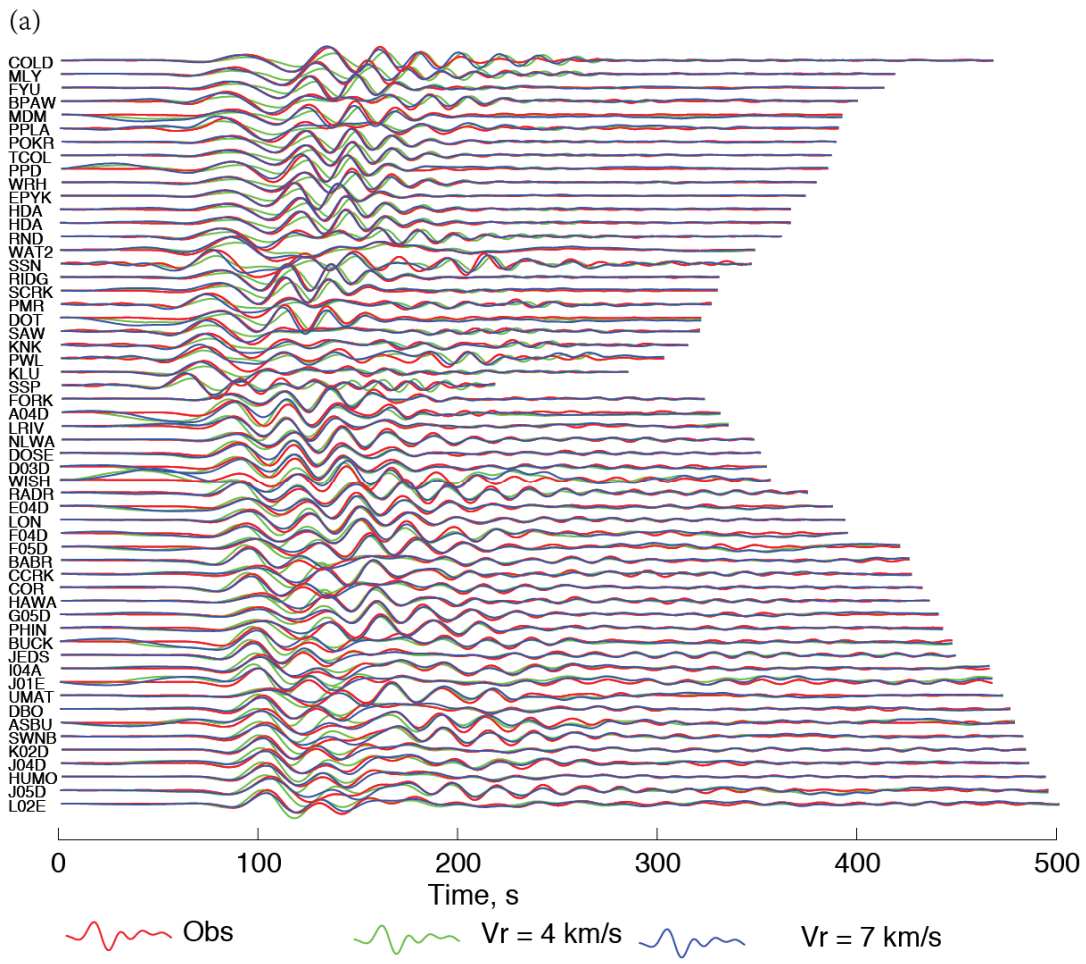

Figure 6.S2. (a) Observed and predicted Love wave (G1) waveforms from 56 regional stations for joint linear-fault model (LFM) inversions with different rupture velocities. The Green functions are from recordings of the EGF event with phase velocity corrections for differential path lengths using the regional seismic velocity model. Observed waveforms are plotted in red. Modeled waveforms for input rupture velocities of 4.0 and 7.0 km/s are plotted in green and black, respectively. (b) The same style display as (a), for 46 Rayleigh wave (R1) waveform recordings.

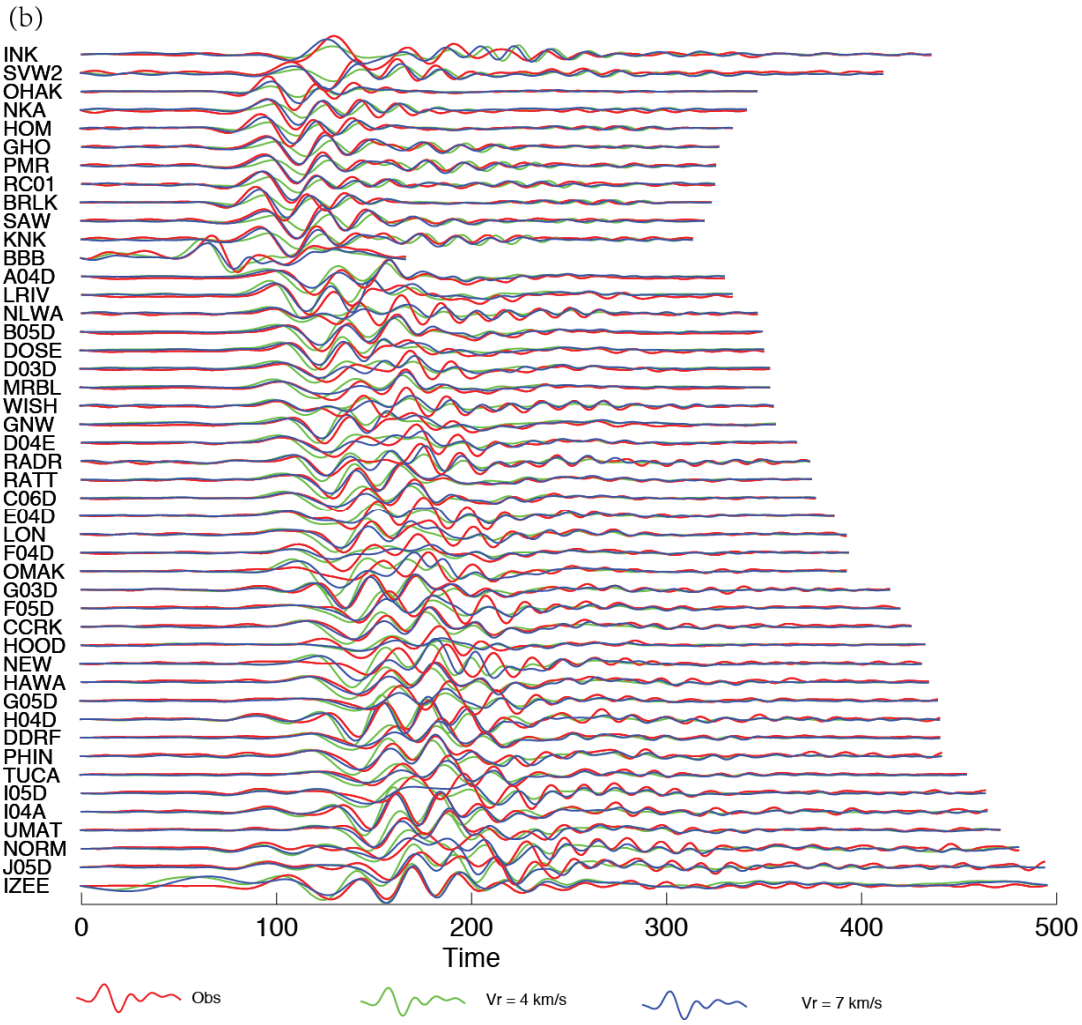

Figure 6.S2 continued.

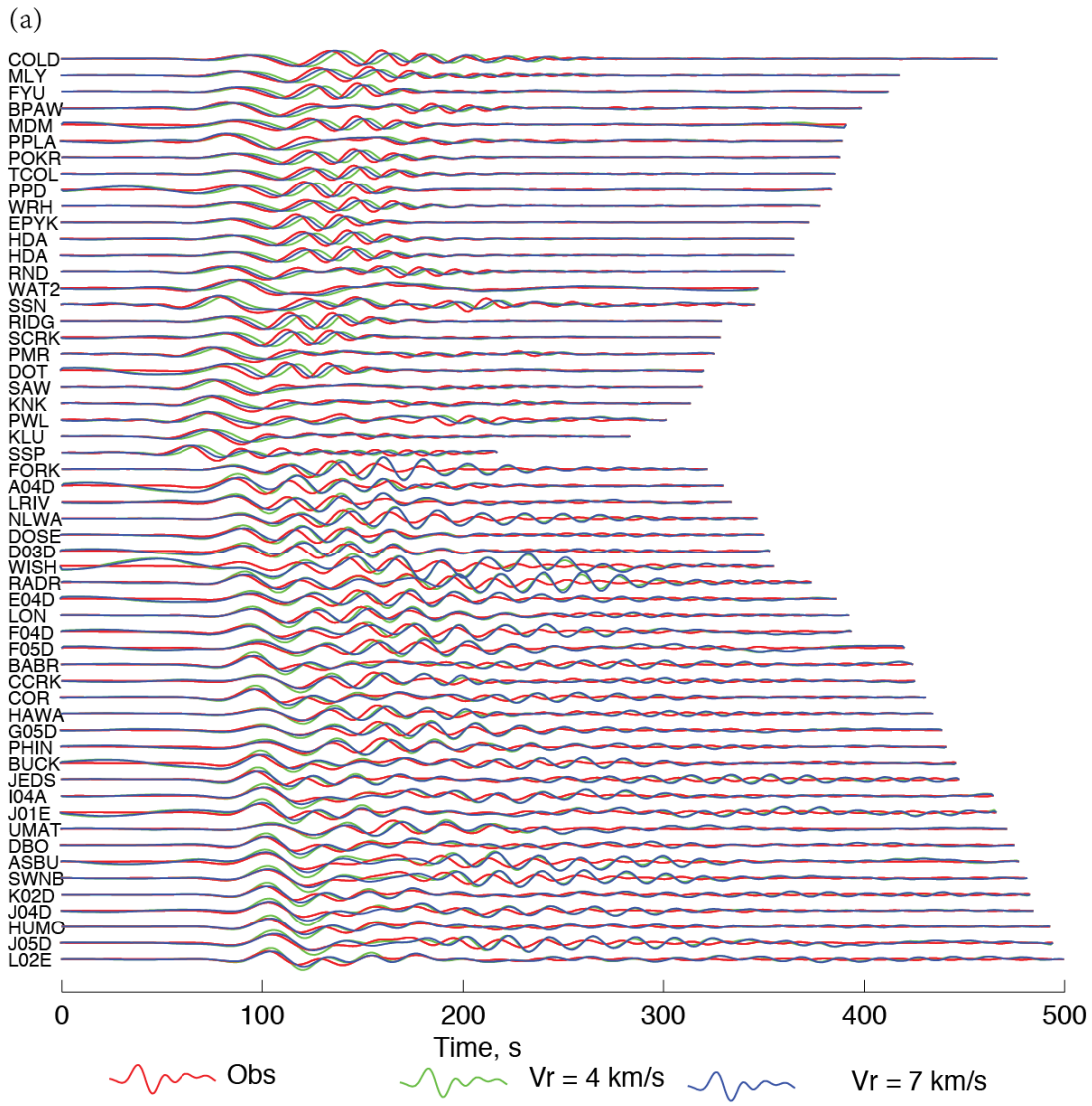

Figure 6.S3. (a) Observed and predicted Love wave (G1) waveforms from 56 regional stations for forward modeling using the finite-fault model results with different rupture velocities. The Green's functions are from recordings of the EGF event with phase velocity corrections for differential path lengths using the regional seismic velocity model. Observed waveforms are plotted in red. Modeled waveforms for finite-fault model results with inversion rupture velocities of 4.0 and 7.0 km/s are plotted in green, and black, respectively. (b) The same style display as (a), except for 46 Rayleigh wave (R1) waveform recordings.

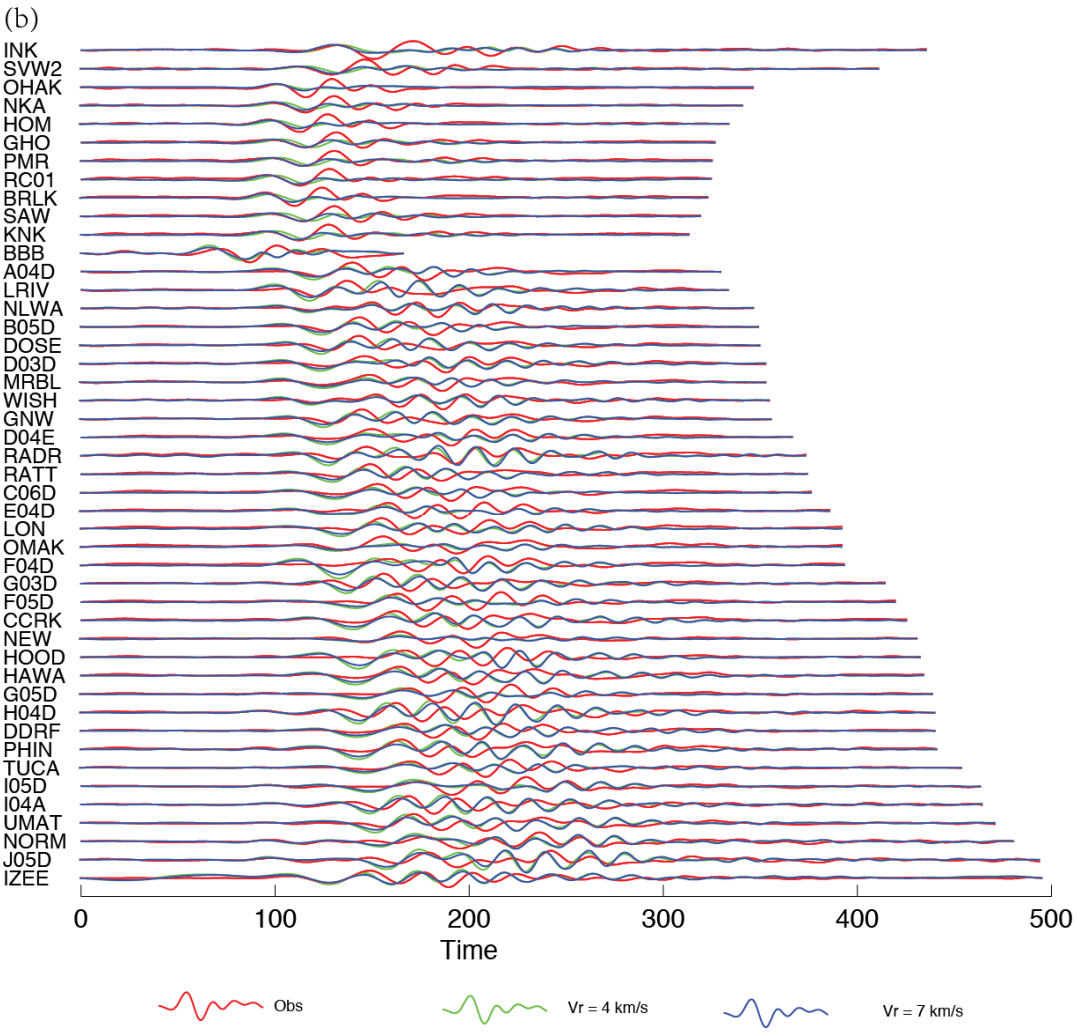

Figure 6.S3. Continued

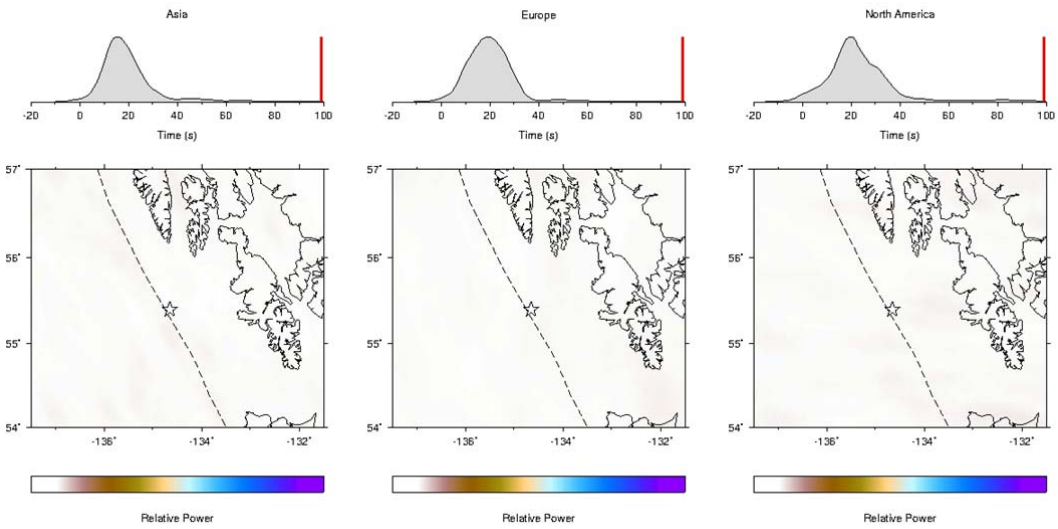

Movie S1. Evolution of beam power in time and space for the three arrays shown in Figure 6.12. Beam power is calculated in a passband of 0.5-2.0 s from beams created with fourth-root stacking, therefore it is an indicator of waveform coherence as well as amplitude. Although energy drifts in the direction of each array, the northward progression of the rupture is a robust feature that is independent of array azimuth.

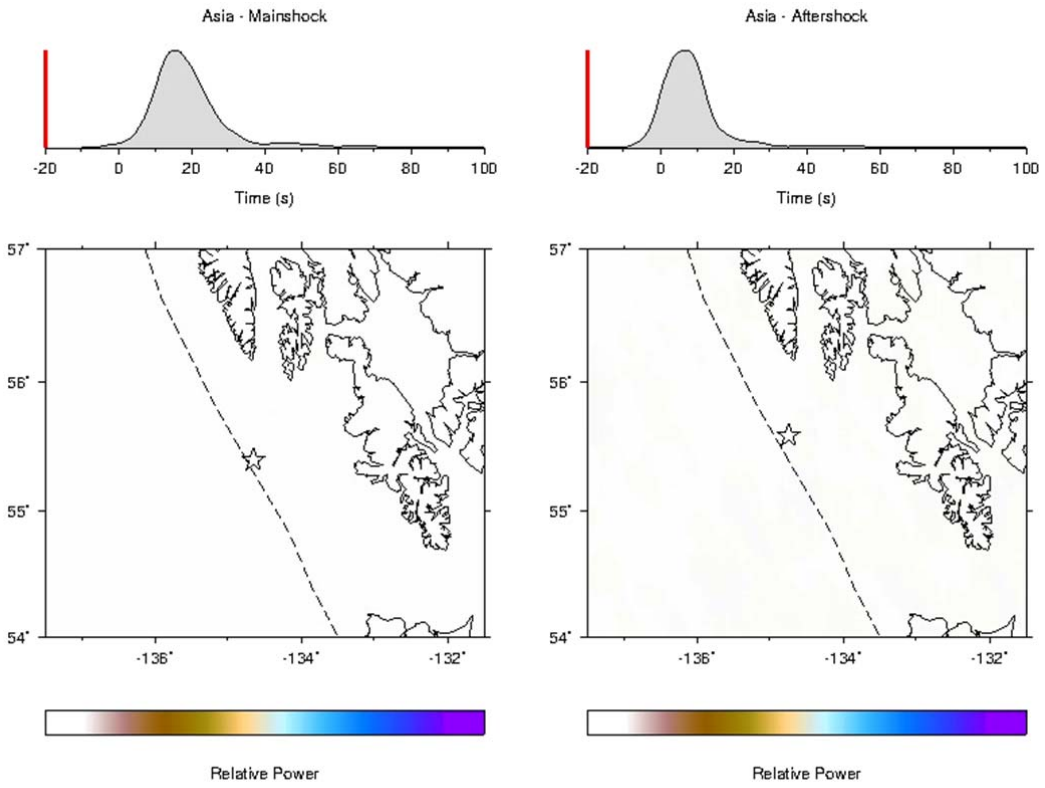

Movie S2. Comparison of back-projections for (left) the mainshock and (right) the M_w 5.9 aftershock that occurred on 1/31/2013 at 09:53:44 (UTC), using data from the Asia array of seismometers. Biases from the array response function are similar for the two events, yet the energy for the smaller aftershock is symmetric about the epicenter, with only modest along-strike smearing. This implies that the strong northward distribution of energy for the mainshock back-projection is not an artifact of the array response and instead reflects actual short-period rupture properties.

Chapter 7

Rupture process of the 2010 M_w 7.8 Mentawai tsunami earthquake from joint inversion of near-field hr-GPS and teleseismic body wave recordings constrained by tsunami observations

Abstract

The 25 October 2010 Mentawai tsunami earthquake (M_w 7.8) ruptured the shallow portion of the Sunda megathrust seaward of the Mentawai Islands, offshore of Sumatra, Indonesia, generating a strong tsunami that took 509 lives. The rupture zone was up-dip of those of the 12 September 2007 M_w 8.5 and 7.9 underthrusting earthquakes. High-rate (1-s sampling) GPS instruments of the SuGAr network deployed on the Mentawai Islands and Sumatra mainland recorded time-varying and static ground displacements at epicentral distances from 49 to 322 km. Azimuthally-distributed tsunami recordings from two deep water sensors and two tide gauges that have local high-resolution bathymetric information provide additional constraints on the source process. Finite-fault rupture models, obtained by joint inversion of the hr-GPS time series and numerous teleseismic broadband P and S wave seismograms together with iterative forward modeling of the tsunami recordings, indicate rupture propagation ~50 km up dip and ~100 km northwest along strike from the hypocenter, with a rupture velocity of ~1.8 km/s. Subregions with large slip extend from 7-10 km depth ~80 km northwest from the hypocenter

with a maximum slip of 8 m and from ~5 km depth to beneath thin horizontal sedimentary layers beyond the prism deformation front for ~100 km along strike, with a localized region having > 15 m of slip. The seismic moment is 7.2×10^{20} Nm. The rupture model indicates that local heterogeneities in the shallow megathrust can accumulate strain that allows some regions near the toe of accretionary prisms to fail in tsunami earthquakes.

7.1. Introduction

The Australian plate is converging with the southeastern segment of the Eurasian plate, called the Sunda block, at a relative plate motion rate of ~59 mm/year [*Bock et al.,* 2003; *Chlieh et al.,* 2008]. The plate motion is oblique to the Sumatran subduction zone, with slip partitioning having generated a forearc sliver along Sumatra (Figure 7.1). The boundary-parallel shear motion is mainly accommodated along the Sumatran fault, and the boundary-perpendicular convergent motion is mainly accommodated by underthrusting along the Sunda megathrust at a rate of ~45 mm/year [*Chlieh et al.,* 2008].

Recent Sunda megathrust earthquakes

During the past decade much of the Sunda megathrust has slipped in large earthquakes, with the 26 December 2004 Sumatra-Andaman (M_w 9.2) and 28 March 2005 Nias (M_w 8.6) events rupturing the zone from 0°N to 14°N [*Lay et al.,* 2005; *Ammon et al.,* 2005; *Shearer and Bürgmann*, 2010]. The subduction interface from 2°S to 5°S, near the Pagai Islands (southeastern Mentawai Islands), subsequently

ruptured in three large events. On 12 September 2007, the M_w 8.5 Bengkulu and M_w 7.9 Pagai-Sipora events (Figure 7.1) occurred on the central and deeper portion of the megathrust with seismic moments of $M_0 = 6.7 \times 10^{21}$ Nm and 8.1×10^{20} Nm, respectively [http://www.globalcmt.org/]. The great Bengkulu event had maximum slip of 5-7 m [*Konca et al.,* 2008], and generated a moderately damaging tsunami that impacted 250 km along the coast, with peak runup heights of up to 4 m and inundation distances of up to 500 m [*Borrero et al.,* 2009].

On 25 October 2010 an M_w 7.8 thrust earthquake ruptured the shallow portion of the Sunda megathrust seaward of the Pagai islands [14:42:21.4 UTC, 3.49°S, 100.14°E, Badan Meteorologi, Klimatologi dan Geofisika (BMKG)]. Estimates of short period body wave magnitude (m_b = 6.1 - 6.5) and surface wave magnitude (M_S = 7.1 - 7.6) from various organizations are tabulated by the ISC [http://www.isc.ac.uk/iscbulletin/search/bulletin/]. The Global Centroid Moment Tensor (GCMT) solution has $M_0 = 6.8 \times 10^{20}$ Nm (M_w 7.8) [http://www.globalcmt.org/], with a centroid depth of 12 km, a centroid time shift of 37.3 s, and a best-double-couple with strike $\phi = 316°$, dip $\delta = 8°$, and rake $\lambda = 96°$. W-phase inversion yielded a seismic moment $M_0 = 5 \times 10^{20}$ Nm (M_w 7.7) for a 12 km deep source with $\delta = 10°$ [*Lay et al.,* 2011b].

Although lower in seismic magnitudes and seismic moment than the 2007 events, the 2010 earthquake produced a stronger tsunami, with 3-9 m runup that inundated as far as 600 m inland on the Pagai Islands. Peak runup of 16.9 m occurred on the small island of Sibigau [*Hill et al.*, 2012]. The tsunami caused widespread destruction that

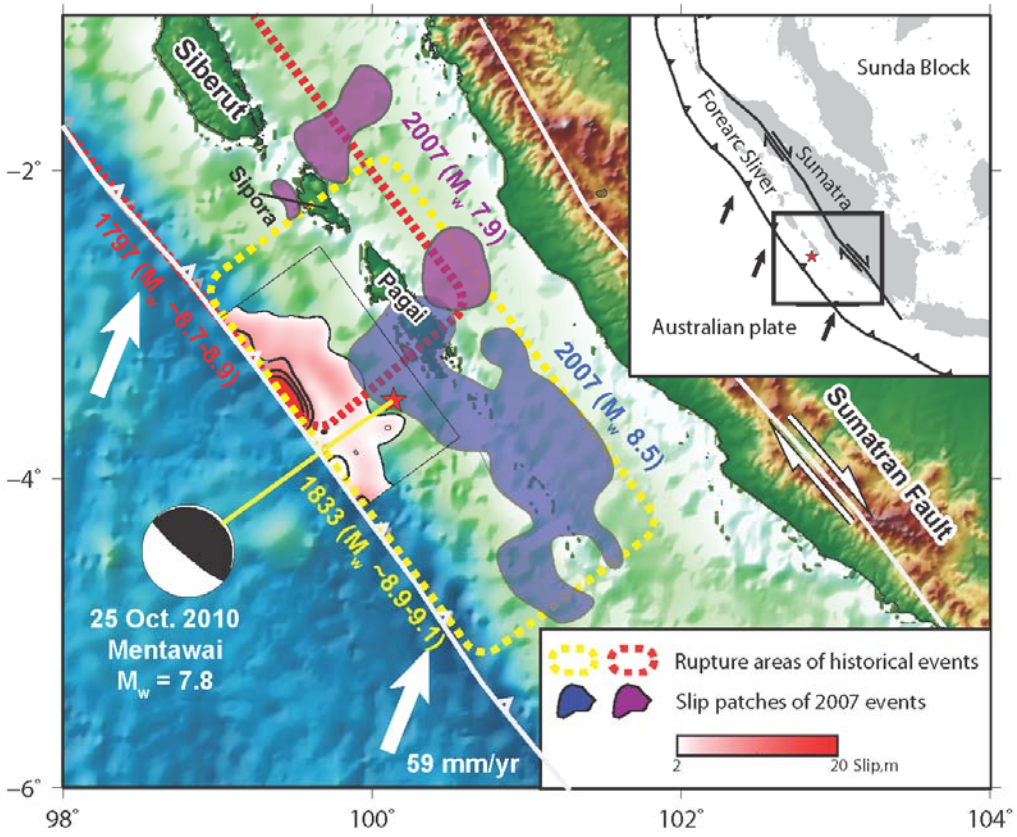

Figure 7.1. Maps of the study area and regional plate tectonic setting. The inset map locates the Australian Plate which subducts beneath the Sunda Block of the Eurasian Plate along the Sunda trench. The relative plate motion, referenced to the Sunda Block, is marked with black arrows. The Sunda trench is marked with barbed solid lines. The Sumatran fault is marked with a black curve with one-sided arrows to represent the shearing motion. A forearc sliver is located between the Sunda trench and the Sumatran fault. The epicenter of the 25 October 2010 Mentawai event is marked with a red star. The box identifies the region that is enlarged in the main map. The Global Centroid-Moment Tensor solution is shown for the 25 October 2010 Mentawai, M_w 7.8 event (black filled focal mechanism). The slip distribution of the Mentawai event is indicated with a red-scaled contour map with 6-m slip increment contours. The rupture areas with slip >1 m for the 12 September 2007, M_w = 8.5 and M_w = 7.9 events [*Konca et al.* 2008] are marked with blue and purple-filled patches respectively. The rupture areas of the 1797 and 1833 events are outlined with red and yellow dashed lines, respectively [*Chlieh et al.,* 2008; *Natawidjaja et al.,* 2006]. The approximate location of the trench is indicated with the barbed curve. The Sumatran Fault is indicated with a white curve, with one sided arrows showing shearing motion. The plate motion between the Australian Plate and Sunda block is indicated with white-filled arrows. Names of some Mentawai Islands, including Siberut, Sipora and Pagai Islands, are labeled.

displaced more than 20,000 people and affected about 4,000 households. 509 people were killed [*Hill et al*., 2012]. The unusually large tsunami for a moderate magnitude earthquake ($M_S \leq 7.6$), classifies the 2010 event as a 'tsunami earthquake'[*Kanamori*, 1972]. The 2010 Mentawai earthquake was not strongly felt locally, as has also been the case for other tsunami earthquakes, limiting immediate reaction to the event and exacerbating the losses from tsunami. The weak shaking is associated with the relatively low radiated seismic energy $E_R = 9.2 \times 10^{14}$ J ($E_R/M_0 = 1.4 \times 10^{-6}$) and low source strength for seismic wave periods shorter than 100 s [*Lay et al*., 2011b]. The location up-dip of the preceding large 2007 interplate ruptures is of particular significance, as it is often assumed that isolated shallow megathrust ruptures will not occur seaward of deeper underthrusting events, and that stable creep or afterslip [e.g., *Hsu et al*., 2006] will instead accommodate the relative plate motions.

Historical earthquakes

The plate interface near the Mentawai islands ruptured previously in the 1797 (M_w ~8.5-8.7) and 1833 (M_w ~ 8.6-8.9) events, which had estimated rupture zones (Figure 7.1) that appear to have overlapped near Sipora and the Pagai Islands [*Natawidjaja et al.*, 2006; *Chlieh et al.*, 2008] along the 2010 Mentawai rupture zone. It is unclear whether the region of overlap of the 1797 and 1833 rupture zones involved repeated slip or along-dip separation of slip. The 1797 event produced uplift of up to 0.8 m on the southwest coast of the Pagai Islands, and the 1833 event produced uplift of ~2 m on the same coast [*Natawidjaja et al*., 2006], indicating that the down-dip limit of slip was northeast of the islands for both events. The estimated

magnitudes of the historic events may be amplified by afterslip and back-thrusting that augmented uplift of the coral reefs. Whether slip extended to the trench for either event is not well constrained. There is some documentation of tsunami runup near Padang on the mainland of ~5-10 m in the 1797 event and 3-4 m in the 1833 event, which is comparable to that of the 2007 Bengkulu event [*Natawidjaja et al.*, 2006], but there are no reports of runup heights on the Mentawai islands. It is plausible that these two events did rupture the full width of the seismogenic megathrust, given their documented strong shaking and large tsunami. This possibility is weakly supported by modeling of the uplift patterns on the islands, but the observed deformation does not resolve the up-dip limit of slip for either event. It is also unclear why the 2007 events were smaller than the earlier events (Figure 7.1) and why the 2010 rupture did not occur at the time of the earlier events.

In ~1314, the area between the Mentawai islands and the trench ruptured in a shallow thrust event that was larger and/or deeper than the 2010 Mentawai event [*Philibosian et al.*, 2012]. The estimated magnitude of the 1314 event based on modeling of coral microatolls trades-off with the slip location, but the event is distinctive from the further down-dip 2007 events. At least two shallow paleo-earthquakes also appear to have shocked the shallow portion of the megathrust near the Mentawai islands ~1500 yr before the 1314 event, indicating an earthquake recurrence time of ~1000 years [*Philibosian et al.*, 2012].

The region of the 1797 rupture zone from latitudes -0.5° to -3° that has not ruptured recently is identified as the Mentawai (or Padang) seismic gap, and is a

shaking and tsunami threat to the Mentawai Islands, the city of Padang, and surrounding coastal areas. With over two hundred years of plate motion since the last event, and clear evidence of interplate locking [*Chlieh et al.*, 2008] southeastward from the Batu Islands to the Pagai Islands (along Siberut and Sipora Islands), there is substantial accumulated moment deficit in the Mentawai gap comparable to that released in the 1833 event to the southeast.

Prior results for the 2010 event

The faulting process of the 2010 Mentawai event has been investigated using subsets of seismic, geodetic, and tsunami datasets [*Lay et al.,* 2011b; *Newman et al.,* 2011; *Bilek et al*., 2011; *Hill et al.,* 2012; *Satake et al.,* 2013]. These prior investigations reveal some consistent characteristics of the tsunami earthquake, but differ in estimated slip distribution due to the varying intrinsic resolution provided by each data type and observational configuration.

Teleseismic body and surface wave inversions [*Lay et al.,* 2011b; *Newman et al.,* 2011; *Bilek et al*., 2011] inferred primary slip patches located near the hypocenter along with overall northwestward along-strike expansion of the slip zone with total rupture duration in excess of 110 s. *Lay et al.* [2011b] suggested that low seismic moment, but large slip, also occurred in low rigidity material extending out to the trench. Low average rupture velocity of ~1.5 km/s was estimated by *Lay et al*. [2011b] and *Newman et al.* [2011], compatible with surface wave directivity analysis by *Bilek et al.* [2011]. *Lay et al*. [2011b] showed that their slip models from various seismic data sets, with peak slip of 3.5-4.3 m were generally consistent with a

tsunami recording from DART buoy 56001 (13.961°S, 110.004°E), although the amplitudes were 10-30% underestimated. *Newman et al.* [2011] modeled the same DART signal, finding severe under- and over-prediction of the DART amplitudes for models with peak slip of 1.8 m and 9.6 m (the latter model being scaled to account for a rigidity decrease to try to match large runup observations), respectively. This mismatch of the tsunami signal appears to be due to non-self-consistent scaling of their preferred slip model. Due to the shallow dip and depth, teleseismic wave analyses have limited resolution of rupture velocity and along-dip moment distribution, and slip estimation is highly uncertain due to trade-off with assumed rigidity structure.

Hill et al. [2012] analyzed regional GPS recordings from the Sumatra GPS Array (SuGAr) stations located along the Mentawai Islands and tsunami runup and inundation observations from an extensive field survey. Kinematic GPS ground motions were determined with 1 s time sampling, allowing direct resolution of northwestward rupture expansion and isolation of ~30% additional postseismic deformation relative to 24-hour static solutions. The coseismic static motions at the GPS sites are small, with the largest horizontal motion being only 22 cm southwestward at the station closest to the epicenter. Linear slip inversion using only the kinematic GPS static offsets yielded a slip patch northwest of the hypocenter with peak slip of 86 cm for a fault dip of 7°. Recognizing that this low slip gives <15 cm seafloor uplift that cannot be reconciled with the large tsunami runup, models with *a priori* slip constraints with smooth spatial decay were obtained with the intent of

producing sufficient seafloor uplift (~2+ m) to match the local runup data. This yielded a preferred model with imposed slip of 12 m extending 120 km along the trench strike concentrated within 40 km from the upper wedge deformation front (no slip was allowed further seaward under flat-lying sediments in the trench that extend to 1.5 km depth below seafloor). This large slip was placed far enough off-shore that it can be reconciled with the small GPS offsets, but is intrinsically poorly resolved by those data. An elastic version of this model under-predicted a deep-water tsunami (DART 56001) recording, so additional inelastic deformation of shallow sediments that about doubled the seafloor uplift was considered as a means to improve the amplitude match. The overall fit achieved to the DART signal was still relatively poor, at best being comparable to the fit for the elastic seismic models of *Lay et al*. [2011b].

The seismic and geodetic data sets provide very limited spatial resolution of the slip distribution near the trench, but the large near-trench slip inferred by *Lay et al*. [2011b] is more compatible with the GPS observations than the inflated large slip deeper on the megathrust in the solution of *Newman et al*. [2011]. Tsunami observations tend to be particularly sensitive to very shallow rupture, both in terms of requiring sufficient seafloor deformation to account for the tsunami amplitudes, as exploited by *Hill et al.* [2012], and in providing good spatial resolution if time varying records are available. Two significant slip patches in the shallowest part of the megathrust were resolved by inversions using only tsunami recordings from buoys and tide-gauges by *Satake et al*. [2013]. This spatial resolution is enabled by

use of a very nearby deep-water GPS buoy (GITEWS SUMATRA-03; Figure 7.2) located just to the north of the rupture zone. Inversion including 11 tsunami recordings from along Sumatra and at distant islands in the Indian Ocean yielded a model with slip of up to 6.1 m close to the trench and ~3 m deeper on the megathrust extending 100 km northwest of the hypocenter, with an estimated seismic moment of 1.0×10^{21} Nm. The inversion provided good fits to the DART and GPS buoy observations, and reasonable fits to the first cycle of regional tide-gauge recordings, but no attempt was made to reconcile the model with seismic or geodetic observations.

The investigations of the rupture process of the 2010 Mentawai earthquake discussed above have established that it was a tsunami earthquake, with large slip on the shallow megathrust, up-dip of preceding large interplate ruptures. However, the seismic, geodetic, and tsunami data have not been well-reconciled, and there are large differences in inferred slip distributions based on analysis of subsets of the full suite of data. The goal in this paper is to more fully exploit the collective time series of seismic, geodetic and tsunami recordings to obtain a self-consistent unified model for the coseismic rupture process of this important event.

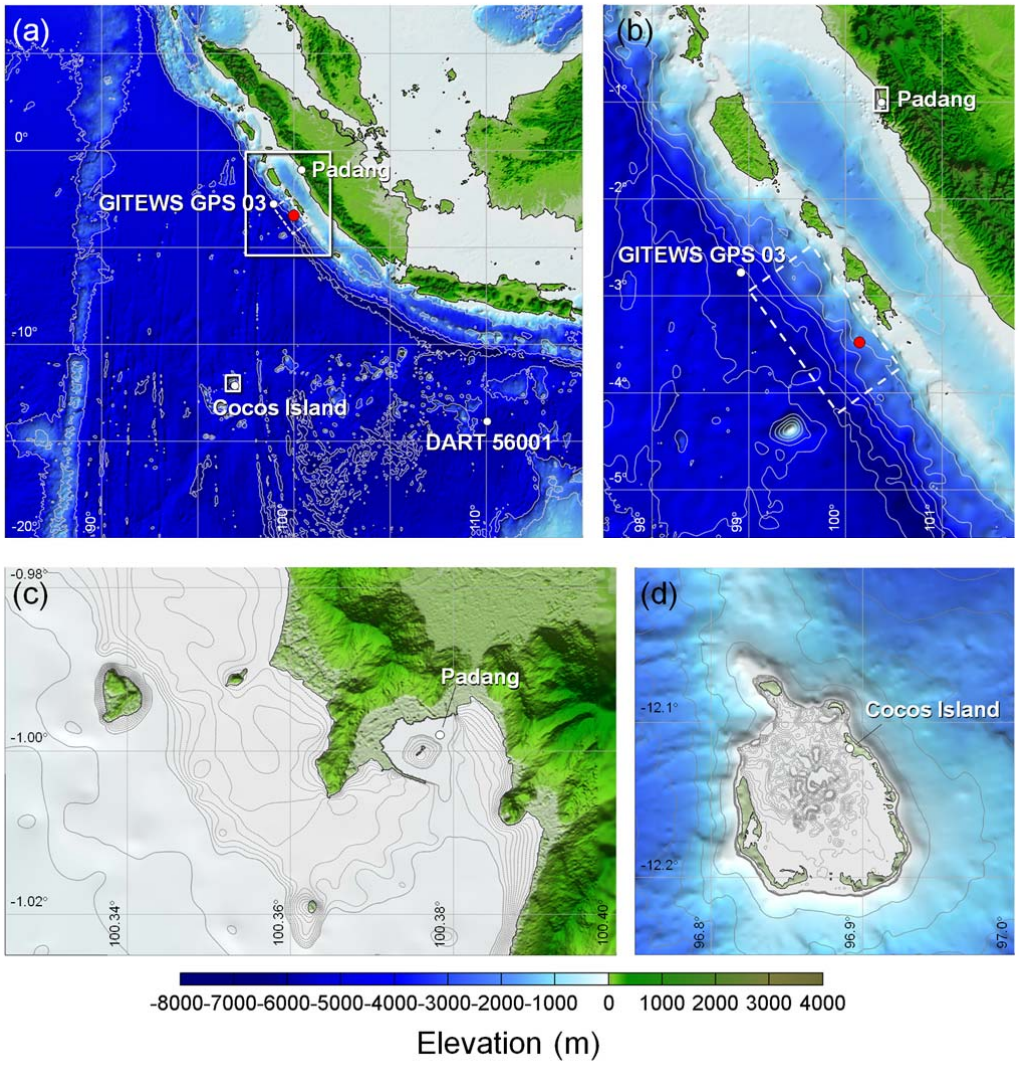

Figure 7.2. Location map and nested grid system for modeling of the 25 October 2010 Mentawai earthquake tsunami. **(a)** Level-1 grid over northeast Indian Ocean with the outlines of the level-2 grids over the near-field region and Cocos Island. Grey solid lines indicate the depth contours at 2000-m intervals. **(b)** Level-2 grid with the outline of the level-3 grid over the Padang coastal region. Grey solid lines indicate depth contours at 1000-m intervals. **(c)** Level-3 grid over Cocos Island. Grey solid lines indicate depth contours at 500-m intervals and grey dot lines indicate depth contours at 1-m intervals. **(d)** Level-4 grid at Padang Harbor. Grey solid lines indicate depth contours at 10-m intervals and grey dot lines indicate depth contours at 1-m intervals. White dash line indicates the fault area the 25 October 2010 Mentawai earthquake. White circles indicate water-level stations and red circle indicates the epicenter.

7.2. Data and methods

An improved kinematic rupture model for the 2010 Mentawai tsunami earthquake is sought using linear finite-fault slip inversions of regional hr-GPS ground motions and teleseismic body waves, with iterative modeling of high quality tsunami recordings from deep water buoys and tide-gauges that have well-defined local bathymetry. Joint inversion of teleseismic waves and geodetic near-source displacements is well established as a sound strategy for improving slip model stability and resolution, particularly when dynamic motions captured by hr-GPS solutions are available, as this adds critical timing sensitivity to the near-source information [e.g., *Yue and Lay,* 2013]. The finite fault models from seismic and geodetic inversions can then be used in iterative forward modeling of far and/or near-field tsunami observations, exploring ranges of model parameters that are not well constrained by the seismic and geodetic data sets [e.g., *Yamazaki et al.,* 2011b, 2013; *Lay et al*., 2011c, 2013a,b]. Joint inversion with the tsunami observations directly may be possible, but presents issues of linearization of the tsunami calculations and choices in the model parameterization relative to the seismic and geodetic observations that require detailed investigation in the future; we proceed with the well-established iterative modeling approach for this study, as this can achieve unified models compatible with the salient features of all data sets involved.

7.2.1 Seismic wave dataset

The teleseismic body wave dataset is comprised of 53 P wave and 24 SH wave ground displacement recordings from stations of the Federation of Digital Seismic

Networks (FDSN), accessed through the Incorporated Research Institutions for Seismology (IRIS) data management center. The data are selected from hundreds of available FDSN seismograms to ensure good azimuthal coverage and high signal-to-noise ratios, for epicentral distances from 40° to 90°. Instrument responses are deconvolved to provide ground displacement with a bandpass filter having corner frequencies of 0.005 and 0.9 Hz. 120-s-long time windows are used, starting 10 s prior to initial P or SH arrivals. The P wave signals provide information about seismic radiation for periods as short as several seconds, but are very depleted in shorter period energy due to the nature of the source process.

We also conduct joint inversions with surface wave source time functions like those used in *Lay et al*. [2011b] and *Yue and Lay* [2013], but do not include those observations in the models presented here, as the R1 STF technique requires use of a single rake over the fault plane and gives results that are similar to the model that we do present.

7.2.2 hr-GPS dataset

We use the 3-component ground motion solutions for 11 high-rate SuGAr GPS stations presented by *Hill et al.* [2012]. The high-rate (1-s sampling) kinematic GPS solutions are generated using Precise Point Positioning (PPP) mode in the GIPSY-OASIS II V6.0 software [*Zumberge et al*., 1997]. Details of the processing, and comparisons with daily (averaged over 24-hour) solutions are provided in *Hill et al*. [2012]. The time-varying signals in these hr-GPS signals include body and surface wave arrivals emanating from the entire slip zone that help to constrain the space-time

distribution of slip.

7.2.3 Fault parameterization and waveform calculations

Our preferred finite fault model is parameterized with 72 subfaults with 12 columns with 14.25 km spacing along strike (324°), and 6 rows with 15 km spacing along dip (7.5°) (Figure 7.3a). The total fault model area is thus 171 x 90 km^2. A uniform dip angle is used based on the shallow megathrust reflection profile of *Singh et al.* [2011]; the dip of the megathrust increases at depths below our slip zone. The BMKG epicenter of 3.49°S, 100.14°E, determined from local network stations is used, but the hypocentral depth is reduced from 19 km (BMKG hypocentral depth) to 12 km to place it on the model plate interface, as that is better resolved by the reflection profile. It has been suggested that the rupture near the prism deformation front may splay onto a sub-vertical fault just a few kilometers wide [*Singh et al.* 2011], but *Hill et al*. [2012] debate this interpretation of the reflection profiles. The rupture could potentially extend ~15 km further seaward than the deformation front under flat lying sediments. Our fault model extends beyond the deformation front by about 7.5 km with uniform shallow dip, reaching the seafloor of our one-dimensional structure. We can neither resolve, nor rule out possible minor splay faulting near the toe of the wedge, but do not believe it produced significant seismic, geodetic or tsunami signal if it occurred. This is because the shallow wedge is only a few kilometers thick and any uplift from splay faulting will be very concentrated, which is inefficient for tsunami excitation.

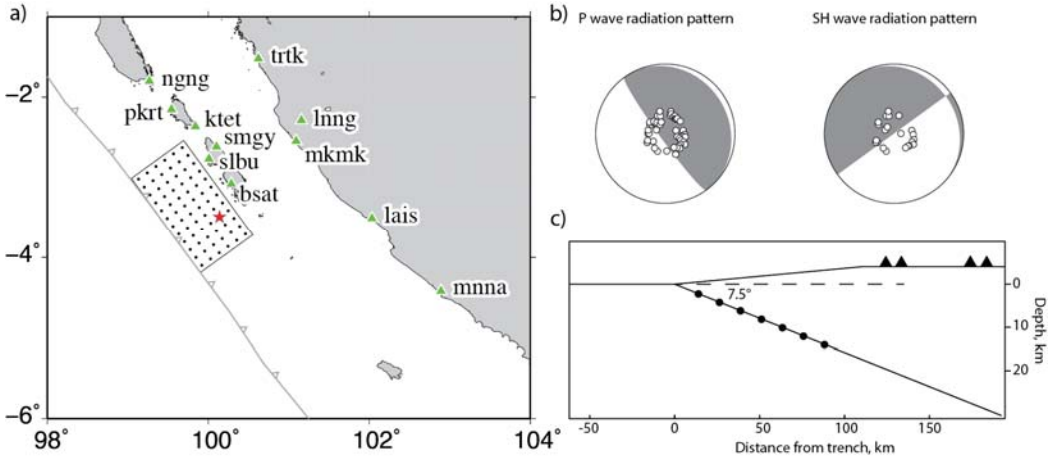

Figure 7.3. Rupture model parameterization. **a**) Map of the rupture model grid, parameterized with 12 nodes along strike with 14.25 km spacing and 6 nodes along dip with 15 km spacing. The epicenter is indicated by a red star. The locations of local hr-GPS stations used in the inversion are marked by green triangles with station names. **b**) The azimuths and take-off angles of teleseismic P/SH wave recordings used in our inversion are projected onto the lower hemisphere equal area stereographic projections along with P/SH wave radiation nodes. **c**) Cross-section indicating the fault model and ocean bottom geometry. A single dip angle of 7.5° is used for the fault plane.

We use a multi-time window linear inversion [*Hartzell and Heaton*, 1983], in which the source time function of each subfault is parameterized with 4 symmetric triangles with 2 s rise times and 2 s shifts, which allow up to a 10 s long source time function for each subfault. We use two components of the slip-vector for each subevent to parameterize for a rake-varying slip on each subfault and apply a non-negative least squares inversion [*Lawson and Hanson*, 1995], in which the rake of each subfault is allowed to vary between 45° and 135°, straddling pure thrust motion. We apply a Laplacian regularization [*Hartzell and Heaton*, 1983], which constrains the second order gradient for each parameter to be zero. The degree of smoothing for the hr-GPS and seismic joint inversions was chosen by iterative

modeling of the tsunami observations for a wide suite of smoothing parameters. The peak amplitude and spatial spread of slip in the model varies with the regularization, and these affect the forward predictions of the tsunami. We adopt smoothing that reconciles the information from the different data sets.

The teleseismic Green's functions are generated using a reflectivity method that accounts for interaction in 1-D layered structures on both source and receiver sides [*Kikuchi et al.*, 1993]. The local 1-D layered model is estimated from a combination of regional tomography [*Collings et al.*, 2012], reflection survey [*Singh et al*., 2011] and a model previously used along the 2006 Java tsunami earthquake rupture [*Ammon et a*l., 2006], and is used for the source side; a typical continental model is used for the receiver side. The parameters of the local 1D velocity model are listed in supplementary materials. The same band-pass filter used for the data is applied to the Green functions.

To model the time-dependent near-field ground displacements recorded by hr-GPS, Green functions for the full dynamic and static elastic deformation field must be used. To exploit the short-period information for very near-field displacements, we applied a frequency-wavenumber (F-K) integration method that includes all near-field terms (Computer Programs in Seismology, Robert Herrmann). The F-K method accounts for both dynamic and static near-field ground displacements. We compute the Green functions for the same local 1D layered model as used for the teleseismic calculations.

We calculated a dense Green functions database for epicentral distances of

0-500 km and source depths of 0-50 km with 1 km increment for distance and depth. We use the nearest Green functions for each source grid node for each station, incurring minor errors (<0.5 km) in propagation distance, which are insignificant compared to the model grid spacing of ~15 km. Both Green functions and data are low-pass filtered at a corner frequency of 0.1 Hz, to eliminate any short-period multi-pathing artifacts in the hr-GPS data processing, as well as any short-period propagation effects not accounted for by the 1-D velocity structure. The hr-GPS signals are thus slightly smoothed versions of the original time series shown in *Hill et al*. [2012]. Each trace has a 200-s long time window, starting at the origin time of the hypocenter and 1 s time sampling.

7.2.4 Relative weighting between hr-GPS and teleseismic datasets

Relative weighting is always a challenge for joint inversions of distinct datasets. We need to weight regional displacement field observations with errors in centimeters and teleseismic displacement records with errors in micrometers. Weighting the datasets by their associated absolute errors will not suffice when combining teleseismic and regional datasets. The strategy that we adopt to identify a preferred relative weighting between data sets involved conducting a grid search over specified relative weighting factors ranging from 0.1 – 10. The overall misfit residual versus relative weighting curve exhibits a U-shaped function. The elevated residuals on the edges indicate that one dataset is over-weighted so that the inversion fits the over-weighted dataset without fitting the other dataset. The desired relative weighting balances the information in the two datasets forming the minimum in the U-shaped

function. This leads to relative weights of ~1 to 4, with the teleseismic data given equal or greater weight than the hr-GPS data. Corresponding inversions with different relative weighting were used to produce tsunami simulations, with the fit to observed tsunami waves being optimized when the hr-GPS and teleseismic datasets are equally weighted. Thus we use relative weights of 1.

The rupture velocity for the kinematic inversions was allowed to vary over a range of 1.5 – 2.5 km/s, guided by the results of short-period back-projections and directivity measurements from *Lay et al*. [2011b], *Newman et al*. [2011] and *Bilek et al*. [2011]. The preferred rupture velocity of 1.8 km/s was based on optimizing the tsunami wave fitting for the tsunami recording from the GPS buoy, as this signal has the greatest sensitivity to placement of slip along-strike.

7.2.5 Tsunami modeling procedure

We iteratively adjusted the data weighting, rupture velocity, spacing and lateral extent of the finite-fault model grid in the joint inversion of the hr-GPS and teleseismic signals to reproduce the tsunami observations through modeling of nonlinear and dispersive ocean wave processes. The iterative modeling approach utilizes 4 high-quality tsunami recordings that include the deep-water signals from DART 56001 and the GPS buoy (GITEWS SUMATRA-03) as well as the tide gauge data at Padang harbor and Cocos Island, where reasonably accurate bathymetry is available. These are a subset of the observations used by *Satake et al*. [2013], but they are the highest quality signals from four azimuthal quadrants as shown in Figure 7.2. In particular, the GPS buoy is very close to the rupture and thus provides water-level

records associated with fine spatial and temporal scales of the slip distribution. The more distant observations, which reflect integrated characteristics of the source, can provide overall assessment of the larger-scale processes and moment magnitude.

The shock-capturing dispersive wave model NEOWAVE of *Yamazaki et al*. [2009, 2011a] describes the tsunami from its generation by an earthquake rupture model to propagation across the ocean reaching the four water-level stations. For a given finite-fault inversion of the seismic and geodetic signals, the planar fault model of *Okada* [1985] defines the kinematic seafloor deformation with time-varying subfault contributions and provides the seafloor vertical and horizontal displacement and velocity as input to NEOWAVE. The staggered finite difference model builds on the nonlinear shallow-water equations with a vertical velocity term to account for weakly-dispersive waves and a momentum conservation scheme to describe bores or hydraulic jumps that might develop at the shore. The vertical velocity term also accounts for the time sequence of seafloor uplift and subsidence, while the method of *Tanioka and Satake* [1996] approximates the vertical motions resulting from the seafloor horizontal deformation on the slope of the upper plate near the trench. This dynamic tsunami source mechanism is instrumental in the fine-tuning of the rupture model to reproduce the highly sensitive water-level records at the adjacent GPS buoy.

The digital elevation model consists of datasets with varying resolution and coverage. The 30 arcsec (~900 m) GEBCO dataset of the British Oceanographic Center provides the background bathymetry and topography across the modeled region as shown in Figure 7.2a. The Digital Bathymetric Model of Badan Nasional

Penanggulangan Bencana (BNPB), Indonesia covers a region from the outer slopes of the Mentawai Island ridge to the adjacent Sumatra coast at 3 arcsec (~90 m) resolution. The topography in this region is derived from the 1-arcsec (~30 m) SRTM-X dataset of German Aerospace Center (DLR) and augmented by 0.15-arcsec (~5 m) LiDAR data at Padang from the Indonesian Geospatial Information Agency, Badan Informasi Geospasial (BIG). A gridded dataset at 9 arcsec (~250 m) resolution from Geoscience Australia defines the bathymetry and topography in the Cocos Island region [*Mleczko and Sagar*, 2010]. We have converted the datasets to the WGS84 datum and MSL using the Geographical Information System (GIS) software ArcGIS 9.1-3 and the coordinate conversion software Corpscon 6.0. The source data, which varies in resolution from 5 to 900 m, have been blended and rectified with orthoimages and nautical charts for development of computation grids using the Generic Mapping Tools of *Wessel and Smith* [1991].

Modeling of the tsunami at the two deepwater buoys and the two tide gauges requires up to four levels of two-way nested grids. The level-1 grid extends across the continental margin from Sumatra to Java and covers a large portion of the northeast Indian Ocean as shown in Figure 7.2a. The 1 arcmin (~1800 m) resolution captures wave propagation over large-scale bathymetric features across the ocean for computation of the DART signals. The 12 arcsec (~360 m) level-2 grid in Figure 7.2b describes transformation of the tsunami in the source region to provide accurate data at the GPS buoy and across the Mentawai Islands to reach the Sumatra coast. A level-3 grid resolves the coastal region around Padang at 1.5 arcsec (~45 m) and

provides a transition to the level-4 grid in the vicinity of the harbor as shown in Figure 7.2c with 0.3 arcsec (~9 m) resolution. A separate level-2 grid covers the Cocos Island region including the adjacent seamounts and atolls at 12 arcsec (~360 m) resolution and provides a transition to the 1.5 arcsec (~45 m) level-3 grid around the island as shown in Figure 7.2d. Because of the lower-resolution bathymetry data, we carefully redigitized the coastal boundaries and bathymetry at Padang Harbor and Cocos Island to provide accurate description of the waveforms at the tide gauges for the iterative modeling procedures.

Computation of the runup and inundation observations reported by *Hill et al.* [2012] and *Satake et al.* [2013] will require both very detailed digital elevation models and intensive computations not amenable to the iterative modeling approach. Although the high-resolution SRTM-X dataset covers the Mentawai Islands and the adjacent Sumatra coast, the topography includes canopies of thick tropical vegetation. Even for near-field tsunamis, the runup depends to a greater extent on the local bathymetry and topography than the rupture mechanism [Yamazaki *et al*., 2013]. The uncertainties in modeling runup and inundation and lack of timing information are a challenge for meaningful efforts to fine-tune source rupture parameters based on the tsunami model output. We prefer to model the high-quality tsunami recordings at the four well-positioned stations and defer the runup and inundation to a future study.

7.3. Modeling results

Numerous iterations involving inversion for finite fault solutions using both

hr-GPS and teleseismic data sets followed by forward modeling of the tsunami observations were performed for different assumed source parameters (varying grid spacing and along-strike and down-dip extent, rupture velocity, subfault source durations, relative weights of seismic and geodetic data, etc.). This yielded a preferred characterization of the source process compatible with all three data types for the final model parameterization shown in Figure 7.3. As with all finite source models, there are many parameters and the solution is non-unique, so we discuss the salient features of the preferred model and the basis for its preference, recognizing that formal estimates of uncertainties are of limited value for this problem.

7.3.1 Overall rupture characteristics of the final model

The preferred rupture model is displayed in Figure 7.4a. The rupture propagated primarily up dip and along strike toward the northwest, as found in earlier studies. The hypocenter is near the bottom edge of the model grid, which is seaward of the Mentawai Islands. This prevents the model from producing any significant vertical motion of the seafloor between the islands and mainland that would otherwise produce early arrival of a negative wave at Padang at odds with the observation. As demonstrated by *Hill et al*. [2012], deep slip on the megathrust close to the islands also produces strong GPS displacements, which are not desired given that the near-trench slip required by the tsunami observations is sufficient to account for the GPS signals. A high seismic moment patch is located over an area of ~80 km along strike and ~30 km along dip at depths from 7 to 10 km, with a maximum slip of ~8 m. The edge of this region is ~30 km from the hypocenter and begins to slip ~15 s after

the rupture initiation. A shallower region of moderate seismic moment but large slip ruptures the shallowest part of the model at depths less than 5 km near the trench, extending ~100 km along strike. This has a localized high-slip subregion about 45 km long with a maximum slip of ~23 m up-dip of the main seismic moment patch, and a secondary peak of slip about 45 km further to the northwest. The shallow sliding extends about 7.5 km seaward of the deformation front, but the precise upper limit of slip below the sediments is not resolved by the data, and it could be limited to the deformation front, which is along the grid points in the first row of the model. The shallow slip to the southeast in the model is also not spatially resolved by the data and may be an artifact.

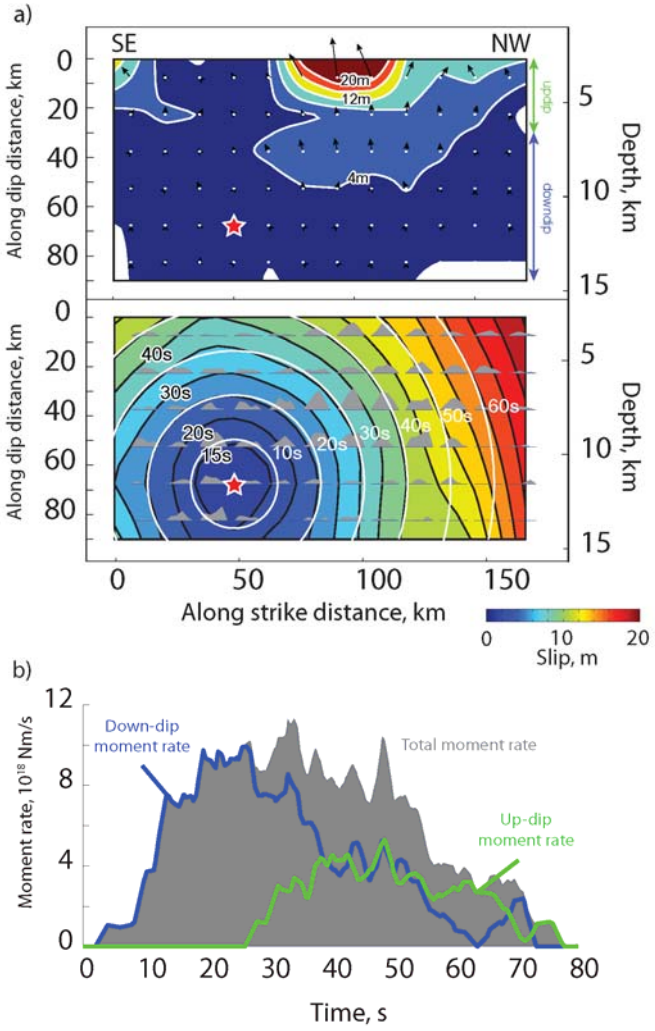

Figure 7.4. a) Rupture-plane views of the slip distribution for the preferred model with a rupture velocity of 1.8 km/s. Slip is shown in the upper panel and subfault source time functions in the lower panel. The absolute depths of the nodes are shown on the right. The maximum slip of ~23 m occurs near the trench. Another near-trench rupture patch locates ~45 km further to the northwest along the trench. A patch with maximum slip of 8 m locates from 7-10 km deep northwest of the epicenter. The total seismic moment is 7.2 10^{20} Nm (M_w 7.8). The hypocenter is marked with a red-filled star. The average slip direction at each node is indicated with black arrows. The up-dip and down-dip rupture area designations are assigned to the top two rows and the rest of the rows, respectively. Source time functions of each subfault node are shown as gray filled polygons. The centroid time of each node is contoured as the background colored map. Constant rupture velocity expansion time counters are marked as white concentric circles. **b)** The overall source time function is shown as a gray filled polygon. The up-dip and down-dip rupture source time functions are plotted with green and blue curves, respectively.

The seismic moment associated with the central slip patch (38% of the total moment) is larger than that of the shallower slip patch (24% of the total moment). However, the estimated slip for the up-dip patch is significantly larger due to the lower shear modulus of the shallow layers in the velocity model. The shallow shear velocity in the final source model structure ranges from 1.7 km/s at the ocean bottom to 2.3 km/s at 6 km depth, and the rigidity is inferred from these low velocities. We lowered the very shallow sediment velocities somewhat from those imaged by *Collings et al*. [2012] (~2.5 km/s) to allow slip to increase to match the local tsunami amplitudes for the moment estimated from the inversion stage. This enhancement of slip is compatible with the seismic and geodetic data, but is most directly driven by the matching of the tsunami signal from the nearby GPS buoy, as described below. There is poor resolution of the peak slip as it depends on the model discretization and rupture velocity, but the basic feature of patchy near trench large slip is supported by the tsunami data. Individual subfault source time functions tend to be relatively smooth and triangular or trapezoidal in shape, lacking sharp peaks. This is controlled primarily by the relatively smooth teleseismic P wave signals. The total source duration continues for about 80 s, with the northwestern limit of the rupture being bounded by the location of the GPS buoy, which does not appear to directly overlie significant seafloor displacement.

We designate the shallowest two rows of the model grid as the up-dip fault portion and the deeper four rows as the down-dip portion (Figure 7.4a). The moment rate functions for the separate up-dip and down-dip portions are shown in Figure

7.4b. Overall, the down-dip region has ~70% of the total seismic moment, while the up-dip region has ~30% of the total moment release. The moment rate during the first 25 s is dominated by the down-dip region. This region reaches its peak moment rate around 20 s then decreases steadily to about 60 s with a broad triangular source function overall. The up-dip moment rate begins around 25 s, with a ramping increase that plateaus for ~45 s. These depth-varying contributions to the total moment rate function suggest a two-stage energy release that affects the observed waveforms.

7.3.2 Finite Fault Model predictions

Teleseismic P and SH waves at northern stations show two dominant cycles beginning at 0 and ~40 s (Figure 7.5). These are mainly matched by the deeper and shallower slip patches, respectively, as shown by the separate model calculations displayed below the total waveform comparisons. This pattern of slip is compatible with the teleseismic body wave inversion shown by *Lay et al*. [2011b], which also had two distinct slip patches along dip. The shallow large-slip patch is compatible with the constrained slip inversions of *Hill et al*. [2012], which were parameterized to concentrate slip up-dip with smooth decrease along dip. It is unclear whether there is any distinct spectral radiation character for the two regions, as the short-period P wave back-projections shown by *Lay et al.* [2011b] do not resolve the along-dip placement of coherent bursts of short-period radiation. The average teleseismic source spectrum shown by *Lay et al.* [2011b] further suggests some compound source structure, with indications of spectral corner frequencies near 0.05 Hz and 0.2

Hz that reflect the observed ground displacement character of several lower frequency oscillations with superimposed short-period oscillations apparent in Figure 7.5. The preferred model captures this quite well for the final, balanced weighting of the seismic and geodetic data sets in the joint inversion. The joint model accounts for 74% of the observed P and SH signal power, whereas separate inversions of just the seismic data account for about 78%. Comparison of all of the observed and synthetic body waves is shown in supplementary Figure 7.S1.

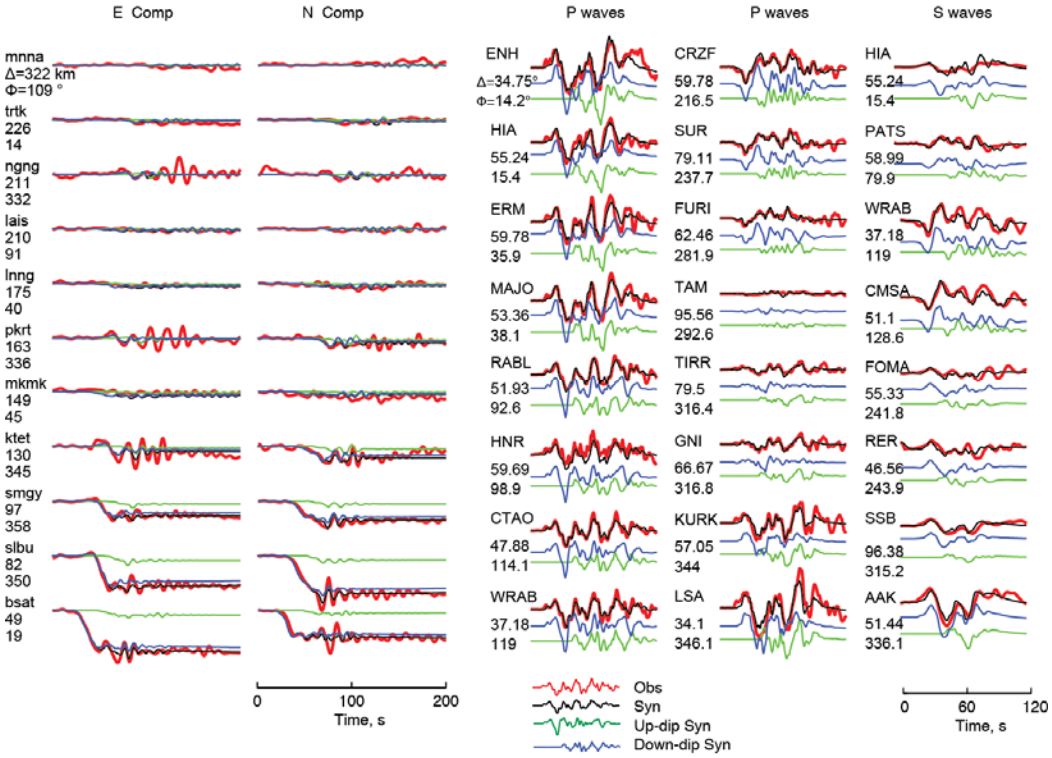

Figure 7.5. Observed (red) and modeled (black) ground displacement signals for hr-GPS and selected teleseismic P-waves and S-waves for the preferred joint inversion. The contributions to the total motion from up-dip and down-dip regions of the model (Figure 7.7.4) are plotted with green and blue curves, respectively. Only horizontal components of the hr-GPS records are shown, ordered by epicentral distance. Teleseismic records are ordered by azimuth.

The model comparisons with the hr-GPS data (Figure 7.5, 6) show good

prediction of the timing of the rise time and total static offsets of the closer stations, with some, but not all of the later short period oscillations being accounted for. The joint inversion under-predicts some of the localized short-period oscillations, but even separate inversion of just the hr-GPS signals does not provide significantly improved fits to the time-varying features at stations to the north (NGNG, PKRT, and KTET). We attribute these to either deficiencies of the local 1D velocity model used to compute the time-varying Green functions, errors in estimating the short-period hr-GPS ground motions, or our kinematic model intrinsically not accounting for off-fault local low seismic moment triggered aftershocks along the northwestern direction. We explored the timing and possible move-out of some of the small features without successfully isolating any small subevents with negligible static contributions but sufficient surface wave excitation to match the features better than the average joint model.

Decomposition of the hr-GPS signal predictions into contributions from the up-dip and down-dip regions of the fault indicates different relative contributions compared with the teleseismic dataset, as apparent in Figure 7.5. The static offsets at the hr-GPS stations (Figure 7.6 shows the observed and predicted values in map view) are mainly accounted for by slip in the down-dip region (recognizing that all slip in this model is shallow in an absolute sense). The up-dip region produces minor static displacements and seismic oscillations. This is controlled by the relative amplitude decay with distance of static and time-varying displacements, and corresponds to the modeling non-uniqueness of the GPS static offsets discussed by *Hill et al.* [2012].

What differs most for our model is that we are inverting the full time-dependent motions in the hr-GPS records, with the timing of the ramping displacements and superimposed oscillations from body and surface arrivals helping to constrain the distance to the slip that accounts for the overall static offsets shown in Figure 7.5 and 6.

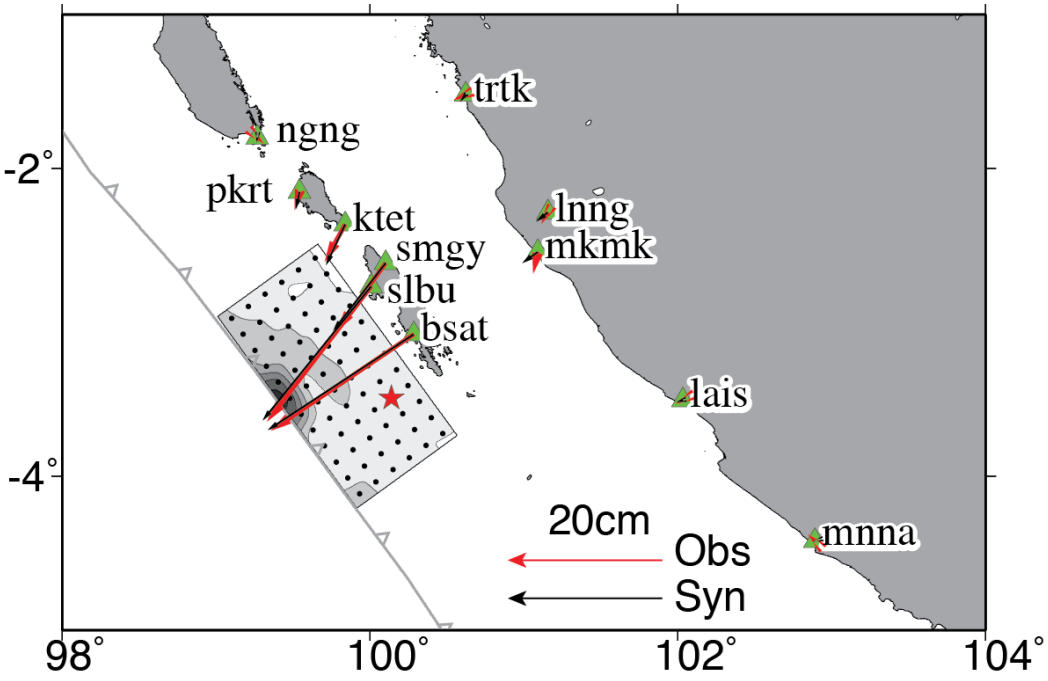

Figure 7.6. Observed (red) and computed (black) static horizontal displacements for 11 hr-GPS stations. Station locations are marked with green triangles with station names. The rupture pattern of the preferred model is plotted with grey-scaled color. The trench location is marked with a barbed grey curve.

We performed separate inversions of just the hr-GPS signals, isolating the time varying and static motions, to evaluate the added spatial resolution provided by the former (Figure 7.S2). This was done by computing ground velocity signals from the displacement records to isolate the dynamic part of the regional wave-field; we measure the static displacements from the hr-GPS data at times after all dynamic

waves have passed. The same operations are applied to the Green functions, with separate non-negative inversions of the velocity records and static displacements. We find that the main moment release patch is spatially resolved by the dynamic ground velocities, and that some slip near the trench is consistently found in the inversions for various spatial smoothing factors. However, for inversions of the static ground displacements, no slip is resolved near the trench when using low spatial smoothing factors and very shallow slip only appears when heavy spatial smoothing is applied (Figure 7.S2). We also performed inversions in which we removed the shallowest model row, finding stable features in the ground velocity inversions over the deeper model grid, but residual waveform misfit increases by 13%, due to inability of deeper slip to match timing of some motions. We found <1% misfit increase for the static inversions with the truncated model grid, indicating that deeper slip could compensate fully for the lack of very shallow model grid. These results indicate that the shallowest model row parameters are in the null space for the static displacement information, as noted by *Hill et al*. [2012], but do contribute to the time varying signals somewhat. The time varying features of the hr-GPS data thus provide improved absolute resolution of the slip in the deeper part of the model along with limited resolution of near trench slip due to timing of seismic wave arrivals, as found for previous inversions of hr-GPS data for offshore megathrust ruptures [e.g., *Yue and Lay*, 2011].

7.3.3 Tsunami model predictions

The iterative tsunami modeling adds critical resolution of the very shallow slip

in our finite fault model, primarily associated with the waveform at the nearby GPS buoy. The time-dependent seafloor deformation drives the tsunami model that in turn describes the evolution of the ocean waves around the landform and across the ocean. Figure 7.7 shows the fault slip distribution, total seafloor uplift and subsidence, and maximum tsunami wave amplitude for our final model. The seafloor displacement pattern directly reflects the fault slip characteristics. The up-dip slip patch results in an elongated region of 1 to 2 m uplift and minor subsidence toward the Mentawai Islands. The up-dip slip gives rise to near-trench uplift of 5 m over an elongated patch and 1-2 m toward the northwest adjacent to the GPS buoy. The effects of seafloor motions are filtered by dispersion before reaching the water surface. The elongated down-dip and up-dip patches produce 1.4 and 2.9 m of tsunami wave amplitude, while the near-trench uplift patches in the northwest rupture region produces distinct waves of ~1.8 m amplitude. The tsunami waves are amplified over the shelves fronting the Mentawai Islands and focused in an offshore direction normal to the trench.

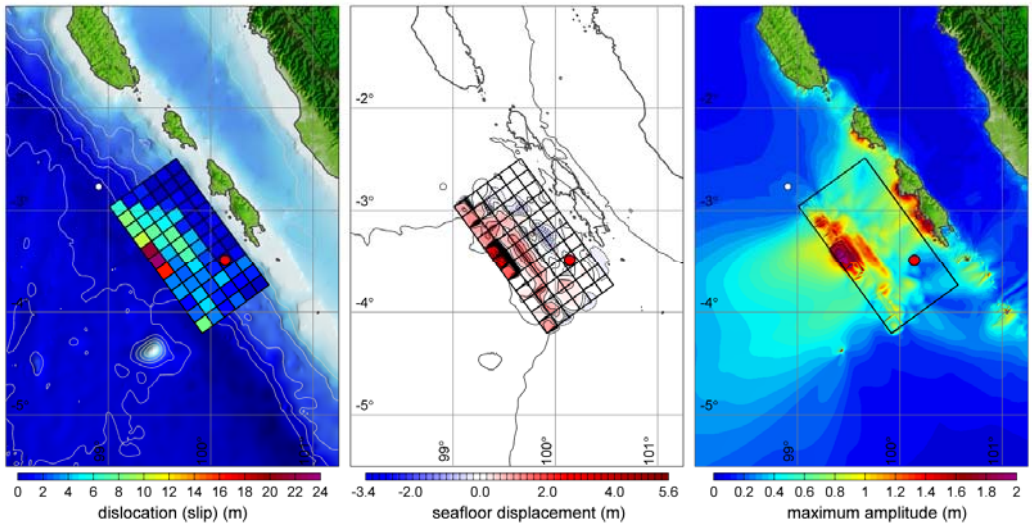

Figure 7.7. Map of the fault slip (left), rock surface displacement (middle), and maximum tsunami wave amplitude (right) for the rupture model of the 25 October 2010 Mentawai earthquake obtained by iterative modeling of hr-GPS, teleseismic P and S waves, and tsunami records. In the left panel, grey solid lines indicate depth contours at 1000-m intervals. In the middle panel, solid lines indicate uplift contours at 0.5 m intervals and dash lines indicate subsidence contours at 0.2-m contours. White circles indicate water-level stations and red circles indicate the epicenter.

The excitation from these seafloor motions shapes the tsunami signals in the buoy and tide-gauge recordings that are essential to the iterative modeling approach. Figure 7.8 illustrates the evolution of the near and far-field tsunamis in relation to the seafloor motions (See Supplemental Animations S1 and S2 for full sequence of the event). When the rupture stops at 0:01:20 (hr:min:s), the long-crested waves generated by uplift along the trench and the elongated down-dip slip patch have already begun to propagate away from source. Diffraction at the crest termini results in two oblong systems of waves that are modulated by radiation from isolated slip patches over the rupture area. The radiated waves from the two near-trench uplift

patches, superposed on the diffracted waves from the elongated patch along the trench, reach the GPS buoy at 0:04:30 and 0:07:00. The offshore component of the tsunami is dominated by the long-crested wave from the trench; the wave from the down-dip patch diminishes through reverse shoaling as it propagates into deeper water. The two onshore waves shoal over the continental slope and merge into a single wave over the shelf, exacerbating the impacts to the Mentawai Islands. The snapshots at 0:30:00 and 0:45:00 show the wave field between the islands and mainland is defined by diffraction through the channels between the Mentawai Islands. The offshore wave field is dominated by a distinct crest generated at the trench followed by radiated waves from oscillations of the tsunami source and leakage of standing edge waves on the continental margin. The initial wave crest reaches Cocos Island at 1:18:00 and the DART buoy at 2:06:00. The wave field shows significant scattering around Cocos Island due to diffraction of the tsunami waves and resonance oscillations in the island group.

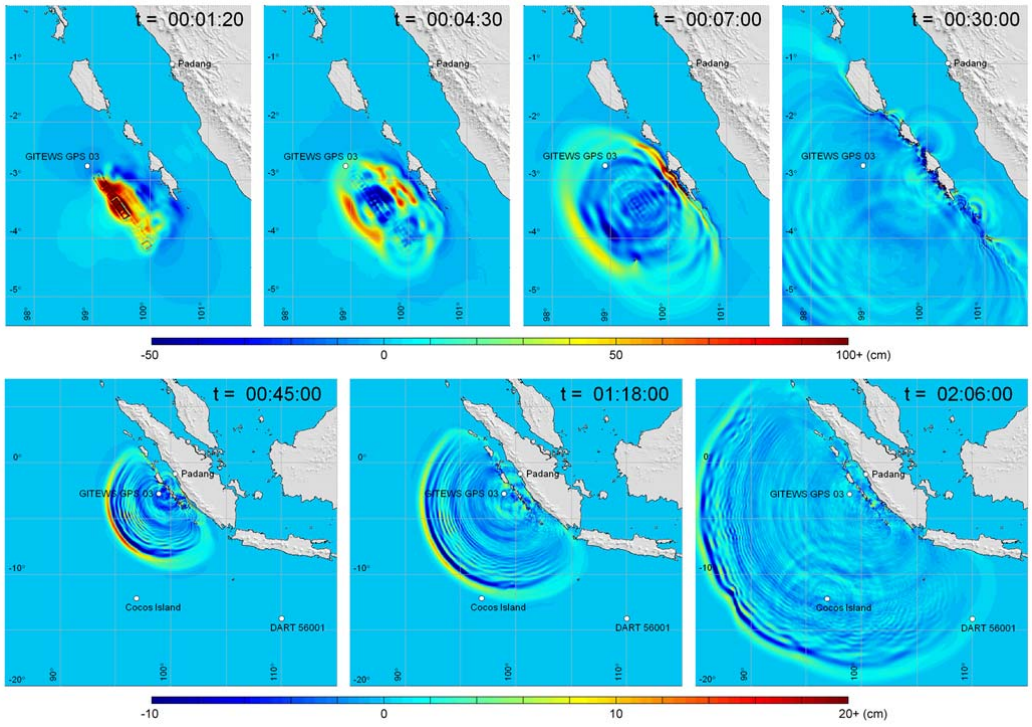

Figure 7.8. Snapshots from Supplementary Animations S1 and S2 showing evolution of the tsunami. The near-field tsunami consists of two oblong wave systems generated by the elongated, up-dip and down-dip slip patches. Onshore waves from the two patches merge over the continental shelf exacerbating the impacts to the Mentawai Islands. The offshore waves from the down-dip patch attenuate rapidly over the continental slope due to reverse shoaling. The far-field tsunami is dominated by the up-dip slip.

Comparisons of observed and computed tsunami signals for the final model are shown in Figure 7.9. The computed spectra are based on 6 hours of data from the earthquake initiation time and the results from the GPS buoy are omitted due to the short duration. The initial positive wave with double peaks at the GPS buoy is accounted for primarily by the variable slip along the shallowest row in the model. The two regions of localized seafloor uplift nearest to the buoy produces the double peaks, while the diffracted wave from the elongated, large slip patch account for the pulse in the background. Matching the timing of the two peaks places tight constraint

on the along-strike location of the slip, which gave resolution of the rupture velocity of 1.8±0.1 km/s for the final grid spacing. This sensitivity is due to the location of the buoy along the rupture direction, and *Satake et al*. [2013] similarly noted that this one observation strongly influenced the placement of shallow slip in their tsunami inversion. The early arrival of the second wave with multiple peaks points to a down-dip slip patch that is closer to the epicenter than what is predicted by the present model.

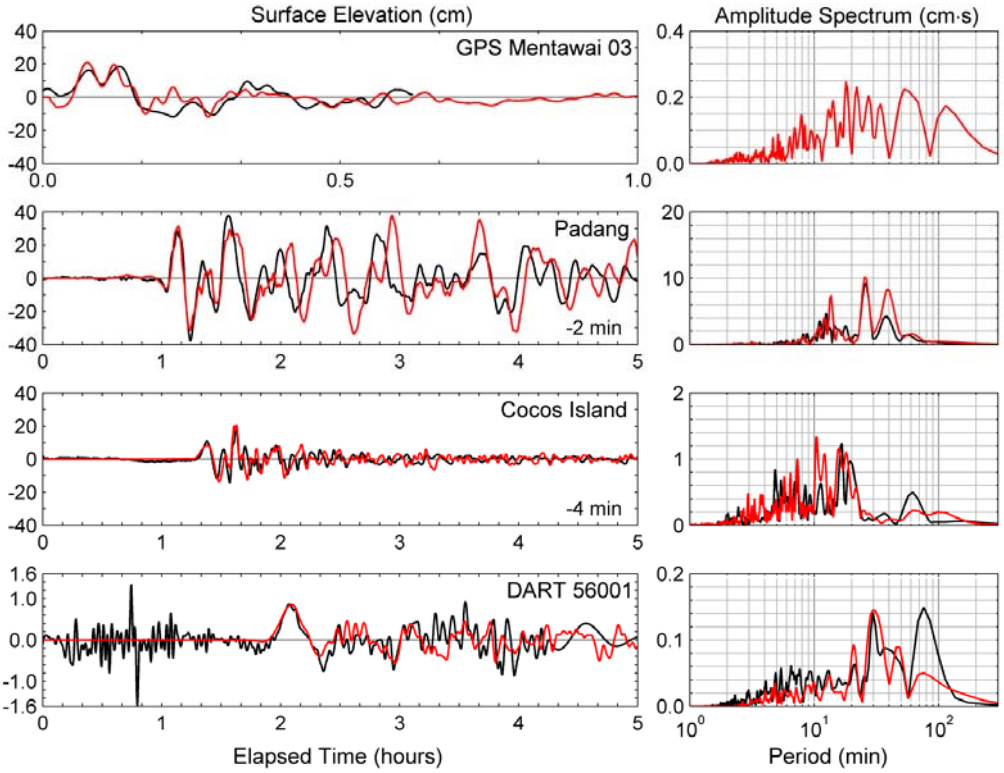

Figure 7.9. Comparison of observed (black) and computed (red) sea surface elevation time series (left) and spectra (right) for the 25 October 2010 Mentawai earthquake tsunami. The location of water level stations is shown in Figure 7.7.2. The computed series at Padang and Cocos Island have been shifted by -2 and -4 min to align with the recorded signals.

The tsunami signals at the Padang and Cocos Island tide gauges and DART

56001 are matched reasonably well by the preferred model computations for over an hour after arrival and across the frequency range of interest. The computed tsunami at Padang is about two minutes late, but has very similar waveform to the recording. A time shift aligns the signals for comparison. As apparent in Figure 7.8 and Supplemental Animation S1, the tsunami signal at Padang results from superposition of diffracted waves around the Mentawai Islands through shallow passages. We explored extensions of the model grid further northwest, finding that with slip extending as far as the GPS buoy, the timing could match the Padang records, but this produced strong arrivals not matching the signal at the GPS buoy. The overall Padang signal is not sensitive to the location and strength of very shallow slip on the fault as the resulting wave merges with that from the down-dip slip before reaching the Mentawai Basin. The signal reflects the overall slip distribution more than localized complexity. We did find that the region of down-dip slip must have the spatial extent found in the preferred model to match the period of the signal at Padang. The arrival time error and subsequent de-phasing might be attributed to the weakly dispersive properties of NEOWAVE that interfere with the nonlinear processes as the tsunami propagates from the Mentawai ridge into the Mentawai Basin through reverse shoaling [*Bai and Cheung*, 2013]. Small errors in the bathymetry can also accumulate travel time and phasing anomalies, even if the source model is accurate.

The waveform fit to the tide gauge signal at Cocos Island is very good after implementation of a 4 min time advance to the computed data. The agreement is

greatly improved over the direct inversion results of *Satake et al*. [2013], apparently due to the detailed bathymetry of the atoll shown in Figure 7.2. We found from the iterative modeling approach that the signal is sensitive to the presence of strong slip at shallow depth in the model. This is due to the dominance of the tsunami waves from the shallow slip over those from the down-dip patch as illustrated in Figure 7.8 and Supplementary Animation S2. DART 56001 recorded weak diffracted waves in the strike direction. The signal reflects the spatial extent and magnitude of the rupture, but does not resolve the localized pattern of heterogeneous slip. The agreement between the recorded and computed signals is very good in both amplitude and timing for over an hour after the main tsunami arrival (earlier short-period water oscillations from the mainshock seismic waves are not modeled). The fit to this signal is better than those achieved by the seismic models of *Lay et al.* [2011b] or *Newman et al*. [2011] and the geodetic model of *Hill et al*. [2012]. It is comparable to that of the tsunami inversion model by *Satake et al.* [2013].

Collectively, the various data sets add complementary constraints on the final rupture model. The combination of data types guides the convergence on a unified model that accounts for each data type almost as well as a separate inversion fit. While the diversity of data types compounds the difficulty of formally assessing error in the model parameters, we believe the first-order kinematics and slip pattern of our preferred model are a realistic source representation compatible with all of the data within reasonable limits of our confidence in the propagation effects.

Stress drop and shallow slip enhancement

Calculation of static stress drop for a finite fault model with non-uniform slip is complex [e.g., *Noda et al.*, 2013]. The area and slip distribution are affected by the model parameterization, smoothing, and intrinsic resolution of the model parameters, and it is necessary to adopt thresholds for defining the slip and area estimates. For the 2010 Mentawai earthquake we constrain the area to that with significant slip spanning the 5^{th} to 11^{th} columns along strike and the top 4 rows along dip. The average slip over this 7695 km^2 area is ~6.5 m. The corresponding static stress drop estimate is 0.9 MPa, which is lower than the typical several MPa stress drop of interplate events. The estimated stress drop is similar to that for the 2006 Java tsunami earthquake (0.85 MPa) estimated from finite fault model inversion [*Ammon et al.,* 2006], twice the stress drop (~0.3 MPa) of the 1994 Java tsunami earthquake estimated from the source function spectrum corner frequency [*Abercrombie et al.,* 2001], and one order of magnitude larger than estimated stress drop (< 0.1 Mpa) of 1992 Nicaragua earthquake [*Velasco et al*., 1995; *Ye et al.,* 2013]. These four tsunami events all have low static stress drop <1 MPa, indicating this is a common feature for tsunami events.

The plate convergence rate normal to the trench direction is 45 mm/yr [*Chlieh et al.,* 2008]. If we assume that strain accumulation all occurred since the great 1833 event in this region, with 100% locking, the accumulated slip deficit before 2010 was <8 m. *Chlieh et al*. [2008] estimate that the prism near the trench is ~ 40-50% locked, suggesting a ~4 m average slip deficit for a heterogeneously locked interface. While we believe there is very little resolution of near-trench locking, the estimated deficit

is consistent with the average slip of the 2010 Mentawai event, so it is plausible that the event released much of the strain accumulated since 1833.

The localized peak slip near the trench (up to 23 m) is significantly higher than the post-1833 slip deficit (8 m). The peak slip value is not a stable feature in finite fault model inversions, as it strongly depends on the smoothing factor used in our inversion. If the estimated peak slip value is correct, there may have been a patch that did not slip during the 1833 event, or there could be enhanced shallow slip during the dynamic rupture of 2010. Enhanced shallow slip near the trench occurred for the 2011 Tohoku event [*Lay et al.,* 2011a; *Yue and Lay,* 2011; *Ito et al.,* 2011; *Ide et al.,* 2011], with >60 m slip estimated near the trench in finite fault model inversions and repeated bathymetry measurements, exceeding the ~20 m co-seismic slip near the hypocenter in a region that had been 100% locked [*Loveless and Meade,* 2011]. For great megathrust events, dynamic overshoot of shallow slip may result from up-dip propagation of the rupture interacting with the free surface boundary condition, causing 'fling' of the overlying wedge. For the 2010 Mentawai event, the rupture does appear to have propagated seaward, but only over modest rupture extent. Dynamical modeling is required to evaluate whether overshoot is involved in the enhanced slip in the localized patch.

7.4. Discussion

Differences from previous models

Our preferred finite-fault model has similar overall northwestward directivity

and faulting geometry, but larger slip near the trench than in previous models. *Lay et al* [2011] and *Newman et al.* [2011] analyzed teleseismic datasets, finding limited (~5 m) rupture extending to the trench. *Hill et al.* [2012] perfomed forward modeling of geodetic data finding peak slip of ~12 m directly up-dip from the hypocenter. *Satake et al.* [2013] inverted tsunami observations with a coarse grid model, finding two near-trench rupture patches with slip of ~6.1 m and ~4 m each. Our modeling combines all of the data sets, and also finds two shallow patches, but with larger slip than in the model of *Satake et al.* [2013]. Peak slip amplitude in finite-fault models is rarely well-constrained, being strongly controlled by the regularization approach and reference velocity structure. The low shear velocity in our model near the toe scales up the shallow slip significantly, but there is substantial uncertainty in the precise structure. Our inversion regularization is selected by forward modeling of the tsunami signals. Tsunami waves, due to intrinsic low frequency content, are not sensitive to details of localized slip. Either slip over a small area, as ~20 m slip over 15×15 km^2 subfaults (as in our model), or more distributed slip over a larger area, such as ~6 m slip over 40×40 km^2 subfaults (as in *Satake et al.* [2013]), can fit the tsunami waves comparably well. Seismic potency, given by slip × area, in the vicinity of the peak slip in our model is compatible with that in *Satake et al.* [2013]. While not strongly resolved, we believe it is likely that slip >15 m occurred in a localized region. Near-trench deformation observations are needed to resolve the precise amount of slip.

The tsunami data confirm that the 2010 Mentawai tsunami earthquake has patchy

shallow co-seismic slip extending to near the toe of the accretionary prism. The plate interface near the trench is overlain by sediments with low rigidity, and this environment has often been assumed to be a low-seismicity area with slip velocity-strengthening friction that leads to stable sliding [e.g., *Byrne et al*., 1988; *Scholz*, 1988; *Lay et al.,* 2012]. Neither of the preceding 2007 thrusting events ruptured up to the region that failed in 2010, as is commonly observed or at least believed to be the case for great interplate ruptures. Some great events, like the 2011 Tohoku earthquake, do have co-seismic slip extending all the way to the trench, apparently driven by very large slip at greater depth, while large tsunami earthquakes like the 1896 Sanriku [*Kanamori,* 1972], 1992 Nicaragua [*Kanamori and Kikuchi,* 1993; *Imamura et al.,* 1993; *Velasco et al.,* 1994; *Satake,* 1994], 2006 Java [*Ammon et al.,* 2006], and 2010 Mentawai rupture entirely within the shallow part of the trench. Tsunami events typically have long source durations, limited short-period energy radiation, and low energy/moment ratio [*Polet and Kanamori,* 2000; *Lay and Bilek,* 2007; *Lay et al.,* 2012], and all of these characteristics are found for the 2010 Mentawai earthquake, along with the low static stress drop discussed above.

7.4.1 Pre-event seismicity and fault locking

Efforts to image the pre-2007 state of locking of the megathrust using SuGAr GPS observations and coral records [*Chlieh et al.* 2008] did not resolve strong locking far offshore in the vicinity of the 2010 rupture zone due to lack of resolution, with the 60% locking region being outlined by green dashes in Figure 7.10.

The 2007 earthquakes produced moderate size aftershocks around the region that

failed in 2010, but only one event is located within the 2010 co-seismic slip zone, as indicated by the GCMT focal mechanisms shown in Figure 7.10. Many of these are interplate thrust mechanisms, but some are intraplate extensional or upper plate back-thrust faulting. Most of the aftershocks locate along the margins of the large-slip zones for the 2007 event, but none extend into the shallowest megathrust region, consistent with presence of an up-dip seismic front.

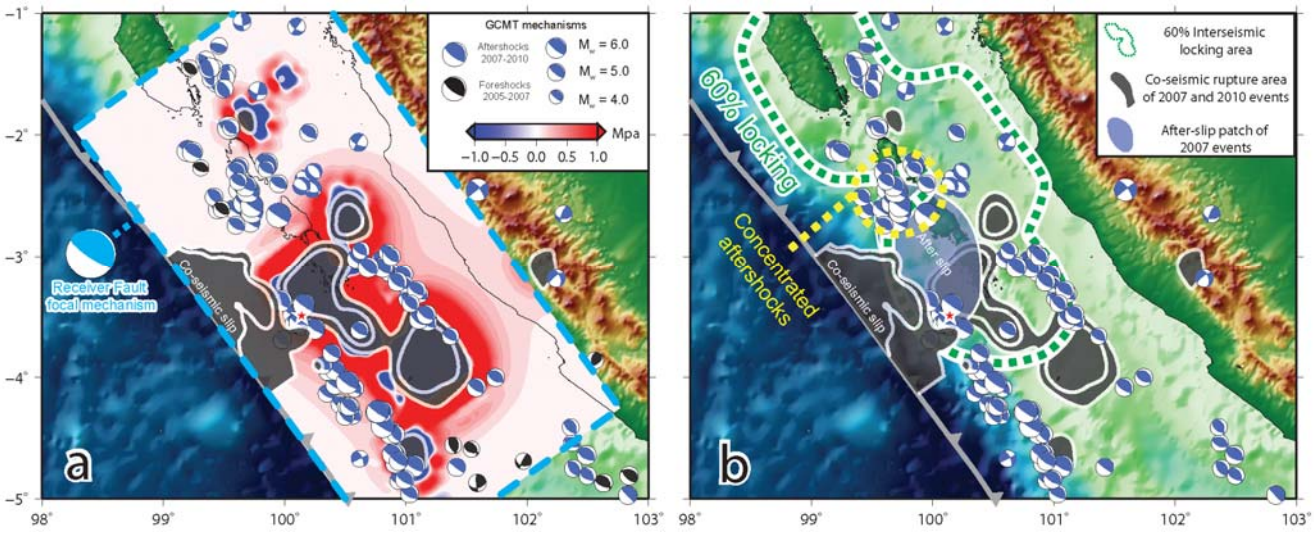

Figure 7.10. Comparison of the 2010 slip model with prior event slip models, regional focal mechanisms, and estimates of prior slip deficity. In both a and b the co-seismic slip areas of the 2007 Bengkulu and Kapalauan and 2010 Mentawai events are indicated with white contoured (2 m and 6 m), grey-filled patches. GCMT foreshock and aftershock solutions are plotted in black and blue filled focal mechanisms respectively. a). The Coulomb stress change produced by the 2007 events on the megathrust geometry (cyan-filled mechanism) is mapped with a blue-red color map (legend) within the region of the cyan-dashed lines. Foreshock and aftershock (2007-2010) focal mechanisms are plotted with black- or blue-fill, respectively. b). The 60%-locked inter-seismic area preceding 2007 [*Chlieh et al.,* 2008] is outlined with green-dashed line. An afterslip region [*Lubis et al.,* 2012] is indicated with a transparent blue-filled patch. An area with concentrated seismic activity collocated with a gap in inter-seismic locking is outlined with black-dashed line.

We calculate the co-seismic Coulomb stress change caused by the 2007

Bengkulu and Pagai-Sipora events using the finite-fault models obtained by *Konca et al.* [2008], and assuming a shallow thrust faulting orientation as a target loading geometry. The results are shown in Figure 7.10a. Near Sipora Island, located in between large-slip areas of the 2007 events, there is a concentration of aftershocks highlighted in Figure 7.10b. This is a region with little Coulomb stress increase (<0.1 Mpa) from the large events. The pre-2007 locking pattern shows a gap with reduced value near Sipora island. This indicates a region with reduced strain accumulation that may have acted as a barrier to rupture expansion in the 2007 events, but experienced accelerated post-event deformation.

A zone of afterslip has been reported down-dip of the 2010 rupture zone [*Lubis et al*., 2013] for the interval within 15 months after the 2007 events, as indicated in Figure 7.10. The maximum afterslip amount was 0.5 m near the Pagai Islands, after pore-elastic and visco-elastic deformation was removed. This afterslip region locates between the 2007 and 2010 co-seismic rupture patches and the concentrated aftershock area, with few aftershocks within the region. This area may experience predominantly slow slip, with visco-elastic deformation or stable slip that could also have delimited the 2007 rupture extent. Afterslip may also have occurred up-dip of the Bengkulu rupture zone extending from the shallow aftershock activity to the trench [J.-P. Avouac and Louis Tsang, personal communications, 2014], but the shallow region of the 2010 failure is likely to have remained fully locked, receiving progressive loading from the adjacent 2007 earthquakes, their afterslip and their aftershocks.

Most of the 2007 events interplate thrust aftershocks are located within the driving stress increase surrounding the large-slip regions of the 2007 events. This increase overlaps the down-dip edge of the 2010 rupture zone, consistent with stress loading near its hypocenter. The region northwestward from the 2007 events as far as the 1935 (M_S 7.7) rupture [*Rivera et al*., 2002] southeast of the 2005 Nias (M_w 8.7) earthquake zone has presumably accumulated strain since 1797 [e.g., *Chlieh et al.,* 2008; *Nalbant et al*., 2013].

7.4.2 2010 event **a***ftershock distribution*

Larger aftershocks within one month after the 2010 Mentawai event with faulting solutions in the GCMT catalog mostly locate in the vicinity of the near-trench slip patch with normal fault focal mechanisms (Figure 7.11). Relocations of these events together with the GCMT depths suggest that the hypocentral depths are 10-20 km, placing these normal events in the subducting slab [*Bilek et al.,* 2011]. Bending of the subducting plate as it approaches the trench causes shallow tensile stress normal to the trench direction that produces normal faults. These can be activated by Coulomb stress changes from the interplate thrusting. Significant normal faulting aftershocks have also been reported for previous tsunami events, notably the 1994 and 2006 Java tsunami earthquakes [*El Hariri and Bilek,* 2011]. We calculated the coseismic Coulomb stress change at 15 km depth on a target normal faulting focal mechanism (Figure 7.11a), and find that most of the extensional activity locates within the zone with Coulomb stress increase of > 1.0 MPa.

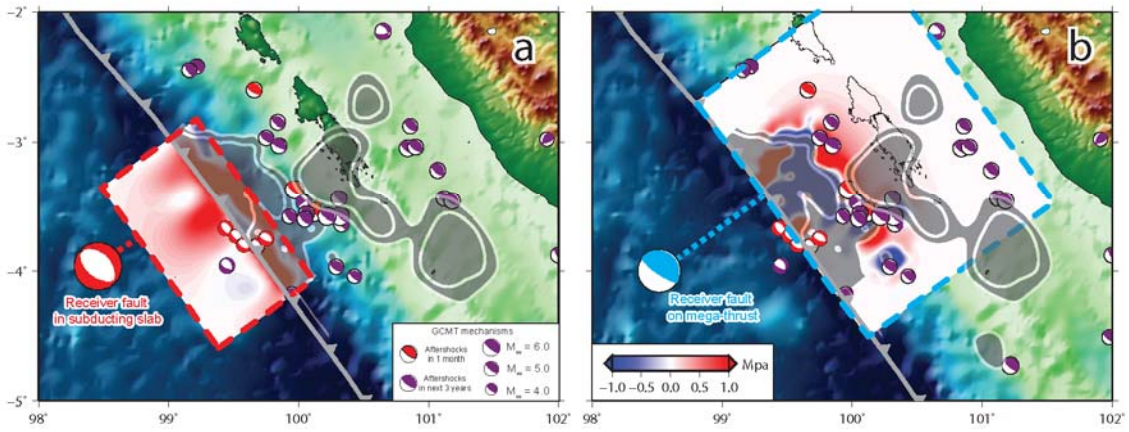

Figure 7.11. Comparison of the 2010 slip model Coulomb stress changes on extensional and compressional faulting geometries near the rupture zone. In both panels, the co-seismic rupture patches of the 2007 and 2010 mainshocks are plotted as in Figure 7.10. The global centroid moment tensor best double couple mechanism for aftershocks within 1 month and from 1 month to 3 years after the 2010 Mentawai event are plotted with red and purple mechanisms, respectively. a). The Coulomb stress change caused by the 2010 Mentawai event is projected to a normal fault geometry at 15 km depth and plotted with the blue-red scale. The focal mechanism of the receiver fault is shown. b). Coseismic Coulomb stress change caused by the 2010 Mentawai event is projected to the fault geometry of the megathrust and plotted in a blue-red color scale. The receiver fault mechanism is indicated with a cyan focal mechanism. The color scale of both Coulomb stress maps are shown in the bottom left of panel b.

There were two interplate thrust aftershocks down-dip from the 2010 rupture, and subsequent activity over the next 3 years locates near the hypocenter and down-dip edge of the 2010 Mentawai rupture. These events also appear to be confined to regions on the margins of the large-slip zone of the 2007 Bengkulu event. Calculated Coulomb stress change produced by the 2010 event for thrust events along the dipping megathrust (Figure 7.11b) also shows most events locating within regions of increased driving stress >1.0 MPa. Some regional activity is beyond the likely influence of the 2010 event and may represent continuing aftershocks of the

2007 ruptures or a return to background activity. The large slip, activation of surrounding extensional faulting, and lack of aftershock activity co-located with the coseismic slip suggest significant, if not total stress release on the megathrust region in the 2010 rupture zone [e.g., *El Hariri and Bilek*, 2011].

7.5 Conclusions

Using an iterative modeling strategy involving joint inversion of hr-GPS and teleseismic datasets and forward modeling of high-quality tsunami observations, we obtained a self-consistent co-seismic rupture model for the 2010 Mentawai tsunami earthquake compatible with all three datasets. In our preferred finite fault model co-seismic slip reaches the toe of the accretionary prism with a localized zone of slip of up to ~23 m near the trench. The slip distribution involves initial rupture of a fault patch at depths from 7 to 10 km with an overall triangular source time function followed by shallower rupture along the trench at depths less than 5 km with a prolonged plateau-shaped source time function. A relatively low stress drop (0.9 MPa) is estimated for our finite fault model, which is lower than typical thrusting events but consistent with previous tsunami earthquake stress drops. The large slip near the trench may present some dynamic enhancement of slip or possibly localized accumulation of strain that dates back to before the 1797 and 1833 ruptures.

The rupture area of the 2010 Mentawai event is up-dip of the rupture zones of the 2007 Bengkulu and Pagai-Sipora events, and aftershock and afterslip zones of those events frame the down-dip edge of the 2010 rupture. The regional megathrust

has localized patches of strong or weak coupling that appear to be activated differently with afterslip or aftershock concentrations. There was little direct indication of locking of the 2010 rupture zone before or after the 2007 events, and there is no clear distinction relative to the uppermost megathrust regions to the southeast and northwest to guide the assessment of further tsunami earthquake activity in the region. The most important lesson from this earthquake is that it is not safe to assume aseismic behavior of the megathrust region up-dip of large interplate ruptures that do not rupture all the way to the trench. While some areas may accommodate the plate motion aseismically at the toe of the accretionary prism, others will have the potential to fail in devastating tsunami earthquakes like the 2010 Mentawai event.

7.6 Acknowledgements.

This work made use of GMT, SAC and Matlab software. The IRIS data management center was used to access the seismic data from Global Seismic Network and Federation of Digital Seismic Network stations. The GITEWS GPS buoy data in Mentawai was provided by the Badan Meteorology and Geofisika (BMKG), Indonesia. DART buoy data were obtained from the NOAA National Data Buoy Center. The authors would like to thank Jane Sexton of Geoscience Australia for the digital elevation model of Cocos Islands and the tide gauge coordinates. The SuGAr network is jointly operated by the Earth Observatory of Singapore and the Indonesia Institute of Sciences (LIPI). We thank the Associate Editor and two anonymous

reviewers for their helpful reviews. This work was supported in part by NSF grant EAR1245717 (T.L.).

7.7 References

Abercrombie, R. E., M. Antolik, K. Felzer, and G. Ekström (2001), The 1994 Java tsunami earthquake: Slip over a subducting seamount, *J. Geophys. Res.*, *106*(B4), 6595-6607.

Ammon, C. J., et al. (2005), Rupture Process of the 2004 Sumatra-Andaman Earthquake, *Science*, *308*(5725), 1133-1139.

Ammon, C. J., H. Kanamori, T. Lay, and A. A. Velasco (2006), The 17 July 2006 Java tsunami earthquake, *Geophys. Res. Lett.*, *33*(24), L24308, doi:10.1029/2006GL028005.

Bai, Y. and K.F. Cheung (2013), Dispersion and nonlinearity of multi-layer non-hydrostatic free-surface flow, *J. of Fluid Mechanics*, *726*, 226-260.

Bilek, S. L., E. R. Engdahl, H. R. DeShon, and M. El Hariri (2011), The 25 October 2010 Sumatra tsunami earthquake: Slip in a slow patch, *Geophys. Res. Lett.*, *38*(14), L14306, doi:10.1029/2011GL047864.

Bock, Y., L. Prawirodirdjo, J. F. Genrich, C. W. Stevens, R. McCaffrey, C. Subarya, S. S. O. Puntodewo, and E. Calais (2003), Crustal motion in Indonesia from Global Positioning System measurements, *J. Geophys. Res.*, *108*(B8), 2367.

Borrero, J. C., R. Weiss, E. A. Okal, R. Hidayat, D. Arcas, and V. V. Titov (2009), The tsunami of 2007 September 12, Bengkulu province, Sumatra, Indonesia: post-tsunami field survey and numerical modelling, *Geophy. J. Int.*, *178*(1), 180-194.

Byrne, D. E., D. M. Davis and L. R. Sykes (1988), Loci and maximum size of thrust earthquakes and the mechanics of the shallow region of subduction zones, *Tectonics, 7*, 833-857, doi:10.1029/TC007i004p00833.

Chlieh, M., J. P. Avouac, K. Sieh, D. H. Natawidjaja, and J. Galetzka (2008),

Heterogeneous coupling of the Sumatran megathrust constrained by geodetic and paleogeodetic measurements, *J. Geophys. Res.*, *113*(B5), B05305, doi:10.1029/2007JB004981.

Collings, R., D. Lange, A. Rietbrock, F. Tilmann, D. Natawidjaja, B. Suwargadi, M. Miller, and J. Saul (2012), Structure and seismogenic properties of the Mentawai segment of the Sumatra subduction zone revealed by local earthquake traveltime tomography, *J. Geophys. Res.*, *117*(B1), B01312, doi:10.1029/2011JB 008469.

El Hariri, M., and S. L. Bilek (2011), Stress changes and aftershock distribution of the 1994 and 2006 Java subduction zone earthquake sequences, *J. Geophys. Res.*, *116*(B6), B06306, doi:10.1029/2010JB008124.

Hartzell, S. H., & Heaton, T. H. (1983). Inversion of strong ground motion and teleseismic waveform data for the fault rupture history of the 1979 Imperial Valley, California, earthquake. *Bull. Seism. Soc. Am., 73*(6A), 1553-1583.

Hill, E. M., et al. (2012), The 2010 M_w 7.8 Mentawai earthquake: Very shallow source of a rare tsunami earthquake determined from tsunami field survey and near-field GPS data, *J. Geophys. Res.*, *117*(B6), B06402, doi:10.1029/2012JB009159.

Hsu, Y.-J., et al. (2006), Frictional afterslip following the 2005 Nias-Simeulue earthquake, Sumatra, *Science*, *312*, 1921-1926.

Ide, S., A. Baltay, and G. C. Beroza (2011), Shallow dynamic overshoot and energetic deep rupture in the 2011 M_w 9.0 Tohoku-Oki Earthquake, *Science*, *332*(6036), 1426-1429.

Imamura, F., N. Shuto, S. Ide, Y. Yoshida, and K. Abe (1993), Estimate of the tsunami source of the 1992 Nicaraguan earthquake from tsunami data, *Geophys. Res. Lett.*, *20*, 1515–1518, doi:10.1029/93GL01396.

Ito, Y., T. Tsuji, Y. Osada, M. Kido, D. Inazu, Y. Hayashi, H. Tsushima, R. Hino, and H. Fujimoto (2011), Frontal wedge deformation near the source region of the 2011 Tohoku-Oki earthquake, *Geophys. Res. Lett.*, *38*(7), L00G05.

Kanamori, H. (1972), Mechanism of tsunami earthquakes, *Phys. Earth Planet. Inter*., *6*, 346–359, doi:10.1016/0031-9201(72)90058-1.

Kanamori, H., and M. Kikuchi (1993), The 1992 Nicaragua earthquake: A slow tsunami earthquake associated with subducted sediments, *Nature*, *361*, 714–716, doi:10.1038/361714a0.

Kikuchi M., H. Kanamori, and K. Satake (1993). Source complexity of the 1988 Armenian earthquake: evidence for a slow after-slip event, *J. Geophys. Res.*, *98*(B9), 15-797, doi: 10.1029/93JB01568.

Konca, A. O., et al. (2008), Partial rupture of a locked patch of the Sumatra megathrust during the 2007 earthquake sequence, *Nature*, *456*, 631–635, doi:10.1038/nature07572.

Lawson, C. L., and R. J. Hanson (1995), *Solving least squares problems*, Society for Industrial Mathematics.

Lay, T., H. Kanamori, , C. J. Ammon., M. Nettles, S. N. Ward, R.C. Aster, et al. (2005). The great Sumatra-Andaman earthquake of 26 December 2004, *Science*, 308(5725), 1127-1133.

Lay, T., and S. Bilek (2007), Anomalous earthquake ruptures at shallow depths on subduction zone megathrusts, in *The Seismogenic Zone of Subduction Thrust Faults*, edited by T. H. Dixon and J. C. Moore, pp. 476–511, Columbia Univ. Press, New York.

Lay, T., C. J. Ammon, H. Kanamori, L. Xue, and M. J. Kim (2011a), Possible large near-trench slip during the 2011 M_w 9.0 off the Pacific coast of Tohoku Earthquake. *Earth, Planets Space*, *63*(7), 687-692, doi:10.5047/eps.2011.05.033.

Lay, T., C. J. Ammon, H. Kanamori, Y. Yamazaki, K. F. Cheung, and A. R. Hutko (2011b), The 25 October 2010 Mentawai tsunami earthquake (M_w 7.8) and the tsunami hazard presented by shallow megathrust ruptures, *Geophys. Res. Lett.*, *38*(6), L06302.

Lay, T., Y. Yamazaki, C. J. Ammon, K. F. Cheung, K.F., and H. Kanamori (2011c), The 2011 M_w 9.0 off the Pacific coast of Tohoku Earthquake: Comparison of deep-water tsunami signals with finite-fault rupture model predictions, *Earth Planets Space*, 63(7), 797-801, coi:10.5047/eps.2011.05.030.

Lay, T., H. Kanamori, C. J. Ammon, K. D. Koper, A. R. Hutko, L. Ye, H. Yue, and T.

M. Rushing (2012), Depth-varying rupture properties of subduction zone megathrust faults, *J. Geophys. Res.,* 117(B4), B04311, doi:10.1029/2011JB009133.

Lay, T., L. Ye, H. Kanamori, Y. Yamazaki, K. F. Cheung, K. Kwong, and K. D. Koper (2013a). The October 28, 2012 M_w 7.8 Haida Gwaii underthrusting earthquake and tsunami: Slip partitioning along the Queen Charlotte Fault transpressional plate boundary, *Earth Planet. Sci. Lett*., 375, 57-70, doi:10.1016/j.epsl.2013.05.005.

Lay, T., L. Ye, H. Kanamori, Y. Yamazaki, K. F. Cheung, and C. J. Ammon (2013b). The February 6, 2013 M_w 8.0 Santa Cruz Islands earthquake and tsunami, *Tectonophys.*, 608,1109-1121, doi:10.1016/j.tecto.2013.07.001.

Loveless, J. P., and B. J. Meade (2011), Spatial correlation of interseismic coupling and coseismic rupture extent of the 2011 M_w = 9.0 Tohoku-oki earthquake, *Geophys. Res. Lett.*, *38*(17), L17306.

Lubis, A. M., A. Hashima, and T. Sato (2013), Analysis of afterslip distribution following the 2007 September 12 southern Sumatra earthquake using poroelastic and viscoelastic media, *Geophys. J. Int.*, *192*(1), 18-37.

Mleczko, R. and S. Sagar (2010), *The Creation of High Resolution Bathymetry Grids for Cocos (Keeling) Island*. Record 2010/38, GeoCat No. 70663, Geocience Australia, Canberra, Australia.

Nalbant, S., J. McCloskey, S. Steacy, M. NicBhloscaidh, and S. Murphy (2013), Interseismic coupling, stress evolution, and earthquake slip on the Sunda megathrust, *Geophys. Res. Lett., 40*, 4204-4208, doi:10.1022/grl.50776.

Natawidjaja, D. H., K. Sieh, M. Chlieh, J. Galetzka, B. W. Suwargadi, H. Cheng, R. L. Edwards, J.-P. Avouac, and S. N. Ward (2006), Source parameters of the great Sumatran megathrust earthquakes of 1797 and 1833 inferred from coral microatolls, *J. Geophys. Res.*, *111*, B06403, doi:10.1029/2005JB004025.

Newman, A. V., G. Hayes, Y. Wei, and J. Convers (2011), The 25 October 2010 Mentawai tsunami earthquake, from real-time discriminants, finite-fault rupture, and tsunami excitation, *Geophys. Res. Lett.*, *38*(5), L05302,

doi:10.1029/2010GL046498.

Noda, H., N. Lapusta, and H. Kanamori (2013), Comparison of average stress drop measures for ruptures with heterogeneous stress change and implications for earthquake physics, *Geophys. J. Int., 193*, 1691-1712, doi:10.1093/gji/ggt074.

Okada, Y. (1985), Surface deformation due to shear and tensile faults in a half space, *Bull. Seism. Soc. Am.* 75(4), 1135-1154.

Philibosian, B., et al. (2012), An ancient shallow slip event on the Mentawai segment of the Sunda megathrust, Sumatra, *J. Geophys. Res., 117*, B05401, doi:10.1029/2011JB009075.

Polet, J., and H. Kanamori (2000), Shallow subduction zone earthquakes and their tsunamigenic potential, *Geophys. J. Int., 142*, 684–702, doi:10.1046/j.1365-246x.2000.00205.x.

Rivera, L., K. Sieh, D. Helmberger, and D. Natawidjaja (2002), A comparative study of the Sumatran subduction-zone earthquakes of 1935 and 1984, *Bull. Seism. Soc. Am., 92*, 1721-1736.

Satake, K. (1994), Mechanism of the 1992 Nicaragua tsunami earthquake, *Geophys. Res. Lett.*, 21, 2519–2522, doi:10.1029/94GL02338.

Satake, K., et al. (2013). Tsunami source of the 2010 Mentawai, Indonesia earthquake inferred from tsunami field survey and waveform modeling. *Pure and Applied Geophysics*, 1-16, doi:10.1007/s00024-012-0536-y.

Scholz, C. H. (1988), Earthquakes and friction laws, *Nature, 391*, 37-42, doi:10.1038/34097.

Shearer, P., and R. Bürgmann (2010), Lesson learned from the 2004 Sumatra-Andaman megathrust rupture, *Ann. Rev. Earth Planet. Sci., 103*, 38-131, doi:10.1146/annurev-earth-040809-152537.

Singh, S. C., N. Hananto, M. Mukti, H. Permana, Y. Djajadihardja, and H. Harjono (2011), Seismic images of the megathrust rupture during the 25th October 2010 Pagai earthquake, SW Sumatra: Frontal rupture and large tsunami, *Geophys. Res. Lett.*, *38*(16), L16313, doi:10.1029/2011GL048935.

Tanioka, Y., and K. Satake (1996), Tsunami generation by horizontal displacement of

ocean bottom, *Geophys. Res. Lett.*, *23*, 861-864.

Velasco, A. A., C. J. Ammon, T. Lay, and J. Zhang (1994), Imaging a slow bilateral rupture with broadband seismic waves: The September 2, 1992 Nicaraguan tsunami earthquake, *Geophys. Res. Lett.*, *21*, 2629–2632, doi:10.1029/94GL02402.

Wessel, P., and W. H. F. Smith (1991), Free software helps map and display data, *Eos Trans. AGU, 72*(41), 445–446.

Yamazaki, Y., Z. Kowalik, and K. F. Cheung (2009), Depth-integrated, non-hydrostatic model for wave breaking and runup, *Int. J. Numer. Methods Fluids* 61(5), 473-497.

Yamazaki, Y., K. F. Cheung, and Z. Kowalik (2011a), Depth-integrated, non-hydrostatic model with grid nesting for tsunami generation, propagation, and runup. *Int. J. Numer. Methods Fluids* 67(12), 2081-2107.

Yamazaki, Y., T. Lay, K. F. Cheung, H. Yue and H. Kanamori (2011b). Modeling regional and remote tsunami observations with finite-fault slip models for the 11 March 2011 Tohoku earthquake (M_w 9.0), *Geophys. Res. Lett.*, **38**, L00G15, doi:10.1029/2011GL049130.

Yamazaki, Y., K. F. Cheung, and T. Lay (2013), Generation mechanism and near-field dynamics of the 2011 Tohoku tsunami, *Bull. Seism. Soc. Am.*, 103, 1444-1455, doi: 10.1785/0120120103.

Ye, L., T. Lay, H. Kanamori (2013), Large earthquake rupture process variations on the Middle America megathrust, *Earth and Planet. Sci. Lett., 381*, 147-155, doi:10.1016/j.epsl.2013.08.042.

Yue, H., and T. Lay (2011), Inversion of high-rate (1 sps) GPS data for rupture process of the 11 March 2011 Tohoku earthquake (M_w 9.1), *Geophys. Res. Lett.*, *38*, L00G09, doi:10.1029/2011GL048700.

Yue, H., and T. Lay (2013), Source rupture models for the M_w 9.0 2011 Tohoku earthquake from joint inversions of high-rate geodetic and seismic data, *Bull. Seism. Soc. Am.*, *103*, 1242-1255, doi:10.1785/0120120119.

Zumberge, J. F., M. B. Heflin, D. C. Jefferson, M. M. Watkins, and F. H. Webb (1997), Precise point positioning for the efficient and robust analysis of GPS data from large networks, *J. Geophys. Res.*, *102*(B3), 5005-5017.

7. 8 Auxiliary Figures

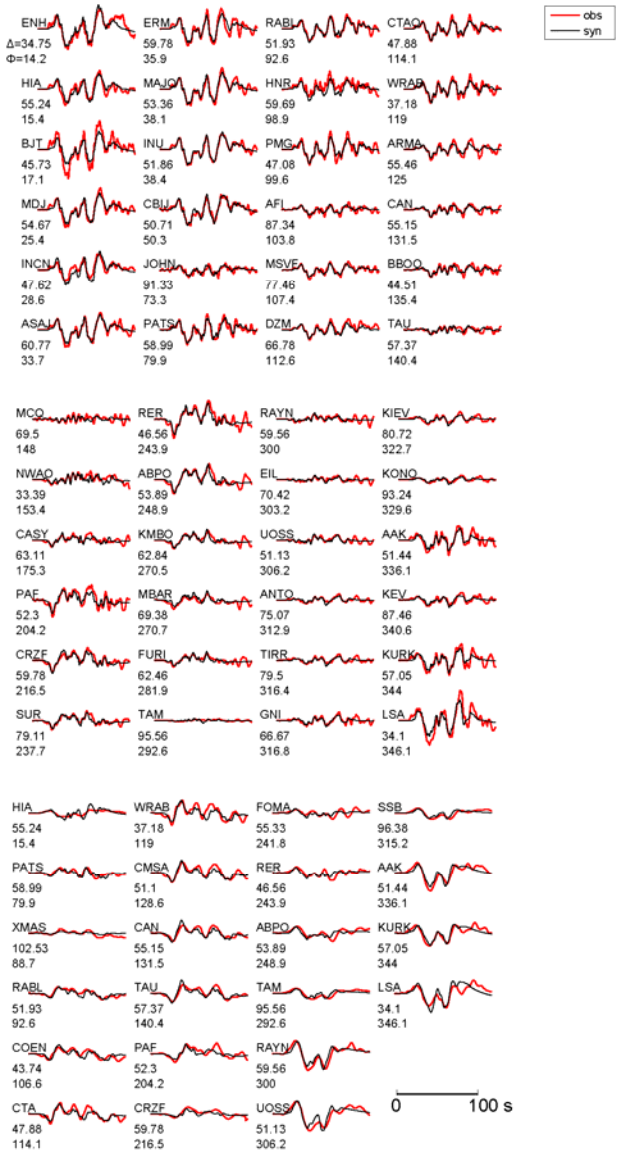

Figure 7. S1. Observed (red) and modeled (black) ground displacement signals for all teleseismic P-waves and S-waves for the preferred joint inversion. Teleseismic records are ordered by azimuth.

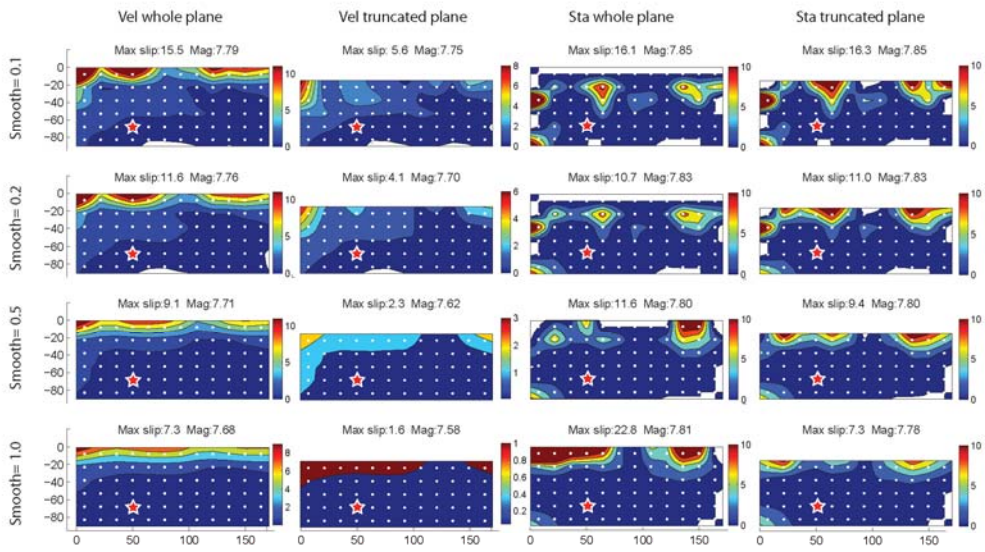

Figure 7.S2. Slip distribution of rupture models inverted with dynamic and static regional displacement observations. From left to right, each column presents inversion results inverted with velocity waveforms with the whole fault plane, velocity waveforms with the truncated fault plane, static displacement with the whole fault plane, static displacement with truncated fault plane, respectively. From top to bottom, each row presents results of smoothing factor selected as 0.1,0.2,0.5 and 1.0. In each panel, the hypocenter location is presented with a red filled star with color scale marked on the right.

Chapter 8

Localized fault slip to the trench in the 2010 Maule, Chile M_w = 8.8 earthquake from joint inversion of high-rate GPS, teleseismic body waves, InSAR, and tsunami observations

Abstract

The 27 February 2010, M_w 8.8 Maule earthquake ruptured ~500 km along the plate boundary offshore of central Chile between 34°S and 38.5°S. Intense ground shaking and large tsunami inundation combined to take more than 500 lives. The co-seismic slip distribution has previously been investigated using geodetic, seismic and tsunami observations, yielding consistent locations of the largest slip in a region extending from 34°S to 35.5°S. However, it remains uncertain whether co-seismic fault offset extended to the trench, which is important for interpreting both shallow frictional behavior and potential for tsunami earthquakes in the region. Joint inversion of high-rate GPS, teleseismic body waves, InSAR, and tsunami observations yields a kinematic rupture model with improved resolution of slip near the trench. Two up-dip large-slip (>15 m) patches are resolved along a bi-lateral rupture with relatively uniform 5-10 m slip down-dip beneath the coast. Both up-dip patches have significant slip in localized regions extending to the trench. The peak slip is ~22 m at a depth of ~15 km on the central megathrust, located ~200 km north from the hypocenter and overlapping the rupture zone of the 1928 M ~8 event. The slip decreases at shallower depth, but is still about ~20 m near the trench. The peak slip is ~15 m in a shallow near-trench patch located ~150 km southwest of the hypocenter. Checker-board resolution tests demonstrate that the tsunami data are critical to resolution of slip near the trench, with other data sets allowing, but not requiring slip far offshore. The stability of the joint inversion reduces the need for regularization. Larger events in the aftershock sequence have a complementary distribution to the co-seismic slip pattern, filling in gaps or outlining edges of large-slip zones. Two clusters of normal faulting events locate seaward along the plate motion direction from the localized regions of large near-trench slip, suggesting that proximity of slip to the trench enhanced extensional faulting in the underthrusting plate.

8.1. Introduction

On 27 February 2010, the devastating Maule earthquake (M_w 8.8, M_s 8.3, seismic moment $M_0 = 1.86 \times 10^{22}$ Nm, http://www.globalcmt.org/) struck the coastal region of central Chile. The epicenter (36.29°S, 73.24°W, 06:34:08 UTC http://www.sismologia.cl/) was ~330 km southwest of Santiago. The rupture extended ~250 km to the NNE and ~250 km to the SSW, spanning ~500 km along strike from 34°S to 38.5°S. The earthquake generated a damaging tsunami, with 29 m maximum run-up water height reported at Constitución (http://www.ngdc.noaa.gov/hazard/tsu.shtml). The ground shaking and tsunami together caused more than 500 fatalities and estimated damage of $30B.

The 2010 Maule earthquake occurred on the plate boundary megathrust fault in the subduction zone where the Nazca plate is underthrusting the South American plate at a convergence rate of ~66 mm/yr [*Angermann et al.,* 1999; *Moreno et al.,* 2012]. In the last century, the megathrust north of the 2010 Maule event ruptured in 1906 (M ~ 8.4) and 1985 (M_w 7.8), and the 2010 rupture overlaps the 1928 (M ~8) rupture zone. The megathrust to the south ruptured in the immense 1960 M_w 9.5 event [*Beck et al.*, 1998; *Lay et al.*, 2010], with some possible overlap of the 2010 rupture with the northernmost end of the 1960 rupture. The megathrust region between Concepción and Constitución was recognized as a seismic gap, with the last previous rupture being in 1835 [*Lay et al*., 2010; *Lay,* 2011; *Lorito et al.,* 2011]. The pre-shock slip-deficit pattern had been investigated by GPS observations [*Moreno et al.,* 2010],

and indicated that the plate interface along the 2010 rupture was particularly strongly locked (>75%) in patches extending from 34°S-35°S and 35.5°S-37.5°S.

The 2010 Maule mainshock co-seismic slip pattern has been investigated in numerous studies. Most indicate an asymmetric bilateral rupture, with larger slip in the NNE direction. *Lay et al.* [2010] and *Koper et al.* [2012] used teleseismic body and surface waves to resolve a bilateral rupture model that expanded ~450 km along strike. Significant near trench slip (> 10 m) is found in northern and southern patches in their models, but it is recognized that the teleseismic body wave data do not unambiguously resolve the shallow slip. *Tong et al.* [2010], *Pollitz et al.* [2011], *Vigny et al.* [2011], *Lin et al* [2013] and *Moreno et al.* [2012], used geodetic observations including InSAR data, coastal leveling, campaign GPS static offsets, and hr-GPS time series to investigate the co-seismic slip distribution. The along-strike slip distributions in these models are generally similar, with bilateral rupture expanding ~500 km along strike, but the slip amount and along-dip slip distribution varies among the geodesy-based inversions, largely as a result of non-uniform spatial sampling of different data types. Most of these models indicate little slip near the trench, with the exception that *Moreno et al.* [2012] found ~5 m of slip near the trench up-dip of the northern slip patch in their model. *Vigny et al.* [2011] suggested that the rupture of the 2010 Maule event likely reached to shallow depth, possibly extending to the trench, but their data could not resolve this. *Delouis et al.* [2011] developed a co-seismic rupture model using hr-GPS, InSAR images for a descending orbit, and teleseismic body and surface waves. In their study ~5 m of slip is also found near the

trench up-dip of the northern rupture patch. *Lorito et al.* [2012] investigated the co-seismic slip pattern by inverting the tsunami and InSAR datasets. Their rupture model resembles the geodesy-based solutions, with no significant slip resolved near the trench.

The basic rupture pattern of the 2010 Maule event is generally consistent across all of the studies mentioned above. The along-strike slip distribution is particularly well constrained by the on-land observations from L-band PALSAR InSAR phase data on board ALOS satellite [Shimada et al., 2010]. However, the along-dip slip distribution is less well resolved, with the amount of slip near the trench being uncertain. This is not an uncommon situation for older great events for which much fewer data are available, and the general tendency has been to assume that co-seismic slip during great megathrust events does not extend to the toe of the sedimentary prism. However, the 2011 Tohoku, Japan M_w 9.0 event has demonstrated that large slip on the megathrust can drive slip to the trench, so this assumption is not secure [e.g., *Fujiwara et al*., 2011; *Kido et al*., 2011; *Lay et al*., 2011b; *Kozdon and Dunham*, 2014]. The apparent lack of slip extending to the trench for the 2010 Maule event has been interpreted in the context of frictional models for the megathrust and mechanical analysis of the forearc structure and morphology [e.g., *Cubas et al*., 2012], and such interpretations directly depend on confidence in the lack of coseismic slip. The importance of evaluating the potential for near trench tsunami earthquakes up-dip of great earthquake slip zones was demonstrated by the 2010 Mentawai M_w 7.8 tsunami

earthquake, which ruptured up-dip of the 2007 M_w 8.5 Indonesia earthquake and produced a catastrophic tsunami [*Lay et al.*, 2011a; *Yue et al.*, 2014].

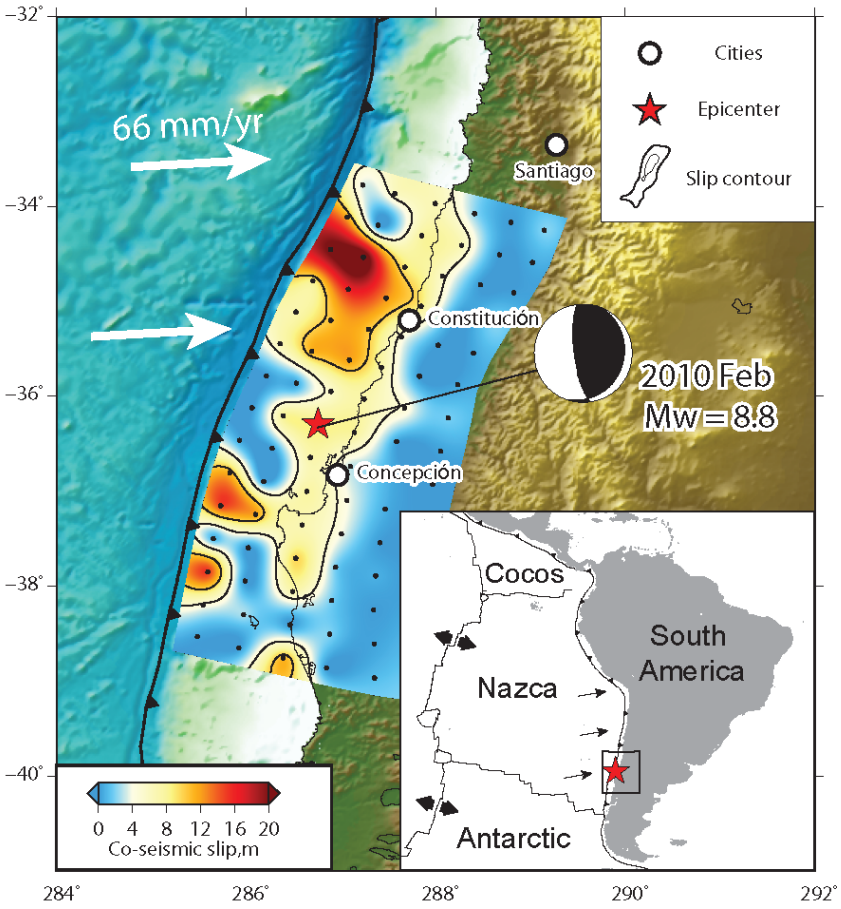

Figure 8.1. The 27 February 2010 M_w 8.8 Maule, Chile earthquake rupture zone and regional plate tectonic setting. The inset map indicates the Nazca plate subducting beneath the South American plate along the Chile trench. The relative plate motion, referenced to the South American plate, is marked with black arrows. The Chile trench is marked with a barbed line. The epicenter of the 2010 Maule event is indicated with a red star. The box identifies the region that is enlarged in the main map. The main map shows the Global Centroid-Moment Tensor best double-couple solution for the 2010 Maule event. The final slip distribution is shown with a blue-red scaled contour map with 5 m and 10 m slip contour lines. Center locations of each sub-fault used in the inversion are marked with black dots. The location of the trench is indicated with the barbed curve. The relative plate motion between the Nazca and South American plates is indicated with white arrows. Major cities, Concepción, Constitución and Santiago, are marked with white-filled circles.

It is known that slip at shallow depth near the trench is poorly resolved by on-shore geodetic data [e.g., *Miyazaki et al.,* 2011; *Ohta et al.*, 2012], and that typical regularization of geodetic inversions penalizes distant slip such that resulting models intrinsically tend to have reduced slip up-dip near the trench. Teleseismic observations are also usually unable to stably resolve near-trench slip, due to low resolution for shallow, nearly horizontal shear dislocations for both body and surface waves. It has been demonstrated that joint inversion of high-rate GPS (hr-GPS) and teleseismic datasets can improve resolution of near-trench slip because it exploits the dynamic wave motions in the GPS recordings [*Yue and Lay,* 2013], however near-trench slip is still relatively less well resolved compared with down-dip slip. Offshore geodetic measurements are of great value [e.g., *Kido et al.*, 2011], but remain unavailable for most subduction zones. In contrast to land-based geodetic and seismic datasets, tsunami observations can provide good resolution of near trench slip, due to both the strong tsunami generation by shallow rupture and the good spatial resolution provided by slow tsunami waves [e.g., *Maeda et al*., 2011; *Yamazaki et al.*, 2011; *Satake et al*., 2013], but the long wavelengths involved do limit detailed slip characterization.

We have previously incorporated tsunami modeling into our source inversions using iterative inversion of seismic and geodetic data and forward modeling of tsunami observations, adjusting poorly constrained inversion parameters to achieve compatible models [*Yamazaki et al.,* 2011; *Yue et al.,* 2014]. Multiple iterations are typically required to achieve a model consistent with all observations. In this study,

tsunami observations are explicitly included in joint linearized inversion with seismic and geodetic data to exploit the information of all datasets and to achieve stable inversion results. We find that the joint inversion improves the resolution of the slip near the trench as well as across the entire fault plane. Localized regions of large slip are found to extend to the trench, while other regions had no coseismic slip at shallow depths, up-dip of deeper slip zones.

8.2. Data and Methods

8.2.1 Fault parameterization

The rupture model is initially parameterized with a dip-varying fault surface with a scale of 600×240 km^2. The fault plane is discretized into 15 subfaults along strike and 6 along dip, with the dimension of each subfault being 40×40 km^2. The hypocenter (36.29°S, 73.24°W) is located on the 8^{th} subfault-center node along strike and 3^{rd} node along dip. Then the rectangular fault plane was adapted to the 3D slab interface model resolved from gravity observations [Figure 8.2, *Tassara and Echaurren,* 2012], keeping the same subfault depths but shifting the horizontal coordinates. Parameters describing the geometry of each subfault, including local strike, dip and length scale, were adjusted from the curvature of the 3D fault model. The adjusted dimensions of subfaults ranges from 38 to 45 km (Figure 8.2). A single rake angle of 104°, from the USGS W-phase moment tensor best double-couple solution, is assigned to all subfaults. The rake angle of 116° from the Global centroid-moment tensor (GCMT) solution was also tested and does not change the

rupture pattern significantly, but does not fit the data as well. We also performed inversions with varying rake for each subfault, finding that it did not change the rupture pattern significantly, and did not produce significant improvement in the data fitting. Our preferred model is for the single rake (104°) inversion.

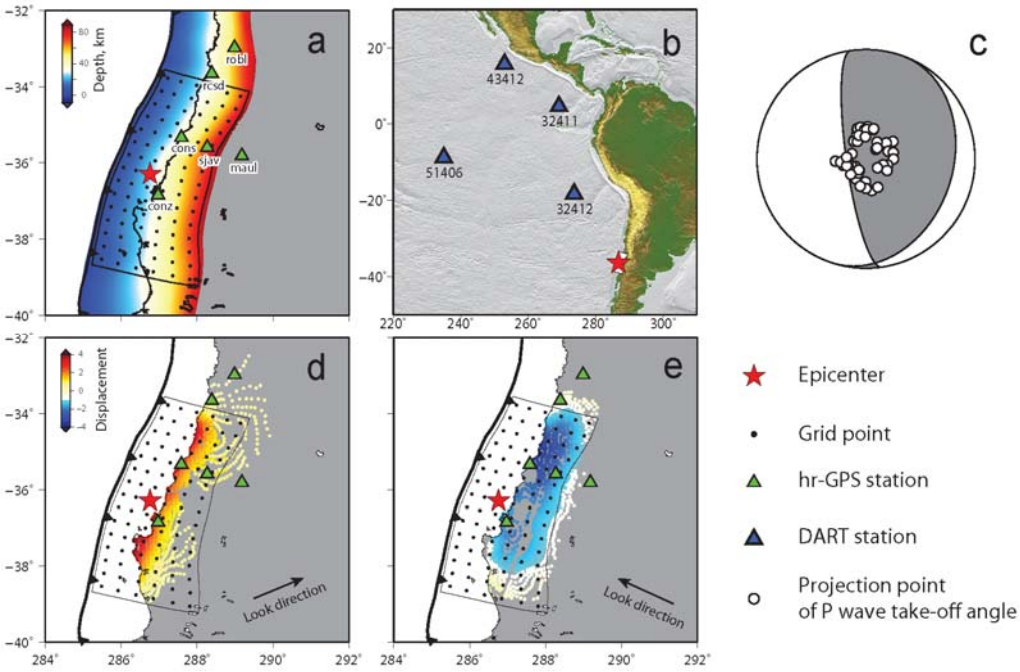

Figure 8.2. Rupture model parameterization and datasets used in the joint inversion. **a**) Map of the rupture model grid, parameterized with 15 nodes along strike and 6 nodes along dip. The black polygon defines the fault model surface. Locations and geometry of each subfault are adapted to the 3D plate boundary model [*Tassara and Echaurren,* 2012] shown with blue-red color scale. Approximate subfault dimensions are 40 × 40 km^2. Center locations of all subfaults are indicated with black dots. Locations of high-rate GPS stations are marked with green-filled triangles with station names. **b**) Locations of 4 DART stations (blue-filled triangles), with station names indicated. Ocean bathymetry gradient is shown with a gray-scaled map. **c**) The azimuths and take-off angles of teleseismic P and SH wave ground motion recordings used in our inversion are projected onto the lower hemisphere equal area stereographic projection along with P wave radiation nodes. **d)** and **e**) Sample points of ground displacements projected to the (Line of Sight) LOS direction of ascending (**d**) and descending (**e**) orbits. Displacements in LOS direction are shown by a blue-red color scale with the color bar shown on the top left of **d**. The look direction is indicated with a black arrow.

We adopt a multi-time-window algorithm to parameterize the subfault source time function [*Hartzell and Heaton*, 1983], in which the source time function of each subfault is parameterized with a series of triangles with an initial time calculated for an assumed maximum rupture velocity. The algorithm of *Yue and Lay* [2013] is used to combine different datasets in a joint inversion. Data processing and Green functions computation are each dataset are described in the following.

8.2.2 hr-GPS dataset

Our 1-s sampled hr-GPS dataset is essentially the same as described in detail and modeled in *Vigny et al.* [2011]. The original hr-GPS recordings were processed with TRACK software developed at MIT. We use the LC combination and IGS precise orbits, and apply a smoothing filter on the backward solution to estimate the atmospheric delays using 24-hour data and fixing any non-integer biases to a constant value. TRACK computes a relative position with respect to a fixed reference station, and station SILL was selected as the reference, because it is close enough to the hypocenter to ensure high accuracy of relative location. The processed hr-GPS records are essentially the relative position between each station and the reference station (SILL). Stations within 500 km epicentral distance are used in our joint inversion; more distant stations have low signal-to-noise ratios and intrinsic insensitivity to fault finiteness.

Three-component records of 6 hr-GPS stations (Figure 8.2a) were used in joint inversion. Because TRACK computes relative position from a reference station, some

coherent signal at 230-250s is apparent at all stations (Figure 8.3), which is caused by the ground shaking from surface waves arriving at the reference station. To remove this coherent signal, we cut the hr-GPS records at 180 s, after the dynamic waves have passed the closer stations but not yet reached the reference station. The waveforms after 180 s at the 6 stations were averaged to extract the common dynamic motions at the reference station. The stacked displacement was then removed from all traces, suppressing the coherent phases (Figure 8.3). We found this procedure more stable than explicitly predicting the SILL motions and differencing the signals.

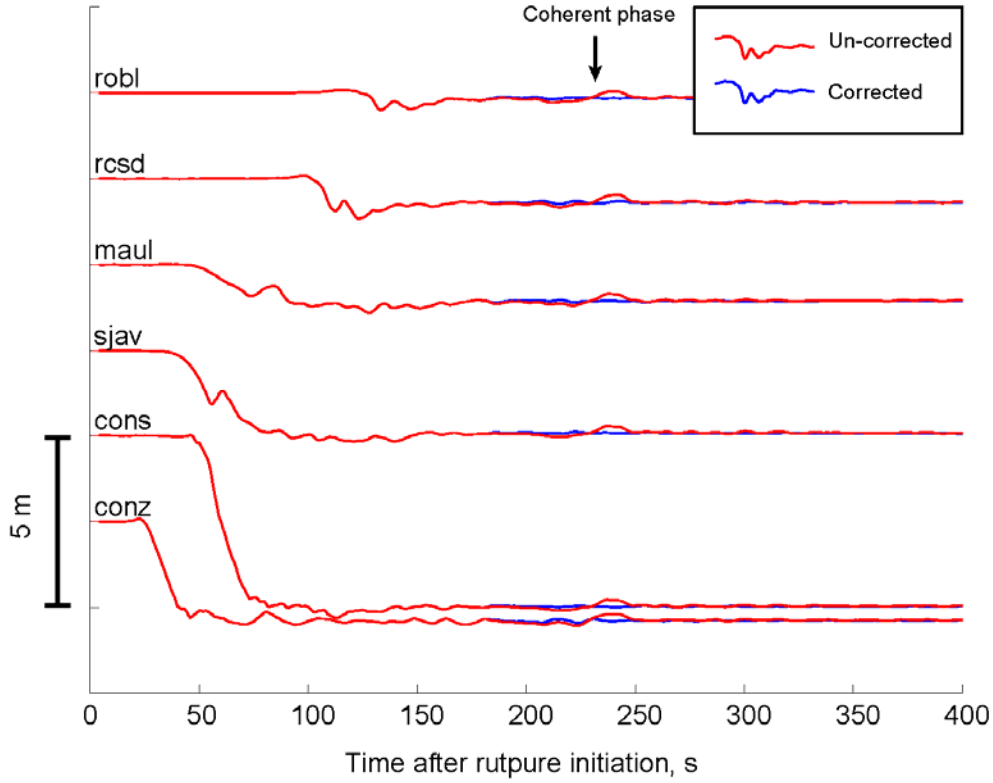

Figure 8.3. Time histories of the east-west (downward is westward) ground displacement components at 6 hr-GPS stations, referenced to station SILL, are plotted in red. A coherent feature, caused by arrival of surface waves at station SILL, is apparent at about 230 s in all records. The coherent signal was estimated by averaging signals for the 6 records after their dynamic motions had ended (after 180 s). The coherent signal was then removed from all of the records, giving corrected waveforms plotted in blue.

To model the time-dependent near-field ground displacements recorded by hr-GPS, Green functions for the full dynamic and static elastic deformation field must be used. To exploit the short-period information for very near-field displacements, we applied a frequency-wavenumber (F-K) integration method that includes all near-field terms (Computer Programs in Seismology, Robert Herrmann) to compute Green's functions for four nearby stations, *conz, cons, sjav* and *maul*. The F-K method accounts for both dynamic and static near-field ground displacements. The 1D layered model for the Green's function computation was extracted from a local tomography model [*Haberland et al.,* 2009]. The parameters of the 1D model are listed in the supplementary materials. Parameters of the local 1D model are listed in supplementary materials. A 300 s long time window is used for both data and Green functions. Both data and Green functions are filtered with a 1 pass 4^{th} order Butterworth low pass filter with a corner frequency of 0.1 Hz.

The four hr-GPS stations listed above locate within 500 km from all subfaults, and the flat-layered Earth model is sufficient to capture the first order wave propagation behavior. For more distant stations *rcsd* and *robl*, Earth curvature is accounted for using Green functions calculated by mode summation for a spherical Earth model. We summed all modes for the Preliminary Reference Earth Model (PREM) up to 80 mHz [*Yue and Lay,* 2011]. PREM is not a realistic regional structure to capture the high frequency wave propagation in continental lithosphere, thus we applied a low-pass filter with lower corner frequency, at 0.06 Hz, to utilize the low frequency energy in both data and Green functions for these two stations. This corner frequency proved

effective for inverting hr-GPS records of the Tohoku earthquake [*Yue and Lay*, 2011].

8.2.3 Teleseismic dataset

The teleseismic body wave dataset is comprised of 43 P wave and 18 SH wave ground displacement recordings (Figure 8.2c) from stations of the Federation of Digital Seismic Networks (FDSN), accessed through the Incorporated Research Institutions for Seismology (IRIS) data management center. The data were selected from hundreds of available FDSN seismograms to ensure good azimuthal coverage and high signal-to-noise ratios, for epicentral distances from 40° to 90°. Instrument responses were deconvolved to provide ground displacement with a bandpass filter having corner frequencies of 0.005 and 0.9 Hz. 180-sec-long time windows were used, starting 10 sec prior to initial P or SH arrivals. The P wave signals provide information about seismic radiation for periods as short as several seconds, but are depleted in shorter period energy due to the nature of the source process.

The teleseismic Green functions are generated using a reflectivity method that accounts for body wave interactions in 1-D layered structures on both source and receiver sides [*Kikuchi et al.*, 1993]. The same local source velocity model was used in the Green function's computation as that used in hr-GPS Green's function computation. A typical continental model was used for the receiver side. The same band-pass filter used for the data is applied to the Green functions.

8.2.4 InSAR dataset

The InSAR dataset used in this study is the same as described in detail in *Tong et al.* [2010], comprised of 1080 samples of descending orbit and 821 samples of

ascending orbit (Figure 8.2d,e). The InSAR sampling covers the full length of the fault plane and extends from the coastline to ~150 km inland. The combination of ascending and descending images provides observations of co-seismic deformation in two directions, which provides well-constrained slip distribution, especially for the along-strike distribution and the down-dip slip termination [*Tong et al.* 2010].

The Green functions used to model the co-seismic ground deformation for the InSAR modeling are computed from a FORTRAN code developed by *Wang et al.* [2003]. This uses an orthonormalization method [*Wang,* 1999] to compute static ground displacement fields for a rectangular dislocation source in layered media. The same local source velocity model used in hr-GPS and teleseismic Green's function computation, after removing the water layer, is adopted to compute the static ground displacements. Three component ground displacements were computed and projected to the two length of sight (LOS) directions for each InSAR sample point.

8.2.5 Tsunami dataset

Wave heights recorded at 4 DART (Deep-ocean Assessment and Reporting of Tsunamis) ocean bottom pressure stations are used in our joint inversion (Figure 8.2b). Detided wave height recorded at 1 sample per minute is accessed from NOAA (http://ngdc.noaa.gov/hazard/dart/2010chile_dart.html).

Issues about linear inversion validity arise when including tsunami data in linearized finite-fault inversion, associated with non-linear wave excitation and propagation in very shallow water. The non-linear wave propagation makes it very challenging to model short wavelength wave heights recorded near the coast, such as

in tide gauge recordings. However, for deep ocean wave height, such as the DART data, the scaling and combining of tsunami waves intrinsic to a many subfault model can be reasonably assumed to follow a linear relationship for the direct main tsunami pulse [e.g., *Satake et al.,* 2013]. For the deep ocean records, modeling with linear and non-linear codes produce very similar results for the main tsunami pulse dominated by long wavelength arrivals, indicating that the non-linear wave effects are not too important for the deep ocean recordings. In our inversions, the tsunami waveforms are windowed to include only the signal around the main arrival of each tsunami recording, omitting later reflections from the coast that are more sensitive to the non-linearity of excitation and shallow water propagation affecting the short wavelength signals.

8.2.6 Tsunami Green functions generation and correction

The tsunami Green functions are computed with COMCOT (Cornell Multi-Grid Coupled Tsunami Model code; http://ceeserver.cee.cornell.edu/pll-group/comcot.htm), a linear non-dispersive code that solves the shallow water wave equations. We use the 1 arc-min ocean bathymetry model resampled from GEBCO_08 (http://www.gebco.net/data_and_products/gridded_bathymetry_data/). The Green functions for each subfault are for vertical ground displacements calculated by the Okada model [*Okada,* 1992]. The vertical displacement of the ocean floor is taken as the initial ocean surface height and then COMCOT solves for the resulting wave propagation. Horizontal displacements in the presence of irregular bathymetry also produce ocean floor uplift [*Tanioka and Satake,* 1996]. We use the method of

[*Tanioka and Satake,* 1996] to calculate the co-seismic horizontal displacements from the Okada model, performing a vector product with the ocean bathymetry normal vector to scale up the uplift-based tsunami Green functions. The horizontal displacements contribute 10~20% of the total uplift. Co-seismic displacements calculate for the source velocity model using *Wang et al.* [2003] were also used to scale up the Green functions to simulate ground deformation consistent with hr-GPS and InSAR Green's functions.

It has been observed that for the 2011 Tohoku earthquake and other large events, modeled tsunami based on different computational methods tend to arrive earlier than observed tsunami, with about a ~1% velocity discrepancy [*Simons et al.,* 2011; *Yamazaki et al.,* 2012]. This can amount to as much as 10 min error when propagating across the Pacific Ocean [*Watada et al.,* 2014], and clearly presents a limitation for resolving slip distribution for large megathrust earthquakes. The causes of this mis-modeling have been investigated by *Tsai et al.* [2013] and *Watada et al.* [2014]. It appears that most of the velocity discrepancy results from neglecting the contributions from coupling between the gravity of the water column and the elasticity of the ocean floor. There is also a contribution from water density increase with depth, which is usually ignored. In addition, dispersion effects of the oceanic waveguide do play an ortant role in short period tsunami wave propagation, and some tsunami modeling codes do not account for this. The combination of the three sources of error requires correction of the tsunami dispersion curve in which >1% velocity

correction is applied to all wavenumbers [*Tsai et al.,* 2013]. Application of these corrections can eliminate the tsunami travel time discrepancies.

Because absolute timing is critical for our joint inversion, we apply corrections to our tsunami Green functions to ensure accurate propagation effects. Since our tsunami synthetics are generated with a non-dispersive algorithm, all three corrections need to be applied to our Green functions dataset. Our calculation of the corrected tsunami phase velocity, c, is given by:

$$c = c_0 - c_1 - c_2 - c_3 \quad (1)$$

Where

$$c_0 = \sqrt{gh} \quad (2)$$

$$c_1 = \sqrt{gh}\left[1 - \sqrt{\frac{\tanh(kh)}{kh}}\right] \quad (3)$$

$$c_2 \approx \sqrt{gh}\frac{(1-v)\rho g}{2\mu k} \quad (4)$$

$$c_3 \approx \sqrt{gh}\frac{\Delta\rho}{4\rho_{avg}} \quad (5)$$

c_0 is the non-dispersive velocity for the shallow water equation, c_1 accounts for the dispersion of the shallow water wave equation [*Mei,* 1989], c_2 is caused by the water column gravity and ocean floor elasticity coupling [*Tsai et al.,* 2013], and c_3 is caused by effect of water density gradient with depth [*Tsai et al.,* 2013]. In these equations, h is the water depth, k is wavenumber, $v = 0.3$ and $\mu = 73GPa$ are the Poission's ratio and shear modulus of the elastic ocean floor. We used the elastic parameters of the PREM model averaged over the upper 500 km depth to approximate the penetration depth for tsunami waves with similar wavelength. $\Delta\rho = 19kg/m^3$ is the density variation of the water column and $\rho_{avg} = 1036\,kg/m^3$ is the average

density of the water layer. To apply these corrections to the Green functions, these expressions in the wavenumber domain are converted to the frequency domain by the relationship $k = \omega/c \approx \omega/\sqrt{gh}$.

Note that c_1 and c_2 both depend on k or ω, indicating they are both dispersive. The c_1 term (shallow water wave equation dispersion) causes shorter period waves to travel slower, which is normal dispersion; however, the c_2 term (gravity-elasticity coupling) makes longer period waves travel slower because they couple more with ocean floor elasticity, producing reverse dispersion. The COMCOT Green functions provide a reference state for which all wave periods travel at the same velocity c_0, and capture the first-order propagation effects such as geometric spreading and focusing/defocusing. By applying corrections for each period we produce dispersed Green functions that have correct arrival times, assuming the propagation effects are linear, without changing the amplitude other than as a result of dispersion. Because the velocity corrections are small (1-5%) relative to the ocean bathymetry contrasts there should not be significant change in the geometric spreading at each period.

Our phase correction procedure includes

1. Calculate the bathymetry profile along the great circle through the smoothed ETOPO1 model, for each source-receiver pair. For the corrections we assume the tsunami propagates along the great circle, which could be biased by the near coast bathymetry gradient. However, all of our tsunami observations are in the deep ocean basin, and no source-receiver path approaches the continental boundary, thus the wave paths are little impacted by the near coast bathymetry gradient. In additions, the

tsunami waves used in our study are very low frequency, associated with wave-lengths of hundreds of kilometers, which are not sensitive to the detailed bathymetry along the path. Therefore we used a smoothed bathymetry model to make corrections.

2. Discretize the path into *n* segments and calculate the non-dispersive arrival time by $t_0 = \sum_{i=1}^{n} \frac{d_i}{\sqrt{gh_i}}$, where i is the index of each segment along the path. h_i is the associated bathymetry at each segment.

3. Fourier transform the original tsunami Green's function.

4. Calculate the dispersive velocity correction at each segment *i* using equations (2), (3), (4) and (5) for each frequency of the Green function spectrum:

$$\mathrm{c}_i(\omega) = c_{i0} - c_{i1}(\omega) - c_{i2}(\omega) - c_{i3}$$

5. Calculate the corrected arrival time of each frequency by $t_{(\omega)} = \sum_{i=1}^{n} \frac{d_i}{c_i(\omega)}$ and obtain the differential arrival time by $\Delta t_{(\omega)} = t_{(\omega)} - t_0$

6. Convert the differential arrival time to phases by $\Delta\varphi(\omega) = -2\pi i\omega\Delta t_{(\omega)}$, where $i = \sqrt{-1}$.

7. Apply the phase correction to each frequency of the Green functions and convert back to the time domain.

This phase correction is applied to each source-receiver pair. Examples of the original and corrected Green functions are shown in Figure 8.4. The corrected Green functions for shallow subfaults acquire a more dispersive shape, with low frequency energy arriving earlier than high frequency energy. This dispersive effect has significant effect on the waveforms of the Green's functions. Corrections for down-dip Green

functions provide more of a uniform waveform shift, due to weak excitation of short-period tsunami energy. Weak, early negative energy is apparent in the corrected Green's functions, caused by the reverse dispersion of gravity-elastic coupling as noted by *Watada et al.* [2014]. The corrections are larger for more distant stations, because the velocity corrections accumulate with distance.

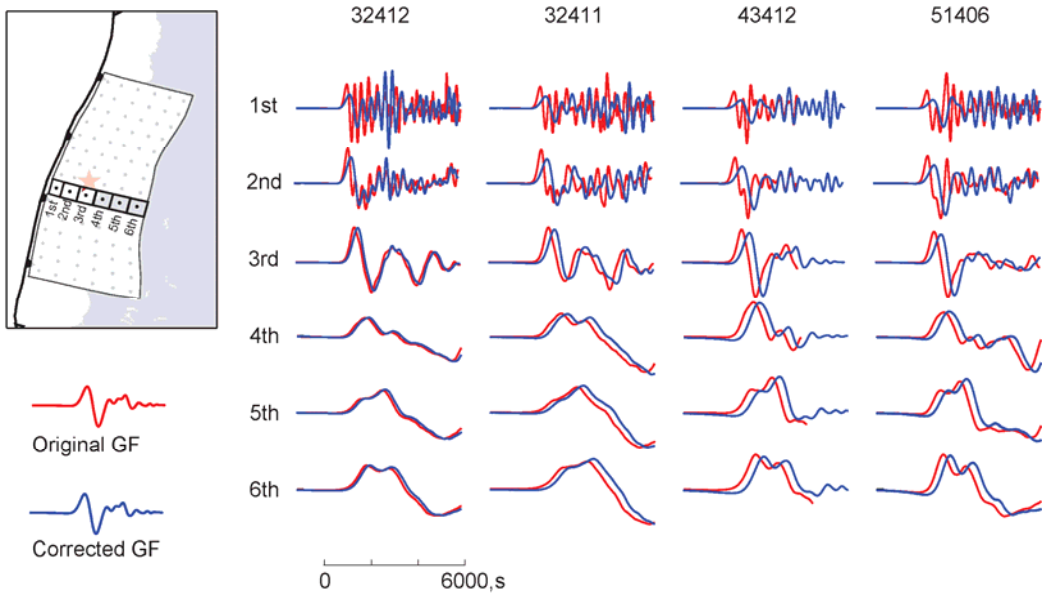

Figure 8.4. Initial dispersion-free and dispersion-corrected tsunami Green's functions are plotted in red and blue, respectively. The 7th column of subfaults in the finite-source model is selected to demonstrate the effect of the dispersive phase correction. The location and indexing of the subfaults is shown in the top left panel. The waveforms are ordered by subfault index in the vertical direction and epicentral distance in the horizontal direction. Subfault index and DART station name (see Figure 8.2b) are shown on the left and top of each row and column, respectively. The time scale is presented at the bottom. The phase correction, which is a cumulative effect of wave propagation, is more significant at larger distances. Dispersive effects are more obvious for up-dip subfaults, while for down-dip subfaults the corrections behave more like a time shift.

These corrected tsunami Green function can now be directly used in our joint inversion using absolute time (as for the hr-GPS signals), without empirically adjusting the arrival times of tsunami synthetics as has been done in previous studies.

Earlier analyses of the tsunami signals for the 2010 Maule event have noted the issue of dispersion correction and bias in the absolute times due to ignoring elasticity of the underlying medium, but this is the first study to correct for all the known effects.

8.2.6 Checker-board test

Checker-board tests are commonly used to investigate inversion stability and data resolution. Here we present checker-board tests to evaluate intrinsic resolution provided by each type of dataset and to explore the potential advantage of joint inversion. In our checker-board tests the input model is specified with 2 m of slip for every other 2×2 subfault group (Figure 8.5a). A rupture velocity of 2.8 km/s is used to set the initial time of each subfault. Synthetics for all four datasets are generated with the same Green functions used in the inversion. A 10% level of white noise is added to all synthetics. In the inversion of checker-board synthetics, we prescribed the rupture velocity to be 10% higher than the input rupture velocity, and used relatively long (20 s) sub-fault source durations to capture the source duration of all subfaults. For the inversions of actual data, the rupture velocity may not be uniform and the precise rupture velocity is not well known, so we will similarly specify a high enough rupture velocity and long enough subfault source durations to avoid kinematically biasing the results [*Yue and Lay,* 2013]. Some regularization or smoothing is applied to the checker-board inversions to stabilize the results, similar to what we apply to actual data.

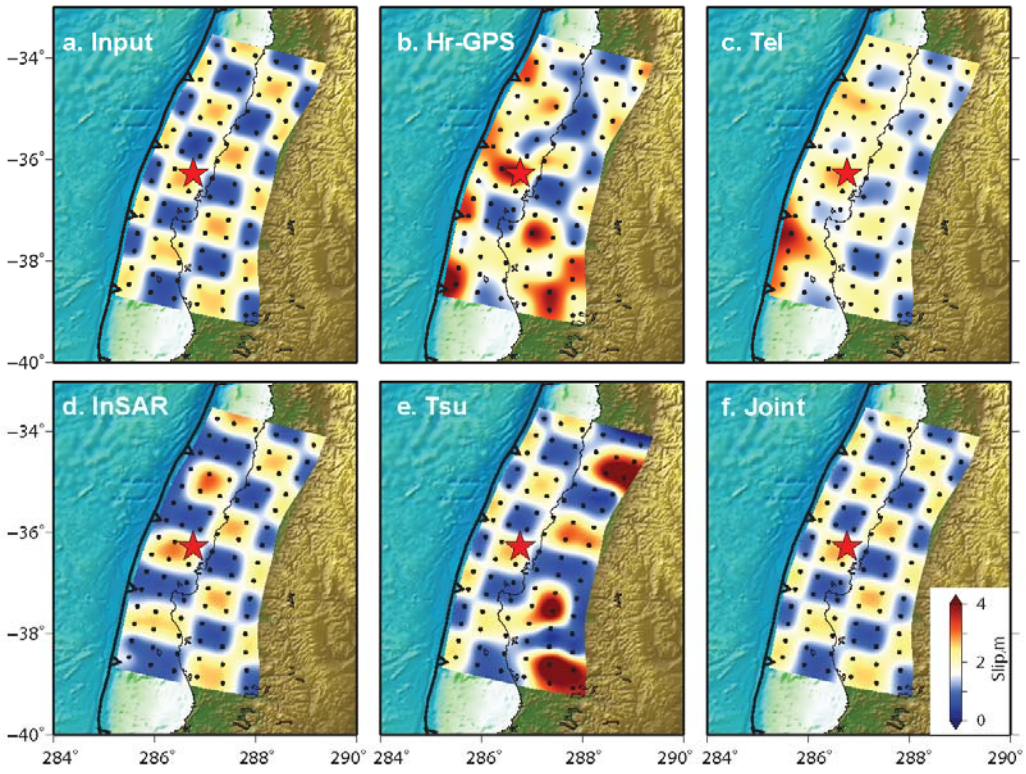

Figure 8.5. Checker-board tests of inversions with all datasets separately and jointly. **a**) The input model, with 2 m slip assigned to every other 2×2 subfault patch. Noise, rupture velocity uncertainties and regularization are adopted in all inversions as discussed in the text. **b**) Inversion of the hr-GPS dataset resolves the central region of the slip pattern, but has substantial distortion and over-estimation of slip on more distant patches. **c**) Inversion of the teleseismic dataset has good down-dip resolution but diminished resolution of shallow slip near the trench. **d**) The InSAR dataset provides good down-dip resolution along the entire model, but the slip pattern near the trench is smeared from down-dip. **e**) The tsunami dataset provides good resolution of near-trench slip but limited resolution of down-dip rupture. **f**) The joint inversion combines the complementary advantages of the datasets and allows accurate recovery of the input model.

We performed checker-board inversions for all datasets separately and jointly. Representative results are shown in Figure 8.5. We have previously found that hr-GPS data provide good resolution and inversion stability if the station distribution is ideal [*Yue and Lay,* 2011, 2013]. For the 2010 Maule event, most hr-GPS stations are located north along the fault plane (Figure 8.3a), such that the slip to the south is not

well constrained (Figure 8.5b). In particular, slip on the southern half of the shallowest row is over-estimated in the hr-GPS inversion. The patchiness of the input model is generally resolved in the hr-GPS inversion, but the amplitude is not well constrained for the patches further from the stations. The teleseismic body wave dataset has generally good resolution for down-dip slip (Figure 8.5c), but poor resolution of slip near the trench. Neither the shallow slip pattern nor the slip amplitude is well constrained by the teleseismic-only inversion. The InSAR dataset provides very good resolution for down-dip slip (Figure 8.5d), as a result of the continuous data sampling on land. However, the InSAR data have very limited resolution of up-dip slip, with the shallow model contaminated by smearing from the second row. The resolution provided by the tsunami dataset (Figure 8.5e) is opposite to that of the InSAR dataset: the slip near the trench and in the top 3 rows is very well resolved but there is poor resolution down-dip beneath the land. The deeper slip does not produce much tsunami excitation. Joint inversion (Figure 8.5f) combines the advantage of all datasets and resolves both the slip pattern and slip amount very well.

For the joint inversion we are combining a mix of data that have explicit time-dependent sensitivity (teleseismic body waves, dynamic waves in the hr-GPS, and tsunami signals) with static offset information (static motions in the hr-GPS, InSAR). The kinematic model is directly constrained by the time-varying information, but is informed by the static information, which requires spatially consistent slip. We specify a maximum initial rupture velocity even while allowing flexibility in the time history via the multi-time window algorithm. The initial rupture velocity is commonly

estimated by determining inversion residual trade-off curves [e.g., *Yue et al.,* 2013]. Here we used a trade-off curve for the joint inversion, finding a preferred initial rupture velocity of 3.0 km/s. This is compatible with earlier studies, which utilize rupture velocities in the range 2.0 to 3.0 km/s.

Relative weighting always presents an important issue for joint inversions. The hr-GPS and InSAR geodetic datasets provide error estimates for the data for each sample point that can weight the covariance matrix of the Green functions. However, for the teleseismic and tsunami datasets, the most significant error comes from the uncertainty of the Green functions, making it hard to formally estimate the intrinsic error in the joint inversion problem. Our previous approach has been to normalize each dataset by some measure of corresponding maximum amplitude and to test the dataset weighting relative to the natural weighting (equal weighting of the normalized datasets) to seek a minimum residual. For the 2010 Maule event, we found that reasonable variation of relative weighting does not introduce significant changes of the slip pattern or data fitting, and we finally chose to assign all datasets natural weighting.

Regularization approaches are generally necessary in geophysical inversions, which are mostly under-determined, to stabilize the inversion. In our previous joint inversion work, we have explored different levels of regularization seeking to match independent observations, such as ocean bottom displacements [*Yue and Lay,* 2011] or tsunami waves [*Yue et al.,* 2013]. For the joint inversion of the 2010 Maule event, we found that the slip estimation across the fault plane is sufficiently well-constrained

that smoothing beyond the intrinsic grid parameterization is not necessary to stabilize the inversion result. So for the final inversion result, no further regularization was applied; this leads to some roughness of the solution, but it means that the model is not dominated by smoothing criteria as is typically the case.

8.3. Results and Discussion

The preferred finite fault model is shown in a fault plane view in Figure 8.6. The rupture has a bi-lateral propagation pattern that is dominated by a northern slip concentration, as in most previous studies. The northern slip distribution extends ~280 km along strike from the hypocenter, with the peak slip being located ~200 km north of the hypocenter at ~16 km depth. Significant slip of up to ~20 m is located up-dip of the peak slip patch, extending to the trench toe. A southern slip patch extends ~200 km along strike from the hypocenter. The peak slip (~15m) is located near the trench. The near-trench fault region up-dip from the hypocenter has little slip. No significant slip is found in the lower two rows of the model, which shows a consistent down-dip slip limit to that resolved by InSAR data [*Tong et al.,* 2010]. This down-dip limit may be controlled by the intersection of the upper plate Moho interface with the subduction slab, as has also been found for the 2012 Costa Rica M_w = 7.6 event [*Yue et al.,* 2013]. The cumulative seismic moment of our rupture model is 2.8×10^{22} Nm, given a moment magnitude of M_w = 8.9; this is higher than the 1.9×10^{22} Nm value for the point-source GCMT solution. In part this may represent the dip-varying geometry of the plate interface model, but the model moment can be reduced to 2.2×10^{22} Nm,

by trimming down-dip and southerly subfaults that have little slip. Parameters of our inversion results are listed in the supplementary materials.

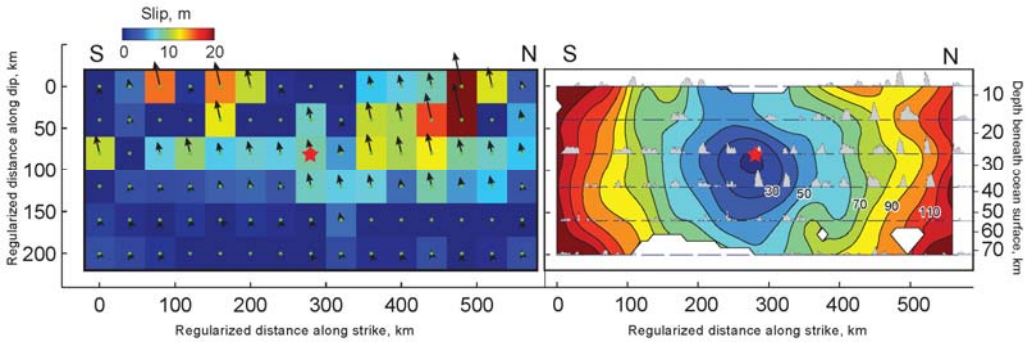

Figure 8.6. a) Rupture-plane views of the slip distribution for the preferred model with a rupture velocity of 3.0 km/s. The scale of each subfault is adjusted to be 40 × 40 km^2. Center locations of each subfault are presented with green dots, with a black arrow presenting the rake direction scaled by the slip amount, which is also used for the color scale on the left. The largest slip occurred north of the hypocenter, with a maximum slip of ~22 m ~200 km north of the hypocenter in the second row. Up-dip from this large-slip region substantial slip (~20 m) occurred in the shallowest subfault extending to the trench. Rupture propagated to the south ~200 km, with averaged slip of ~ 8 m along the third row. The maximum slip of ~15 m in the south occurred near the trench. Slip up-dip from the hypocenter is insignificant. **b**) Source time functions for each subfault node are shown as gray-filled polygons. The centroid time of each node is contoured as the background colored map. Absolute depths are indicated on the right. In both panels, the hypocenter is indicated with a red-filled star.

Fits of the joint inversion synthetics to all datasets are shown in Figure 8.7. Satisfactory matches of all 4 datasets are found. The residual of data fits to hr-GPS, InSAR, and tsunami observations is at a level of several percent, while for the teleseismic dataset the residual level is ~20% (Figure 8.7a). The residual of InSAR data with descending orbit is larger than the residual for the ascending orbit. Several loci of significant InSAR residual (~50 cm) are located near the coast (Figure 8.7b). Considering the intrinsic uncertainty of the InSAR observations (~10 cm), this

discrepancy is not explained by data error. The descending InSAR dataset was acquired ~1 week after the mainshock, so it is likely contaminated by afterslip or early aftershocks. No contamination by afterslip is present in the hr-GPS, teleseismic and tsunami datasets. The observed InSAR residual is comparable to the discrepancy with the hr-GPS observations when projected to the corresponding LOS direction. Therefore, the observed localized misfit of the InSAR dataset is plausibly caused by afterslip.

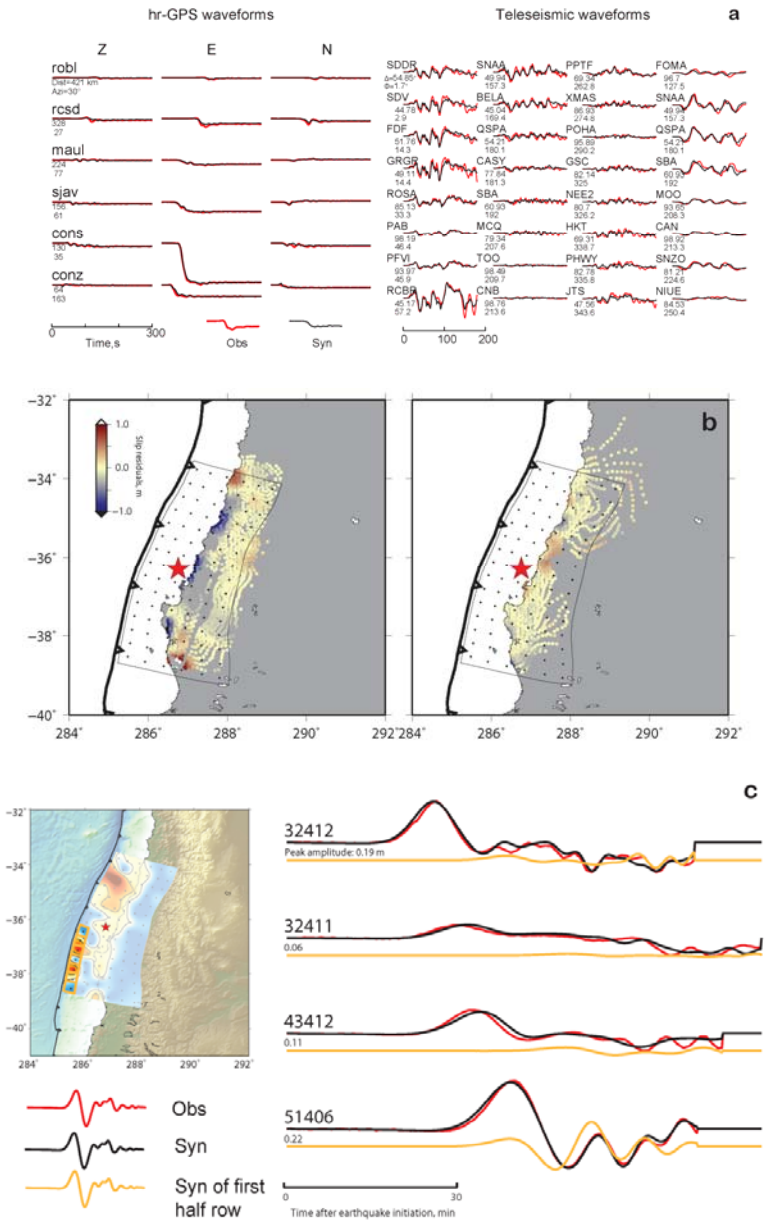

Figure 8.7. Data fits for the preferred joint inversion model. **a**) Observed (red) and modeled (black) ground displacement signals for hr-GPS and selected teleseismic P-waves and S-waves. Station names, epicentral distances and azimuth of each record are indicated. **b**) Residual displacements in LOS direction of each InSAR sample point are shown with a blue-red color scale for descending (left) and ascending (right) orbits respectively. The epicenter is indicated with a red-filled star. Center locations of all subfaults are shown with black dots with the fault model boundary indicated with a black polygon. **c**) Observed (red) and modeled (black) tsunami height at four DART stations. Station names and peak amplitude are shown. Waveform contributions from

the 1st to 7th subfault along strike in the first row, marked by orange rectangles in the left panel, are plotted in orange.

The near-trench slip in the southern part of the rupture is not evident in most previous inversions of geodetic data. Contributions to data fits from this slip patch are insignificant for the hr-GPS, teleseismic and InSAR datasets, but the contribution is significant for some of the tsunami observations. The observed and modeled tsunami waveforms are plotted in Figure 8.7c, and the isolated contribution from the 7 subfaults on the top-left row of the model is plotted for comparison. The contributions from the 7 subfaults to fits to the tsunami waves have significant azimuthal pattern, with the largest signals being for DART 51406. Because the velocity of tsunami waves is about 200 m/s, a 200 km long line source along the trench strike direction generates more coherent tsunami signal to station 51406 (the station most perpendicular to the fault) than a line source along the trench dip direction. Station 51406 has two significant peaks, indicating two strong shallow slip patches in the 2010 Maule earthquake. The southern shallow slip accounts for the second peak. Because the other tsunami observations are from stations further to the northwest, the arrival from the southern shallow slip arrives late in the recordings, obscured by dispersion of earlier arriving signals. Lacking tsunami observations to the south, we cannot tightly bound the shallow slip in the south, but it is supported by the data at DART 51406.

To further test the robustness of the shallow slip patches, an inversion was performed in which the shallowest model row was removed. All other inversion

parameters are the same as for the preferred model. The resulting slip model is shown in Figure 8.8, compared with the complete fault plane model. The along-strike slip distribution is not significantly impacted by truncation of the top model row, but the slip on the second row is enhanced. The fault model truncation does not significantly degrade the data fits for the hr-GPS, teleseismic and InSAR datasets, as expected based on the checker-board tests (Figure 8.5). However, the truncation degrades the fit to the tsunami waveforms. This is shown in Figure 8.8, where waveforms predicted by the complete and truncated fault models are compared with the observations. The truncated fault model fails to fit either the arrival time or the peak amplitude of each observation. We infer that the patchy distribution of large near-trench slip is necessary to fit the tsunami data, and that it cannot be ruled out by inversions of the other data sets.

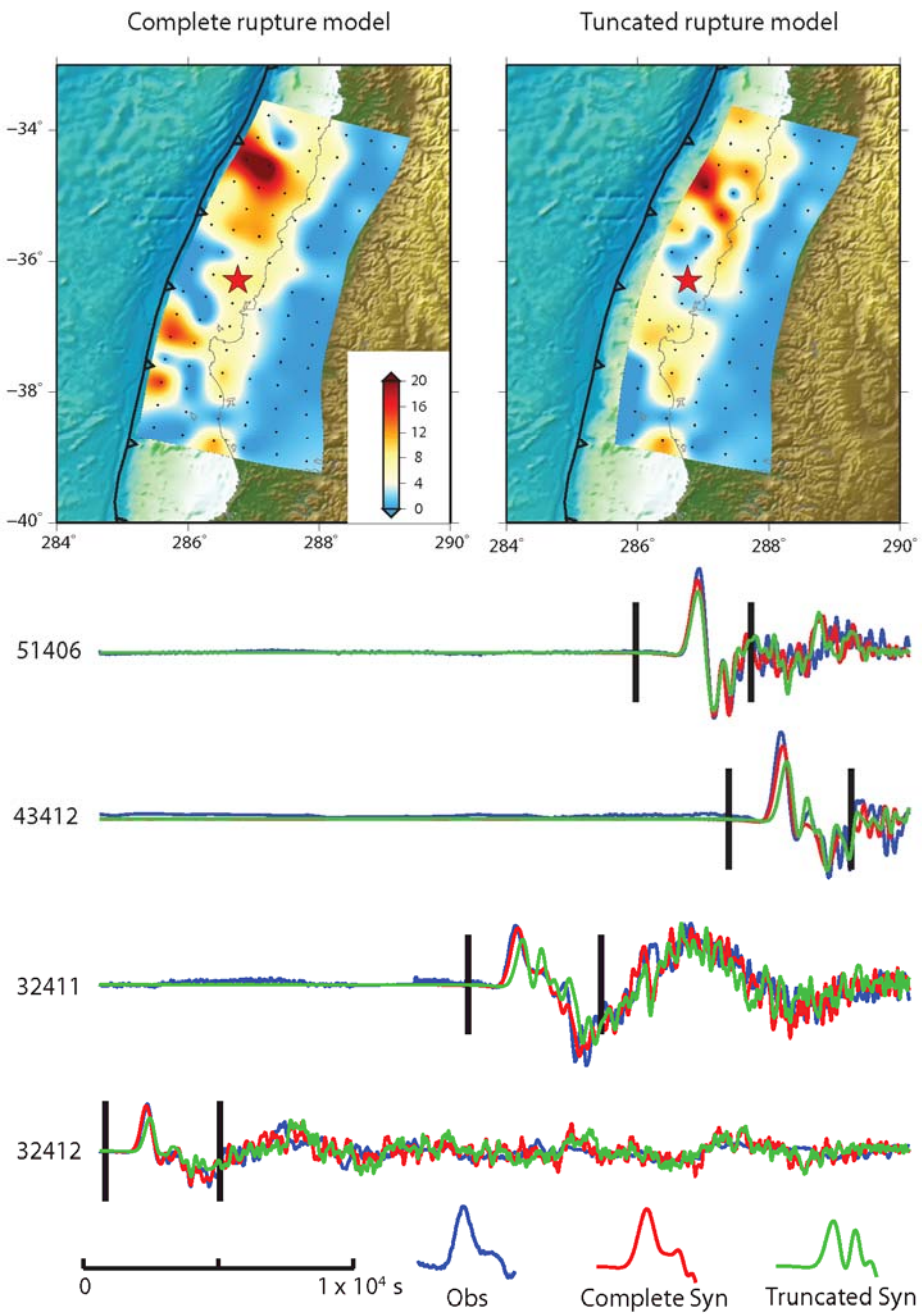

Figure 8.8. Inversion results using complete and truncated fault models are shown at the top. All parameters are identical in these inversions, except the shallowest row of subfaults is removed in the truncated fault model. Both models are plotted with the same color scale. Corresponding computed tsunami waveforms are plotted in red and green below, compared with the observed tsunami waveforms plotted in blue. The time window used in the joint inversion is bracketed by black bars. The time scale for all traces is indicated at the bottom.

Comparisons of our joint rupture model for the 2010 Maule event with results of other studies are shown in Figure 8.9. *Koper et al.* [2012] inverted teleseismic body waves; *Moreno et al.* [2012] inverted InSAR and campaign GPS statics; *Lorito et al.* [2011] inverted InSAR and tsunami data; *Delouis et al.* [2010] inverted hr-GPS, InSAR, and teleseismic body waves, and obtained good fits to teleseismic R_1 STFs. Other models based on geodetic inversions, e.g. *Tong et al.* [2010], *Pollitz et al.* [2011], *Vigny et al.* [2011] and *Lin et al.* [2013], were compared but are not shown here because their results are generally similar to *Moreno et al.* [2012].

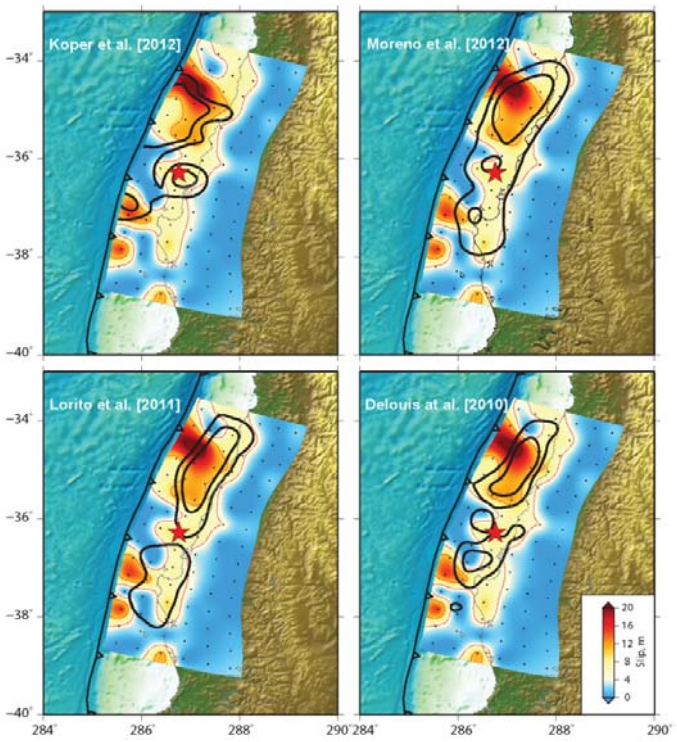

Figure 8.9. Comparison of slip models for the preferred joint inversion model and other finite-fault models. The preferred rupture model is plotted with blue-red color scale with 5 m and 10 m slip contours plotted in red. The 5 m and 10 m slip contours of other models are plotted in black in each panel. **a**) The rupture model of *Koper et al.* [2012] was inverted using teleseismic P and SH waves. **b**) The rupture model of *Moreno et al.* [2012] was inverted using campaign GPS and InSAR datasets. **c**) The rupture model of *Lorito et al.* [2011] was inverted with InSAR and tsunami observations. **d)** The rupture model of *Delouis et al.* [2010] was inverted with hr-GPS, teleseismic body waves, and InSAR datasets.

The geodesy-based inversions have similar along-strike slip patterns, but there are differences in the along-dip slip distributions. In the inversions of *Tong et al.* [2010], *Pollitz et al.* [2011], and *Lin et al.* [2013] there is no significant slip near the trench. However, the rupture model of *Moreno et al.* [2012] has ~ 5 m of slip near the trench in the north, as does the solution of *Vigny et al.* [2011], in the vicinity of our shallow slip patch. The larger slip in our model is almost invisible to the geodetic observations, and likely is mapped into a broadened region of large slip in the northern slip patch.

The teleseismic body wave inversions of *Lay et al.* [2011] and *Koper et al.* [2012] (Figure 8.9) are the only prior models that indicate more than 10 m of slip near trench. The teleseismic models differ primarily in their choice of rupture velocity, with the slip distribution expanding proportional to the assumed velocity. The slip distribution in our preferred model is more distributed than in that of *Koper et al.* [2012], due to the constraints from InSAR and hr-GPS observations. In the model of *Koper et al.* [2012] the slip near the trench is more smeared, similar to our regularized checker-board test, and our joint model resolves more along strike variation in the near-trench row. Our model has very little slip up-dip of the hypocenter, which is consistent with prior geodetic and seismic models, but appears to be less affected by inversion smoothing.

Lorito et al. [2012] included tsunami records in their inversion, but their model does not place significant slip near the trench. Many of the tsunami records analyzed by *Lorito et al.* [2012] are tide-gauge recordings, which require very detailed near coast bathymetry models for accurate modeling, and those stations along the Chilean

coast are not as sensitive to slip near the trench as the deep water DART observations. *Lorito et al*. [2012] use the same software (COMCOT) to compute their tsunami Green functions but did not apply velocity correction to the calculated Green's functions. As discussed above the uncorrected tsunami Green function are expected to have ~1% early arrival times, so unless they are corrected, the inversion will tend to place slip landward to match the onset time of the tsunami recordings. We find a corresponding tendency if we use the uncorrected tsunami Green functions in the inversion. The dispersion corrections clearly trade-off directly with the slip placement, but we believe that it is theoretically and observationally well-justified to make the corrections.

Comparisons of our preferred rupture model with aftershock characteristics from the GCMT catalog and National Earthquake Information Center (NEIC) bulletin are shown in Figure 8.10. The GCMT catalog comprises M_w >4.0 earthquakes, providing faulting patterns for all of the larger events. For this region the GCMT centroid locations are generally consistent with aftershock relocations using local seismic networks [*Lange et al.,* 2012] so we plot the best-double couple mechanisms at the centroid locations. The GCMT events have a clear complementary distribution with the co-seismic rupture pattern. The majority of thrusting aftershocks consistent with rupture of the plate interface are located in low-slip regions of the co-seismic rupture. The low-slip region up-dip from the hypocenter has concentrated thrust aftershock activity, suggesting that it is not a locked zone that would be likely to rupture in a large tsunami earthquake in the near future. The margins of regions of thrust

aftershocks are quite well defined by the 5 m slip contour of the rupture model. Larger thrust aftershocks also distribute outside the co-seismic slip zone to the north and south. Few thrust aftershocks are located down-dip from our co-seismic rupture model, and this region has significant afterslip reported by *Lin et al.* [2013], indicating predominance of down-dip creep. The lack of large thrust aftershocks within the co-seismic large-slip areas is consistent with near complete stress release.

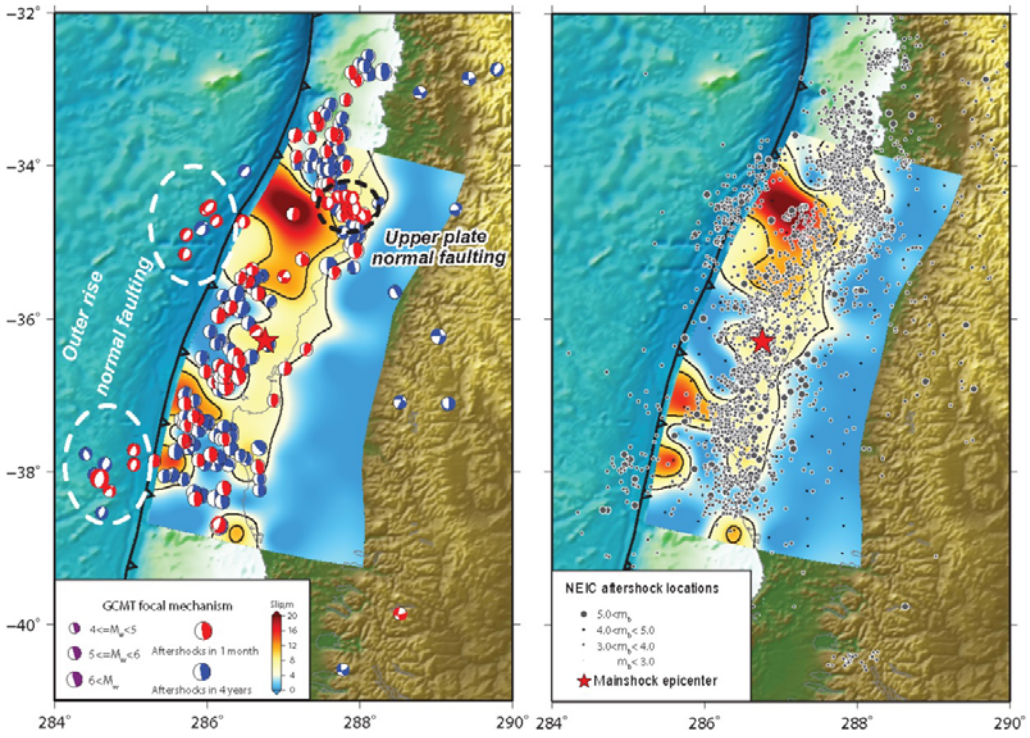

Figure 8.10. a) Focal mechanisms from the GCMT catalog are superimposed on the preferred rupture model. Aftershocks within and after the first month following the mainshock are plotted in red and blue, respectively. Focal mechanisms are scaled by their moment magnitude (M_w) with the scale shown in the legend. Two clusters of outer-rise normal faulting and one cluster of crustal normal faulting in the upper plate are outlined with white- and black-dashed circles. **b)** Aftershock epicenters from the NEIC catalog are plotted with black filled circles, with size scaled by the body wave magnitude (m_b). In both figures, the mainshock epicenter is marked with a red-filled star.

Two clusters of outer rise normal faulting events are identified near 35°S and 38°S, located seaward along the plate motion direction relative to the regions of large

near-trench slip. Outer rise normal faulting has been particularly extensive for several large earthquakes that rupture to the trench and for tsunami earthquakes that do the same. The bending of the subducting plate is expected to cause extensional faulting and horst and graben formation perpendicular to the plate convergence direction, accounting for trench slope normal faulting at shallow depth in the subducting plate [e.g., *Lay et al.,* 2009, 2011c; *Bilek et al.,* 2011; *Yue et al.,* 2014]. Very shallow coseismic slip appears to be particularly effective at triggering outer rise normal faulting seaward of the shallow slip region.

Another cluster of shallow normal faulting is apparent landward of the peak co-seismic slip in the northern part of the model (Figure 8.10). These events, relocated by *Lange et al.* [2012] and *Rietbrock et al.* [2012], mostly locate in the crust of the upper plate, and are likely induced by the concentrated dilatation stress change caused by the large-slip patch [*Ryder et al.*, 2012]. This zone of normal faulting was not active prior to the 2010 Maule event, consistent with a compressional environment before the main shock.

The NEIC catalog locations for aftershocks are also plotted in Figure 8.10. This includes many smaller earthquakes with m_b<4, a large percentage of which locate in the crust of the over-riding plate. The NEIC catalog thus has a different pattern from the GCMT catalog, with activity overlying the co-seismic large-slip area along the coast. The shallow micro-seismicity may indicate damage to the upper plate caused by co-seismic rupture, or a complex pattern of co-seismic stress adjustment [*Lange et al.,* 2012].

The slip distribution near the toe of the sedimentary prism during a large earthquake plays an important role in the tsunami generation and subsequent seismic hazard. If the rupture does not reach the trench, the possibility of a tsunami event in the future is raised, or the strain may be released in aseismic creep. The frictional stability of the shallowest portion of the megathrust has long been viewed as velocity strengthening with a well-defined seismic front, but that assumption is challenged by the observation of coseismic rupture reaching the trench for the 2011 Tohoku earthquake and the occurrence of a tsunami earthquake which ruptured along the toe of the sedimentary wedge along the Sunda trench after the 12 September 2007 M_w 8.5 and 7.9 Benkulu-Mentawai earthquake sequence [*Konca et al.,* 2008]. The slip distribution resolved by the geodetic observations on the Mentawai islands, within ~100 km from the trench establish there no co-seismic slip during the 2007 events reached the trench in the area that ruptured three years later in the 2010 M_w = 7.8 Mentawai tsunami earthquake. Concern about this possibility for the 2010 Maule rupture zone appears to be reduced given the large amount of slip that did reach the trench seaward of large-slip patches on the deeper megathrust, along with the intensive thrust faulting aftershock activity in the region that did not have large shallow co-seismic slip. This suggests that the potential for a tsunami earthquake along this region of the subduction zone is not high.

8.4. Conclusions

With joint inversion, using regional hr-GPS, teleseismic body waves, InSAR and tsunami observations, we obtained a robust and detailed rupture model of the 2010 Maule earthquake. The along strike slip distribution shows a bi-lateral rupture pattern, dominated the northward rupturing, which is consistent with previous geodesy based studies.

The resolution to slips near the trench is enhanced by the tsunami dataset, that in our preferred rupture model significant slips (> 10m) near the trench were resolved in the up-dip of both rupture patches. The near trench rupturing is consistent with the clustering of normal faulting in the outer-rise direction. The significant near trench rupturing, combined with intensive thrust faulting aftershock activity in the region that did not have large shallow co-seismic slip, reduced the potential of a consequence tsunami earthquake in the future.

The co-seismic slip pattern shows a clear complementary relationship with thrusting aftershocks. The lack of large thrust aftershocks within the co-seismic large-slip areas is consistent with near complete stress release.

8.5 Acknowledgements.

This work made use of GMT, SAC and Matlab software. The IRIS data management center was used to access the seismic data from Global Seismic Network and Federation of Digital Seismic Network stations. DART buoy data were obtained from the NOAA National Data Buoy Center. This work was supported in part by NSF grant EAR1245717 (T.L.).

8.6 References

Angermann, D., J. Klotz, and C. Reigber (1999), Space-geodetic estimation of the Nazca-South America Euler vector, *Earth Planet. Sci. Lett.*, *171*(3), 329-334. doi:10.1016/S0012-821X(99)00173-9.

Beck, S., S. Barrientos, E. Kausel, and M. Reyes (1998), Source characteristics of historic earthquakes along the central Chile subduction zone, *J. South American Earth Sci., 11*, 115-129.

Bilek, S. L., E. R. Engdahl, H. R. DeShon, and M. El Hariri (2011), The 25 October 2010 Sumatra tsunami earthquake: Slip in a slow patch, *Geophys. Res. Lett.*, *38*(14), L14306, doi:10.1029/2011GL047864.

Cubas, N., J.-P. Avouac, P. Souloumiac, and Y. Leroy (2013), Megathrust friction determined from mechanical analysis of the forearc in the Maule earthquake area, *Earth Planet. Sci. Lett., 381*, 92-103, doi:10.1016/j.epsl.2013.07.037.

Delouis, B., J.-M. Nocquet, and M. Vallée (2010), Slip distribution of the February 27, 2010 M_w= 8.8 Maule Earthquake, central Chile, from static and high−rate GPS, InSAR, and broadband teleseismic data, *Geophys. Res. Lett.*, *37*, L17305. doi:10.1029/2010GL043899.

Fujiwara, T., S. Kodaira, T. No, Y. Kaiho, N. Takahashi, and Y. Kaneda (2011), The 2011 Tohoku-Oki earthquake: displacement reaching the trench axis, *Science, 334*, 1240, doi:10.1126/science.1211554.

Hartzell, S. H., and T. H. Heaton (1983), Inversion of strong ground motion and teleseismic waveform data for the fault rupture history of the 1979 Imperial Valley, California, earthquake, *Bull. Seism. Soc. Amer.,73*(6A), 1553-1583.

Haberland, C., A. Rietbrock, D. Lange, K. Bataille, and T. Dahm (2009), Structure of the seismogenic zone of the southcentral Chilean margin revealed by local earthquake traveltime tomography, *J. Geophys. Res., 114, B01317,* doi:10.1029/2008JB005802.

Kido, M., Y. Osada, H. Fujimoto, R. Hino, and Y. Ito (2011), Trench-normal variation in observed seafloor displacement associated with the 2011 Tohoku-Oki

earthquake, *Geophys. Res. Lett., 38*, L24303, doi:10.1029/2011GL050057.

Kikuchi M., H. Kanamori, and K. Satake (1993). Source complexity of the 1988 Armenian earthquake: evidence for a slow after-slip event, *J. Geophys. Res., 98*, 15-797, doi:10.1029/93JB01568.

Konca, A. O., et al. (2008), Partial rupture of a locked patch of the Sumatra megathrust during the 2007 earthquake sequence, *Nature*, *456*, 631–635, doi:10.1038/nature07572.

Koper, K. D., A. R. Hutko, T. Lay, and O. Sufri (2012), Imaging short−period seismic radiation from the 27 February 2010 Chile (M_W 8.8) earthquake by back−projection of P, PP, and PKIKP waves, *J. Geophys. Res., 117,* B02308, doi:10.1029/2011JB008576.

Kozdon, J. E., and E. M. Dunham (2014), Constraining shallow slip and tsunami excitation in megathrust ruptures using seismic and acoustic waves recorded on ocean-bottom sensor networks, *Earth Planet. Sci. Lett., 396*, 56-65, doi:/10.1016/j.epsl.2014.04.001.

Lange, D., et al. (2012), Aftershock seismicity of the 27 February 2010 M_w 8.8 Maule earthquake rupture zone, *Earth Planet. Sci. Lett.*, *317-318*, 413-425, doi:10.1016/j.epsl.2011.11.034.

Lay, T. (2011), Earthquakes: a Chilean surprise, *Nature*, *471*(7337), 174-175, doi:10.1038/471174a.

Lay, T., H. Kanamori, C. J. Ammon, A. R. Hutko, K. Furlong, and L. Rivera (2009). The 2006-2007 Kuril Islands great earthquake sequence, *J. Geophys. Res., 114*, B113208, doi:10.1029/2008JB006280.

Lay, T., C. J. Ammon, H. Kanamori, K. D. Koper, O. Sufri, and A. R. Hutko (2010), Teleseismic inversion for rupture process of the 27 February 2010 Chile (M_w 8.8) earthquake. *Geophys. Res. Lett.*, *37,* L13301, doi:10.1029/2010GL043379.

Lay, T., C. J. Ammon, H. Kanamori, Y. Yamazaki, K. F. Cheung, and A. R. Hutko (2011a), The 25 October 2010 Mentawai tsunami earthquake (M_w 7.8) and the tsunami hazard presented by shallow megathrust ruptures, *Geophysical Research Letters*, *38*(6), L06302.

Lay, T., C. J. Ammon, H. Kanamori, L. Xue, and M. J. Kim (2011b), Possible large near-trench slip during the 2011 M_w 9.0 off the Pacific coast of Tohoku Earthquake. *Earth, Planets Space*, *63*(7), 687-692, doi:10.5047/eps.2011.05.033.

Lay, T., C. J. Ammon, H. Kanamori, M. J. Kim, and L. Xue (2011c). Outer trench-slope faulting and the 2011 M_w 9.0 off the Pacific coast of Tohoku Earthquake, *Earth, Planets, and Space*, *63*(7), doi:10.5047/eps.2011.05.006, 713-718.

Lin, Y. N. N., et al. (2013), Coseismic and postseismic slip associated with the 2010 Maule Earthquake, Chile: Characterizing the Arauco Peninsula barrier effect. *J. Geophys. Res.*, *118*, doi:10.1002/jgrb.50207.

Lorito, S., et al. (2011), Limited overlap between the seismic gap and coseismic slip of the great 2010 Chile earthquake, *Nature Geosci.*, *4*(3), 173-177. doi:10.1038/ngeo1073.

Maeda, T., T. Furumura, S. Sakai, and M. Shinohara (2011), Significant tsunami observed at ocean-bottom pressure gauges during the 2011 off the Pacific coast of Tohoku earthquake, *Earth Planets Space, 63*, 803-808, doi:10.5047/eps.2011.06.005.

Mei, C. C. (1989). The applied dynamics of ocean surface waves (Vol. 1). World scientific.

Miyazaki, S. I., J. J. McGuire, and P. Segall (2011), Seismic and aseismic fault slip before and during the 2011 off the Pacific coast of Tohoku Earthquake, *Earth Planets Space*, *63*(7), 637. doi:10.5047/eps.2011.07.001.

Moreno, M., M. Rosenau, and O. Oncken (2010), 2010 Maule earthquake slip correlates with pre-seismic locking of Andean subduction zone, *Nature*, *467*, 198-202, doi:10.1038/nature09349.

Moreno, M., D. Melnick, M. Rosenau, J. Baez, J. Klotz, O. Oncken, and H. Hase (2012), Toward understanding tectonic control on the M_w 8.8 2010 Maule Chile earthquake, *Earth Planet. Sci. Lett.*, *321-322*, 152-165. doi:10.1016/j.epsl.2012.01.006.

Ohta, Y., et al. (2012), Quasi real-time fault model estimation for near-field tsunami

forecasting based on RTK-GPS analysis: application to the 2011 Tohoku-Oki earthquake (M_w 9.0), *J. Geophys. Res., 117*, doi:10.1029/2011JB008750.

Okada, Y. (1992), Internal deformation due to shear and tensile faults in a half-space, *Bull. Seism. Soc. Amer., 82,* 1018-1040.

Pollitz, F. F., et al. (2011), Coseismic slip distribution of the February 27, 2010 M_w 8.8 Maule, Chile earthquake, *Geophys. Res. Lett.*, *38*, L09309, doi:10.1029/2010GL047065.

Rietbrock, A., I. Ryder, G. Hayes, C. Haberland, D. Comte, S. Roecker, and H. Lyon−Caen (2012), Aftershock seismicity of the 2010 Maule M_w= 8.8, Chile, earthquake: Correlation between co-seismic slip models and aftershock distribution? *Geophys. Res. Lett.*, *39,* L08310*,* doi:10.1029/2012GL051308.

Ryder, I., et al. (2012), Large extensional aftershocks in the continental forearc triggered by the 2010 Maule earthquake, Chile, *Geophys. J. Int., 188*, 879-890, doi:10.1111/j.1365-246X.2011.05321.x.

Satake, K., Y. Fujii, T. Harada, and Y. Namegaya (2013), Time and space distribution of coseismic slip of the 2011 Tohoku earthquake as inferred from tsunami waveform data, *Bull. Seism. Soc. Amer., 103*, 1473-1492, doi:10.1785/0120120122.

Shimada, M., T. Tadono, and, and A. Rosenqvist (2010), Advanced Land Observing Satellite (ALOS) and Monitoring Global Environmental Change, *Proc. IEEE,* 98(5), 780–799, doi:10.1109/JPROC.2009. 2033724.

Simons, M., et al. (2011), The 2011 magnitude 9.0 Tohoku-Oki earthquake: Mosaicking the megathrust from seconds to centuries. *Science*, *332*, 1421-1425, doi:10.1126/science.1206731.

Tanioka, Y., and K. Satake (1996), Tsunami generation by horizontal displacement of ocean bottom, *Geophys. Res. Lett.*, *23*, 861-864, doi:10.1029/96GL00736.

Tassara, A., and A. Echaurren (2012), Anatomy of the Andean subduction zone: three‐dimensional density model upgraded and compared against global‐scale models, *Geophys. J. Inter.*, *189*, 161-168. doi:10.1111/j.1365-246X.2012.05397.x.

Tong, X., et al. (2010), The 2010 Maule, Chile earthquake: Downdip rupture limit revealed by space geodesy, *Geophys. Res. Lett.*, *37*, L24311, doi:10.1029/2010GL045805.

Tsai, V. C., J. P. Ampuero, H. Kanamori, and D. J. Stevenson (2013), Estimating the effect of Earth elasticity and variable water density on tsunami speeds, *Geophys. Res. Lett.*, *40*, 492-496. doi:10.1002/grl.50147.

Vigny, C., A. Rudloff, J. C. Ruegg, R. Madariaga, J. Campos, and M. Alvarez (2009), Upper plate deformation measured by GPS in the Coquimbo Gap, Chile. *Phys. Earth Planet. Inter., 175*, 86-95, doi:10.1016/j.pepi.2008.02.013.

Vigny, C., et al. (2011), The 2010 M_w 8.8 Maule mega-thrust earthquake of Central Chile, monitored by GPS, *Science*, *332*, 1417-1421. doi:10.1126/science.1204132.

Wang, R. (1999), A simple orthonormalization method for stable and efficient computation of Green's functions, *Bull. Seism. Soc. Amer.*, *89*, 733-741.

Wang, R., F. L. Martín, and F. Roth (2003), Computation of deformation induced by earthquakes in a multi-layered elastic crust—FORTRAN programs EDGRN/EDCMP, *Computers & Geosciences*, *29*, 195-207. doi:10.1016/S0098-3004(02)00111-5

Watada, S., S. Kusumoto, and K. Satake (2014), Traveltime delay and initial phase reversal of distant tsunamis coupled with the self‐gravitating elastic Earth, *J. Geophys. Res.*, doi:10.1002/2013JB010841

Yamazaki, Y., T. Lay, K. F. Cheung, H. Yue, and H. Kanamori (2011), Modeling near‐field tsunami observations to improve finite‐fault slip models for the 11 March 2011 Tohoku earthquake, *Geophys. Res. Lett.*, *38*, L00G15, doi:10.1029/2011GL049130.

Yamazaki, Y., K. F. Cheung, G. Pawlak, and T. Lay (2012), Surges along the Honolulu coast from the 2011 Tohoku tsunami, *Geophys. Res. Lett.*, *39*, L09604, doi:10.1029/2012GL051624.

Yue, H., and T. Lay (2011), Inversion of high-rate (1 sps) GPS data for rupture process of the 11 March 2011 Tohoku earthquake (M_w 9.1), *Geophys. Res. Lett.*, *38*, L00G09, doi:10.1029/2011GL048700.

Yue, H. and T. Lay (2013), Source rupture models for the M_w 9.0 2011 Tohoku earthquake from joint inversions of high-rate geodetic and seismic data, *Bull. Seis. Soc. Amer.*, *103*, 1242-1255, doi:10.1785/0120120119.

Yue, H., T. Lay, L. Rivera, Y. Bai, Y. Yamazaki, K. F. Cheung, E. M. Hill, K. Sieh, W. Konko and A. Muhari (2014), Rupture process of the 2010 M_w 7.8 Mentawai tsunami earthquake from joint inversion of near-field hr-GPS and teleseismic body wave recordings constrained by tsunami observations, *J. Geophys. Res*, revised.

Yue, H., T. Lay, S. Y. Schwartz, L. Rivera, M. Protti, T. H. Dixon, S. Owen, and A. V. Newman (2013), The 5 September 2012 Nicoya, Costa Rica M_w 7.6 earthquake rupture process from joint inversion of high-rate GPS, strong-motion, and teleseismic P wave data and its relationship to adjacent plate boundary interface properties, *J. Geophys. Res*., 118, 5453-5466, doi:10.1002/jgrb.50379.

Chapter 9

Conclusions and Future Works

9.1 Summary of main Results

In this thesis, I show the development of our joint inversion approach and a few important accomplishments and conclusions are summarized as following

1. Hr-GPS, as a non-clipped and broad-band monitoring method of co-seismic ground displacement field, improves the inversion stability. Fitting to hr-GPS dataset, required the static and dynamic displacement to be simultaneously modeled by the inversion model and naturally weighted. Such inversion presents high stability that is independent of some key inversion parameters, e.g. rupture velocity.

2. Joint inversion with hr-GPS, teleseismic body and surface waves, static geodetic and tsunami observations, exploit intrinsic information lies in each dataset, yielding stable and high-resolution rupture model.

3. Tsunami dataset has improved resolution to the near trench rupture, compared with other mentioned observations. Therefore joint inversion with tsunami dataset has stable resolution to the near trench rupturing.

4. In several case studies, when we have intense regional observations to resolve stable rupture pattern, i.e. 2012 Costa Rica event, 2010 Mentawai event and 2010 Maule event, we found strong complementary pattern between the main shock rupture pattern and other seismic activities, e. g. aftershocks, slow-slip events, low-frequency earthquakes. It indicates the stress releasing behavior on the fault interface is mainly controlled by the interface property.

5. During great thrusting events, the area near the trench could either rupture co-seismically, e.g. 2010 Maule earthquake and 2011 Tohoku earthquake, or separately from the main event, i.e. 2007 Bengkulu – 2010 Mentawai earthquake sequence. Detailed co-seismic rupture pattern of large thrusting events need to be investigated to forecast the hazard of tsunami earthquake.

Given multi-scale and crossing-disciplinary observations of large earthquakes in current epoch, we could monitor the rupture pattern of most earthquakes using multiple methods. It makes joint inversion applicable to most large earthquakes. My researches show that joint inversion is efficient to resolve robust and detailed finite fault model. It reveals more information about the co-seismic energy release. To compare with other seismic or non-seismic activities, a robust rupture model is needed to produce un-biased comparison, thus to unveil the intrinsic physics of the rupture process.

9.2 Potential Future Works

My current joint inversion approach combines commonly used observations; however, more observations, e.g. ground tilting, gravity, strain meter observations still could be added in the joint inversion algorithm. I expect variety of observations could reveal more details of the co-seismic rupture pattern.

Qualitatively, we can understand the contributions from each dataset in a joint inversion, while more quantitative calculation about the resolution of each dataset are still needed to guide the weighting between datasets and parameterization of the fault model. I will focus on Evaluating the accuracy and robustness of different inversion techniques, including linear, non-linear inversion techniques, time domain and frequency domain inversion techniques for multiple data types with complementary sensitivity to source and structural properties.

In all of my current inversion works, 1D layered structure is applied to present the velocity structure in the source region. Such simplification is a compromise with the knowledge about the source region and the computational ability. In my future works I will try to us 3D Green's functions in both teleseismic and regional inversion techniques to resolve more robust and detailed rupture models.

Current finite fault model parameterize the fault model in space and time domain,

which generally have thousands of parameters in inversion. Such parameterization method may be redundant to the effective information in the data. I will try to formulate representation of finite fault model parameters in the wave-number domain, to enable inversions in a compressive sensing algorithm. Such representation is supposed to be more efficient to represent the fault model, which may lead to more stable representations of the finite source parameters.

Furthermore, all my current inversion is limited in the kinematic inversion branch, that no dynamic constrains are applied. I am expecting adding more dynamic constrains will make the finite fault model more physically realistic, thus further reveal the physics of the co-seismic rupture process, as also the physics in earthquake cycle.